Confined Flow Vortex Breakdown Study

and

Modeling of Mixing in a Stirred Vessel

A thesis submitted

by

Lewis Mununga **(B.Eng., M.E.)**

for the degree of

Doctor of Philosophy

Department of Mechanical Engineering

Monash University

May 2005

Statement of Originality

This thesis contains no material that has been accepted for the award of a degree or diploma in this or any other university. To the best of the candidate's knowledge and belief, this thesis contains no material previously published or written by another person except where due reference is made in the text of the thesis.

…….

Candidate: Lewis Mununga

31 May 2005

Acknowledgements

As I reach the end of this taxing project, I am obliged to thank many people who have provided a positive contribution during the course of this program; some in a small way while others in a very important way. Obviously, it is not possible to mention everybody. I am deeply indebted to my supervisors Professor Kerry Hourigan and Associate Professor Mark C. Thompson for their guidance and encouragement throughout my research. Professor Kerry Hourigan has been responsible for instigating the investigation of vortex breakdown.

I would like to thank the Department of Mechanical Engineering, through the Head, Professor John Sheridan, for providing a good research environment. Without the good work of the staff of the Department of Mechanical Engineering Workshop, the experimental part of this research could not have been performed. In particular, I am grateful to Mr. Daniel Curtis for his professionalism and never turning down any of my numerous job requests.

I am grateful to Dr. Thomas Leweke for his assistance in the early stages of the experimental research. I also extend my gratitude to my office mate and colleague Shaun Johnson for developing Matlab post-processing codes and also being there as a friend.

The financial assistance provided through the International Postgraduate Research Scholarship (IPRS), the Monash Graduate Scholarship (MGS), the Monash Departmental Scholarship (MDS) and the Travel Grant is very much appreciated.

I would like to thank in a special way Dr Emmanuel Laryea for proof-reading the bulk of the manuscript. I also appreciate the effort of Dr Moses Khor and Mr Kwame Mfodwo for proof-reading sections of the manuscript. Your collective effort helped to reduce the number of grammatical and typographical mistakes in the thesis.

To many of my colleagues in the Department of Mechanical Engineering, friends at

Church of Christ Fellowship Clayton and across Melbourne, who in one way or another helped me feel at home, I say thank you.

I want to whole heartedly thank my family for their love and enduring sacrifice of spending extended periods without me at home. Dorothy, my dear wife, Timothy, Isaac, Patrick and Stella, my children: you are the world to me. Finally, I am grateful to my departed parents for giving me a good foundation upon which my whole life has been based.

Abstract

The research presented in this thesis has two components: the first component deals with vortex breakdown in a closed cylinder and the second is concerned with mixing in a closed cylinder. The study of vortex breakdown is a special case of mixing when a plain disk agitator is used. In which case, the plain disk diameter is equal to the cylinder diameter and is located just above the liquid, assuming the position of the top lid.

Research in the area of vortex breakdown in a closed cylinder has for a long time been devoted to understanding the conditions that are favourable to its formation and sustenance. Vortex breakdown has been known to be beneficial in some applications and harmful in others. It is only in last two decades that investigators have started exploring ways of controlling the vortex breakdown phenomenon.

The study reported in this thesis proposed a new method of controlling vortex breakdown in a closed cylinder with a rotating top endwall and was investigated both experimentally and numerically. In this method, control of vortex breakdown was achieved by co-rotating and counter-rotating a small disk flush mounted in the bottom endwall. Five control disks of varying sizes were used to investigate the effect of the disk size on the vortex breakdown bubble. The bottom endwall was also employed in co- and counter-rotation for comparison. An important aim of this study was to evaluate the effectiveness of this technique by comparing its input power requirement with that of alternative methods.

Results have shown that a condition for the onset of vortex breakdown for the case where only one endwall is rotating is that the swirl number S_n should be equal to unity. This condition was found to be almost similarly for the case of vortex breakdown in the presence of co-rotation. It was found that co-rotation of a control disk and the bottom endwall tend to precipitate the onset of vortex breakdown as well as enhance the

breakdown bubble. However, counter-rotation delayed the onset of vortex breakdown and tended to suppress the breakdown bubble. The results have shown that it is possible to enhance the size of the breakdown bubble so as to cover a substantial volume inside the closed cylinder. Such a large volume of controlled laminar flow is attractive for applications involving cell or tissue growth in bioreactors.

In general, co-rotation and counter-rotation of control disks was more power efficient than both the conventional method of controlling vortex breakdown (variation of the speed of the rotating endwall) and the use of the bottom endwall. The control disk d4 (≈ 20% of the endwall diameter D) was assessed to be more power efficient in co-rotation while d5 (≈ 30% of D) was the best performer in counter-rotation. It is clear that no single control disk was the most suitable size for both co-rotation and counter-rotation. This finding suggests that a careful investigation is needed to establish the most efficient control disk size for a particular application.

The study of mixing in a closed cylinder was conducted only numerically. A mixing vessel without baffles was employed while agitation for mixing was achieved by using first a plain disk and then a bladed paddle impeller. In the study of mixing with a plain disk, the locus of the recirculation center was studied. In addition, the effect of the off-bottom clearance on some mixing global parameters was examined. It was found that increases in the Reynolds number caused the recirculation centre to initially move radially away from the axis of rotation but axially closer to the impeller. Further increases in the Reynolds number tended to move the recirculation centre in the opposite direction. In addition, the off-bottom clearance was observed to influence both the discharge and circulation flow rates.

In the study of mixing with a bladed impeller, the effect of the blade width was investigated. Here, the rotating reference frame method was employed during the solution process. Numerical results have shown that for impellers with blade widths less than about 13%, increases in the blade width generated corresponding increases in the pumping number, power number, pumping effectiveness and pumping efficiency. Both he the pumping effectiveness and pumping efficiency were observed to be constant in the turbulent region for blade widths between 13% and 40% of the cylinder height. The results suggest that the impeller with a 13% blade width was optimum.

Publications

MUNUNGA, L., HOURIGAN, K. & THOMPSON, M.C. (2001), Comparative study of flow in a mixing vessel stirred by a solid disk and a four bladed impeller. *In Proceedings of the 14th Australasian Fluid Mechanics Conference*, Adelaide, Australia, 9-14m December.

MUNUNGA, L., HOURIGAN, K. & THOMPSON, M.C. & JOHNSON, S. (2003), Numerical investigation of discharge flow and circulation flow in an unbaffled mixing vessel agitated by a plain disk. *In Proceedings of the 2nd International Conference on Heat Transfer, Fluid Mechanics and Thermodynamics (HEFAT)*, Victoria Falls, Zambia, 23-26 June.

MUNUNGA, L., HOURIGAN, K. & THOMPSON, M.C. (2003), Numerical study of the effect of blade size on pumping effectiveness of a paddle impeller in an unbaffled mixing vessel. *In Proceedings of the 3rd International Conference on CFD in the Minerals and Process Industries*, CSIRO, Melbourne, Australia, 10-12 December.

MUNUNGA, L., HOURIGAN, K., THOMPSON, M.C. and LEWEKE, T. (2004), Control of vortex breakdown in a torsionally driven closed cylinder by addition of swirl using a small disk. *In Proceedings of the 2004 ASME Heat Transfer/Fluids Engineering Summer Conference*, Charlotte, North Carolina, USA, July 11-15.

MUNUNGA, L., HOURIGAN, K., THOMPSON, M.C. & LEWEKE, T. (2004), Vortex breakdown control by swirl addition using a small disk, *Physics of Fluids Journal*, *vol. 16, no. 12*, p. 4750-4753.

Nomenclature

A	Area
B	Blade width
C	Off-bottom impeller clearance
	Streamline
	Relative speed of wave propagation
CR	Co-rotation
CTR	Counter-rotation
D	Impeller or disk diameter
$d\#$	Control disk number (1 through to 5)
D	Tank diameter
F	Force
Fr	Froude number
G	Gravitational acceleration
H	Free surface deformation
	Height along the swirl axis
H	Cylinder height
K	Ratio between maximum swirl velocity and axial velocity
K	Twist parameter
MRF	Multiple reference frames
N	Rotational speed
	Non-dimensional parameter that characterises critical flow

Np	Power number
Nq	Flow number
Nqc	Circulation flow number
Nqp	Pumping flow number
P	Fluid pressure
P	Fluid power
PBT	Pitch blade turbine
Q	Flow rate
Qc	Circulation flow rate
Qp	Pumping flow rate
R	Radial position
Rc	Vortex core radius
R	Cylinder radius
Re	Reynolds number
	Global Reynolds number
RCL	Lower recirculation centre
RCU	Upper recirculation centre
RRF	Rotating reference frame
S	Source term
SM	Sliding mesh
Sn	Swirl number
T	Non-dimensional time
T	Torque
	Mixing tank height
U	Fluid velocity

U	Velocity vector
V	Y-component of velocity
V	Velocity
Va	Axial velocity
Vs	Swirl velocity
VBO	Vortex breakdown onset
VTC	Viscosity temperature gradient
Vtip	Tip velocity
W	Z-component of velocity
	Azimuthal or swirl velocity
W	Blade width
w'	Axial velocity
z'	Normalized distance from the bottom endwall
Z	Co-ordinate along the swirl axis
	Greek letters
Γ	Diffusion coefficient
E	Angular rotation ratio
	Temperature gradient
He	Pumping effectiveness
Λp	Pumping efficiency
M	Fluid absolute (dynamic) viscosity
ν	Fluid kinematic viscosity
P	Fluid density
τ	Shear stress

Φ	Angle
Ω	Angular velocity
Ω	Angular velocity
	Subscripts
A	Axial
B	Bottom endwall
C	Bubble centre
	Critical
Db	Bottom endwall
d#	Control disk number (1 through to 5)
D	Downstream stagnation point
M	Momentum
NC	No control
Nv	No vortex breakdown
R	Small or control disk
Sb	Side wall and Bottom endwall
S	sidewall
	Swirl
T	Top endwall
U	Upstream stagnation point
VBO	Vortex breakdown onset

Contents

Chapter 1
Introduction

1.1 Prelude

Vortex flows are present in many engineering applications as well as natural flows involving swirling motion of fluid. In nature for instance, vortical flows take place in situations such as hurricanes, tornadoes and ocean currents. In the field of technology, vortex flows cover a wide range of areas including geophysics, aerodynamics, hydraulics and the vast area of process industry. Typically, wakes behind ships, planes and cars, and rolling flow over aircraft delta wings, as shown in Figure 1.1, are among the numerous examples. This goes to show how widespread and, therefore, important are vortex flows in our daily lives.

There are some particular flow conditions that are favourable to structural changes of vortex flows. One such change to the vortex core is known as vortex breakdown. The phenomenon of vortex breakdown was first observed by Peckham and Atkinson (1957). They discerned the breakdown of a vortex in the tip vortices of a delta wing. Since then, there have been many studies devoted to understanding this vortex breakdown phenomenon (Syred and Beer (1973a); Cassidy and Falvey (1970); Syred and Beer (1973b); Escudier and Zehnder (1982)). The work of Hall (1972) provides an insight about these early studies on vortex breakdown.

Vortex breakdown is known to occur in both external flows, such as flow over aircraft wings, as well as internal flows, such as rotating flow in a swirl burner. The present study investigates vortex breakdown in a closed cylinder, which is a simplified and well controlled environment suited for experimental and numerical research.

In this chapter, a brief background to the study of vortex breakdown is presented followed by a description of the development of the flow structure inside the cylinder with a rotating endwall. Some areas of real life application where vortex breakdown occurs and its merits are presented. The chapter concludes by presenting the main objectives of the study, followed by an outline of the thesis layout.

Figure 1.1 NASA F/A-18 Research vehicle at 20 degrees angle of attack showing a strake vortex using smoke. The picture also shows vortex breakdown towards the trailing edge.

Many theoretical studies on vortex breakdown were carried out in the period spanning the sixties to the eighties (Jones(1960), (1964); Gartshore (1962), (1963); Escudier & Keller (1983), (1985)). These studies focused on formulating a theoretical basis for understanding the vortex breakdown formation and its sustenance. This phenomenon is so complex that to date no one has been able to propose a universally acceptable explanation to the question as to what is responsible for vortex breakdown. All theories

that have been proposed so far only go as far as providing a partial explanation while at the same time attracting criticism from other investigators.

Over the past few decades, another group of researchers have devoted their time to describing the flow structure within the breakdown (Faler and Leibovich (1978); Nakamura *et al.* (1986); Payne *et al.* (1988)). While a number of authors have attempted to define vortex breakdown, one of the simplest explanations for this very important physical phenomenon was proposed by Leibovich (1978). He described vortex breakdown as a change in the structure of a vortex as a direct result of a variation in the characteristic ratio of tangential to axial velocity components. In other words, Leibovich means that vortex breakdown is initiated when the Swirl number exceed a critical value. Therefore, vortex breakdown can be considered as an abrupt change in the structure of a vortex core that occurs when a slender vortex is embedded in an axial flow with a gradient.

In the past decade and a half, most studies have continued to focus on the theoretical aspects. Some studies have used physical experiments (Spohn *et al.* (1998); Pereira and Sousa (1999b); Liu *et al.* (2003b)) Spohn *et al.* (1998; Pereira and Sousa (1999a) while others have employed numerical modeling to further the understanding of this breakdown phenomenon (Sorensen and Christensen (1995); Sotiropoulos and Ventikos (2001); Thompson and Hourigan (2003)). It is also encouraging to note that a number of researchers have devoted their time to the important aspect of vortex breakdown control. External flow vortex breakdown control can be traced as far back as the second half of the eighties Schmucker and Gersten (1988), whereas significant studies on internal flow vortex breakdown control, especially those in closed cylinders, have only been published towards the middle of the last decade (Valentine and Jahnke (1994); Bhattacharyya and Pal (1998); Herrada and Shtern (2003a)). The need to control vortex breakdown will be briefly discussed in section 1.3.

As mentioned earlier, vortex breakdown occurs in both external as well as enclosed flows. The application of both types of vortex breakdown will be elaborated later in section 1.3. Enclosed flow studies, within which the present work falls, are conducted in a closed environment such as a closed cylinder with a rotating endwall. The presentation of an alternative method of controlling confined flow vortex breakdown was the subject

of this research and the details follow in the remainder of this thesis.

1.2 Flow Structure

1.2.1 Development of Flow in a Closed Cylinder

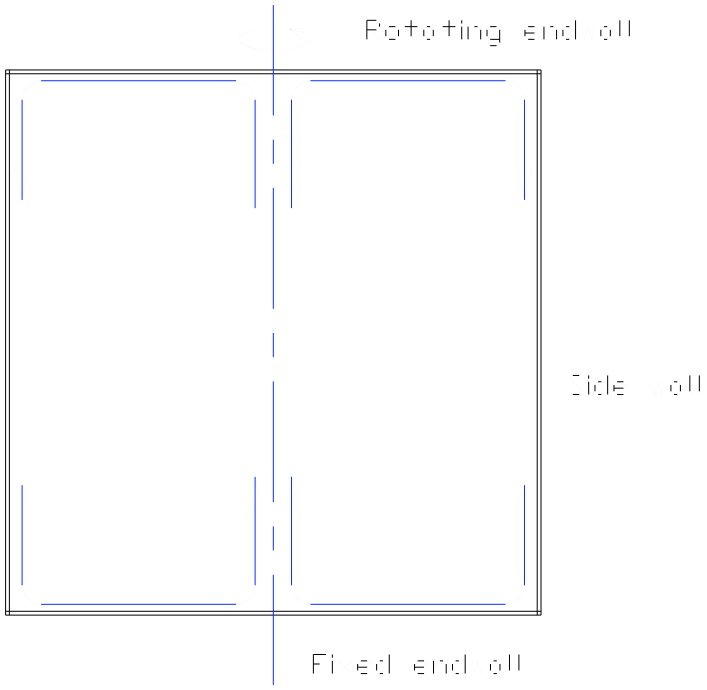

Figure 1.2 Meridional view of the flow structure in a closed cylinder driven by one endwall rotation.

When one endwall is rotating at relatively low Reynolds number a vortical flow forms around the axis of rotation, while two identical circulation loops appear in each half (left and right) of the cylindrical working section (Figure 1.2). These two loops constitute a three dimensional toroidal swirling flow. The above flow structure comes about as a result of the rotating endwall behaving like a centrifugal pump. Attached to the disk is a boundary layer known as the Ekman layer. The fluid in this layer is thrown outward in a spiral motion. Upon meeting the cylindrical vertical wall, the fluid is deflected and subjected to a downward motion along the wall. The fluid next to the vertical wall forms a boundary layer known as the Stewardson layer. The fluid is transported until it reaches

the bottom endwall where it is again deflected, but this time towards the swirl axis. Along the bottom wall, it forms an Ekman layer that is responsible for inward pumping. Since the bottom endwall is stationary, the fluid velocity and consequently the centrifugal force are greatly reduced. The above reductions are compensated by an increase in the pressure gradient in the radial direction. This radial pressure gradient is responsible for the radial pumping effect of the Ekman layer next to the bottom endwall. As the fluid reaches the axis of rotation the two streams, one from the left and the other from the right, merge to form a core vortex around the axis moving the fluid upwards back to the rotating endwall. The rising fluid compensates for the fluid being pumped outwardly by the rotating endwall and this completes the cycle.

Gradually increasing the rotational speed of the rotating endwall causes a wavy like filament of fluid to form within the central portion of the core vortex. This leads to the formation of a stagnation point along the axis of rotation between the mid-horizontal plane and the non-rotating endwall. The stagnation point is then followed, in the downstream direction, by a low velocity recirculation region. With further increases in the rotation rate, the recirculation region grows taking the shape of a greatly swollen stream surface commonly known as the breakdown bubble. The bubble in Figure 1.3 exhibits some degree of symmetric about the rotation axis, but as the Reynolds number increases it tends to lose its symmetricity at the downstream.

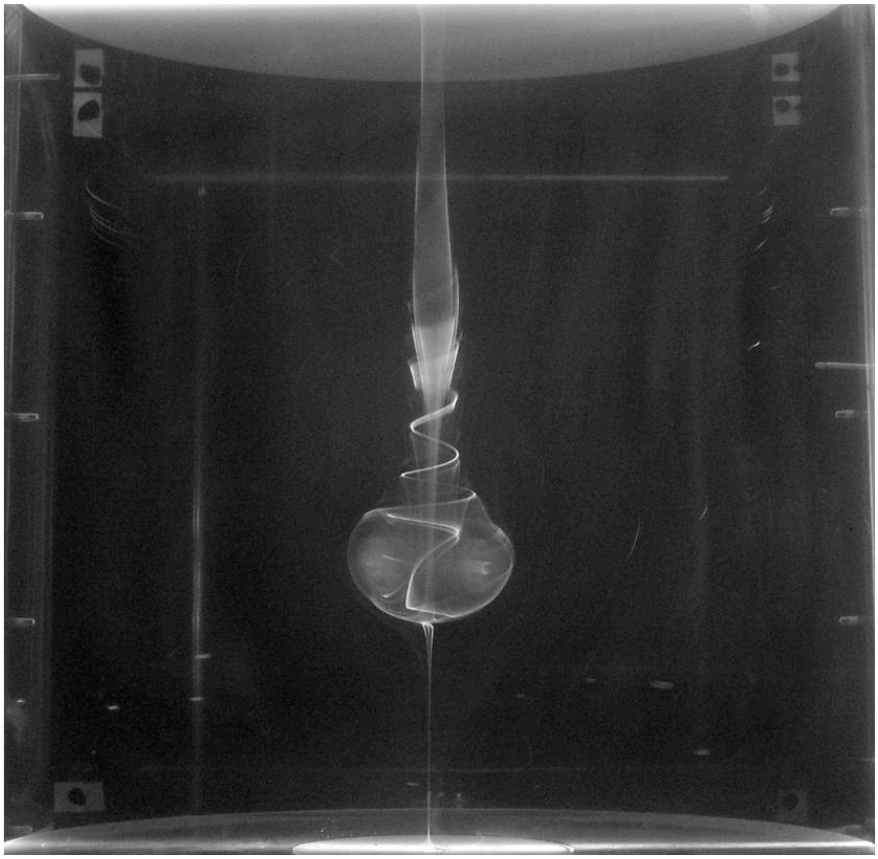

Figure 1.3 Flow visualisation using fluorescent dye technique in a closed cylinder with a rotating top endwall.

Figure 1.4 gives a complete picture of the vortex breakdown evolution as the Reynolds number and aspect ratio assume different values. The parameter space reveals that there are distinct regions where there is no bubble, one, two or three bubbles and it also separates the steady region from the unsteady region. Spohn *et al.* (1998) performed numerical calculations to confirm the existence of these different flow states by comparing with the now regarded as benchmark data of Escudier (1984).

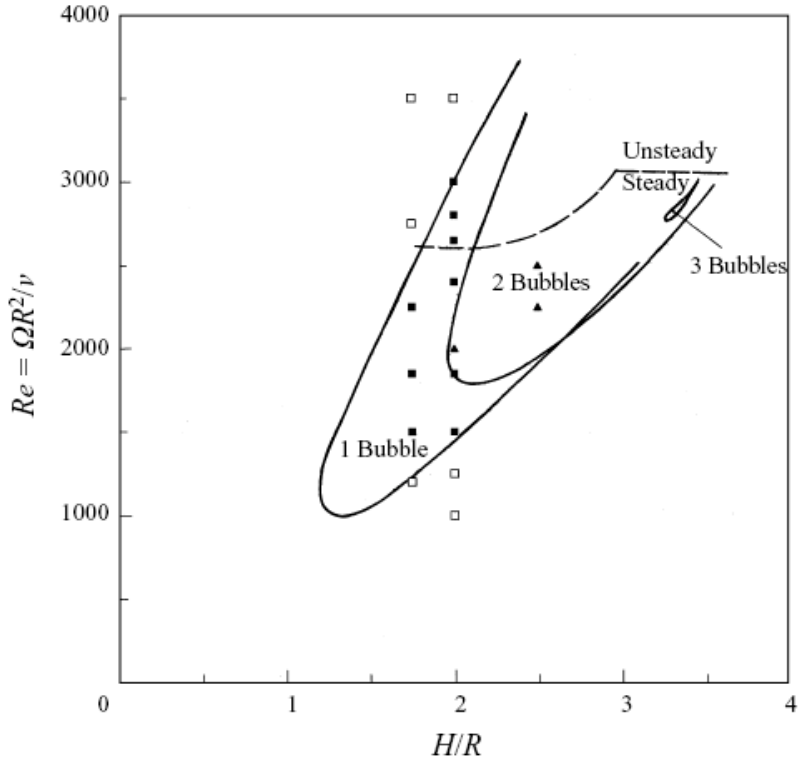

Figure 1.4 Flow states in a parameter space of Reynolds number and aspect ratio (H/R). Spohn et al. (1998) data represented by symbols: □, no vortex breakdown bubble; ■, one bubble; ▲: two bubbles; are compared with Escudier (1984) results.

1.2.2 Flow Structure in the Vortex Breakdown Region

The flow field near a vortex breakdown can be thought of being made up of three main regions namely, the approach or upstream, the breakdown and the downstream regions (Leibovich (1978)). These three distinct parts encompassing the axis of rotation and the vortex breakdown are described in the following sections:

(i) Upstream Region

This region consists of the main core of the approaching vortex and is also known as the vortex core. The flow in the vortex core is characterised by a sudden rise in axial velocities, followed by an equally sudden drop in axial velocity. The axial velocity profiles, especially along the swirl axis, in this jet-like core vortex have been observed

to be higher than outside the core. The flow is generally laminar or moderately turbulent, that is with relatively low turbulent intensities.

(ii) Breakdown Region

This region is characterised by a significant change in the vortex core structure and can sometimes stretch up to 5 vortex core diameter in length along the axis. It is subdivided into three zones. In the first zone, the approaching core vortex flow is decelerated until the axial velocity along the axis is reduced to zero giving rise to the upstream stagnation point. In the second zone, the near axis flow undergoes divergence followed by convergence leading to flow reversal. The flow Reynolds number determines the extent of the vortex breakdown and also the position of the upstream stagnation point. The flow in this two-celled recirculation region is neither axisymmetric nor steady, as noted by Sarpkaya (1971) and Faler and Leibovich (1978). Some researchers have reported that this recirculation region is isolated from the flow in the other parts of the tank, hence closed (Escudier (1984); Liu *et al.* (2001)). Others have argued that the breakdown bubble is an open region (Spohn *et al.* (1998); Sotiropoulos and Ventikos (1998); Sotiropoulos and Ventikos (2001)). These aspects will be discussed in more detail in the next chapter. In the third zone a downstream stagnation point is present and the flow near the axis reverts to its original direction and undergoes some transition leading to turbulence, depending on the Reynolds number.

(iii) Downstream Region

Beyond the breakdown bubble a new vortex core is formed which is expanded compared to the upstream core. The axial velocity in this expanded core vortex gradually increases, however, the centreline velocities are less than in the region outside the vortex core.

1.3 Areas of Application and Need for Control

There are several important technical areas associated with vortex breakdown. In broad terms, these areas include aerodynamics and combustion. In real life applications, the presence of vortex breakdown can be either beneficial or detrimental. Swithenbank and

Chigier (1968) reported that at sufficient degree of swirl an internal recirculation zone, in other words a vortex breakdown bubble was generated and this led to improved combustion. He noted that this low velocity recirculation zone allowed high rate of heat release as products of combustion were recirculated and in turn ignited the incoming fuel/oxidant streams. He further stated that vortex breakdown provided a stable and compact flame. In such applications, it can be said that vortex breakdown is advantageous, for it enhances the combustion process by stabilising the flame and increasing the residence time of the combustion products. Another very common application involves flame stabilisation in furnaces where air and fuel mix in the vortex breakdown region creating a compact and stable flame. Apart from combustion applications, Husain *et al.* (2003) reported that vortex breakdown has also been found to be beneficial in vortex suction devices as it helps to collect hazardous emissions (Shtern and Hussain (1996)).

In the field of aeronautics, vortex breakdown can be both advantageous and detrimental depending on circumstances. Trailing wing tip vortices represent a danger to smaller aircrafts following behind larger ones and vortex breakdown leads to suppression of these vortices, which is beneficial. In the same field of aeronautics, vortex breakdown has been known to be harmful to wing performance. It destroys leading edge vortices shed from a delta wing hence reducing the lift and also causing a loss in wing stability. In addition, vortex breakdown occurs in flows around duck-wing planes where vortices separated from the first small wing can break down in the pressure field of the main wing causing instability of the aircraft.

A totally new area of application is beginning to show potential of capitalising on the presence of vortex breakdown in closed cylinders. This area is concerned with cell or tissue growth research in bioreactors. This research area is currently attracting a lot of interest and funding. The Department of Mechanical Engineering of Monash University is trying to locate scaffolds in a region of a bioreactor where the flow is laminar, hence with low shear stress, and with a significant residence time for nutrient injection. Such a region can be controlled and hence will constitute an ideal environment for cell growth. This laminar and low shear stress region can be provided in the form of recirculation zone or vortex breakdown bubble.

1.4 Objectives

The overall aim of the vortex breakdown study is to evaluate the effectiveness of a proposed new non-intrusive method of controlling the breakdown phenomenon. In so doing, the research investigates whether large changes to the flow structure can be induced by relatively small perturbations to upstream flow. If we consider the simple definition, by Leibovich (1978), of vortex breakdown it can be deduced that the structure of the breakdown can be altered by simply varying the swirl velocity and axial velocity along the swirl axis. It is therefore proposed to control vortex breakdown by independently rotating a small disk concentrically located in the bottom endwall. It is intended to perform both qualitative as well as quantitative assessments of the effectiveness of co- and counter-rotating the small disk to suppress or enhance the vortex breakdown. In other words, we will be interested to know how effectively the perturbation due to the rotation of the small disk is in enhancing and suppressing the vortex breakdown. The effect of the control disk size on the breakdown structure will also be investigated. Another aspect of interest will be to determine the input power, which is the viscous power, required by the small control disk to achieving the above goals. The results achieved using the small control disk will be compared with those obtained using another method such as the rotation of both endwalls.

1.5 Thesis Outline

The thesis is presented in 7 chapters. The study had three components namely: (i) the experimental investigation of vortex breakdown, (ii) the numerical investigation of vortex breakdown, and (iii) the numerical study of mixing. All of these investigations are conducted in closed cylindrical containers. The structure of the thesis is as follows:

With the exception of chapter 7 which deals solely with numerical simulations of mixing, the thesis is concerned with vortex breakdown. The current chapter deals with introductory matters such as the basic flow structure in the cylinder, real life applications of vortex breakdown and the study's objectives. A review of the literature is presented in chapter 2. It covers topics such as the theories of vortex breakdown and the evaluation of previous studies. These studies cover a wide range of subjects from

external flow, to enclosed flow with and without control of the vortex breakdown phenomenon. After establishing some gaps in the literature the present study's contribution is outlined. Chapter 3 is devoted to the treatment of the methods employed in this research. Here, both the experimental rig and instrumentation, and numerical modeling techniques are described. The procedures followed in solving the various problems are also presented.

The next three chapters deal with results from experimental and numerical investigations. Chapter 4 reports on the experimental results for the vortex breakdown study, while chapter 5 deals with the numerical aspect of vortex breakdown. Chapter 6 discusses the results of experimental and numerical studies of vortex breakdown. The chapter also presents an outline of conclusions drawn from the vortex breakdown studies. Directions for potential future studies are also presented to signify the end of the vortex breakdown investigations.

As mentioned before, chapter 7 is solely devoted to the study of mixing in a closed vessel with flow agitated by a plain disk and a bladed impeller. The chapter begins with an introduction followed by a review of the literature. The chapter goes on to describe the methods used in the investigations and presents the results and their discussion. The last part deals with conclusions and recommendations for further research. Of particular importance is section 7.5.1 attempts to show that the study of vortex breakdown in a closed cylinder with a rotating endwall is a special case of mixing using a plain disk agitator. This establishes a link between the two studies.

Chapter 2
Literature Review

2.1 Introduction

Vortex breakdown has been a topic of increased interest among researchers who have tried to first understand the underlying mechanism behind the phenomenon. To date, no single theory or explanation has provided a universally accepted reason for the occurrence of the vortex breakdown phenomenon. Nevertheless, with limited understanding of vortex breakdown a number of researchers have undertaken the task of investigating ways to control this important fluid dynamic process. It is this control aspect that is the main thrust behind the current study.

This chapter provides an overview of the various studies on vortex breakdown with particular emphasis on those concerned with swirling flow in closed cylinders. The first part of this chapter deals with fundamental issues: the various types of vortex breakdown found in different geometries and the main theories that explain the occurrence of vortex breakdown. Then, the phenomenon of vortex breakdown in external and enclosed flow is described. Confined flow vortex breakdown due to the rotation of one endwall is examined followed by a review of studies of vortex breakdown control on delta wings and in closed cylindrical containers. A perspective view of all the reviewed studies is then taken to highlight this study's contribution to the existing body of knowledge. A summary of the chapter concludes the presentation.

2.2 Types of Vortex Breakdown

Vortex breakdown, in its broader sense, can exist in many forms and shapes. Using a liquid dye tracer in a water apparatus, Faler and Leibovich (1977) found that it was possible to disrupt the vortex core by varying the flow rate and the vane angle, hence changing the Reynolds number and Swirl number. They identified seven distinct forms of vortex core disruptions, among them were three types of vortex breakdown more prominent than the others: axisymmetric or bubble, spiral and double helix. An outline of the seven vortex disruptions is given:

2.2.1 Type "O": Axisymmetric Vortex Breakdown

This type of core vortex disruption is very distinct from the other types in that it has two stagnation points, one upstream and the other downstream of a recirculation region, as shown in Figure 2.1. This recirculation region is axisymmetric in some cases; it is a two-celled low velocity zone sometimes known as the bubble type breakdown (or B-type). This type of vortex breakdown can be found in cylindrical vessels with a rotating endwall as well as above delta wings, depending on the aspect ratio. The bubble is also known to be steady in the axial location as long as the Reynolds number is not high enough to instigate unsteadiness.

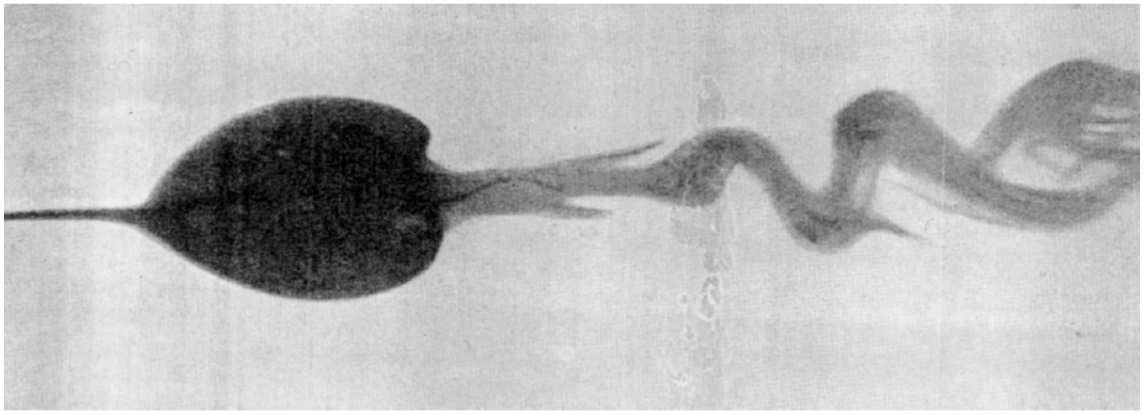

Figure 2.1 Bubble type vortex breakdown (Sarpkaya (1971)).

2.2.2 Type 1

The type "1" breakdown is a variant of the axisymmetric vortex breakdown. Although similar to the bubble type breakdown, type 1 does not have the smooth envelope and a clearly defined downstream vortex core. The flow in the wake region appears to be slightly asymmetric and dominated by turbulence.

2.2.3 Type 2: Spiral Breakdown

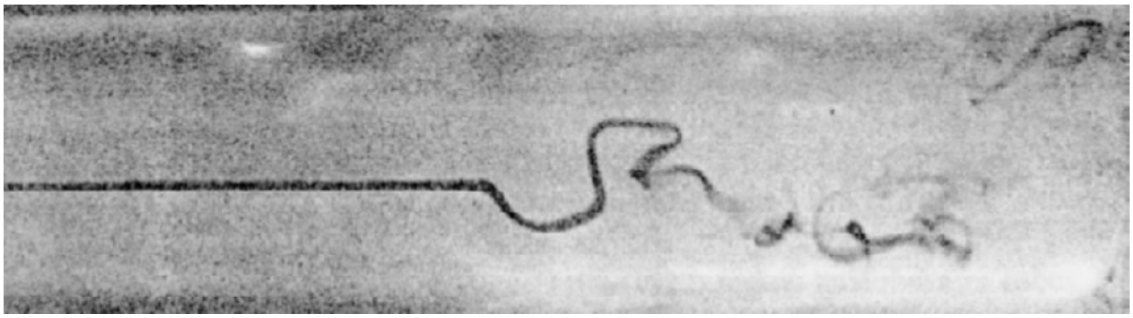

Figure 2.2 Spiral type of vortex breakdown (Faler and Leibovich (1977)).

Figure 2.2 depicts a type 2 breakdown also known as the spiral mode (or S-type) of breakdown. This flow visualisation by Faler and Leibovich (1977) revealed a deceleration of the dye filament along the swirl axis and also the formation of a stagnation point further downstream. This was followed by an abrupt kink leading to a twist of the dye filament taking the form of a corkscrew before degenerating into large-scale turbulence. Using a diverging tube experimental facility, both Sarpkaya (1971) and Faler and Leibovich (1977) observed that the sense of rotation of the spiral in the tube was identical to that of the fluid surrounding the original filament. This observation was in contrast with the flow over delta wings at high angle of attack where the sense of rotation of the spiral is opposite to the rotation of the surrounding flow. It should be noted, however, that the spiral type of breakdown is not present in the torsionally driven cylinders, although something close to it does appear sometimes. Hourigan *et al.* (1995) and Thompson and Hourigan (2003) attributed such spiral-like breakdown in cylinders to technical inaccuracies sometimes due to off-centred dye injection point or small tilt in the spinning lid..

2.2.4 Type 3

Type 3 has the combined features of both the type 2 (spiral breakdown) and the type 4 (flattened bubble) which is described next..

2.2.5 Type 4

This type of disturbance was defined by Faler and Leibovich (1977) as flattened bubble because it had a recirculation region much bigger in width, measuring nearly three times its thickness. The above shape is unlike that of the bubble breakdown which reflects a high degree of symmetry. They also observed this disturbance to be like the type "6" disturbance where the filament undergoes an abrupt upwards rolling motion towards the initial point of deflection to form a tight spiral.

2.2.6 Type 5: Double Helix

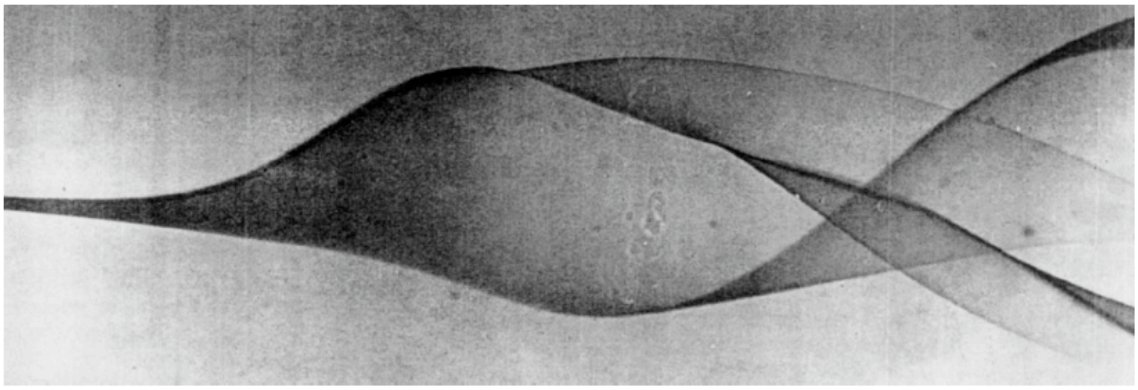

Figure 2.3 Double helix breakdown (Sarpkaya (1971)).

Sarpkaya (1971) was the first researcher to discover the double helix breakdown. He observed that a dye filament introduced into the vortex core appeared to decelerate before expanding into a slightly curved triangular sheet. The two halves of the continuous sheet wrapped around each other in the same direction, hence forming the double helix breakdown. This type of breakdown (Figure 2.3) seems to have no

stagnation point as Sarpkaya only noted a rapid deceleration of the dye filament without stagnation.

2.2.7 Type 6

The development of the type 6 breakdown starts with a dye filament moving gently off the axis at a nearly constant azimuthal location. Upon reaching a relatively significant distance away from the swirl axis, the filament is entrained by the surrounding flow spiralling in the same direction.

In summary, of all the seven types of vortex disturbances only the axisymmetric bubble and the spiral are present at high Reynolds numbers. This explains why these two forms of vortex breakdown are found in many engineering applications. As mentioned earlier, the only forms of vortex breakdown observed above delta wings are the bubble (B-type or type O) and the spiral (S-type), depending on the angle of attack (Payne *et al.* (1988)). However, in cylindrical containers with a rotating endwall only the bubble type has been observed.

2.3 Vortex Breakdown Theories

So far, one can safely say that at least the main types of vortex breakdown are identifiable. The next important task is to know the mechanism and conditions that trigger and sustain vortex breakdown. To that end, a number of theories have been proposed to characterise conditions under which vortex breakdown is likely to take place. Several surveys have been conducted to bring together the most important theories that attempt to explain the formation and existence of vortex breakdown (Escudier (1988); Lucca-Negro and O'Doherty (2001)). Broadly speaking, these theories fall under three main categories according to whether breakdown is associated with wave phenomena, instabilities or flow stagnation. These theories are briefly discussed next.

2.3.1 Wave Phenomena

Benjamin ((1962), (1965), (1967)) defined vortex breakdown as a fundamental

transition similar to the hydraulic jump phenomenon in an open channel flow. He thought of breakdown as an abrupt transition as a fluid going from a uniform state of swirling flow to a state that incorporates axisymmetric standing waves of finite amplitude. Like Benjamin, Squire (1960) suggested the existence of two states namely, the subcritical and the supercritical separated by a critical state. The subcritical state was differentiated from supercritical in that the disturbances could propagate upstream and downstream and the standing waves were supported, while in supercritical flow the only propagation that was possible was in the downstream direction.

The two investigators, however, differed in their interpretation of breakdown (Hall (1972)). Benjamin believed that breakdown was an abrupt change or a transition with finite amplitude between two conjugate states of flow. While Squire interpreted breakdown as an accumulation of disturbances that moved in the upstream direction like a shock wave. The underlying idea of Squire is that if standing waves can exist on a vortex flow, it means that downstream disturbances will propagate upstream and cause breakdown to occur. In his analysis, Squire defined a non-dimensional number k as the ratio between the maximum swirl velocity to the axial velocity. He further reported the existence of a critical value for k above which standing waves could be supported. To separate the critical region of the flow from the other region Squire (1962) introduced another parameter, N, defined by Equation 2.1,

$$N = \frac{C_+ + C_-}{C_+ - C_-} = \frac{u}{C}, \tag{2.1}$$

where u is the axial velocity, C is the relative speed of wave propagation, $C_+ = u + C$ is for the downstream propagation waves; $C_- = u - C$ is for the upstream waves. Therefore the flow is supercritical when N > 1, whereas it is subcritical when N < 1.

Evidence from experimental work seems to support the fact that the flow upstream is supercritical whereas the flow downstream is subcritical. However, other researchers have disputed the above assertion. Grabowski and Berger (1976) reported that vortex breakdown was obtained from flows with both initial supercritical as well as subcritical. Similarly, Breuer found a supercritical/subcritical transition that did not display any breakdown (cited in Althaus *et al.* (1995)). Based on the above evidence, Breuer

concluded that a transition from supercritical to subcritical state was only a necessary but not a sufficient condition for the occurrence of vortex breakdown.

2.3.2 Hydrodynamic Instabilities

The fact that vortex breakdown appears suddenly causing a fundamental change to the structure of the vortex core compelled some investigators to examine the stability of the flow before the onset of breakdown. Leibovich (1984) and Escudier (1988) attempted to provide a comprehensive coverage of the stability theory associated with breakdown. This section presents only a summary of important aspects of the stability theory.

Theoretical studies about the stability of vortex flows have been conducted by many other researchers (Rayleigh (1916); Ludwieg (1962); Howard and Gupta (1962); Leibovich and Stewartson (1983)). Rayleigh appears to be the first to draw a very important conclusion, asserting that a circular inviscid flow is stable if, and only if, its azimuthal momentum increases monotonically outward (Chandrasekhar (1961)) as shown:

$$\frac{d(wr)^2}{dr} > 0, \tag{2.2}$$

where w is the azimuthal or swirl velocity and r is the radial position.

It was not until the work of Jones (1960) that hydraulic instability was associated with the occurrence and sustenance of vortex breakdown. Jones demonstrated that a Rankine vortex was unstable only to spiral disturbances and that a Hall vortex, with constant velocity, was stable to axisymmetric disturbances provided the limits of the Rankine criterion were satisfied (Escudier (1988)).

Howard and Gupta (1962) showed that an inviscid vortex was stable to axisymmetric disturbances, with axial velocity component, when it satisfied the generalised Rayleigh's criterion:

$$\frac{d(r^2w^2)}{dr} > \frac{1}{4}r^3\left(\frac{du}{dr}\right)^2 . \tag{2.3}$$

A more generalised condition for the stability for unbounded columnar vortex, such as trailing vortices, within an inviscid fluid was proposed by Leibovich and Stewartson (1983):

$$w\frac{d}{dr}\left(\frac{w}{r}\right)\left(\frac{d}{dr}\left(\frac{w}{r}\right)\frac{d}{dr}(wr)+\left(\frac{du}{dr}\right)^2\right) < 0 \tag{2.4}$$

.

The above criterion was, however, found to be insufficient because when applied to a stable slender vortex, regions of instability were found to exist although no breakdown was present.

A study by Chao *et al.* (1991) examined the spectral characteristics of swirling flows and the interaction between breakdown and downstream instability. They concluded that the azimuthal instabilities were not just side effects of a primary breakdown but they promoted it as well.

There are also those that argue against the instability theory. For instance, Harvey (1962) reported about a flow that retained a well-organised structure with normal vortex flow restored downstream of the breakdown bubble. He therefore argued that if the breakdown was due to some sort of instability, the perturbation would have grown unchecked resulting in an unsteady flow. Hence, Harvey proposed that this behaviour was related to critical phenomena rather than instabilities. Leibovich (1984) also pointed out that a vortical flow may become unstable without undergoing vortex breakdown and that the reversal of flow in the axial direction can occur without any sign of hydrodynamic instability.

To support the counter argument, Gelfgat *et al.* (1996) investigated the steady and oscillatory states of vortex breakdown in a cylinder with one endwall rotating. An important finding from their study was that the steady state breakdown developed as a natural consequence of the flow progression, and as such was not the result of two-dimensional flow instability. They also noted that the onset of oscillatory instability had nothing to do with vortex breakdown.

2.3.3 Flow Stagnation

An important feature of vortex breakdown is the stagnation of flow along the vortex axis. The stagnation point is an essential ingredient in determining the position and existence of vortex breakdown. In numerical work this estimation is based on the quasi-cylindrical approximation (QCA) or slender vortex approximation. This approximation means that the variations of the vortex in the axial direction are considered small compared to those in the radial direction, hence can be neglected.

Mager (1972) found that at the onset of vortex breakdown the quasi-cylindrical approximation failed because the solution kept diverging. This failure was attributed to the fact that at the point of breakdown onset, and more so as the vortex breakdown evolved, the central vortex underwent a rapid change in the axial direction thereby rendering the QCA invalid. This behaviour is akin to the divergence of the solution seen at the onset of boundary layer separation. Moreover, the similarity between vortex breakdown and boundary layer separation can also be seen as, just downstream of the stagnation point, the streamlines diverge and result in a recirculation region with reversed flow.

Other researchers have shown that the failure of the QCA is related to the critical state which in turn corresponds to a singularity (Shi and Shan (1987)). They showed that calculations based on the QCA must fail following variations in the flow from supercritical to subcritical as the swirl level goes up. Increases in swirl level are accompanied by the tendency of the radial velocity profiles to diverge towards positive and negative infinity. Hall (1972) and Ludwieg (1970) independently proved that the point at which the QCA failed was exactly the critical state.

While the QCA is a useful tool for predicting the occurrence and position of the vortex breakdown, it does not however, predict the flow structure beyond the point of stagnation; neither can it account for the influence of the upstream flow.

So far, there have been many schools of thought in conflict with one another about the theories that explain the existence of vortex breakdown. This phenomenon will continue to be a topical subject for many years to come as researchers seek to gain more insight.

It is the view of this author that none of the above theories adequately explains vortex breakdown and as such breakdown formation and sustenance may be due to the combination of various factors including those covered by the above theories. One can only say that the field of vortex breakdown is still largely unexplored.

2.4 Vortex Breakdown in the Broader Sense

In this section, vortex breakdown will be examined from a broader point of view. The different physical situations in which vortex breakdown takes place will be considered. The geometries in which vortex breakdown occurs can be distinguished as external and internal or enclosed. In particular, we will consider vortex breakdown over delta wings, in a vortex tube, in open and closed cylinders.

2.4.1 Delta Wings

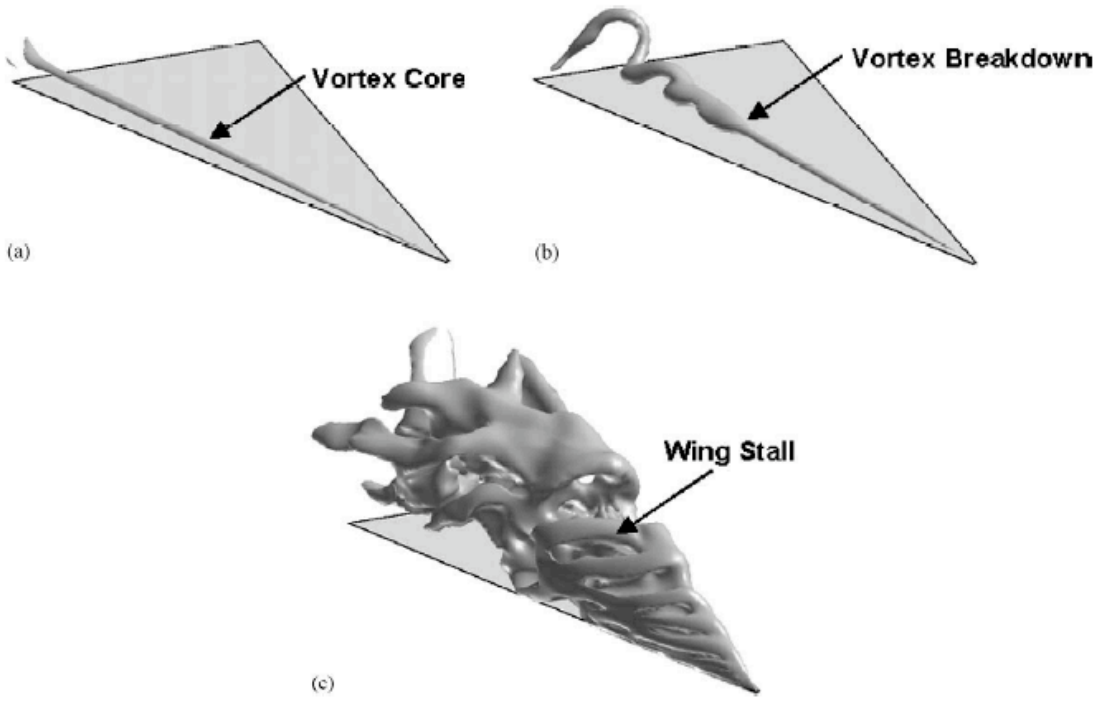

Figure 2.4 Dependence of vortex breakdown on the angle of attack (Gordnier and Visbal (2004).

The phenomenon of vortex breakdown has been investigated by many researchers from as far back as the 1950s. Although some authors may claim to be the first to have discovered this phenomenon, it is Peckham and Atkinson (1957) who are generally credited for the first observation. They noticed that the condensation trail appeared to 'bell-out' before disappearing, as though the core was becoming more diffuse. Their study involved flow over a "Gothic" wing in a low-speed wind tunnel.

The next group of investigators observed a sudden deformation, which is now commonly referred to as vortex breakdown, of the leading-edge vortices trailing from swept delta wings (Elle (1958), (1960); Werle (1960); Lambourne and Bryer (1961)). A publication by Delery (1994) gives an account of Werlė's water tunnel experimental work on a 65° sweep angle delta wing with its chord at 20° to the main stream. Werlė noted the deformation of the normally straight vortex tubes into turbulent breakdown structures.

Recently, Lambert and Gursul (2004), and Gordnier and Visbal (2004) showed that the location of vortex breakdown on a delta wing depended on the attack angle (Figure 2.4). Other researchers investigating vortex breakdown on delta wings concluded that the existence and location of the breakdown depended on both the wing sweep angle and angle of attack (Earnshaw and Lawford (1964); Earnshaw (1964)). Wentz and Kohlman (1969) found that increasing the sweep angle between 45° and 85° led to the formation of the vortex breakdown at a higher angle of attack, at least up to 75°. However, this parametric study also revealed that for sweep angles above 75°, the appearance of vortex breakdown was independent of the angle of attack.

Other researchers have shown that vortex breakdown on delta wings is not dependent only on the sweep angle and angle of attack. For instance, Lowson (1991), using a subsonic wing tunnel at low speed, showed the effect of the Reynolds number on the vortex formation and breakdown. In other studies, Kegelman and Roos (1989) and Panton (1990) showed that the shape of the wing leading edge affected the formation of vortex breakdown.

Research on vortex breakdown on aircraft wings flying at high angle of attack, mainly fighter planes, has been and will continue to be the main source of motivation for vortex

breakdown studies.

2.4.2 Vortex Tube

Harvey (1962) is thought to be the first investigator to have used a vortex tube to examine the vortex breakdown phenomenon. His set up injected air at low velocity and entrained it into swirl using 18 guide vanes installed in the entrance section of the apparatus. He altered the strength of the vortex by adjusting the angle of the vanes. Smoke visualisation technique was used to visualise the vortex breakdown in the diverging tube. Over the years, a large number of experiments have been performed using the vortex tube, also known as the swirl vane apparatus (Leibovich (1984)). The device (Figure 2.5) generally uses water as the working fluid. It is made of a vortex generator followed by a slightly diverging tube in which the embedded vortex is drawn along by the main flow.

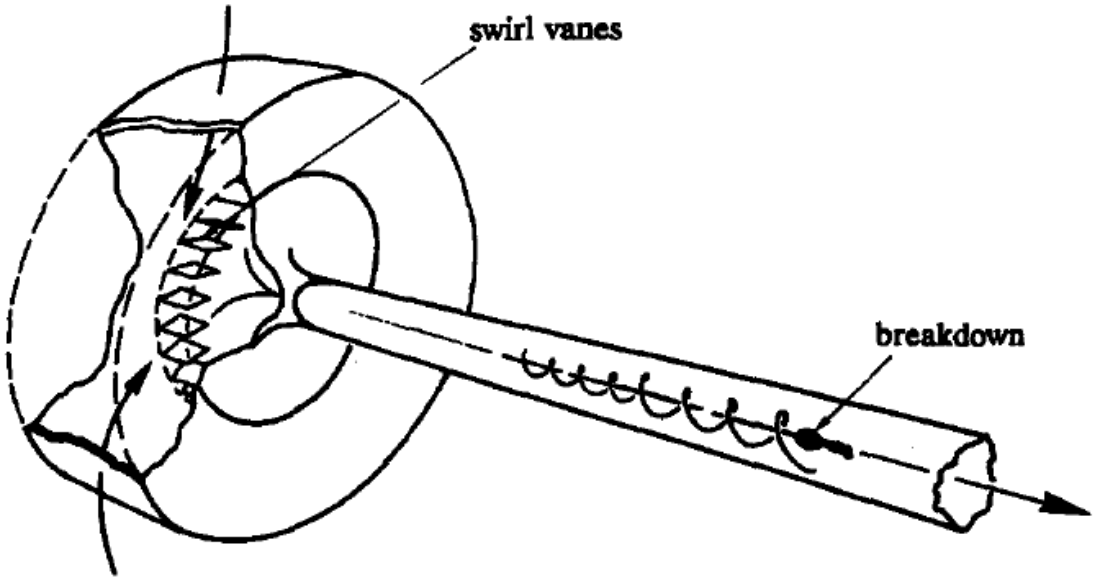

Figure 2.5 Vortex tube arrangement (Harvey (1962)).

Sarpkaya ((1966), (1974)) used a vortex tube similar to Harvey's but with 32 vanes. The working fluid was water and the dye injection method was used for visualisation. It is

this device that Sarpkaya employed to establish the now famous classification of the various types of vortex breakdown.

More reliable quantitative measurements of vortex breakdown in a confined environment were effected by Faler (1976), and Faler and Leibovich (1978). They used Laser Doppler Velocimetry to perform measurements of velocity components. These studies were carried out in a vortex tube device fitted with 32 vanes with water as working fluid.

Vortex breakdown occurring in this type of apparatus is considered as confined flow breakdown and generally involve low Reynolds numbers. For such low Reynolds numbers, extreme care must be taken when interpreting experimental results in relation to real life applications such as in aeronautics.

2.4.3 Vortex Breakdown in Open and Closed Cylinders

Maxworthy (1982) reported that in 1785 Wilcke was perhaps the first to observe vortex breakdown in a closed cylinder with non-rotating endwalls. The closed cylinder was filled with liquid and a small bent wire passing though the centre of the lid was made to rotate, hence producing a circulating flow and also a core vortex around the axis of rotation. At some value of the wire rotation speed, Wilcke noted a stagnation point along the axis and the formation of a recirculation region just downstream. What he observed was essentially a vortex breakdown.

The vast majority of work undertaken to study the vortex breakdown phenomenon has been concerned with external flow over delta wings. However, these external flow studies present a major challenge in modeling since the boundary conditions are difficult to define and control. For this reason, the controlled study of vortex breakdown phenomenon is often undertaken using a closed cylinder with a rotating disk. Some studies have used the bottom endwall (Spohn and Hopfinger (1993); Basu and Khalili (1996)) as the rotating disk while others have used the top endwall (Sorensen and Daube (1989); Liu et al. ((2001), (2003a)); Mununga *et al.* (2004a)). With an enclosed environment it is possible to have well-defined boundary conditions, and more importantly, there are no external disturbances and therefore the parameters of interest

can be easily examined. Previous studies have shown that the structures of the bubbles obtained in closed cylinders with a rotating endwall are in many ways similar to those generated in vortex tubes (Spohn *et al.* (1998)) and external flows.

The majority of studies on vortex breakdown inside a cylindrical container have been concerned with closed containers with two endwalls (top and bottom). This situation entails that no-slip boundary condition is applied to the surfaces of the two endwalls and the side wall in contact with the fluid inside the container. However, few investigators have examined the formation and evolution of the vortex breakdown in open cylinders (Spohn and Hopfinger (1993); Spohn *et al.* (1998); Ogawa and Iwatsu (2002)). Some characteristic features of the flow inside the open and closed cylinders are discussed next.

The open cylinder configuration differs from the closed one in that instead of having a top endwall, the liquid is exposed to the atmosphere, resulting in a free surface. When modeling numerically, such a surface is assigned a slip boundary condition. According to Spohn and Hopfinger (1993) the existence of a free surface causes some experimental challenges which are difficult to overcome. Because the top surface is open to the atmosphere, it is susceptible to surface-active contaminations that may generate a surface film with mechanical properties markedly different from the rest of the fluid inside the container (Davis and Rideal (1963)).

Hyun (1985a) conducted a comparative study of viscous incompressible fluid inside a circular cylindrical tank driven by the spinning bottom endwall disk. In his simulations, he used two kinds of boundary conditions to represent the upper end of the flow domain. In the first instance, the study modeled a closed tank with a rigid lid and in the second an open tank with a free surface. The results from this study revealed that at low Reynolds numbers the change in the top boundary condition did not affect the flow structure. However, at high Reynolds numbers the flow patterns were significantly dependent on the top boundary condition. In addition, Hyun reported that for small aspect ratios the flow in the azimuthal direction was markedly different: a Couette flow was obtained under the closed tank situation whereas a solid-body rotation was prevalent under the free surface situation. Also, the results showed that at a given

vertical height, the azimuthal velocity calculated under the free surface was higher than under the rigid lid case.

Spohn and Hopfinger (1993) conducted a very important study of vortex breakdown in an open cylindrical container with a rotating bottom endwall. They found that in a free surface configuration the conditions of the vortex breakdown and its forms differed substantially form the breakdown observed in the closed cylinder set up. They reported that the most notable difference was that as the Reynolds number increased, the breakdown bubble shifted upstream until it was attached to the free surface and continued to grow in size. Another observation made by Spohn and co-workers was that the rotation of the fluid caused a deformation h of the free surface. This deformation is proportional to the Froude number Fr which is defined as

$$Fr = \frac{\Omega^2 R^2}{gH}. \tag{2.5}$$

However, they noted that for the smallest aspect ratio and the highest Reynolds number considered in their investigation h/H was less than 10%.

The existence of the free surface, noted Spohn et al., meant that the system was very sensitive to external perturbations. They observed that vibrations caused the flow to separate from the sidewall resulting in a completely modified flow structure within the container. They recommended that when performing such experiments particular attention had to be paid to ensure that there were no shocks or vibrations in the laboratory.

Another comparative study was undertaken by Spohn *et al.* (1998). As in Hyun's case, Spohn and co-workers compared the flow inside two containers, one with a rigid cover and the other with a free surface. The significant finding from this experimental study was that if the angular velocity of the spinning bottom endwall was sufficiently increased the evolution of the breakdown bubbles was different in both configurations. They found that in the case of a rigid cover the breakdown bubbles completely disappeared, whereas in the free surface case the bubbles persisted.

2.5 Confined Flow Vortex Breakdown Due to One Endwall Rotation

This section focuses on vortex breakdown studies in closed cylinders without any form of control. Some important studies are reviewed including those related to the onset of vortex breakdown and some characteristics of the vortex breakdown bubble.

2.5.1 Important Early Studies

Vogel (1968) was the first to observe vortex breakdown in a cylindrical enclosure with a rotating endwall. His findings defined the stability limits of swirling flow with vortex breakdown in the parameter space of Reynolds number and aspect ratio. Vogel's experimental visualisation results showed a recirculation region that appeared to resemble a bubble near the axis of rotation. This type of vortex breakdown was later described by Leibovich (1984) as Type B (standing for bubble-type), whereas Sarpkaya (1971) named it as type O. In another study, Ronnenberg (1977) reported findings from his measurements on the entire flow structure, with one case similar to one of Vogel's. These results were in conformity with Vogel's conclusions.

The detailed study of Escudier (1984) is one of the early works, perhaps the most prominent of all, which has now been used as a benchmark by several investigators. In effect, Escudier extended the works of Vogel (1968) and Ronnenberg (1977) by establishing further stability limits (Figure 1.4). Escudier found that as the aspect ratio and Reynolds number increased two and three recirculation regions or rather vortex breakdown bubbles successively formed along the axis of rotation. He further observed that there was a Reynolds number, for each aspect ratio, beyond which the flow became oscillatory and eventually turbulent. Escudier's other contribution was the hysteresis testing, the results of which led him to conclude that the phenomenon was non-existent, at least for the flow regimes that he had tested.

In the years between the 1970s and early 1980s, there have been many numerical studies on swirling flow in cylindrical containers (Pao ((1970), (1972)); Tomlan and Hudson (1971); Lugt and Haussling (1973); Bertela (1979); Bertela and Gori (1982)). These studies, however, were only limited to cases where there was no vortex

breakdown. Lugt and Haussling (1982) are thought to be the first investigators to publish numerical simulation results of vortex breakdown in a cylindrical container. Their results revealed an embedded recirculation region along the swirl axis as observed by Vogel (1968).

2.5.2 Vortex Breakdown Incipience

The onset of vortex breakdown has been a subject of many studies, especially those dealing with external flows (Truneva (1976); Zhang *et al.* (1991); Visbal (1994)). Zhang et al. reported that the adverse pressure gradient upstream of the breakdown was the primary instigator of vortex breakdown. Their results revealed that vortex breakdown occurred at an angle of attack of 38° on a pointed-nose body of revolution. The computational study by Visbal (1994) of vortex breakdown over a delta wing with high angle of attack found that the pressure gradient along the vortex axis significantly affected the incipience of vortex breakdown.

One commonly used tool to test the occurrence of the vortex breakdown bubble is the vortex breakdown criterion by Brown and Lopez (1990). They proposed physical mechanisms for vortex breakdown based on the production of a negative azimuthal component of vorticity on some stream surfaces. The criterion means that the helix angle of velocity should exceed that of vorticity on some stream function.

Watson and Neitzel (1996) used the Brown and Lopez vortex breakdown criterion to confirm the existence of the breakdown phenomenon. Their results conclusively showed that the criterion was valid. They noted that the Brown and Lopez breakdown criterion could be used to accurately assess *a posteriori* the occurrence of the vortex breakdown. However, they concluded that as a predictive method, the Brown and Lopez criterion fell short as it could not be met at locations just upstream of the bubble to signify the forthcoming breakdown.

Another important investigation on vortex breakdown incipience is the analytical work of Nakamura and Uchida (1980). They found that a necessary condition for the swirling flow, upstream of the point where breakdown is supposed to occur was for the non-dimensional angular velocity to take the value of 1.0. This non-dimensional parameter

(ω) is defined as

$$\omega = \frac{\varpi \bar{r}_c}{V_a}, \tag{2.6}$$

where ϖ is the angular velocity and V_a is the axial velocity and $\bar{r}_c$ is the vortex core radius. At this point, they estimated that the pressure calculated from the radial equation of motion was sufficiently closer to the axial one. According to Nakamura and Uchida this value of 1.0 was close to experimental data. As part of the condition for vortex breakdown onset, they observed that a sufficient radial pressure increase from the axis at some cross section upstream was necessary. However, it is not clear how much of an increase was to be considered sufficient.

The emergence of stagnation points in a rotating flow with both endwalls rotating was investigated by Mullin *et al.* ((1998), (2000)). Mullin *et al.* (1998) observed a peculiar phenomenon with small aspect ratio cylinders when the stagnation points appeared to occur off-axis. However, they did not provide an explanation as to why this off-axis stagnation point occurred. In both studies a small cylinder was introduced along the centre line of the flow, but the results suggested that the onset of the breakdown bubble was mainly unaffected by the addition of the stationary inner cylinder. They concluded that the vortex breakdown phenomenon was robust as long as the inner cylinder radius was less than 10% of the outer cylinder. Figure 2.6 depicts a vortex breakdown for a case where the inner cylinder radius was 10% of the outer cylinder radius.

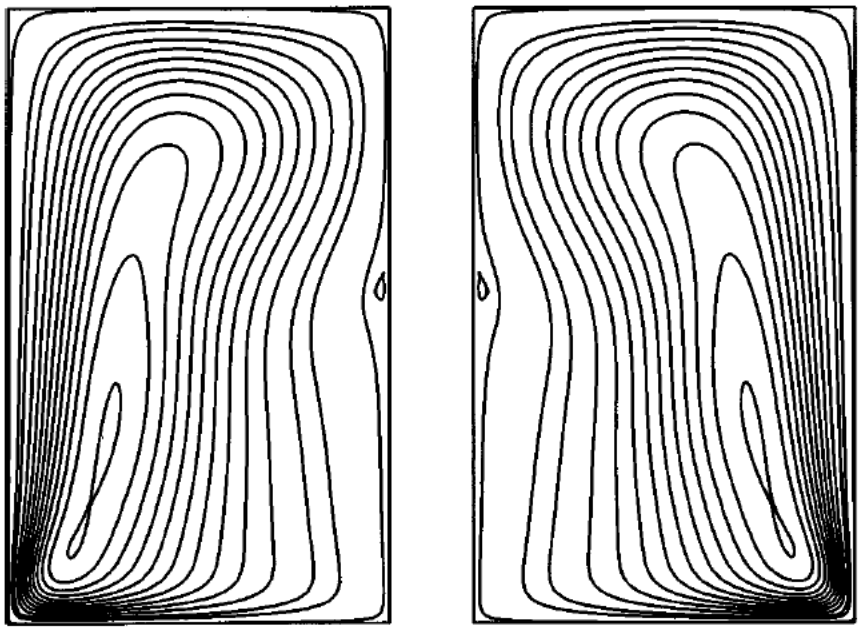

Figure 2.6 Streamline plot showing the recirculation region for the case where there is a centrally located inner cylinder with a 10% radius compared to the outer cylinder (Mullin et al. (2000)).

The hypothesis that the change in axial velocity profile from a jet-like to a wake-like profile, when vortex breakdown occurs, is dependent on the transition of the helical symmetry of the vortex structure was recently tested and validated by Okulov *et al.* (2004). To test the hypothesis, they numerically simulated the axisymmetric steady swirling flow in a cylinder with co-rotating top and bottom endwalls. Results showed that the change in the distribution of axial velocity during vortex breakdown could be associated with the shift from right-handed to left-handed helical symmetry of the vorticity field. The important result from this study is that the necessary condition and prerequisite for vortex breakdown is the existence of a left-handed helical vortex. Associated with this condition was the twist parameter K for the central vortex, the value of which was established to be approximately 0.6, irrespective of the aspect ratio or Reynolds number.

2.5.3 Location and Size of Vortex Breakdown

A theoretical study by Berger and Erlebacher (1995) was designed to explain the

tendency of the vortex breakdown bubble to move upstream with small changes in some governing parameters. Using a simplified model for the axial velocity variation, their numerical results showed that the tendency of the vortex breakdown to move upstream depended on the core Reynolds number, as it increases, or the adverse pressure gradient increase. These results were in qualitative agreement with most numerical and experimental simulations (Escudier (1984); Fujimura *et al.* (2004)).

Lugt and Haussling (1982) made very important observations in their pioneering numerical work. They numerically calculated the swirling flow in a cylindrical container with a rotating cover. The locations of both the upper and lower stagnation points were plotted against Reynolds numbers for a cylinder aspect ratio of 1.58. The upper and lower stagnation points can also be termed as downstream and upstream stagnation points respectively, as is usually the case. One of the important observations they made was that, in the steady state, as the Reynolds number increased both the upper and lower stagnation points moved away from the rotating endwall (lid). Lugt and Haussling also plotted the variation of the bubble size (axial dimension only) with Reynolds number. From their plot, it can be seen that the size of the breakdown bubble initially increases until it reaches a maximum size and eventually shrinks. The above observations were in good agreement with the experimental results of both Vogel (1968) and Ronnenberg (1977).

The detailed study of Escudier (1984) also shed some light on the breakdown bubble size and location. Escudier found that in the single breakdown case, the structure of the bubble underwent some significant changes as the Reynolds number was increased. He reported that his findings about the size and location of the breakdown bubble were in conformity with the observations of Vogel (1968). He also found that for a double breakdown case ($H/R < 2.75$) the downstream stagnation point moved towards and eventually penetrated the breakdown zone upstream so that as the Reynolds number continues to increase there was only one stagnation point but two recirculation regions.

The above studies have revealed that the vortex breakdown bubble undergoes some structural as well as positional changes as the flow condition inside the cylinder is altered. Most of the above mentioned studies have shown how changes in Reynolds

number affect the radial size of the breakdown bubble and the location of the upstream stagnation point. It is important to examine in more detail how the bubble radial and axial dimensions change with increases in Reynolds numbers. In addition, more investigations are needed to understand the migration of the upstream and downstream stagnation points along the swirl axis.

In two very recent studies by Fujimura and Koyama (2002) and Fujimura *et al.* (2004), the vortex breakdown phenomenon in a closed cylindrical container with a rotating top endwall was examined. The results from the latter study plotted the location of the first and second stagnation point, as shown in Figure 2.7. Fujimura et al. found that as the Reynolds number increased, the stagnation points moved toward the upstream region (i.e. towards the fixed bottom endwall). They also observed that this trend persisted as the aspect ratio altered (H/R = 1.50, 1.75, 2.00, 2.50, 3.00 and 3.30). Fujimura and co-workers were pleased to find that their results compared very favourably with the data of previous researchers (Escudier (1984); Lopez (1990); Tsitverblit (1993).

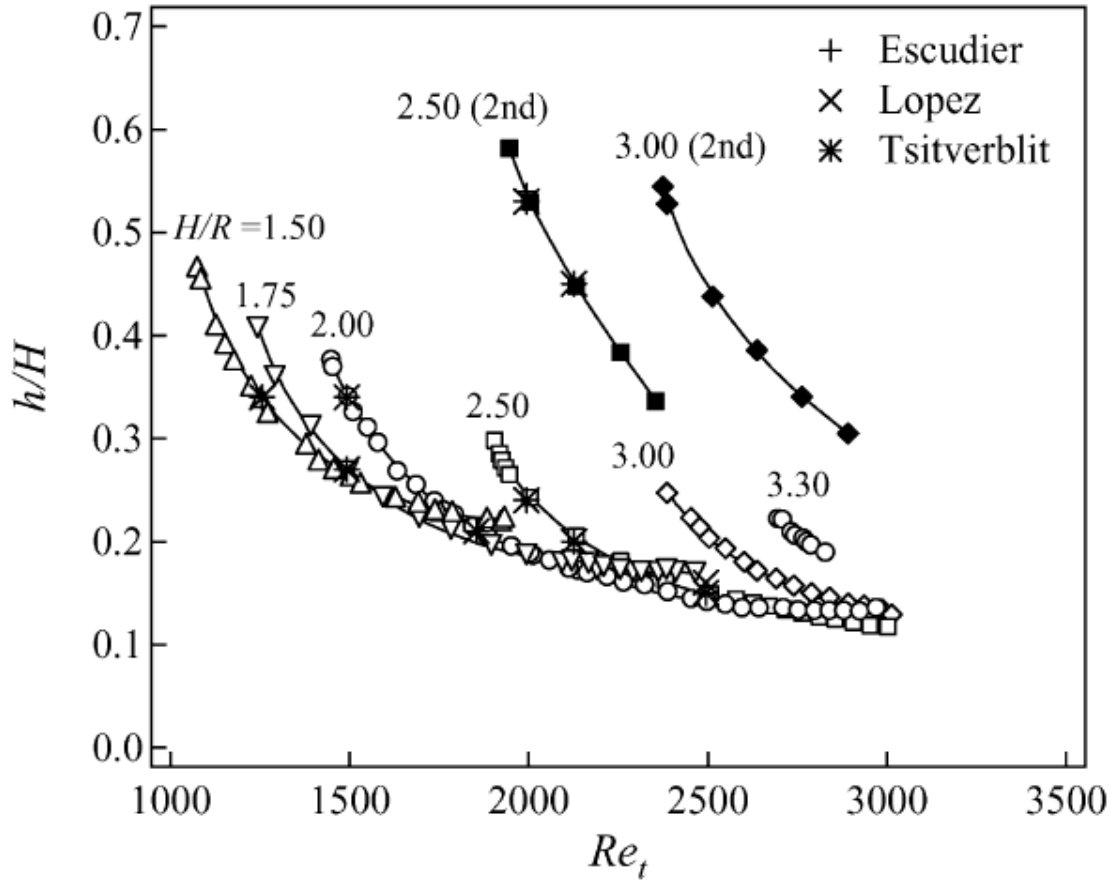

Figure 2.7 Location of the first and second upstream stagnation points when only the top endwall is rotating. Fujimura et al. (2004) experimental results are compared with the data of Escudier (1984), Lopez (1990) and Tsitverblit (1993).

2.5.4 Characteristics of the Bubble Type Breakdown

In this section we look at some characteristics of the vortex breakdown bubble in a closed cylinder by examining data from the existing body of knowledge. Some of the controversial concepts such as whether the breakdown bubble is axisymmetric or asymmetric, open or closed will be highlighted in the following paragraphs.

A study of vortex breakdown on delta wings with a high angle of attack by Visbal (1994) showed that the breakdown bubble was fairly axisymmetric at the onset of vortex breakdown. However, he observed that as the Reynolds number increased asymmetric effects became important. Similarly, Sarpkaya (1971) observed that while

the vortex breakdown bubble was initially closed and perfectly symmetric during its formative stage, as the swirl increased the bubble began to draw in fluid from the downstream end and grew with a spiralling tail having lost its symmetry.

Escudier (1984), on his part, noted that the flow generated by a rotating endwall inside a closed cylinder, hence the breakdown bubble, remained axisymmetric until well into the unsteady-flow flow zones. Examining the data from Figure 1.4 shows that for an aspect ratio H/R = 2 the flow remained steady until the Reynolds number of approximately 2600. On the basis of the above result, the current study was well within the region where the flow and breakdown bubbles were considered to be axisymmetric.

Another observation made by Escudier (1984) was that the vortex breakdown bubble obtained after increasing the Reynolds number to 1492 was well-defined with a stagnation point upstream and another stagnation point (or saddle point) terminating the recirculation zone at the downstream end. This feature he thought was in contrast to what he observed in the case of pipe flow (Escudier and Keller (1983)), where the breakdown zone was open at the downstream end. Surprisingly to Escudier, Leibovich (1978) reported that his observation of vortex breakdown in a pipe was a closed bubble at the downstream end. In another study, Roesner (1990) investigated the recirculation zones in a closed cylinder, first with a rotating top endwall and second with both endwalls rotating. He could not say conclusively whether the breakdown bubble was open or closed. These studies show how controversial some aspects of vortex breakdown can be.

A closed cylindrical container with a rotating bottom was used by Spohn *et al.* (1998) to experimentally study the steady state flow generation of vortex breakdown bubbles. The authors found that the vortex breakdowns generated from this configuration were in many ways similar to those observed in vortex tubes. In particular, they found that the breakdown bubbles were open with inflow and outflow. In addition, Spohn and co-workers noted that the bubbles were highly axisymmetric on the upstream end but asymmetric on the downstream end (Figure 2.8). The bubble shown in Figure 2.8 corresponds to Re = 1852 and H/R = 2.0 and exhibits some degree of asymmetry close to the axis at the downstream end. Spohn et al. also reported the existence of open and

stationary bubbles. Furthermore, they attributed the asymmetry of the flow to the occurrence of asymmetric flow separations on the container wall.

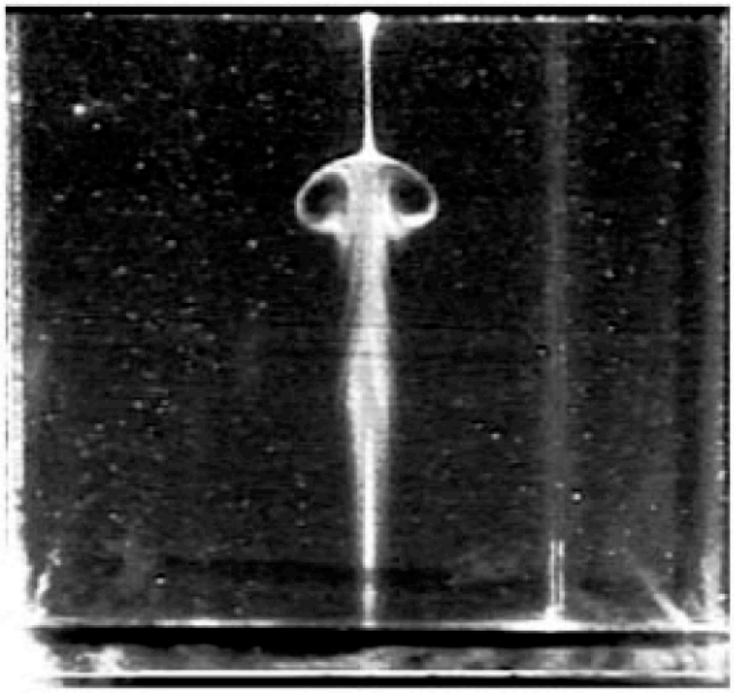

Figure 2.8 Vortex breakdown bubble for Re = 1852 and H/R = 2.0 (Spohn et al. (1998)).

A very detailed recent numerical study of the unsteady three-dimensional flows was performed by Sotiropoulos and Ventikos (2001). By numerically analysing the three-dimensional topology of particle paths they explained the origin of the asymmetry folds at the downstream end of the breakdown bubble. One important explanation was that the asymmetric features of the stationary vortex breakdown bubbles are associated with the Stewartson layer. They also reported that the flow in the interior of stationary breakdown bubbles exhibits chaotic particle paths.

The spin-up and spin-down processes were used by Liu *et al.* (2003b) to investigate the whole velocity field measurement of swirling flow in a closed cylinder with the presence of vortex breakdown. Using symmetry analysis, they found that the overall flow structure in the spin-up process was still largely axisymmetric, whereas in the spin-down process the flow structure rapidly deteriorated exhibiting asymmetry.

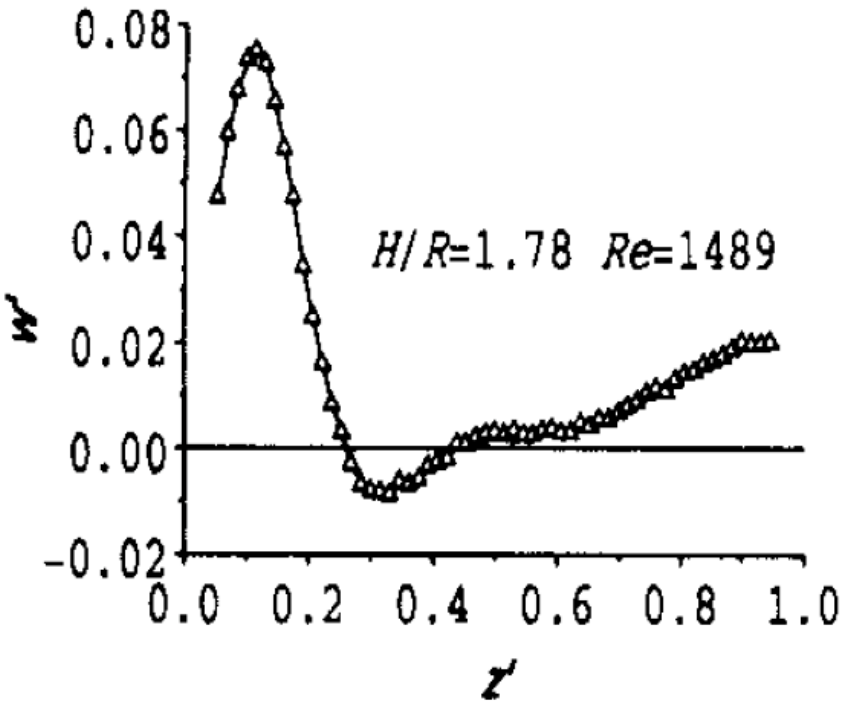

Figure 2.9 Distribution of axial velocity along the axis of rotation for H/R = 1.78 and Re = 1489 (Liu et al., 2001).

A three-dimensional velocity measurement, via LDV, of vortex breakdown in a closed cylinder with a rotating top lid was carried out by Liu *et al.* (2001). The results from that study showed that the bubble type vortex breakdown was a closed low velocity circulating region which was fully isolated from the main flow. However, the only evidence of vortex breakdown being a fully closed region, according to Liu et al., are the plots of axial velocity profile along the axis of rotation (Figure 2.9). In Figure 2.9, *W'* is the axial velocity and *Z'* is the normalised distance from the bottom endwall. This author has observed that although there can appear to be two stagnation points, one upstream and the other downstream of the recirculation zone, flow visualization has shown that in some cases the bubble can be clearly open at the downstream end.

While the debates about whether vortex breakdown bubbles are open or closed continue, another debate about the symmetry of the breakdown bubble has divided researchers into two camps.

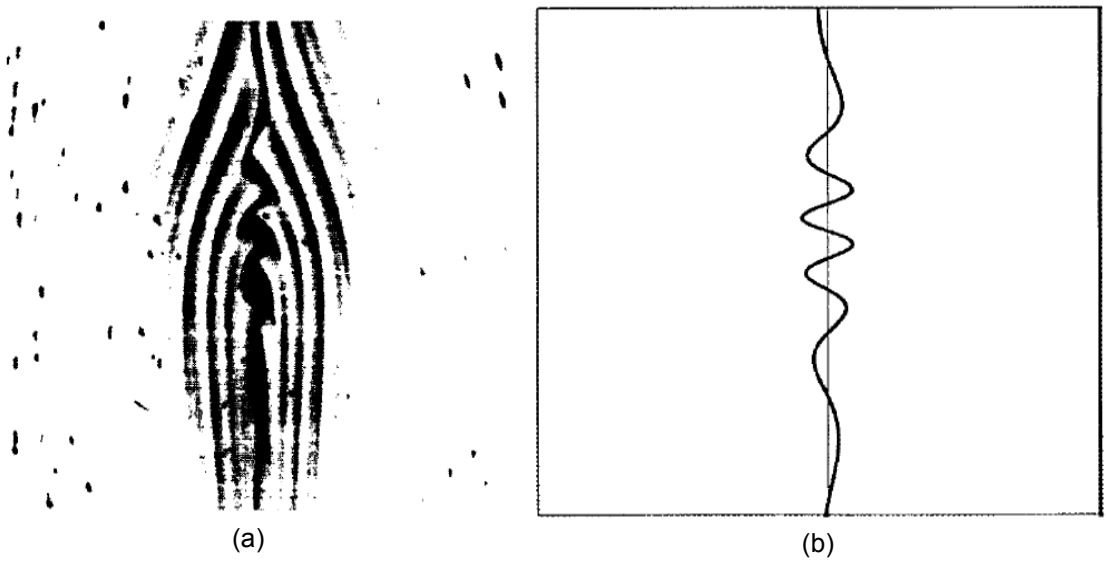

Figure 2.10 Close-up view of the experimental streaklines for Re = 1900. (a) Bottom endwall is rotating and top endwall is fixed. Dye is injected nominally at the center of the top endwall; (b): Predicted particles streakline shown in bold. Particle injection at 5 x 10^{-3} R below the top endwall and 8 x 10^{-3} R off centreline (Hourigan et al. (1995)).

A similarly arguable subject is whether the swirling flow in a closed cylinder is axisymmetric or asymmetric. Spohn and Hopfinger (1993) concluded that the presence of non-axisymmetric streaklines was an indication that the flow was at least not axisymmetric. However, Hourigan *et al.* (1995) conducted both experimental and numerical investigations and demonstrated that the spiral regions (Figures 2.10(a) & (b)) that appear along the axis of rotation can indeed appear in steady axisymmetric flows just before the appearance of the vortex breakdown. The findings of Hourigan et al. supported Escudier (1984)'s conclusion that the vortex breakdown bubble in a closed cylinder is essentially axisymmetric.

To prove their argument, Hourigan *et al.* (1995) numerically released a particle at 0.5% and 0.8% cylinder radius below the top endwall and off the centreline respectively. They predicted two spirals along the centreline (Figure 2.10(b)), as observed experimentally (Figure 2.10(a)). They further noted that the number of turns in the spirals was dependent on the radial offset at which the particle was released.

Detailed 3-D numerical simulations conducted by Ventikos (2002) investigated the structure of the steady vortex breakdown bubbles in a closed cylinder. Ventikos found two fundamental aspects of the bubble type breakdown: the first one being that the bubble is essentially axisymmetric and the second one, that it was extremely difficult to achieve this axisymmetric mode of the bubble in experimental simulations. He indicated that even minute imperfections, such as geometrical imperfections of the sidewall can change the sidewall flow structures, hence the entire flow structure inside the cylinder. He concluded that such disturbances to the flow structure can lead to a fundamental change in the structure of the breakdown bubble; i.e. change from a closed axisymmetric recirculation zone to an open asymmetric structure dominated by chaotic flow dynamics.

To reinforce Ventikos' argument about the effect of imperfections on the structure of the steady vortex breakdown bubble, Thompson and Hourigan (2003) recently undertook investigations on the sensitivity of the bubble to rotating endwall misalignment. As can be seen in Figures 2.11(a) and (b) even a minute vertical misalignment of 0.01° can cause a loss in symmetry and some folding at the downstream end of the breakdown bubble. Figure 2.11(b) clearly shows that the bubble is axisymmetric when perfect alignment is maintained. They also showed that with a misalignment of 0.03° the generated vortex breakdown bubble is clearly open as reported by Spohn *et al.* (1998). Thompson and Hourigan concluded that the asymmetry character of the breakdown bubble reported in experimental studies is due to imperfections in the experimental rig such as misalignment between the axis of rotation of the rotating endwall and the cylinder axis. They also remarked that the level of perfection required to achieve axisymmetric and closed vortex bubble is perhaps too high for experimentalists to achieve.

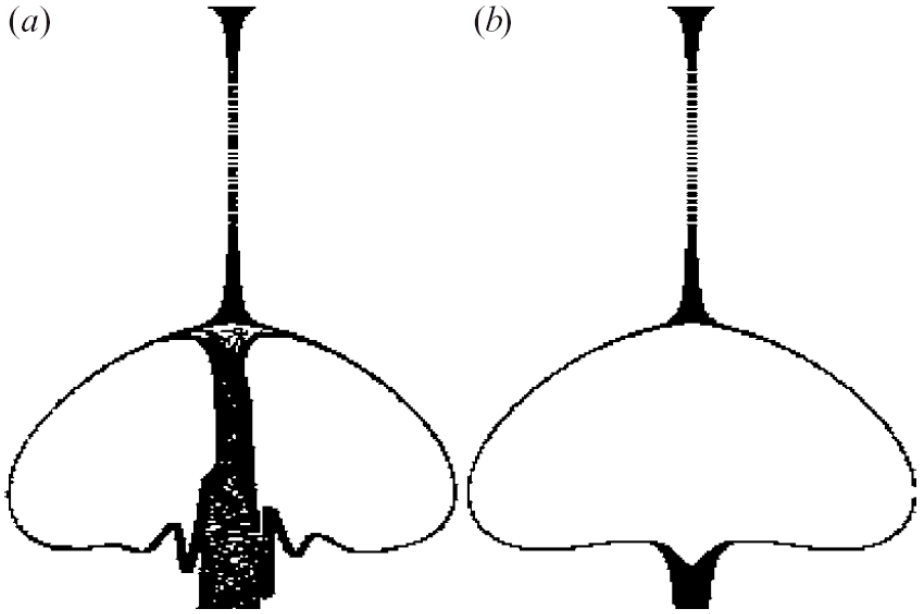

Figure 2.11 Flow visualization: (a) Effect of reducing the vertical misalignment to 0.01; (b) no misalignment (Thompson & Hourigan, 2003).

2.6 Control of Vortex Breakdown

As mentioned in chapter 1, vortex breakdown can be beneficial or detrimental to the performance of a particular application where it is present. This is true of both external and confined flows. Therefore, there is a justifiable need to not only understand the vortex breakdown phenomenon but also to have the ability to control it, so that it can be enhanced where it is advantageous and suppressed where it is detrimental. We will look at the various methods that have been employed over the years to control vortex breakdown, first over slender delta wings and second within closed cylinders. The principal reason for briefly surveying the methods of vortex breakdown control on delta wings is that fundamentally most of these methods rely on the same mechanism to achieve the control function as do the methods employed in closed cylinders.

2.6.1 Control on Delta Wing

A study by Hummel and Srinivasan (1966) concluded that the lift, drag and pitching moment of a delta wing underwent a sudden deterioration as the location of vortex

breakdown moved upstream over the trailing edge, following an increase in the angle of attack. While this case illustrates the destructive nature of vortex breakdown, we also know that it can be beneficial in other cases. It is fair to acknowledge that in the aircraft industry the damaging effect of vortex breakdown far outweighs the benefit. For this reason, this section will concentrate on control methods aimed at minimizing or getting rid of vortex breakdown over delta wings.

Mitchell and Delery (2001) have recently conducted an extensive historical review of diverse control methods over slender delta wings at high angle of attack. The experimental techniques employed to control vortex breakdown fall into, at least, two categories: mechanical devices, and pneumatic techniques. Another method which has been used in the past consists of changing the geometry of the wing. These techniques rely on manipulation of the vortex breakdown such that the velocity field leads to a decrease in the swirl number (i.e. the ratio between the azimuthal momentum and the axial momentum) or change of pressure gradient. This can effectively be achieved when the longitudinal component of velocity of the vortex core is increased or the swirl velocity is reduced. Brief descriptions of the various techniques are presented below:

(i) Wing Geometry Change

It is known that vortex breakdown occurrence and its location are largely dependent on the angle of attack and the sweep angle. Obviously, one would be tempted to vary the above parameters in order to control vortex breakdown so that it can be moved further downstream and if possible completely suppress it. However, varying the angle of attack directly affects the lift of the wing and the sweep angle is fundamental to the flight characteristics of the wing. Therefore, extreme care has to be taken when dealing with these two parameters.

By changing the sweep angle, Gursul *et al.* (1995) managed to control the location of vortex breakdown over a delta wing. The vortex breakdown detected in this study was the helical mode; this was achieved by sensing pressure fluctuations. The control technique involved varying the sweep angle, such that when increased, the breakdown shifted in the downstream direction.

(ii) Mechanical Devices

Investigations were conducted by Rao and Johnson (1981) to examine the influence of leading edge flaps in order to control vortical flows around wings. The results from these studies revealed that flaps were capable of ameliorating the lift to drag ratio of a given wing by up to 18.4%. Also, a study by Klute *et al.* (1996) investigated the influence of an apex flap on the vortex breakdown at high angles of attack. They observed a significant delay in vortex breakdown location.

The shape of the leading edge has also been effectively used to relocate the breakdown region on the wing (Lowson and Riley (1995)). Realising the significant impact the leading edge geometry had on the location of vortex breakdown, Lowson and Riley installed a movable flap at the apex to control vortex breakdown. By adjusting the incidence of the flap the breakdown region was moved by as much as a chord length. In another study, Gangulee and Ng (1995) examined the effect of a flap located inboard of the leading edge and concluded that it promoted vortex breakdown at high angles of attack.

Other mechanical devices employed to control vortex breakdown include, vortex tab (Hoffler and Dhanvada (1985)), apex fences on delta wing (Wahls *et al.* (1986)) and cavity flap (Schaeffler *et al.* (1993)).

(iii) Pneumatic Techniques

(a) Suction

As mentioned previously, the swirl number is an important parameter that determines the occurrence of vortex breakdown. A large number of control methods rely on changing the swirl to axial velocity ratio to influence the occurrence and location of the breakdown. Pneumatic methods used to control vortex breakdown include blowing along the trailing edge, along-the-core blowing, suction and blowing along the leading edges, and pulsed blowing.

Hummel (1967) successfully manipulated the vortex breakdown location by employing suction at the trailing edge. These tests were conducted at high angles of attack, thereby

the suction was able to influence flow around the leading edge and the adverse pressure gradient. The success of this method was due to the reduction in the adverse pressure gradient and an increase in the axial velocity in the vortex core. Another successful study is that of Owens and Perkins (1995), in which suction of the boundary layer delayed the formation of the breakdown. A fairly recent investigation was conducted by Maines *et al.* (1999) involving leading edge suction on a 65° delta wing. The study found a direct relationship between vortex breakdown location and a parameter based on the momentum of suction and the free velocity.

(b) Blowing

A method of controlling vortex breakdown by relying on adverse pressure reduction was implemented by Shih and Ding (1996). They effectively installed vectored trailing edge nozzles to the delta wing and tested it in a water tank towing apparatus. By blowing jets of fluid through nozzles, the vortex breakdown region was shifted downstream. Their design was such that it was possible to adjust the angle of the nozzles, hence creating an asymmetry in the breakdown location.

An improved version of the blowing technique was later designed by Vorobieff and Rockwell (1998). Their device incorporated both trailing edge blowing and deflection of a leading flap on a pitching delta wing model. Results from this method showed that the trailing edge blowing was more efficient than the leading edge flap technique. In another study, Johari and Moreira (1996) designed an even more efficient blowing technique. They implemented intermittent blowing which was not only successful in controlling vortex breakdown but also used much lower flow rate through the blowing orifices than Shih and Ding's design did.

The blowing technique has also been implemented by injecting high momentum fluid along the leading edge and along the vortex core (Cheng-Hsiung and Ni-Yu (1995)). Gu *et al.* (1993) investigated experimentally the effect of steady blowing tangentially along the leading edge of a half-delta wing at high angle of attack and they found that it substantially retarded the onset of vortex breakdown as well as stall. Cheng-Hsiung and Ni-Yu (1995) investigated the effectiveness of blowing along the vortex core over a slender delta wing. They found that, as expected, both higher blowing rates and

frequencies always led to enhanced delay in vortex breakdown. Furthermore, they found that even low blowing frequencies efficiently led to delayed vortex breakdown.

(iv) Coaxial Wire

A recently developed technique to control vortex breakdown over a delta wing involves the use of a very small coaxial wire tethered from the apex of the wing and aligned with the centreline of the leading edge vortex. This method was proposed by Akili and Sahin (2003). Using high-image-density particle image velocimetry, they were able to acquire patterns of instantaneous and averaged vorticity and velocity across the flow domain. They reported that it was possible to alter the onset of vortex breakdown by as much as one chord length of the wing.

What the control methods described in this section did was to change the flow field leading to a decrease in the swirl number or change of adverse pressure gradient. The techniques for controlling vortex breakdown in closed cylinders, as described in the next section, rely on the same principle.

2.6.2 Control in a Closed Cylinder

Vortex breakdown control in closed cylinders has not been investigated as widely as breakdown control over delta wings. In fact most of the literature has only appeared in the last decade. A number of methods have been employed to control vortex breakdown in closed cylinders, these include: rotation of the bottom and top endwalls, temperature gradient and near axis swirl addition. These methods and another that combines the last two techniques as well as the one involving spin-up and spin-down, will be briefly reviewed next.

(i) Near-axis Swirl Addition

Recently Husain *et al.* (2003) employed the concept of near-axis swirl addition using a small centrally located rod rotating independently of the bottom or rotating endwall. To control vortex breakdown, they rotated the rod either in the same direction as the rotating endwall or in the opposite direction, the top endwall being kept stationary. The

central rod size was chosen to be close to the vortex core diameter which was 1/24 compared with the cylinder diameter. They showed that the addition of swirl near the axis of rotation was an effective way of controlling vortex breakdown. Essentially, their findings were that, co-rotating the small rod with respect to the rotating endwall retained a steady flow while suppressing vortex breakdown bubbles, whereas counter-rotating induced centrifugal instability resulting in vortex breakdown enhancement.

Hussain and co-workers showed that the rotation of the rod alone produces two large cells in the meridional plane, as shown in Figure 2.12, and of course additional swirl. They believed that the disappearance of the vortex breakdown, after co-rotation of the small rod, was due to a decrease in the swirl number, below a threshold value corresponding to vortex breakdown onset. Similarly, they argued that co-rotation of the small rod decreases the unfavourable pressure gradient around the axis and thereby suppressing the vortex breakdown bubble.

For the case where the small rod was counter-rotated, Husain *et al.* (2003) explained that the additional swirl caused the generation of centrifugal instability leading to unsteady flow conditions favourable to formation or enhancement of vortex breakdown bubbles. They concluded that for a practical system, in real life, this method using a central rod would not be feasible and went on to suggest the use of swirling jet to achieve the same effect. This method, although effective, raises some fundamental issues as it is intrusive, with the rod passing through the centre of the vortex core and vortex breakdown. It is therefore imperative to design a method that does not interfere with the very flow structure that is being examined and this requirement has been addressed by the current study.

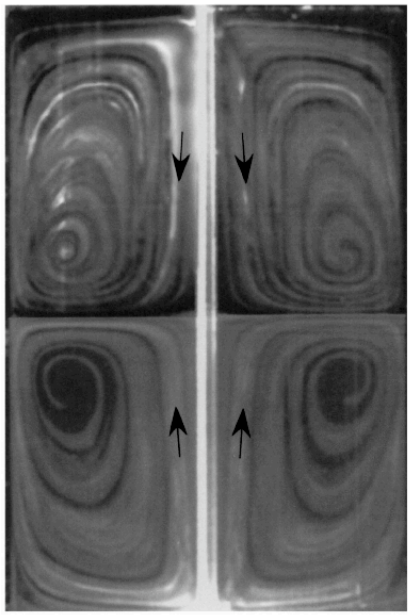

Figure 2.12 Flow visualization when the central rod rotates producing two large cells in the meridional plane. Arrows indicate the flow direction (Husain et al. (2003)).

A study by Mullin *et al.* (1998) investigated the creation of stagnation points in a rotating flow. They studied three different cases: the first case was the usual closed cylinder with two endwalls, the second and third had an inner concentric cylinder where in one instance was kept stationary, and in the other was rotated. In all cases the two endwalls were rotated. Their results showing Reynolds numbers at which vortex breakdown onset occurred for different aspect ratios seems to indicate that rotation of the inner cylinder assists the onset of the recirculation bubble. However, it is interesting to note that the authors thought that the addition of the inner cylinder did not produce any qualitatively different features in the flow, as long as the inner cylinder radius was less than 10% of the outer one. This seems to contradict the finding of Husain *et al.* (2003) that by rotating a small central rod it is possible to suppress vortex breakdown, for co-rotation, and enhance it when counter-rotation is employed. The above difference in research outcomes can be attributed to the fact that the two studies employed two significantly different systems (Mullin et al. vs Husain et al.: aspect ratio = 1.6 vs 3.25; Reynolds number = 2000 vs 2720; radius ratio = 0.1 vs 0.04). The fundamental difference between these two studies is, as remarked by Husain and co-authors, to

completely suppress vortex breakdown, the rotation ratio between the small rod and the endwall should be bigger or equal to approximately 6.0. So, it is not surprising that Mullin *et al.* (1998) did not observe any qualitative difference because their rotation ratio was only 1.0, which was far below the ratio used by Husain *et al.* (2003). For Mullin et al. to observe any qualitative effect they should have used a rotation ratio of 6.0 for co-rotation and 3.0 for counter rotation.

Another important aspect of Mullin *et al.* (1998)'s study was the investigation of the radius ratio effect on the breakdown bubble. The conclusion drawn from this study was that the Reynolds number for the onset of the bubble is greatly affected by the radius ratio (inner cylinder radius over the outer cylinder radius). This was true especially at radius ratio greater than 0.5 where a steep rise in onset Reynolds number was observed.

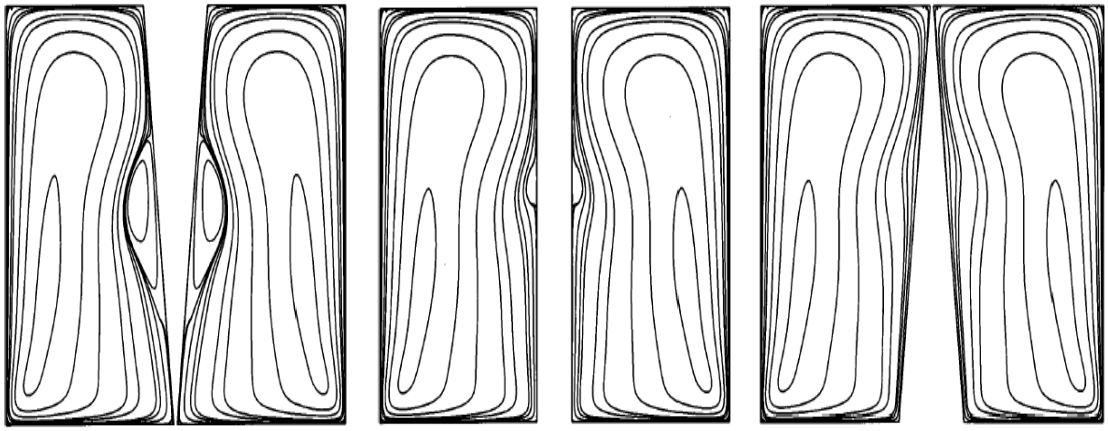

Figure 2.13 Streamline plots for the case of a rotating inner cylinder (a) gap width increasing towards the rotating endwall; (b) straight cylinder; (c) gap width decreasing towards the rotating endwall (Mullin et al. (2000)).

In a related study, Mullin *et al.* (2000) examined the effect of adding an inner cylinder with a sloping vertical wall on the creation of stagnation points. It was found that sloping the inner rotating cylinder, such that the gap increased towards the rotating endwall, as in Figure 2.13(a), markedly enhanced the vortex breakdown bubble.

However, sloping the gap in the opposite direction tended to suppress the breakdown bubble (Figure 2.13(c)). Figure 2.13(b) represents streamline plots with vortex breakdown bubble for the case where the inner cylinder had straight vertical wall. In explaining the observations, they suggested that the sloped rotating wall created an adverse pressure gradient opposing the motion of the fluid, for case (a) hence causing flow reversal; whereas for case (c) a favourable pressure gradient was created hence suppressing the breakdown bubble.

(ii) Temperature Gradient

It is known that when the temperature of a fluid element rises it becomes lighter and tends to rise. Some researchers have used this physical mechanism to control vortex breakdown in closed cylinders. Herrada and Shtern (2003a) used temperature gradient in the axial direction to control vortex breakdown in a sealed cylinder filled with a compressible swirling fluid. This thermal control method was based on a fundamental principle of centrifugal and/or gravitational convection. However, in their paper they focused on the centrifugal effects because they thought that centrifugal forces were a few orders of magnitude larger than the gravitational forces in practical high speed flows. Herrada and Shtern found that an addition thermal convection counter-flowing with respect to the base flow suppressed vortex breakdown, while co-flowing thermal convection enhanced vortex breakdown. Counter-flow was due to a positive temperature gradient ($\varepsilon > 0$), whereas co-flow was due to a negative temperature gradient ($\varepsilon < 0$).

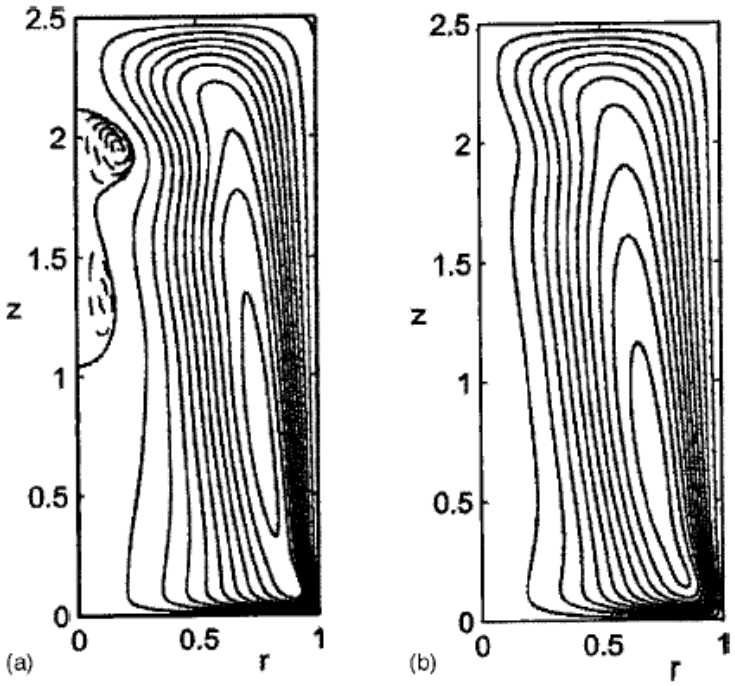

Figure 2.14 Effect of positive temperature gradient on vortex breakdown. (a) base flow with no temperature gradient; (b) disappearance of the vortex breakdown due to a temperature gradient ε = 0.7 (Herrada and Shtern (2003a)).

A recent study by Herrada and Shtern (2003b) investigated the control of vortex breakdown using the combined effect of adding near-axis swirl and thermal gradients. This technique combines the methods used by Husain *et al.* (2003), near-axis swirl addition, and Herrada and Shtern (2003a), temperature gradients (Figure 2.14). The base flow was generated by rotating the bottom endwall and was controlled by spinning the central rod as well as the axial temperature gradient. The important result from the study was that vortex breakdown can be significantly enhanced (suppressed) by applying a moderate negative (positive) temperature gradient in the axial direction. They also noted that strong positive temperature gradients stimulate centrifugal instability leading to flow unsteadiness.

Based on their findings, Herrada and Shtern (2003b) speculated that an addition of co-rotating cold (counter-rotating hot) swirling jet could lead to suppression (enhancing) of vortex breakdown in real life applications.

(iii) Rotation of Both Endwalls

In order to enhance or suppress the vortex breakdown, some researchers have used the rotation of both endwalls (Hyun (1985b); Roesner (1990); Valentine and Jahnke (1994); Bhattacharyya and Pal (1998)).

Roesner (1990) experimentally investigated the vortex breakdown phenomenon in the confined region of a cylinder with independently rotating top and bottom endwalls. He first investigated the case where the top lid was rotating while the bottom was at rest, and later considered the co- and counter-rotation cases where both endwalls were spun. Roesner noted that, if the Reynolds number of the top endwall was slightly below the critical value where the first breakdown bubble is normally expected to occur, a slight co-rotation of the bottom endwall immediately created a recirculation motion along the axis of rotation. On the other hand, if the top disk Reynolds number was slightly above this critical value, a slow counter-rotation of the bottom endwall caused the recirculation region to disappear. The recirculation region along the axis of rotation was a vortex breakdown. It is not clear from the publication what ranges of rotation ratios were considered to be slight co-rotation and slow counter-rotation.

Co-rotation of the endwalls has also been employed by Bhattacharyya and Pal (1998) to control vortex breakdown in a laminar swirling flow inside a cylindrical container. They numerically modeled the flow by inducing a slight co-rotation ($0 < \varepsilon < 0.5$) of the top and bottom endwalls. Here, ε is the angular velocity ratio defined as:

$$\varepsilon = \frac{\Omega_t}{\Omega_b}, \tag{2.7}$$

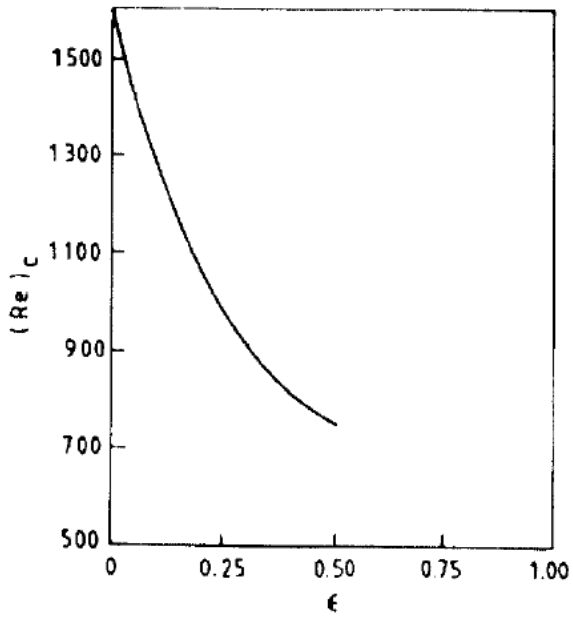

Figure 2.15 Variation of critical Reynolds number (Rec) with rotation ratio ε when aspect ratio H/R = 1.5 (Bhattacharyya and Pal (1998)).

where Ω_t and Ω_b are the angular velocities of the top and the bottom endwalls, respectively. They found that slight co-rotation of the upper endwall promotes the onset of vortex breakdown. This means that with the upper endwall rotating in the same direction as the bottom endwall, the critical Reynolds number for which a vortex breakdown occurred was considerably reduced as shown in Figure 2.15. Another finding from this study was that the vortex breakdown bubble appeared near the faster moving endwall, which in this case was the bottom endwall. This finding is rather peculiar considering that in cases where only one endwall rotates the vortex breakdown almost always appears near the stationary endwall (Escudier (1984)). This observation, as made by Bhattacharyya and Pal, will be investigated in the current study to ascertain its validity.

Valentine and Jahnke (1994) numerically predicted the flow field inside a cylindrical container induced by the rotation of two endwalls at the same rate (i.e. $\varepsilon = 1.0$). They found different types of recirculation bubbles depending on the combination between the Reynolds number and the aspect ratio (*H/R*). They reported that for high aspect ratio

cylinders and relatively low Reynolds numbers, slender recirculation bubbles appeared on the axis of the container. At high Reynolds numbers, they noted the formation of a toroidal vortex around an axial vortex core. The important point to note here, although not emphasised by Valentine and Jahnke, is that co-rotation of the two endwalls was conducive to vortex breakdown formation. With co-rotation, vortex breakdown onset occurred at lower Reynolds numbers than it would have for the cases with only one endwall rotation. They also reported that the shape of the entire flow structure, and in particular the toroidal vortex generated by the rotation of the two endwalls rotating at the same rate, is somehow different from the shape induced by rotating the two endwalls at different rates.

Very recently, Okulov *et al.* (2004) used the co- and counter-rotation of both top and bottom endwalls to simulate swirling flows in a closed cylindrical container. They were able to generate a vortex breakdown while rotating the two endwalls at the same rate ($\varepsilon = 1.0$). Although this study was mainly concerned with the onset of vortex breakdown rather than the control aspect, it still demonstrated that co-rotation of the two endwalls generated flow conditions that were conducive to the occurrence of flow reversal along the axis of rotation or simply vortex breakdown.

At this stage, it is worth mentioning that the vortex breakdown control methods reported so far have only considered mainly the co-rotation case with slight rotation ratios, except in the case of Valentine and Jahnke (1994) and Okulov *et al.* (2004) who considered the case of two endwalls rotating at the same rate. Other studies have also been devoted to the onset on vortex breakdown (Roesner (1990)). More expansive investigations are therefore required to extend the range of rotation ratios and also examine the effect of both co-rotation and counter-rotation on the occurrence, sustenance and suppression of the vortex breakdown.

(iv) Differentially Rotating Cylinder

Watson and Neitzel (1996) used a modified Escudier problem in which the bottom endwall was spun with an angular velocity Ω_1 and both the sidewall and the top endwall rotated with an angular velocity Ω_2 ($0 \le \Omega_2 \le \Omega_1$). They tested the validity of the

Brown and Lopez (1990) vortex breakdown criterion by computing the helix angles of velocity and vorticity. The results showed that the criterion was valid for each case they tested. In addition, the effect of aspect ratio was also investigated by testing three different ratios. One of the most significant findings from this work was that by increasing the aspect ratio, for a given value of Re, the occurrence of the incipient breakdown was delayed. This means that for larger aspect ratios the onset of vortex breakdown occurs at higher angular velocities. The method of differentially rotating separately one endwall and the other endwall together with the sidewall has been employed by other researchers to control vortex breakdown as will be described below.

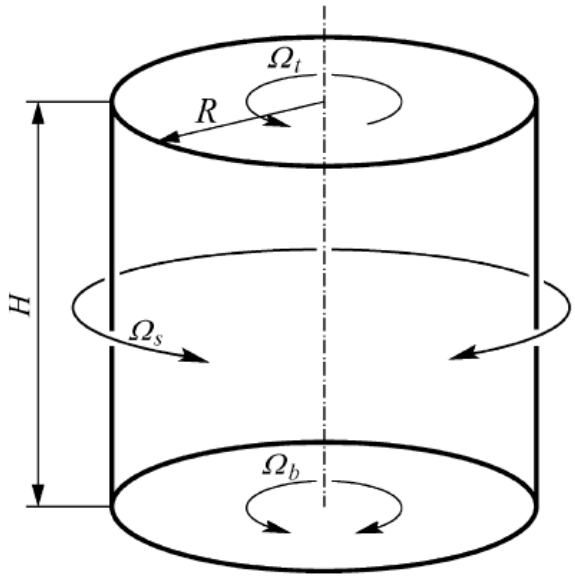

Figure 2.16 Schematic representation of a differentially rotating cylinder (Fujimura et al. (2004)).

A differentially rotating cylindrical container (Figure 2.16) was used by Fujimura *et al.* (2004) to investigate the effect of combined rotation of both endwalls and the side wall of a cylinder. The top endwall was rotated at a constant angular velocity Ω_t, while the side wall and bottom endwall were rotated at a combined angular velocity Ω_{sb}. The overall Reynolds number Re_Δ was computed based on the angular velocity difference $(\Omega_t - \Omega_{sb})$. For the cases investigated $|\Omega_{sb}/\Omega_t| << 1$ and both co-rotation $\Omega_{sb}/\Omega_t > 0$ and counter-rotation $\Omega_{sb}/\Omega_t < 0$ were considered.

Fujimura et al.'s observations of the effect of differential rotations of the container walls on the vortex breakdown revealed two main results: first, for co-rotation as $|\Omega_{sb}/\Omega_t|$ increases the breakdown bubble shifts towards the lower endwall, while for counter-rotation it moves toward the top endwall; and second, if the value of $|\Omega_{sb}/\Omega_t|$ is continuously increased the bubble will ultimately disappear. The results also revealed that for both co- and counter-rotation it is possible to control the size of the vortex breakdown by appropriately choosing the differential Reynolds number Re_Δ and the rotation ratio Ω_{sb}/Ω_t.

(v) Spin-Up and Spin-Down

Bhattacharyya and Pal (1999) implemented vortex breakdown control by the spin-up and spin-down processes. The base flow was generated by rotating the lower endwall or by co-rotating both endwalls. The spin-up process was achieved by impulsively rotating the upper endwall with smaller angular velocity in the same direction as the lower endwall. While the spin-down process was achieved by abruptly bringing to rest the top endwall, which was co-rotating with small rotation ratio ($\varepsilon \leq 0.2$). Before the spin-down process a separation bubble was present whereas before the spin-up process the flow was free of separation bubble.

Prior to starting the spin-up process Bhattacharyya & Pal maintained a steady state flow, with no vortex breakdown, by rotating the bottom endwall with a speed corresponding to Re = 1300, which is lower than the critical Reynolds number $Re_c = 1600$ (for their cylinder) associated with the onset of vortex breakdown. Then the top endwall was abruptly spun to co-rotate with an angular velocity ratio $\varepsilon = 0.1$. It was observed that a transient flow developed due to the sudden perturbation leading to the formation of a single separation bubble on the swirl axis after a non-dimensional time t = 2.1. During this period of transition, the bubble size grew until the flow reached a new steady state after a non-dimensional time t = 4.0.

Before starting the spin-down process, Bhattacharyya & Pal kept a steady state flow inside the cylinder by co-rotating the bottom endwall (Re = 1300) and the top endwall. The rotation ratio was $\varepsilon = 0.1$ which generated a separation bubble along the axis of rotation. The spin-down process was initiated by abruptly stopping the top endwall

causing a transient flow to develop within the cylinder. They observed that a nondimensional time t = 30 was required for the vortex breakdown bubble to completely disappear from the cylinder. This finding seems to contradict the findings of Fujimura *et al.* (1997) and Liu *et al.* (2003b) that the time to settle to the state of rest in a spin-down process was found to be significantly less than the time to achieve a steady state in the spin-up process. Bhattacharyya and Pal (1999) also reported that during the transient period while the bubble was shrinking it was moving towards the slow moving upper endwall. They concluded that the spin-up and spin-down processes can effectively generate and degenerate a separation bubble in a closed cylinder filled with liquid.

The main contribution of the work of Bhattacharyya and Pal (1999) was with respect to the transient flow development of the vortex breakdown bubble. The steady state part had already been reported in previous publications (Valentine and Jahnke (1994); Bhattacharyya & Pal, 1998; Brons *et al.* (1999)). It would have been more informative if Bhattacharyya and Pal (1999) had investigated the effect of spin-up and spin-down with counter-rotation of the two endwalls on the generation and degeneration of the separation bubble. We must realise that the spin-up and spin-down are not strictly vortex breakdown control methods because the steady state result, which is more significant from the control point of view, can be ultimately achieved without necessarily changing the top endwall speed in an abrupt way.

2.7 Scope of the Current Study

The review of the literature on vortex breakdown, as described in this chapter, has highlighted a number of issues which need further investigation. Some of these issues that are addressed in the current thesis are outlined in this section.

Nearly every method of controlling vortex breakdown in a closed cylinder, currently available in the open literature, has shortcomings that inevitably make it unsuitable for some applications. For instance, the temperature gradient method may not be suitable for some applications where the temperature has to be maintained at a certain constant value throughout the entire cylinder. The near-axis swirl addition is a very intrusive

method; the central rod interferes with the vortex core and does affect, to some degree, the vortex breakdown phenomenon which is the subject of control. The rotation of both endwalls and the differentially rotating cylinder methods are expensive designs from the construction point of view as well as energy consumption. The spin-up and spin-down techniques are not pure vortex breakdown control methods as, strictly speaking, they fall under the two endwall rotation category.

Therefore, a new design using a small rotating disk, concentrically located in the bottom endwall, is proposed. The small control disk manipulates the characteristic features of the upstream flow, depending on the direction and rate of rotation, to enhance or suppress the breakdown bubble. The study was conducted numerically and experimentally. Unlike most of the previous studies on vortex breakdown control, this study systematically and comprehensively investigated the effects of: the control disk size, and rotation ratio between the control disk and the top endwall on the vortex breakdown bubble onset, enhancement and suppression. Both co-rotation and counter-rotation were covered over wider ranges of rotation ratios.

The flow generated by the rotating endwall and the small control disk were investigated first separately and then in combination to be able to ascertain the contribution of control disk on vortex breakdown. The aspects of the vortex breakdown bubble that were examined include: the radial and axial sizes, the axial location along the swirl axis, the swirl number and the relative viscous power expended by the control disks.

Only a few researchers have investigated the growth and migration of the vortex breakdown bubble within a closed cylinder. Among those, almost none has examined the size of the breakdown bubble in the axial direction. It is therefore important to determine the whole extent of the breakdown bubble before we can claim knowledge of the structure of the swirling flow in a closed cylinder. This study investigated the location of the breakdown bubble by examining the migration of not only the upstream stagnation point but also the downstream stagnation point and the bubble centre. The size of the breakdown bubble was examined in both axial and radial directions.

Most control methods involving the rotation of both endwalls have not thoroughly investigated the effect of co-rotation and counter-rotation. In addition, some studies

have only examined a single rotation ratio with co-rotation or counter-rotation, while others have investigated only a limited range of rotation ratios (slight co-rotation or slow counter-rotation). The current work covered a wider range of rotation ratios with both co-rotation and counter-rotation, typically for experimental investigations: $-4.0 \leq \varepsilon \leq 5.0$; and for numerical simulations: $-8.0 \leq \varepsilon \leq 10.0$.

The aspect of input power or viscous power, in this case, required during vortex breakdown formation and development has not been reported in the literature, at least as far as this author is aware. This thesis proposes to establish the effectiveness of using a small control disk to control vortex breakdown. The relative viscous power expended to control vortex breakdown was numerically evaluated for the rotating endwall and the control disk and comparisons were made.

The onset of vortex breakdown as a result of flow control has not been sufficiently investigated. This work undertook to numerically simulate flow before the occurrence of vortex breakdown with and without the control disk rotating; the flow was investigated to provide evidence of vortex breakdown. In the same vein, an attempt is made to explain conditions that lead to vortex breakdown formation by computing the swirl number in the super critical flow zone (i.e. upstream of the vortex breakdown). A new parameter, the axial Reynolds number, is introduced to further understand conditions that lead to vortex breakdown.

Finally, although a number of methods have been proposed and implemented to control vortex breakdown in closed cylinders, the technique presented in this study is not only different but also a more efficient method from the point of view of power input. It is shown that using a small rotating disk as a control tool is far more energy efficient than using some of the previous control methods.

2.8 Summary

The chapter has presented a review of the literature on the vortex breakdown topic. The main focus of the review was to examine the vortex breakdown phenomenon in closed cylinders and the various ways, so far available, to control it. It has been shown that there are seven types of vortex breakdown with types ‘O’ (the bubble type) and type 2

(the spiral type) being the most common. The three main theories that explain the occurrence of vortex breakdown have been presented. Studies involving vortex breakdown on delta wings, vortex tube, and open and closed cylinders have been briefly discussed. Previous studies relating to control of vortex breakdown on delta wings and in closed cylindrical containers, which is the main focus of the present study, have been presented. Methods to control vortex breakdown in closed containers including the near-axis swirl addition, temperature gradients, and the rotation of the two endwalls have been evaluated. The contribution of the present study has been highlighted. In the next chapter, the methods employed to experimentally and numerically investigate vortex breakdown are described.

Chapter 3
Experimental and Numerical Methods

3.1 Introduction

This chapter is divided into two main parts. The first part is concerned with experimental methods, while the second deals with numerical methods. The experimental methods section describes the experimental facility used to conduct this study, followed by descriptions of the materials and instruments. The general procedures that were followed to perform the experiments are detailed. The hysteresis test and data processing procedures are also reported. The experimental methods end with validation of selected experimental results. The second part of this chapter begins with a presentation of grid construction followed by governing equations and a few notes on streamlines and stream function. Brief details about the problem setup are elaborated before the techniques employed in numerical solution are described. Non-dimensional numbers used in this work are presented followed by derived quantities, grid resolution study, post-processing and validation of numerical results. A summary of the chapter concludes the presentation.

3.2 Experimental Methods

At the beginning of the project, there was no experimental rig appropriate for the investigation on vortex breakdown. Therefore, a new experimental facility was designed and constructed to carry the experiments that are described in this chapter.

3.2.1 Experimental Rig

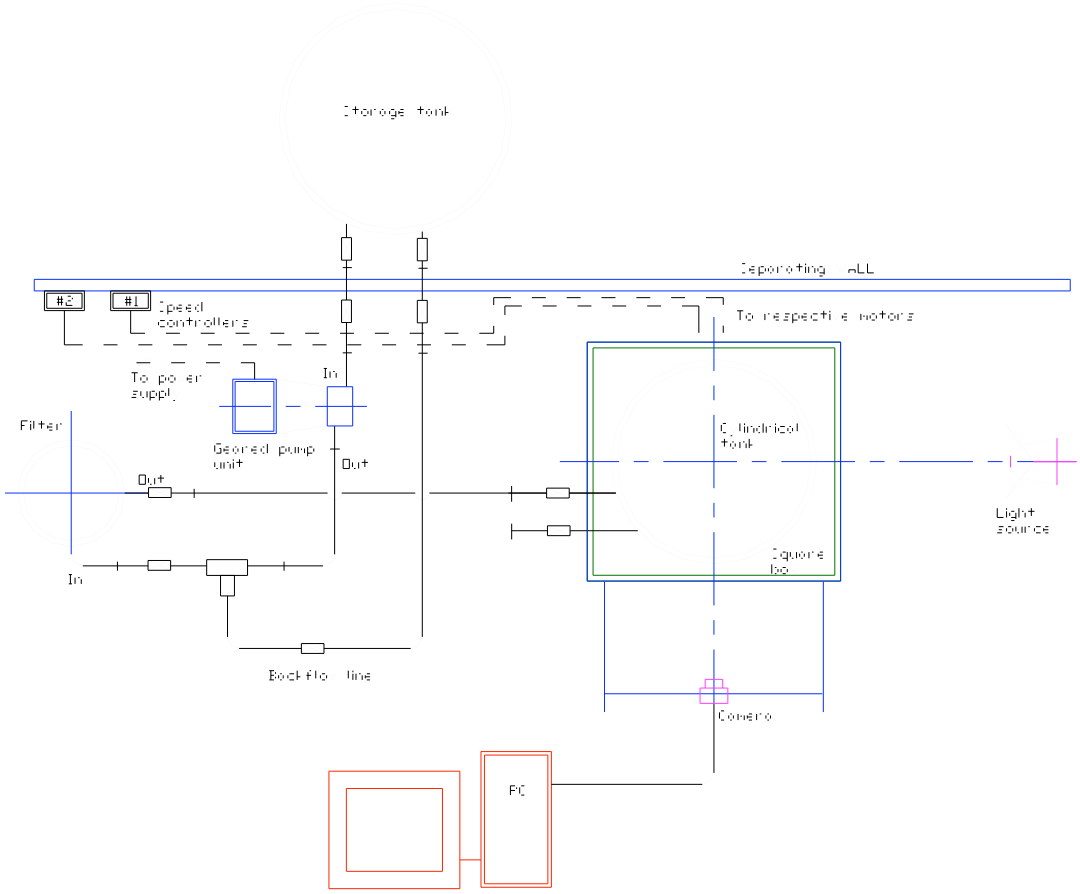

Figure 3.1 Schematic plan view of the experimental setup.

Figures 3.1 and 3.2 depict the configuration of the experimental facility located in the Fluids Laboratory for Aeronautical and Industrial Research, Department of Mechanical Engineering of Monash University. The rig viewed from above is shown in Figure 3.1 while a frontal view schematic is shown in Figure 3.2. This experimental rig was

designed and constructed, from scratch, in the early stage of the research study.

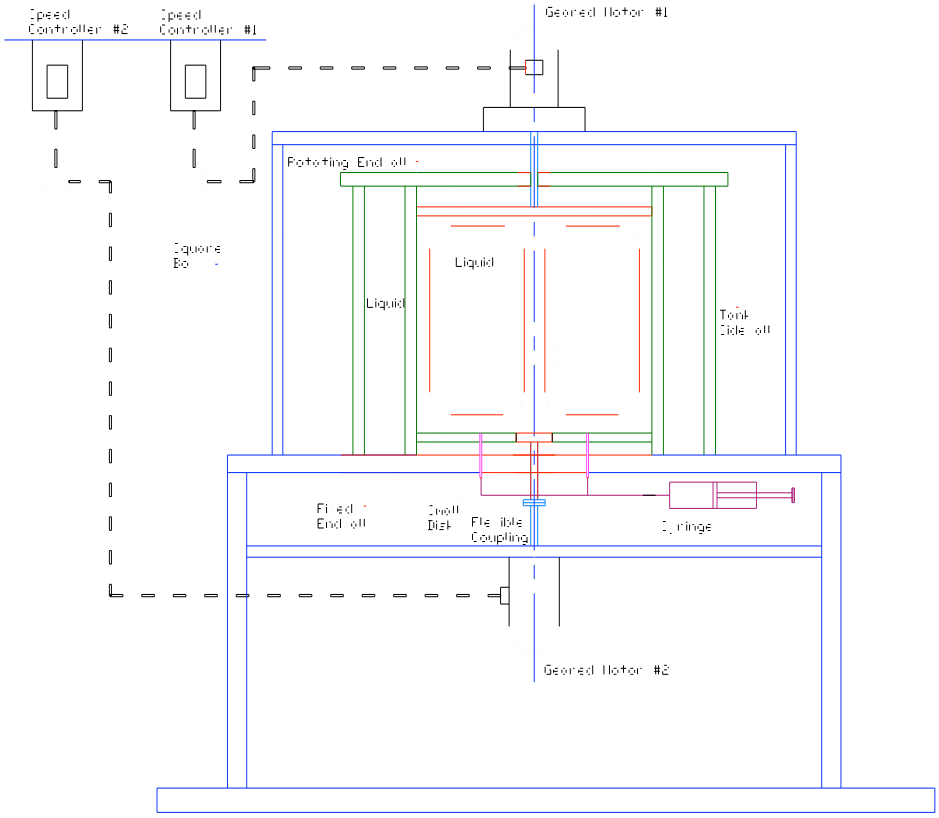

Figure 3.2 Close up front view of the main section of the experimental rig.

The primary purpose of this rig was to provide a research tool to conduct confined flow vortex breakdown experiments. In addition, the experimental facility was also used to filter the experimental fluid. Filtering was of paramount importance because prior to embarking on a series of tests the liquid had to be clear and as free of any foreign particles as it could possibly be. It is important to note that while following the description of the experimental rig, both Figures 3.1 and 3.2 should be inspected to gain a clear picture.

The experimental rig consisted of a cylindrical Perspex tube of a radius R = 243 mm filled with silicone oil of absolute viscosity μ = 0.5 kg/m^{2}s at 25 ºC. Throughout this study only one aspect ratio H/R = 2 was used. H is the height of the fluid column

between the two endwalls and *R* is the inner radius of the cylinder, which is also equal to the radius of the rotating endwall (or top endwall). In the bottom endwall a recess was made to accommodate small the disks (or control disks) of different sizes, the rotation of which would provide the controlling action of the vortex breakdown. Table 3.1 shows the dimensions of the five different small disks employed in this study. The small disk was flush mounted concentrically into the non-rotating endwall.

Table 3.1 Control disks used in the experiments.

Disk	Radius, r (mm)	r/R as %	Effective area as % of large disk
d1	12.5	5.14	0.26
d2	24.5	10.08	1.02
d3	37.0	15.23	2.32
d4	49.0	20.16	4.07
d5	74.5	30.66	9.40

The flow structure within the working section, which is the cylindrical tank, was visualised by shinning a thin sheet of light (≈ 5 mm) emanating from a twin 500 watt floodlight mounted on a stand holder raised approximately at the same level as the centre of the working section. To highlight the flow structures, a small quantity of silicone oil mixed with seeding particles was injected by means of a hypodermic syringe through two small holes in the fixed endwall. Photographs were taken using a digital camera. The rotating endwall and the control disk were independently driven by two electric motors via gearboxes. The motors were operated through frequency inverters (see specifications in Table 3.2). More details regarding the above equipment, instrumentation and materials are provided in the following sections.

Table 3.2 Specifications of the drive units for the rotating endwall and the control disk with their respective controllers.

Description	**Small disk drive unit #2**	**Rotating endwall drive unit #1**
Motor	SEW Geared Motor #2	SEW Geared Motor #1
Output power	1.5 kW	0.75 kW
Output speed	1400@50Hz	389@50Hz
Gearbox ratio	1.0	3.55:1
Output torque	10.2 Nm	18.4 Nm
Accessories	Encoder fitted to the motor	Encoder fitted to the motor
Frequency Inverter	MOVITRAC31C VVVF	MOVITRAC31C VVVF
Power supply	3 phase, 415V	3 phase, 415V
Output power	1.5 kW	0.75 kW
Accessories	Key pad, break resistor, input filter/output choke, speed control card	Key pad, break resistor, input filter/output choke, speed control card

The experimental setup was a closed circuit which allowed pumping the working fluid from the storage tank, through a pipe system via a gear pump and a filter, up to the working section of the rig. The storage tank was a Nylex 350 litre Hazspill recovery drum, chemically compatible with Silicone oil. The pump was an Oberforfer pump model N994RE, coupled to a Lafert 0.55 kW electric motor with a maximum speed of 940 rpm. It had a capacity of 0.3 l/s at 7 m head. The filter bags used were the 1 micron nominal size bags made from Polyester. The 1 micron size was chosen to ensure that no seeding particle would be able to pass through.

The above rig design offers a number of benefits when compared with previous designs. First, it is possible to study the flow structure due to the combined rotation of the top

endwall and control disk without introducing a foreign object into the working section, as was the case in the study of Husain *et al.* (2003). Second, the present control method looks more feasible and attractive than the use of two endwalls (Valentine and Jahnke (1994)) because a small disk leads to less power requirement for the second drive system and a less bulky structure.

3.2.2 Materials

(i) Working Fluid

The working fluid that was used in this work was Silicone oil, also known as Silicone Antifoam, a Shin-Etsu silicone brand. It is a clear and transparent, water-like free flowing liquid. The fluid had the following properties at 25 ºC, a absolute viscosity μ = 0.5 kg/m^{2}s and a density ρ = 969 kg/m^3. One of the reasons for choosing Silicone oil, as opposed to other fluid like Glycerine, is that it does not absorb moisture, i.e. it has an excellent water repellence characteristic. The other reason is that Silicone oil has a lower Viscosity Temperature Coefficient (*VTC*) = 0.60 at 25 ºC as opposed to 0.967 for Glycerine. The *VTC* is defined by the manufacturer of the experimental silicone oil as

$$VTC = 1 - \frac{(\nu)_{98.9}}{(\nu)_{37.8}}. \qquad (3.1)$$

where is the kinematic viscosity of the working fluid. From Equation 3.1, a bigger ratio between the fluid viscosities at 98.9 and 37.8 ºC generates a smaller value of *VTC*. A lower value of *VTC* means that the fluid viscosity is fairly constant when the temperature varies, which increases the accuracy of determining it. It is important to remember that as the fluid temperature increases the viscosity becomes less. Therefore, less variation of the fluid viscosity means that the above ratio is bigger.

Since the fluid temperature could not be kept constant at all times, it was therefore necessary to calibrate it over the temperature range between 21 and 30 ºC (Figure 3.3). The above temperature range included the experimental range. The fluid viscosity at 25 ºC was used to check the accuracy of the calibration. Calibration was performed using a

laboratory Rheometer with an accuracy of better than $\pm 10^{-6}$ mm^2/s.

(ii) Seeding Particles

The seeding particles employed were the S-HGS, silver coated hollow glass spheres. These are smooth borosilicate glass particles with a thin silver coating designed to increase the reflectivity and provide light scattering conducive to successful experimental data. These particles had a mean particle size of about 10 μm and a density of 1.4 kg/m^3.

3.2.3 Instrumentation

(i) Image Acquisition

The camera used for acquiring images was a Minolta Dimage 7Hi with a 5.0 megapixel CCD delivering resolutions as high as 2560 by 1920 pixels. The shutter speed could be varied between 1/2000 and 15 seconds with bulb setting for longer exposure of up to 30 seconds. Images were transferred to a computer for processing and analysis using a USB cable and interface software.

(ii) Temperature Measurement

As mentioned earlier, determining the correct fluid temperature was crucial to the accuracy and reliability of the experimental data. To achieve this, two type T thermocouples were attached to the cylindrical tank to enable direct measurement of temperature inside the working section. These T type thermocouples were made of a positive Copper wire and a negative Constantan wire. The temperature was sampled at two locations, one between the rotating endwall and the horizontal mid-plane and another was placed in the bottom half. The other ends of the thermocouples were coupled to a switch which in turn was connected to a calibrated Anritsu handheld digital thermometer, the accuracy of which was ± 0.5%. The switch had a third thermocouple connected to it and the other end of which was exposed to the ambient temperature. Ambient temperature measurement served as a reference. The ambient temperature reading from the digital thermometer was compared with the reading from a precision

mercury thermometer.

(iii) Rotational Speed

The rotational speeds of the rotating endwall and the small disk were determined from the corresponding frequency inverter readings. In addition, readings from a digital photo tachometer were used to confirm the accuracy of the inverter. The tachometer had a 5 digit display and could measure rotational speeds from 5 to 99,999 rpm with a resolution of 0.1 rpm (5 to 999.9 rpm) and 1 rpm (over 1,000 rpm). Its accuracy was ±0.05%.

3.2.4 Experimental Procedures

(i) Calibration

The first task to be carried out was concerned with determining the "actual" viscosity of the working fluid. This was prompted by the fact that the viscosity value specified by the manufacturer was only for a temperature of 25 ºC, and was also short of accuracy (nominal value of 500 mm^2/s ±5%). In addition, the accuracy of the present results depended in part on how accurately the fluid viscosity was determined at each run.

Calibration was performed using a laboratory Rheometer fitted with a cup, where the fluid was placed and a disk attached to a spindle. The fluid was squeezed between the base of the cup and the disk with the gap set in advance. The additional knowledge of the fluid temperature, rotational speed of the disk and the reading for the torque required to rotate it was enough to determine the absolute viscosity of the fluid. The test was repeated at three temperatures, 21, 25 and 30 ºC using three different fluid samples. It was found that the average absolute viscosity of the experimental fluid varied with temperature according to Figure 3.3 with an accuracy of about ±0.5%. The equation relating the absolute viscosity to the temperature was used to determine the fluid viscosity during the experiments.

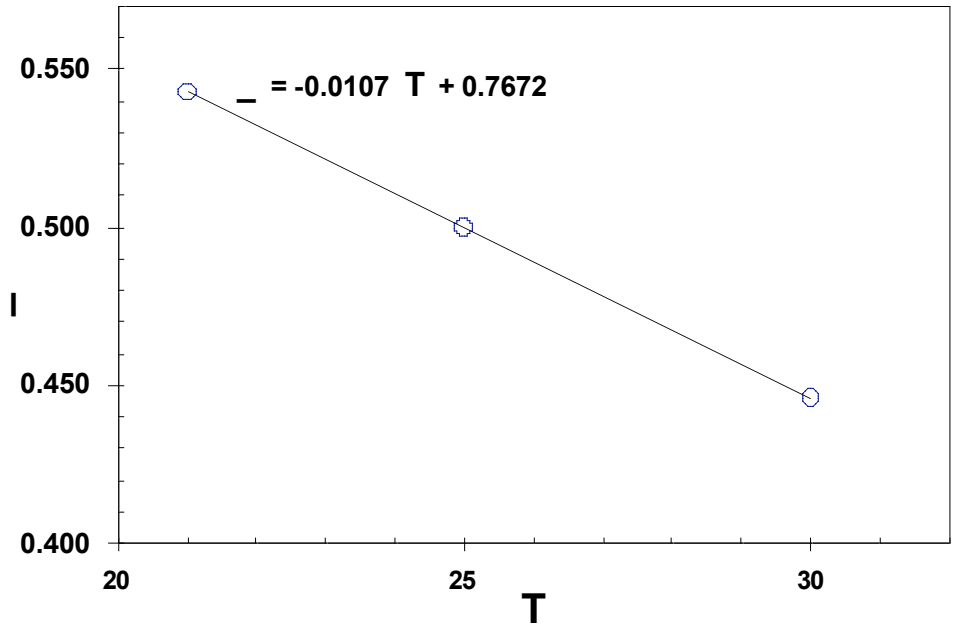

Figure 3.3 Calibration curve for determining the experimental fluid absolute viscosity. Absolute viscosity μ is in kg/m2s and the temperature T is in ºC.

(ii) Procedures

The procedures to be described in this section provide only a general guideline of the way the experiments were conducted. More specific procedures will be briefly presented in relevant sections of the thesis. The experiments can be grouped into three parts namely, vortex breakdown onset, vortex breakdown without control and vortex breakdown with control. In the first instance, procedures common to all experiments will be described and later specific procedures for each type will be presented.

(a) General Procedures

At the beginning of every set of experiments the rotating endwall was spun at a rotation rate within the range of the actual runs. This was done to allow a nearly isothermal state of fluid, hence minimize variations in temperature between the start and the end of the experiment. This initial spin was allowed to proceed for about an hour, after which the fluid temperature was observed to have stabilized. The ambient temperature was taken

using the digital thermometer and this temperature was compared with the reading from a high precision mercury thermometer.

With the light source on, the camera in position and set accordingly, the next step was to check the Reynolds number at which the onset of vortex breakdown occurred. The rotating endwall was rotated until a recirculation zone along the swirl axis just started to form. At this point, both the rotational speed of the endwall and the actual fluid temperature were recorded to compute the Reynolds number. Once these preliminary checks were done satisfactorily, the experiments would then proceed.

(b) Vortex Breakdown Onset

The purpose of these experiments was to determine the effect of co-rotating and counter-rotating the small disk on the onset of vortex breakdown. For the purpose of this work, vortex breakdown onset was defined as the state of flow when the smallest visible bubble was observed along the swirl axis. With the rotating endwall spinning just at the speed at which vortex breakdown occurs, corresponding to $Re \approx 1440$, the small disk was made to rotate with a the minimum possible angular speed, which in the present case was 5.95 rad/s, the flow structure was then observed: (i) for the co-rotation case the vortex breakdown bubble was observed to grow, hence the endwall rotation had to be carefully and gradually decreased to go back to the onset state; (ii) whereas for the case of counter-rotation the endwall rotation rate had to be gradually increased to achieve the critical state of vortex breakdown onset. The small disk rotation rate was subsequently incremented and the endwall angular velocity adjusted accordingly so as to reach the state of vortex breakdown. In all cases, the experiment would continue until when it was not possible to sustain the vortex breakdown state; this depended on the size of the control disk.

(c) Vortex Breakdown without Control

The purpose of these experiments was to validate the experimental rig and its procedure and also to serve as benchmark for comparing the results generated from the vortex breakdown control experiments. The endwall rotational speed was steadily incremented from the vortex breakdown onset level ($Re = 1440$) to approximately $Re = 3000$. Digital

photos were taken at every step and transferred to the laboratory computer for further processing. In these experiments the small disk was kept stationary.

(d) Co-rotation and Counter-rotation Effects

Co-rotation was achieved when the rotating endwall and the small disk revolved in the same direction and counter-rotation was the opposite. These experiments were designed to study the effect that co-rotation and counter-rotation of a small disk had on the vortex breakdown bubble. In these experiments the endwall was spun at a constant angular speed while the small disk was rotated in one direction and pictures of the flow structure were taken. The speed of the control disk was increased in small steps while maintaining the same speed of the endwall. In practice, small adjustments were made to the speed to account for the fractional variations in fluid temperature in order to maintain a constant *Re*. The rotational direction of the small disk was then reversed, while keeping the endwall rotation constant and the experiment proceeded as above.

(iii) Hysteresis Testing

The Hysteresis test was conducted in order to confirm what other researchers (Sorensen and Christensen (1995); Jones (2002)) had already reported. In addition, and since during the experiments the speed of the endwall could be increased or reduced depending on the required adjustment without having to fear that the change of direction would influence the results. Sorensen and Christensen observed Hysteresis in a closed cylinder only for higher Reynolds numbers; such Reynolds numbers are well beyond the range covered in this work.

To test for hysteresis, the endwall was rotated at lower speed (Re = 1350) than the speed at which vortex breakdown onset occurred and then the speed was slowly increased until the first appearance of vortex breakdown (Re $\approx$ 1440). The endwall was gradually brought to rest before spinning it at a higher speed (Re = 1550). Subsequently, the endwall rotation rate was gradually decreased until vortex breakdown onset. In the above two cases, the speed at which vortex breakdown onset occurred was noted to be the same, hence it was concluded that hysteresis in a closed cylinder at relatively lower Reynolds numbers such as 1440 was not present.

3.2.5 Data Processing

The flow visualisation images captured by the Minolta digital camera were transferred to a Pentium 4 (1.7 Ghz and 1 Gigabyte memory) computer for post-processing. The computer was loaded with the MATLAB software. The data that were of interest included the flow visualisation pictures, converted from Tag Image File Format (TIF) to the Joint Photographic Image Group (JPG) format. During this conversion the image size was reduced from about 14,000 kB to about 100 kB. This size reduction was of great benefit considering the huge amount of image data that was stored. The important information extracted from these images included the size and location of the vortex breakdown bubble within the working section. This information was determined using the image analysis routines of the MATLAB package. The data on the size and location of the vortex breakdown bubble were later used to plot a number of graphs presented in this thesis. The accuracy of the above data was estimated to be within ± 3%.

3.2.6 Estimation of Uncertainties

The uncertainties in the Reynolds numbers associated with the rotating endwall Re (Equation 3.13) and the control disks Re_r (Equation 3.14) were computed based on the uncertainties in the rotational speed, the cylinder and control disk radii, and the fluid viscosity. Representative figures of the above uncertainties are as follows:

- Radii: the uncertainties related to the cylinder and control disks radii were estimated to be about ± 1% and ± 0.5% respectively.

- Rotational speed: the uncertainty in the angular velocity of the rotating endwall and the control disks was ± 0.5%

- Viscosity: the uncertainty associated with the fluid viscosity was estimated to be about ± 1%.

- Based on the above figures, the uncertainties in the Re and Re_r were calculated to be ± 3.5% and ± 2.5% respectively. The rotational speed ratio ε (Equation 4.1) had an uncertainty estimated to be ± 1%. These uncertainties represent the worst case scenario.

3.2.7 Validation

Initial experimental results were compared with available data from the literature for two reasons, to inspire confidence in the experimental facility and also in the method employed to acquire these results. The results are for experiments involving the top endwall rotation only. Comparisons with two benchmark results are shown in the following sections.

(i) Experimental Data of Escudier (1984)

Flow visualisation result shown in Figure 3.4(a) indicates that vortex breakdown onset occurs at a Re = 1440 which compares favourably, to within experimental error, with Escudier's finding ($Re \approx 1450$) as shown in Figure 3.5. Similarly, it can be seen that a single breakdown bubble was obtained for Re = 1614 in Figure 3.4(b), a double breakdown bubble for Re = 2096 in Figure 3.4(c) and a return to a single bubble as the Reynolds number increases to 2532 in Figure 3.4(d). These results are in general agreement with Escudier's results.

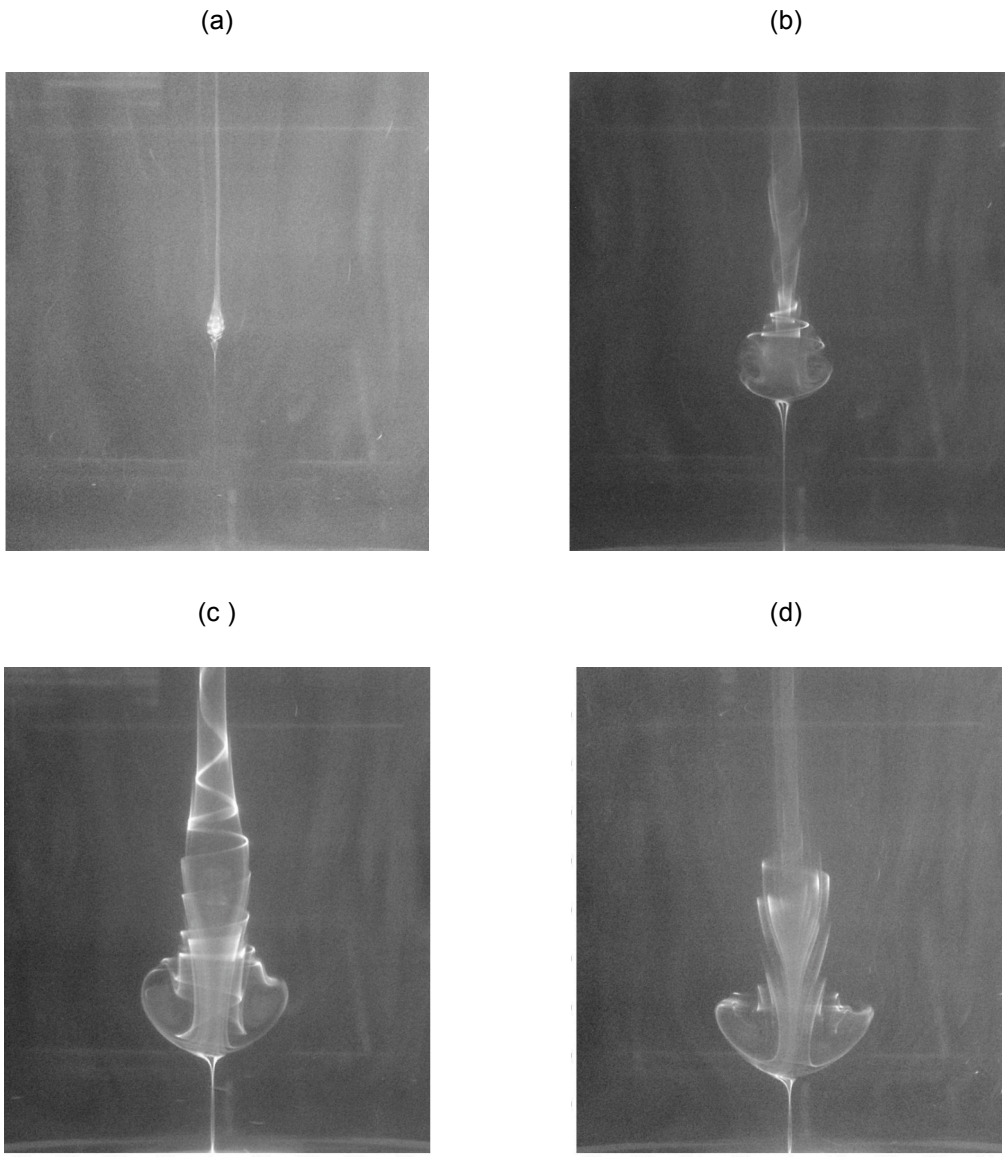

Figure 3.4 Vortex breakdown (VB) flow visualization in confined flow driven by the rotating endwall: (a) VB onset (Re = 1440); (b) single VB bubble (Re = 1614); (c) double VB bubble (Re = 2096); (d) single VB bubble (Re = 2532).

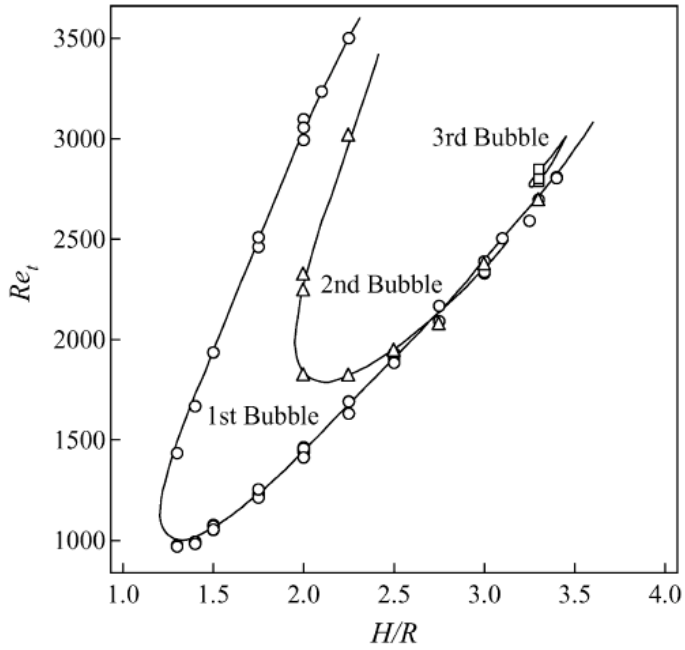

Figure 3.5 Regime boundaries for the 1st, 2nd and 3rd vortex breakdown when only one of the two endwalls is rotating. Of particular interest is the aspect ration H/R = 2.0 (Escudier (1984)).

(ii) Experimental Data of Fujimura et al. (1997)

Figure 3.6 shows the migration of the first or main vortex breakdown bubble along the axis of rotation. The position of the upstream stagnation point, as obtained by the present work is compared with the data of Fujimura *et al.* (1997) for the same aspect ratio $H/R = 2$. The axial position is normalised by the tank height ($H = 2R$) and shown as a percentage. There is a very good agreement between the current results and those of Fujimura et al. The slight disparity observed in the lower Reynolds number region is only about 2%, which is generally acceptable as being within experimental error margin.

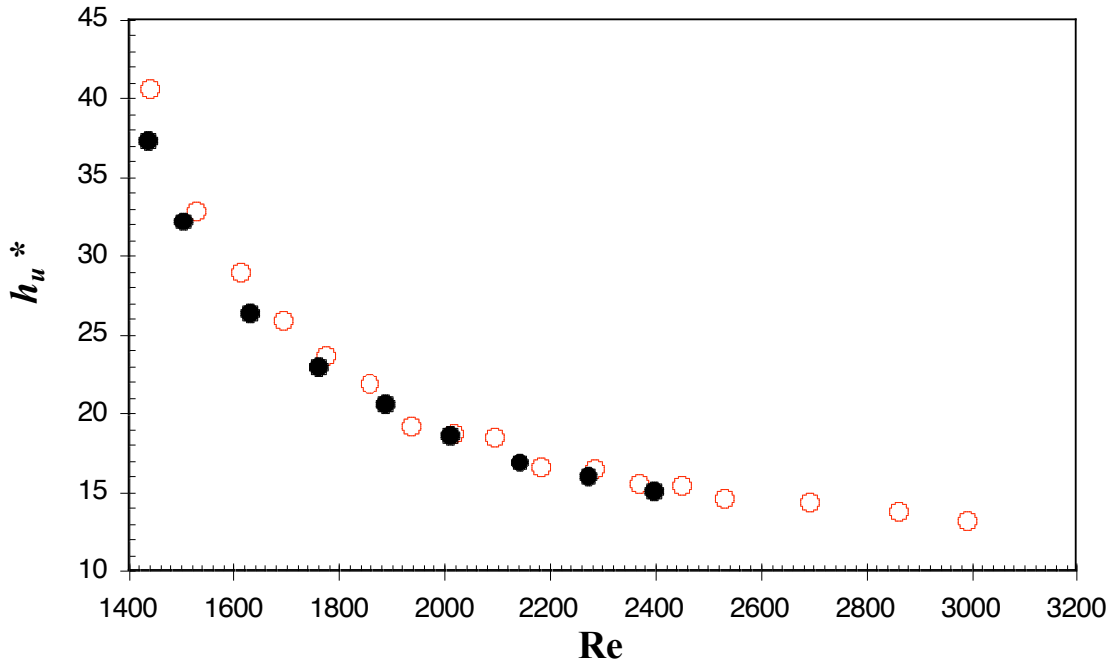

Figure 3.6 Variation of the location of the upstream stagnation point along the swirl axis with Reynolds number. Present work data is shown as open symbols and the data of Fujimura et al. (1997) represented by filled symbols. The aspect ratio H/R = 2.0.

3.3 Numerical Methods

The numerical solution method employed involved three distinct stages namely, pre-processing, processing and post-processing. Brief details about these tasks are presented in the following sections.

3.3.1 Grid Construction

Pre-processing was conducted using the commercial software GAMBIT version 2.0.4. Grid construction involved geometry creation, meshing of edges followed by face meshing and naming of different zones. Taking advantage of the symmetrical nature of the geometry only one half of the cylinder (Figure 3. 7) was modeled.

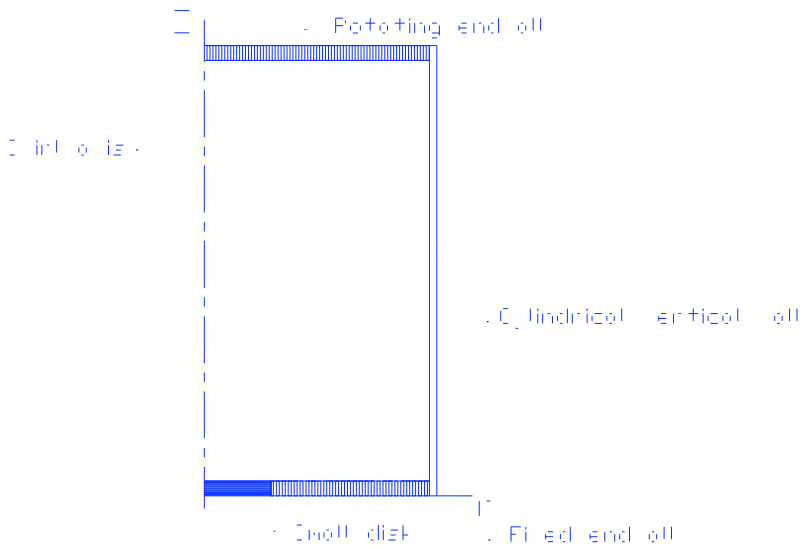

Figure 3.7 Model geometry represented as one half of the cylinder.

The geometry shown in Figure 3.7 was meshed using structured non-uniform mapped quadrilateral or rectangular elements, which are the most appropriate and efficient for problems similar to the present one. The grid was constructed such that in the regions next to the rotating endwall, the vertical wall and the fixed endwall, including the small disk, it was very compressed. This near wall compression was necessary in order to accurately capture the flow details in those regions with very high gradients. Near the swirl axis the grid was moderately dense to ensure that details of vortex breakdown bubbles could be captured.

The next step was to assign names to the different zone types as follows: the swirl axis was assigned AXIS zone type, whereas the WALL zone type was specified for the rotating endwall, cylindrical vertical wall, fixed endwall and small disk. The region between the above zones was defined as INTERIOR zone, which represents the fluid zone. The task of generating many models, including those constructed for the grid resolution study (see section 3.3.8), was simplified by making use of the GAMBIT journal files which automated the geometry creation and meshing tasks. In the end, six different grids were constructed according to the size of the five small disks and also the case where the entire bottom endwall was rotated. Figure 3.8 shows a typical grid used

in this study.

After the zone types had been named, a qualitative inspection of the grid was performed to check for local variations in cell sizes and ensure that they were minimized. To ensure that the quality of the mesh was satisfactory the size ratio between successive cells was limited to 10%, which is less than the maximum 20% recommended in most CFD literature. Finally, a check was made to make sure that the axis of rotation was the x-axis as required for axisymmetric model and the grid was saved.

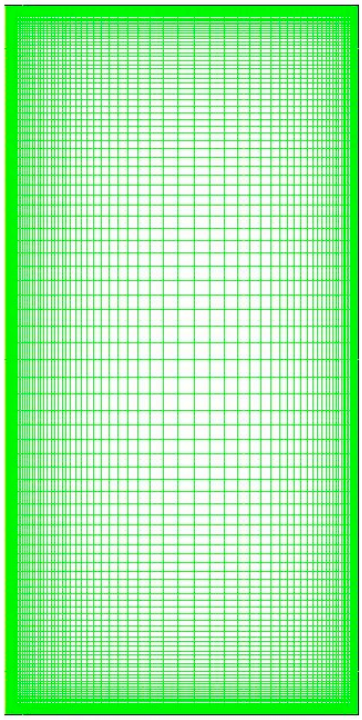

Figure 3.8 Typical grid: 130 grid points in the axial direction (vertical) and 85 grid points in the radial direction (horizontal). This grid has a total of 11050 quadrilateral cells.

3.3.2 Governing Equations

FLUENT version 6.1.18 code was used to perform numerical computations of the conservation of mass and momentum equations on every cell in the computational domain shown in Figure 3.8. In this section, the conservation equations are presented without being too elaborate. Further details can be found in Versteeg and Malalasekera

(1995) and Anderson (1995).

The general, and yet compact, form of the mass conservation or continuity equation is represented by

$$\frac{\partial \rho}{\partial t} = \nabla \cdot (\rho \mathbf{u}). \tag{3.2}$$

In Equation 3.2, ρ is the fluid density and $\mathbf{u}$ its velocity. For a steady and incompressible flow the density is constant and Equation 3.2 reduces to

$$\nabla \mathbf{u} = 0. \tag{3.3}$$

The vector form of the momentum equation for unsteady and incompressible Newtonian flow given by

$$\rho \frac{\partial \mathbf{u}}{\partial t} + \rho(\mathbf{u} \cdot \nabla)\mathbf{u} = -\frac{1}{\rho}\nabla P + \nu \nabla^2 \mathbf{u} + \mathbf{S}. \tag{3.4}$$

In Equation 3.4, the left-hand side comprises the terms for the local acceleration and convection whereas the right-hand side shows the pressure gradient, the viscous and the source terms.

The conservation of momentum in the radial (r), azimuthal (θ) and axial (x) directions is given by Equations 3.5(a-c) respectively. These equations constitute what is known as the Navier-Stokes equations for a compressible and unsteady 2D or axisymmetric flow:

$$\rho\left(\frac{\partial V_r}{\partial t} + V_r \frac{\partial V_r}{\partial r} + V_x \frac{\partial V_r}{\partial x} - \frac{V_\theta^2}{r}\right) = -\frac{\partial P}{\partial r} + \mu\left(\frac{\partial^2 V_r}{\partial r^2} + \frac{1}{r}\frac{\partial V_r}{\partial r} + \frac{\partial^2 V_r}{\partial x^2} - \frac{V_r}{r^2}\right) + S_r \tag{3.5a}$$

$$\rho\left(\frac{\partial V_\theta}{\partial t} + V_r \frac{\partial V_\theta}{\partial r} + V_x \frac{\partial V_\theta}{\partial x} + \frac{V_r V_\theta}{r}\right) = \mu\left(\frac{\partial^2 V_\theta}{\partial r^2} + \frac{1}{r}\frac{\partial V_\theta}{\partial r} + \frac{\partial^2 V_\theta}{\partial x^2} - \frac{V_\theta}{r^2}\right) + S_\theta, \tag{3.5b}$$

$$\rho\left(\frac{\partial V_x}{\partial t} + V_r \frac{\partial V_x}{\partial r} + V_x \frac{\partial V_x}{\partial x}\right) = -\frac{\partial P}{\partial x} + \mu\left(\frac{\partial^2 V_x}{\partial r^2} + \frac{1}{r}\frac{\partial V_x}{\partial r} + \frac{\partial^2 V_x}{\partial x^2}\right) + S_x. \tag{3.5c}$$

Equations 3.4 and 3.5 are in a general form. However, the equations solved for the current problem of vortex breakdown did not include the time derivative terms, because the flow was incompressible, as well as the momentum source terms. These equations were then solved throughout the discretised computational domain, using the discretisation techniques described in section 1.3.5.

3.3.3 Streamlines and Stream Function

Numerical flow visualisation uses, among other tools, streamlines to reveal flow patterns. In addition, stream functions relate streamlines to the statement of conservation of mass (Equation 3.3). A streamline can be defined as an imaginary curve in the flow such that the velocity vector of every fluid particle is tangent to it at a particular instant. It therefore follows that there can be no fluid flow crossing a streamline. An important property of a stream function is that it is constant along a streamline and the difference between constant values of stream function defining two streamlines is the volume rate of flow between the streamlines. The mathematical relationship between the two terms is briefly described below. Detailed analysis can be found in standard Fluid Mechanics textbooks.

In cylindrical coordinates, a streamfunction relates to the fluid velocity components as follows:

$$V_r = -\frac{1}{r}\frac{\partial \Psi}{\partial x}, \tag{3.6a}$$

$$V_x = \frac{1}{r}\frac{\partial \Psi}{\partial r}. \tag{3.6b}$$

For axisymmetric incompressible flow, the continuity equation (Equation 3.3) is defined by

$$\frac{1}{r}\frac{\partial (rV_r)}{\partial r} + \frac{\partial V_x}{\partial x} = 0. \tag{3.7}$$

By substituting V_r and V_x into Equation 3.7 the following expression is obtained:

$$-\frac{1}{r}\frac{\partial}{\partial r}\left(\frac{\partial \Psi}{\partial x}\right)+\frac{1}{r}\frac{\partial}{\partial x}\left(\frac{\partial \Psi}{\partial r}\right)\equiv 0\,. \tag{3.8}$$

Thus, the streamfunction automatically satisfies the continuity equation.

3.3.4 Problem Setup Procedure

CFD computations were performed using the commercial software FLUENT version 6.1.18. In the FLUENT environment, the grid created from GAMBIT was read (imported) and checked for errors. The experimental material was created and the following properties were specified: density ρ = 969 kg/m3, absolute viscosity ע = 0.520 kg/ms. These properties were considered to be constant for simulations purposes only, as the flow is fully determined by the Reynolds number.

In line with the specifications given during grid construction, the following boundary conditions were assigned to the different zones: swirl axis – AXIS; default interior – INTERIOR; fluid – FLUID (the newly created fluid); rotating endwall, fixed endwall, small disk and cylindrical vertical wall – WALL. All stationary WALL zones had a NO SLIP boundary condition and all rotating WALL zones were defined as moving walls and given a specific angular velocity depending on the flow condition to be modeled.

The segregated solver, with its default implicit formulation procedure, was chosen. This solver was chosen because of its suitability to incompressible flows where body forces are not strong, as is the present case. In addition, the fact that the continuity and momentum equations are sequentially solved, rather than coupled, simplifies the computations. The laminar, steady and axisymmetric swirl options were selected and so was the absolute velocity formulation. The flow was assumed to be laminar for the range of Reynolds numbers considered in this study in accordance with findings from previous researchers (Benay (1984); Bhattacharyya and Pal (1998)). Details about the solution controls are given in the next section.

3.3.5 Solution Techniques

All the equations of flow as well as the swirl velocity were activated; this was done to enable the CFD code to solve them in the discretised flow domain. The default under-

relaxation factors were maintained as they seemed to perform well. Two convergence criteria were used: first, the normalized and scaled residuals for the continuity x, r and swirl velocities were set such that the solution was considered converged when their respective values dropped below 10^{-6}. This meant that the solution was not changing when the condition was met. Second, surface monitors were used as convergence monitoring tools. Custom equations were created for the integral of shear strain rate over the active surface of both the rotating endwall and the small disk (refer to section 1.3.7). The evaluated integrals on these surfaces were printed on the screen for every iteration and the convergence criterion was considered satisfied once the changes in the monitored values did not exceed 0.01% after at least 500 iterations. Such stringent convergence conditions, when both criteria are met, ensured that the final results were fully converged.

(i) Discretization of Equations

In order to be able to solve the Navier-Stokes Equations 3.5(a-c) it was imperative that they were transformed from continuous to discrete formulation through a process of approximation also know as discretisation. It is important to bear in mind that the computation domain has already been discretised when generating the grid. Through this discretisation process, partial differential equations are rewritten in algebraic form.

The steady convection and diffusion of a property ϕ, in the absence of source terms, can be expressed by

$$\frac{d}{dx}(\rho u \phi) = \frac{d}{dx}\left(\Gamma \frac{d\phi}{dx}\right). \tag{3.9}$$

And the continuity condition is represented as

$$\frac{d}{dx}(\rho u) = 0\,. \tag{3.10}$$

Figure 3.9, showing a control volume V, is used to briefly illustrate the discretisation process for a steady one-dimensional convection-diffusion.

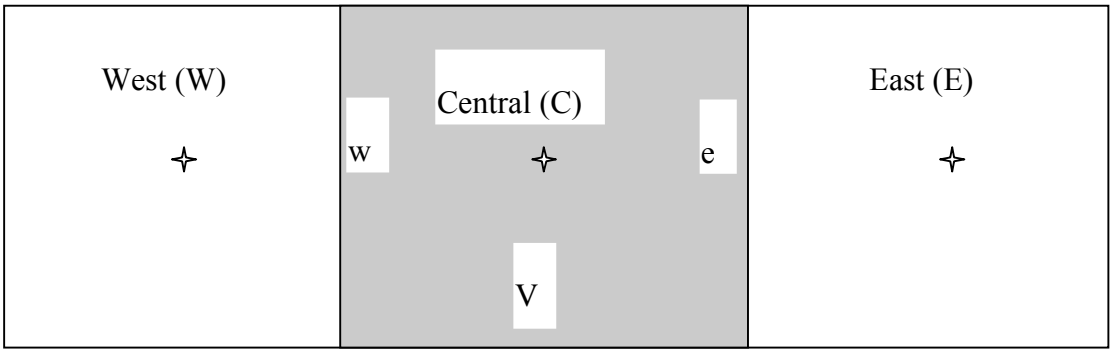

Figure 3.9 Discretisation diagram for a one-dimensional control volume.

If we let $F = \rho u$ and $D = \frac{\mu}{\delta x}$ and use the central difference scheme, the convection-diffusion equation can be represented in a discretised form as follows:

$$F_e \Phi_e - F_w \Phi_w = D_e(\Phi_E - \Phi_C) - D_w(\Phi_C - \Phi_W), \tag{3.11}$$

and it follows that the continuity equation becomes

$$F_e - F_w = 0, \tag{3.12}$$

where δx is the spacing between two neighbouring nodes. Further details on discretisation methods can be obtained from Versteeg and Malalasekera (1995).

F_e and F_w are computed from a known velocity field, but the transport properties of ϕ at the faces *e* and *w* are evaluated by solving Equation 3.11. The different schemes used to solve the Navier-Stokes equations for the present research, are briefly described in the following sections.

(ii) Second Order Upwind Scheme

When the second order accuracy is used, quantities at cell faces are calculated by

employing a multidimensional linear reconstruction approach. For this work, the second order upwind discretisation scheme was used to discretize the momentum equations. In this second order upwind differencing, a Taylor series expansion is employed to describe the upwind gradients. This means that the face value for each variable is computed from gradients involving the upwind neighbour and its neighbours. It offers greater accuracy than the first order upwind method; however, it requires additional computational effort.

(iii) PRESTO

FLUENT uses the STANDARD pressure interpolation scheme as its default to interpolate pressure values at the cell faces, however this scheme does not work well when the flow is highly swirling with high-pressure gradients. Therefore, the PRESTO (PREssure STaggering Option) scheme was used in this work. The PRESTO scheme uses the discrete continuity balance for a ``staggered'' control volume about the face to compute the face pressure. This procedure is similar to the staggered-grid schemes used with structured meshes (Patanka (1980)).

(iv) SIMPLEC

SIMPLEC or SIMPLE-Consistent is a modified version of the standard SIMPLE algorithm (Patanka (1980)), which is the default scheme employed by FLUENT for the pressure-velocity coupling in the segregated solver. When the flow is relatively uncomplicated (such laminar flows with no additional models activated) in which convergence is limited by the pressure-velocity coupling, SIMPLEC can often lead to a converged solution more quickly. The pressure-correction under-relaxation factor is generally set to 1.0 when SIMPLEC is used, which aids in speeding convergence. In some problems, however, increasing the pressure-correction under-relaxation factor to 1.0 can lead to instability, and for this reason, this work used a very conservative value of 0.3.

3.3.6 Non-dimensional numbers

In order to characterise and analyse the flow, a number of non-dimensional parameters

have been used throughout this thesis. It is therefore appropriate to define of them in this section. The tank radius R was used to normalise most linear dimensions as shown in Table 3.3.

Table 3.3 Normalised variables.

Variable	Normalised variable	Comment
h	h* = h/H or h/2R	h and z are used to represent the coordinate along the swirl axis which can be the height at which one of the stagnation points of the vortex breakdown bubble is located.
z	z* = z/2R	
r	r* = r/R	r is the radial coordinate

Four Reynolds numbers were used in this work namely, Re, Re_r, Re_c and Re_a. Equations 3.13-16 define these Reynolds numbers:

The Reynolds number Re represents the Reynolds number of the rotating or top endwall, therefore the Reynolds number was based on Ω and R, which are its angular velocity and radius respectively. Mathematically Re is defined as

$$\mathrm{Re} = \frac{\rho \Omega R^2}{\mu}. \tag{3.13}$$

The Reynolds number of the small disk is designated Re_r and is represented by

$$\mathrm{Re}_r = \frac{\rho \Omega_r r^2}{\mu}, \tag{3.14}$$

where Ω_r and r are the appropriate angular velocity and length scale.

Re_c is the critical Reynolds number of the rotating disk corresponding to the onset of vortex breakdown. This Reynolds number is used in cases where both the top endwall and the control disk are both rotating and therefore the onset of vortex breakdown occurs at different Reynolds numbers depending on the rotation ratio and whether it is a co-rotation or counter-rotation case. Re_c is given as

$$\mathrm{Re}_c = \frac{\rho \Omega_c R^2}{\mu}, \tag{3.15}$$

where Ω_c is the corresponding angular velocity of the rotating disk.

The last Reynolds number is the axial Reynolds number Re_a. The axial Reynolds number is based on the maximum axial velocity along the swirl axis and is defined as

$$\mathrm{Re}_a = \frac{\rho V_{a-\max} R}{\mu}. \tag{3.16}$$

Another important parameter known as the swirl number S_n and defined by

$$S_n = \frac{V_{s-\max}}{V_{a-\max}}, \tag{3.17}$$

is the ratio between the maximum axial velocity $V_{a-\max}$ along the swirl axis and its corresponding maximum swirl velocity $V_{s-\max}$. The maximum swirl velocity is taken from the horizontal plane profile at the axial coordinate of the maximum axial velocity. The definition of the swirl number (Equation 3.17) is in conformity with the swirl ratio described by Delery (1994).

3.3.7 Derived quantities

As one of the objectives of this project was to determine how power effective was the proposed control system relative to previous methods that used the rotation of both endwalls, it was imperative to design a way of estimating the input power expended in rotating both the endwall and the small disk. To achieve this, the expended power P necessary to overcome viscous resistance was computed from integration of the train energy over the effective surfaces of the rotating endwall and the small disk. A brief derivation is illustrated below:

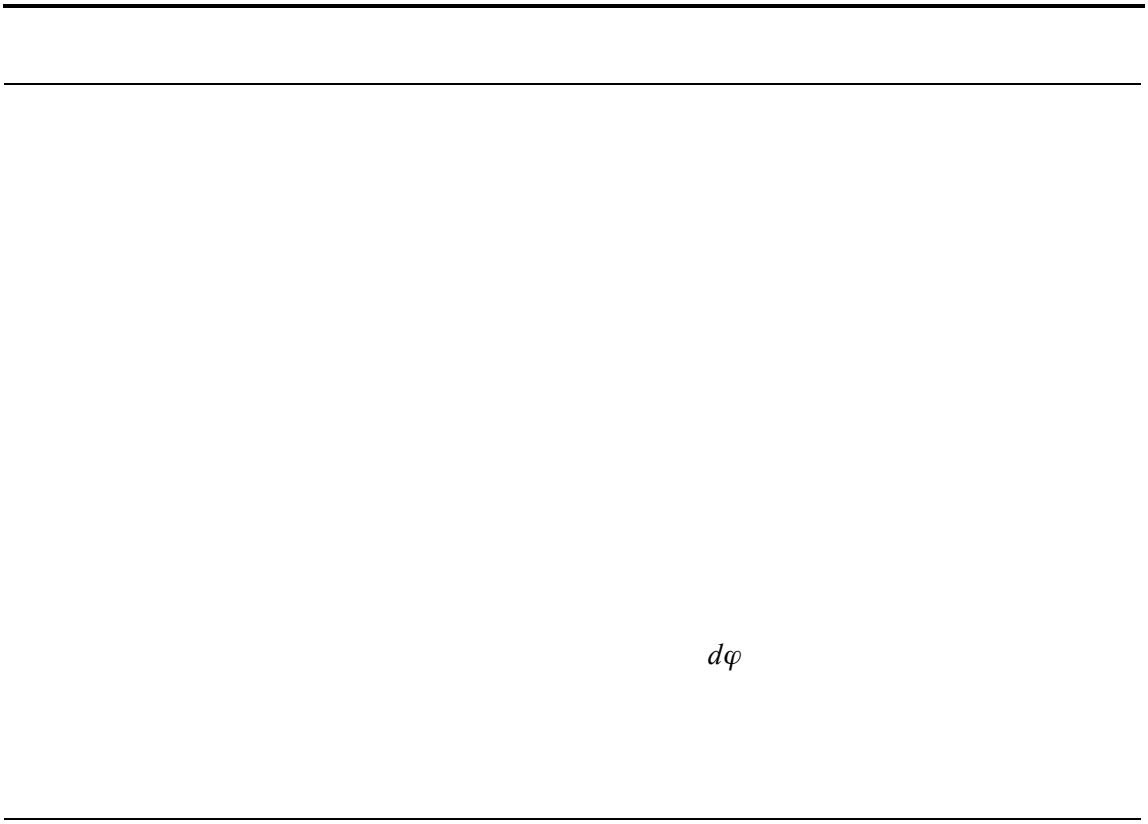

Figure 3.10 Fluid element used to derive the expression for the expended viscous power.

The general expression for the shear stress is given by

$$\tau = \mu \frac{\partial v}{\partial z}. \tag{3.18}$$

For an element of fluid, as shown in Figure 3.10, the shearing force acting on it can be expressed as

$$dF = \tau dA, \tag{3.19}$$

where

$$dA = dr\,ds, \tag{3.20}$$

and ds the small arc length is,

$$ds = r d\varphi . \tag{3.21}$$

The elemental area integrated over 360 º is,

$$2\pi r dr .$$

Equation 3.19 becomes,

$$dF = \left(\mu \frac{\partial v}{\partial z} \right) 2\pi r dr , \tag{3.22}$$

where $\frac{\partial v}{\partial z}$ is the strain rate and v is the fluid velocity.

The torque required to rotate the disk against the viscous resistance is

$$T = 2\pi \mu \int_0^R \left(\frac{\partial v}{\partial z} \right) r^2 dr . \tag{3.23}$$

And the corresponding power is given by,

$$P = 2\pi \Omega \mu \int_0^R \left(\frac{\partial v}{\partial z} \right) r^2 dr , \tag{3.24}$$

where Ω is the angular velocity of the disk.

Equation 3.23 was created inside the FLUENT environment as a custom function, and its results were used as convergence monitors in addition to being used to calculate the required viscous power defined by Equation 3.24. This power is essentially the power input to the fluid as a result of the disk rotation.

3.3.8 Grid Resolution Study

It is important that numerical predictions obtained through CFD calculations are verified to not depend on the grid upon which the solution is based. Therefore, a grid

resolution study was performed. This study was undertaken to determine a grid that was optimum, in terms of the minimum spatial resolution required, to accurately and efficiently capture all the salient flow features in the range of Reynolds numbers considered. This was achieved by providing sufficient mesh density along solid surfaces and the swirl axis to minimize interpolation errors. Six meshes were constructed (Table 3. 4) and the selection of the best grid was based on the computed value of the integral of the strain rate over the effective surface of the rotating endwall. This surface was chosen because it is the area in the flow domain with the strongest gradients.

Table 3.4 Details of grids used in the resolution study.

Grid ID	Grid size	Strain rate integral	Deviation from Grid F
A	82 x 50	60.07	17.09
B	94 x 68	66.51	8.20
C	106 x 78	70.85	2.21
D	130 x 85	71.52	1.28
E	155 x 115	72.1	0.48
F	188 x 135	72.45	0.00

From Table 3.4 and Figure 3.11, it can be seen that coarser grids generated lower values of the strain rate integral. This value increased as the grid became denser. Grid F was considered as reference, because of its very high mesh density, for comparison against the results obtained from the other. Results from grids D and E exhibit only small deviations from the strain rate integral of grid F despite the significantly higher grid density of the latter. In terms of mesh size, grids D and E represent about 43% and 70% of grid F respectively and yet they only represent a loss of accuracy, with respect to grid F results, of about 1.28% and 0.48% respectively. For the above reasons, grid D

was selected as the appropriate mesh for further simulations. This grid is similar in size to the grid used by Bhattacharyya and Pal (1999) as their optimum grid after a grid resolution study. Subsequent grids were slightly modified from grid D to account for the various sizes of the control disks.

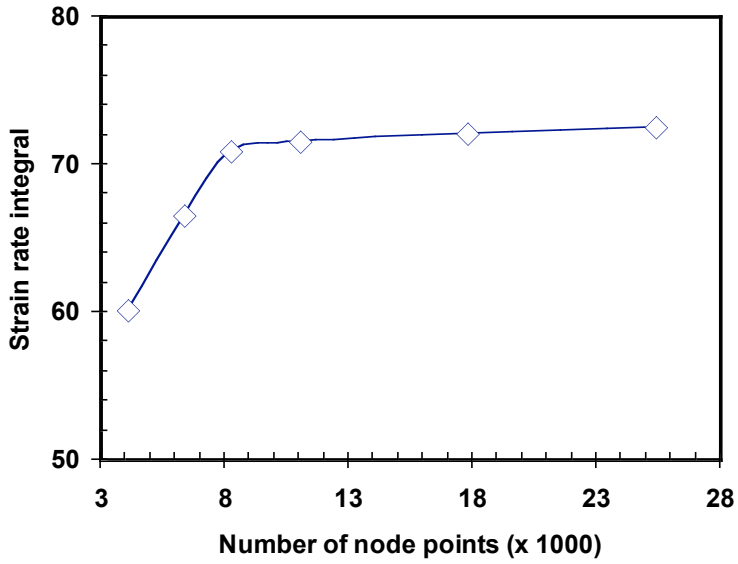

Figure 3.11 Grid resolution study showing the variation of the strain rate integral with grid density.

3.3.9 Post-Processing

The final stage of the CFD work involved post-processing of numerical data. The first objective of post-processing was to examine the accuracy of the numerical results. The qualitative assessment of the solutions was performed within the FLUENT environment using its visualisation capability. Among the aspects that were examined included the overall flow pattern and resolution of important flow features, such as the appearance of the vortex breakdown bubble. Flow visualisation in FLUENT was done using the display of contours, vectors and path lines. Quantitative examination of the simulation results was done by looking at the values of the custom function variables, the integral of the strain rate and the torque evaluated by Equation 3.29.

Most of the quantitative and qualitative results were derived from MATLAB

computations. A number of script files were developed to perform various tasks such as: converting FLUENT data, plotting vectors, stream lines, open and closed contours of stream functions, velocity vectors; calculating the size of the vortex breakdown bubble and determining its location, plotting velocity profiles, etc …

3.3.10 Validation of Numerical Results

Figure 3.12 compares numerical predictions with results from this study's experiments, on one hand, and the experimental results by Fujimura *et al.* (1997), on the other hand. It is obvious that the results obtained from numerical simulations are in good agreement with the two sets of experimental data. This test was used to validate the numerical method and the accuracy of the solution techniques employed. Based on the confidence gained from these initial results, a series of numerical computations were performed and their results are presented in chapter 5.

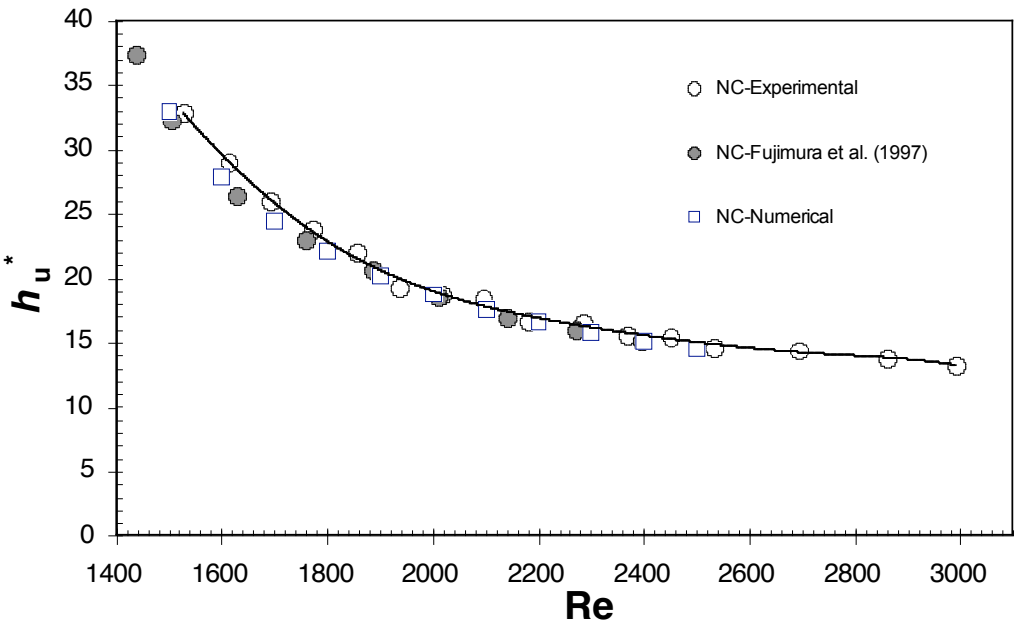

Figure 3.12 Validation of numerical predictions using current experimental results and the data of Fujimura et al. (1997). The figure shows the variation of the upstream stagnation point of the main bubble with Reynolds number for the case where there is no vortex breakdown control (NC).

3.4 Summary

This chapter was primarily concerned with the presentation of methods and procedures used in the implementation of experiments as well as numerical simulations. The experimental part of this presentation consisted of a description of the experimental rig, materials and instruments used in the study. Procedures followed during the experiments and the processing of experimental data have been elaborated. The experimental methods ended with a report on data validation.

The numerical methods outlined in this chapter included an account of the grid construction, a presentation of the governing equations used in the numerical computations and a brief theory about streamlines and stream function. The details of the numerical modeling and solutions techniques employed have been discussed. A number of derived quantities and non-dimensional numbers used in the study have been presented. The chapter has ended by outlining details involved in post-processing and a presentation of the grid resolution study undertaken to validate the numerical methods. The next chapter presents experimental results.

Chapter 4
Experimental Investigation of Vortex Breakdown

4.1 Introduction

This chapter presents experimental results for the vortex breakdown investigation in a closed cylinder. The general methods for the experiments were described in chapter 3; therefore only additional specific aspects of the methodology are described in this chapter. Section 4.2 presents some aspects of the procedures employed during the experiments and also defines some important non-dimensional quantities used in this chapter. The actual experimental results are presented in section 4.3, which is divided into two main parts. The first part describes the experimental results of vortex breakdown due to the rotation of the top endwall (rotating endwall) alone. The second part deals with the results of vortex breakdown in the presence of some controlling effect, which in this case is due to the rotation of a small disk also referred to as a control disk. The chapter ends with a brief summary highlighting important findings of the experimental study.

4.2 Methodology

The general methodology of how the experiments, the results of which are presented here, were conducted was outlined in chapter 3. In this section, and the rest of this chapter, only particular details not adequately discussed before will be described.

4.2.1 Procedural Aspects

It is important to recollect at this stage that five control disk were utilised in this experimental investigation. These disks were referred to as d1, d2, d3, d4 and d5 and their diameters were as follows: 5.1%, 10.1%, 15.2%, 20.2% and 30.7% of the rotating endwall diameter (as shown in Table 3.1). Co-rotation involved the rotation of each of the control disks in the same direction as the rotating endwall, whereas in counter-rotation the control disks were spun in the opposite direction.

In the Matlab environment, the flow visualization pictures, which were captured during the experiments, were analysed in order to determine the radius, upstream and downstream stagnation points heights and centre of the main vortex breakdown bubble. The centre of the main vortex breakdown was taken to be at the intersection between the horizontal line cutting the bubble at its largest radius and the centre line representing the swirl axis. Whilst it was relatively easier to determine the position of the upstream stagnation point, it was difficult to locate the downstream stagnation point, especially when the main breakdown bubble appeared open at the downstream end. This explains why only few data related to the height of the downstream stagnation point are presented.

4.2.2 Non-dimensional Quantities

A number of non-dimensional quantities used in the investigation are presented in this chapter as well as subsequent chapters. These dimensionless numbers include Reynolds numbers, normalised lengths and a rotation ratio.

(i) Reynolds numbers

Three Reynolds numbers are used to categorise the flow regime in the enclosed cylinder, namely: the top or rotating endwall Reynolds number (Re) defined by Equation 3.19; the control disk Reynolds number (Re_r) defined by Equation 3.20; the critical Reynolds number (Re_c) which corresponds to the vortex breakdown onset, with and without control, defined by Equation 3.21.

(ii) Normalised Lengths

Two main normalised lengths have been used: r* to represent lengths in the radial direction and h^* to describe length in the axial direction. Table 3.3 shows r^* normalised by R, the radius of the inner cylinder, and h^* normalised by $2R$. These normalised lengths or coordinates were expressed in terms of percentage (%) in the plotted graphs of this chapter. Furthermore, h_u^*, h_d^* and h_c^*, stand for the normalised height of the upstream and downstream stagnation points and the centre of the first or main vortex breakdown respectively.

(iii) Rotation Ratio

Another important dimensionless number is the rotation ratio ε, which is the ratio between the angular velocity of the small disk Ω_r and that for the rotating endwall Ω as defined by

$$\varepsilon = \frac{\Omega_r}{\Omega}. \tag{4.1}$$

4.3 Results

The experimental results presented in the following sections include pictures showing visualization of different flow patterns inside the closed cylinder and graphical representations of relationships between several vortex breakdown variables. Dependent variables include the normalised radial size or radius of the breakdown bubble and the height of the stagnation points and the centre of the breakdown bubble. The independent

variables are the rotating endwall Reynolds number and the rotation ratio. Most of the results include co-rotation and counter-rotation data in order to ascertain and compare their separate effects on the variables of interest. Results for the experiments with no-control are presented first followed by those concerned with control of vortex breakdown.

4.3.1 One Endwall Rotation

Preliminary results for experiments where the rotating endwall was steadily rotated while the control disk was kept stationary were used to validate the current the experimental rig as well as the procedures employed. These results were also used to provide a benchmark to compare subsequent results generated with the control disk with a view to establishing the net effect of control on the vortex breakdown bubble.

(i) Flow Visualization

Figures 4.1(a-e) illustrate flow visualization results for the experiments in which only the rotating endwall was rotated at a constant angular velocity (Ω), this case will be referred to as the "no-control" case. The well known experimental results of Escudier (1984), for an aspect ratio of H/R = 2.0 (Figure 3.5) were used as a yardstick and good agreement with the present results (Figure 4. 1) was noted. The following observations can be made: the onset of vortex breakdown occurred at Re = 1440 Figure 4.1(a)); at Re = 1476 there appeared a small recirculation bubble (Figure 4. 1(b)); at Re = 2132 the second breakdown bubble appeared downstream of the first bubble (Figure 4.1(c)); as the Reynolds number reaches 2474 the second recirculation bubble opened up at the downstream end and therefore ceased to be a breakdown bubble (Figure 4.1(d)); and finally at Re = 2928 the second bubble completely disappeared while the first breakdown bubble looked deformed taking the shape of a bowl supporting a downstream vortex core (Figure 4.1(e)). Other results for Re > 3000, not shown here, confirmed the total disappearance of the breakdown bubble.

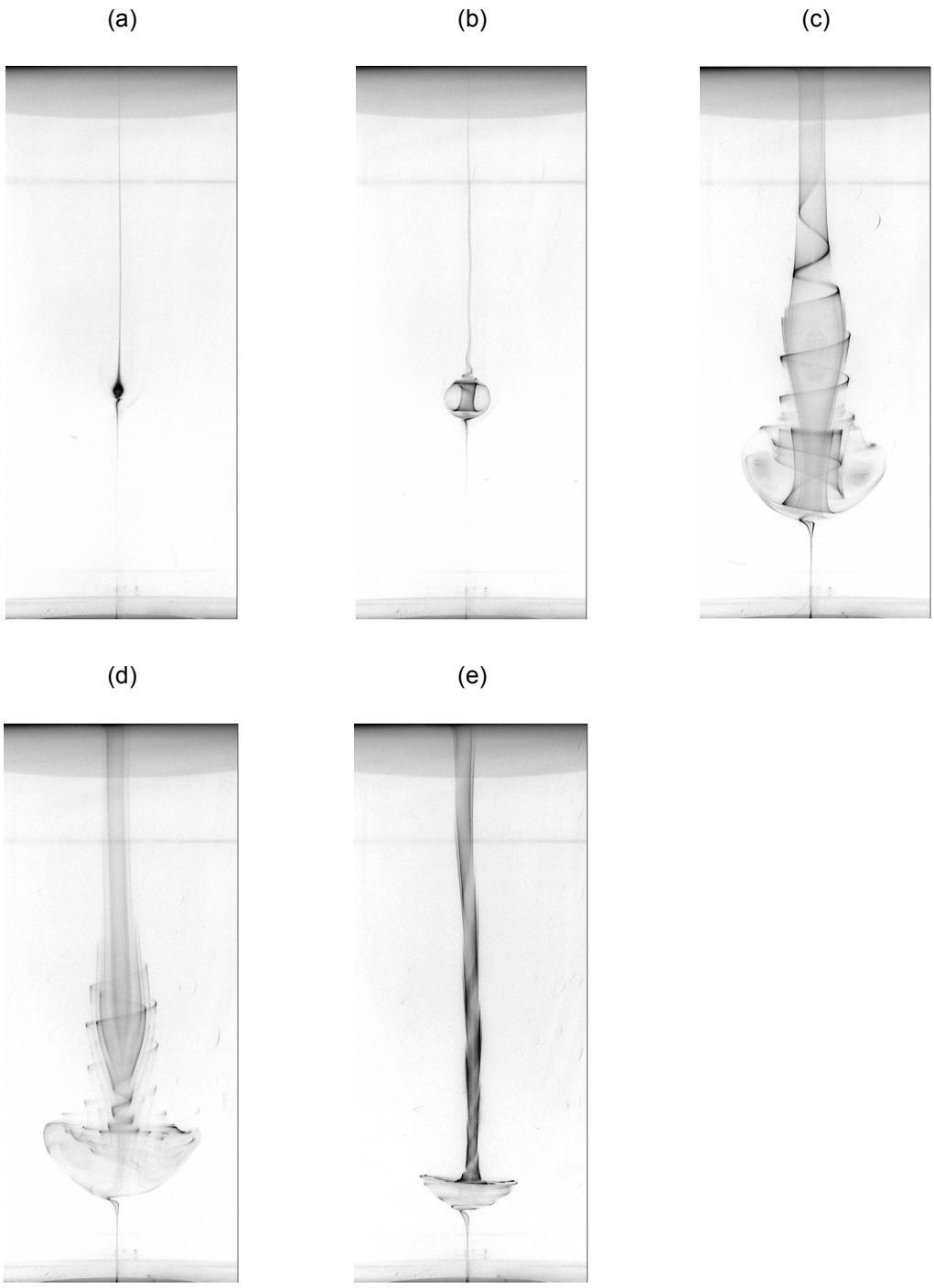

Figure 4.1 Flow visualization of vortex breakdown with no-control at various Reynolds numbers: (a) Re = 1440; (b) Re = 1476; (c) Re = 2132; (d) Re = 2474; (e) Re = 2928.

(ii) Bubble Radius

The growth of the vortex breakdown bubble with respect to the rotating endwall Reynolds number was examined and the results are presented in Figure 4.2. The bubble size was seen to increase with corresponding increases in the Reynolds number until it reached a maximum value well beyond the two-bubble region and then a rapid size reduction phase was observed. From Figure 4.2, it can be seen that the maximum bubble size occurs in the region between Re = 2350, just after the disappearance of the second bubble, and Re = 2700, which is well into the second single bubble zone.

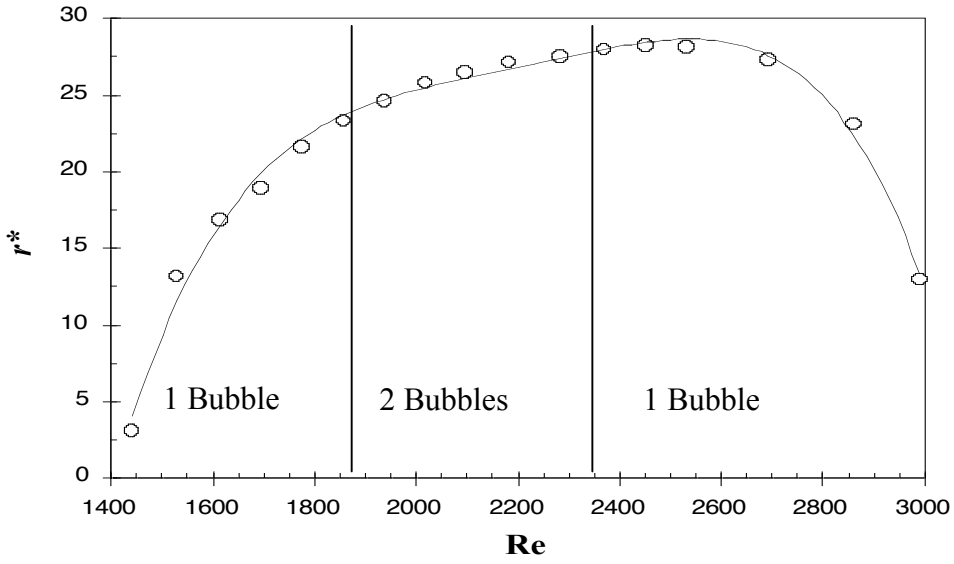

Figure 4.2 Evolution of the normalised radial size of vortex breakdown bubble with respect to the rotating endwall Reynolds number.

(iii) Upstream Stagnation Point

Figure 4.3 shows the variation of the axial location of the upstream, downstream and centre of the breakdown bubble with the rotating endwall Reynolds number. The data of Fujimura *et al.* (1997) are compared with the current results primarily for validation purposes. The breakdown bubble was observed to migrate upstream, away from the rotating endwall, as the Reynolds number was increased. It is also important to note that

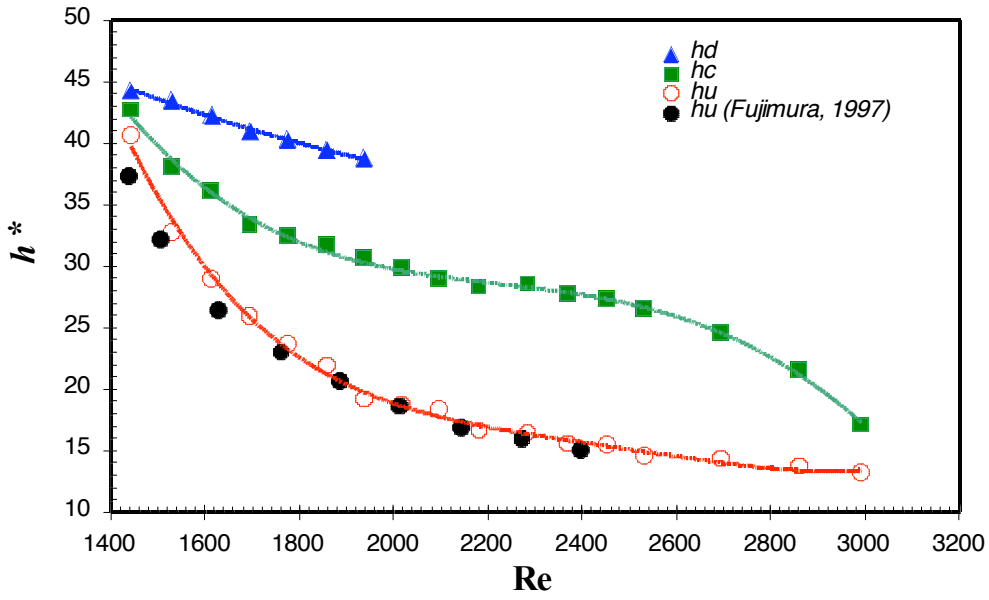

Figure 4.3 Axial location of the main vortex breakdown bubble for different endwall Reynolds numbers. The data of Fujimura et al. (1997) are compared with the current experimental results.

as the Reynolds number continued to increase, the rate of decrease of the upstream stagnation point height slowed down leading to an asymptotic level depicted in Figure 4.3 as a flattened curve (bottom curve). The current results for the upstream stagnation point were found to be within 2% of Fujimura et al.'s data for the same aspect ratio H/R = 2.0. The centre of the bubble was seen to have a characteristic movement similar to the upstream stagnation point, except near the breakdown onset region and the region where the bubble size appeared to shrink, leading to its eventual disappearance. Furthermore, the data representing the migration of the downstream stagnation point also show a downward trend indicating that the entire breakdown bubble was in fact moving towards the non-rotating endwall at the bottom. As noted above, the fact that only few data points are shown to describe the movement of the downstream stagnation point was due to the difficulty in identifying the point as the Reynolds number increased; this difficulty was partly attributed to the fact that beyond a $Re \approx 1850$ the second breakdown bubble appeared to spring from inside the first bubble. The size of the bubble in the axial direction can also be deduced from the heights of the two

stagnation points and the centre of the bubble at each Reynolds number. Therefore, it can be stated that the bubble size in the axial direction appeared to generally increase with increases in rotational velocity of the top endwall.

4.3.2 Control of Vortex Breakdown with a Small Rotating Disk

The vortex breakdown control method proposed in this study consisted of co-rotating and counter-rotating a small control disk with respect to the rotating endwall (Figure 3.2). Experimental results for vortex breakdown control are presented below starting with results of vortex breakdown onset. The effects of the rotating endwall rotation, in other words *Re*, and the control disk size on the main breakdown bubble and the bottom bubble are investigated.

(i) Vortex Breakdown Onset

Experiments were conducted to test the occurrence of the onset of vortex breakdown under the combined influence of the rotation of the top endwall and the control disks (d1, d2, d3, d4 and d5). However, experiments conducted with the control disk d5 were inconclusive because of practical limitations; even at the smallest rotation rate obtainable using the bottom drive unit2 (Figure 3.2) the rotational effect of d5 was too strong to generate or sustain the vortex breakdown onset state. This was true for both co-rotation and counter-rotation. As a result, there is no curve to represent d5 in Figure 4.4.

Figure 4.4 displays the dependence of the critical Reynolds number on the rotation ratio and also the sense of rotation (co- or counter-rotation). In general, the results showed that for co-rotation the higher the rotation ratio the lower the critical Reynolds number associated with the onset of vortex breakdown. However, the opposite effect was true when the control disk was counter-rotated with respect to the rotating endwall. In addition, the results revealed that the smallest control disk d1 only marginally altered the Reynolds number at which vortex breakdown first occurred; this is represented by an almost horizontal line in the graph. However, the biggest control disk, d4 in this case, had a significant effect on the value of the critical Reynolds number, as shown by the steeply falling (co-rotation) and rising (counter-rotation) curves in Figure 4.4.

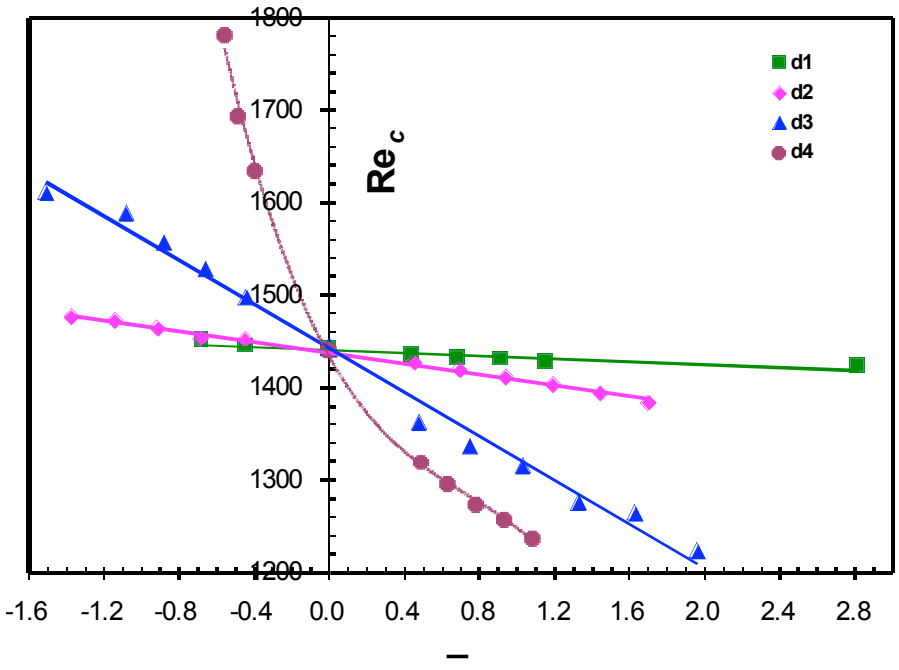

Figure 4.4 Variation of the critical Reynolds number Re_c with rotation ratio ε (+ve is for co-rotation and –ve for counter-rotation). The effect of the small disk size is shown with the help of four different disk sizes.

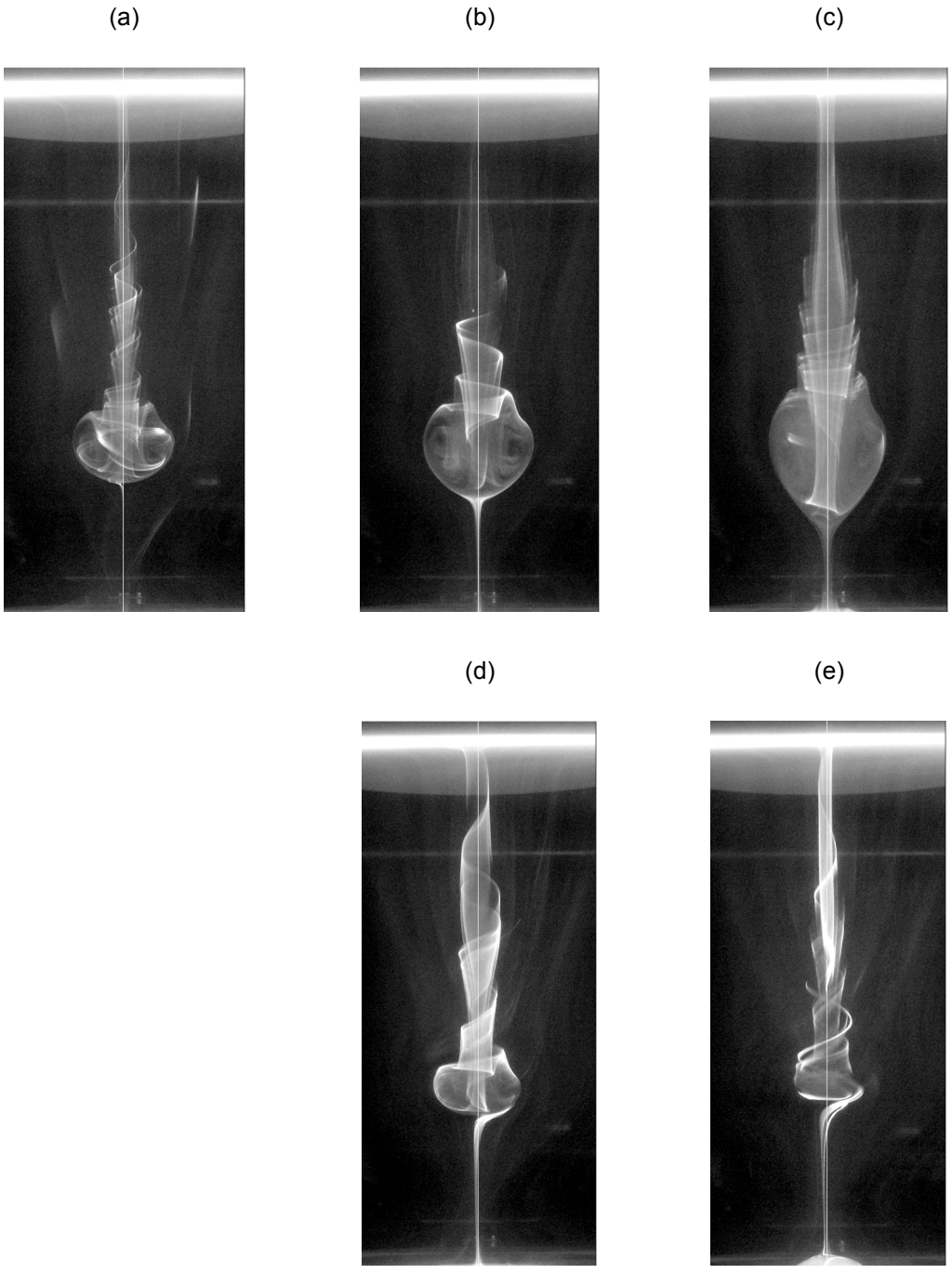

Figure 4.5 Flow visualization of vortex breakdown due to the top endwall rotation at Re = 1660 and the effect of the small disk d3 rotation ratio ε: (a) no-control; (b) ε = 0.39, (c) ε = 1.23; (d) ε = - 0.39, (e) ε = -1.23.

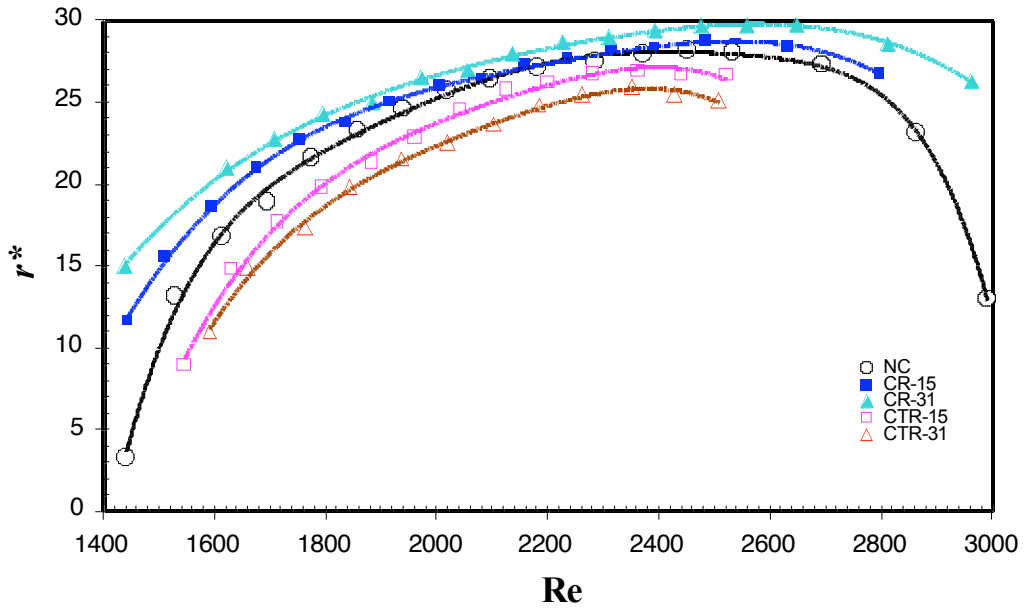

Figure 4.6 Variation of the normalised breakdown bubble radius with Reynolds number. Co-rotation and counter-rotation cases are considered for the control disk d3.

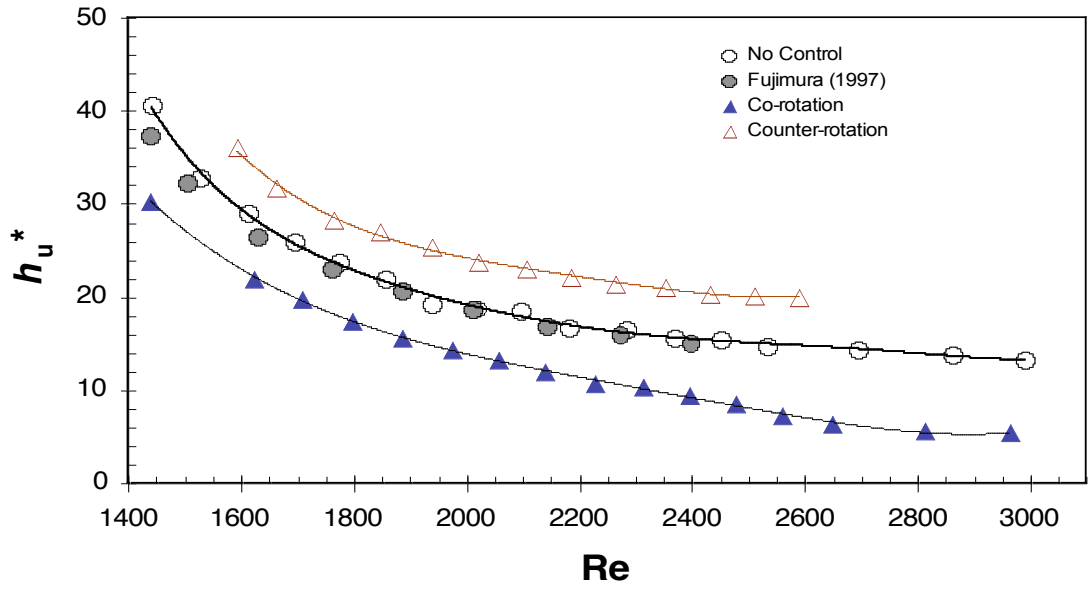

Figure 4.7 Variation of the normalised upstream stagnation point height with Reynolds number. Current results for no-control are compared with the data of Fujimura et al. (1997). Co-rotation and counter-rotation cases are considered for d3 at Re_r = 31.

(ii) Effects of Co- and Counter-Rotation

The results presented in Figure 4.5 were obtained by rotating the top endwall at a constant angular velocity corresponding to $Re2 = 1660$, while control was achieved by co-rotating and counter-rotating the control disk d3. Figure 4.5 shows flow visualization pictures obtained when the rotating endwall and the control disk d3 were co-rotated at $\varepsilon = 0.39$ (Figure 4.5(b)), $\varepsilon = 1.23$ (Figure 4.5(c)) and counter-rotated at the same rates (Figures 4.5(d-e)). Figure 4.5(a) represents the initial vortex breakdown bubble generated by the rotation of the rotating endwall only (no-control). The purpose of these experiments was to show how co-rotating and counter-rotating the control disk transformed the initial vortex breakdown. It was observed, as depicted in the pictures, that co-rotation of the control disk increased the size of the breakdown bubble, whereas counter-rotation decreased its size. Furthermore, the bubbles resulting from co-rotation looked stretched in the axial direction with Figure 4.5(c) showing a tendency of the second bubble appearing downstream of the first.

Other results not shown here revealed that with higher rotation ratios counter-rotating d3 led to the complete disappearance of the breakdown bubble. It was also noted that as the speed of the control disk increased, irrespective of the direction, another bubble started to form on top of the disk. This other bubble, to be referred to as the "bottom bubble", can be seen in Figure 4.5(c) for co-rotation and Figure 4.5(e) for counter-rotation. It can be observed form these pictures that the size (i.e. height and radius) of the bottom bubble was roughly unchanged for the same rotation ratio, whether in co-rotation or counter-rotation. The bottom bubble will be further investigated later in this chapter.

The normalised radial size (% of R) of the vortex breakdown bubble is plotted against the rotating endwall Reynolds number (Figure 4.6). The results show the variation of the bubble radius with Reynolds number for the no-control, co-rotation ($Re_r = 15$ and 31) and counter-rotation ($Re_r = 15$ and 31) cases. The effects of co-rotating and counter-rotating the control disk on the radius of the main bubble are clearly shown. It is obvious that co-rotation of the control disk d3 tended to increase the radial size of the breakdown bubble, while counter-rotation tended to decrease it. In addition, the effect

of the control disk rotation on the breakdown bubble was observed to be relatively more pronounced at lower Reynolds numbers and those beyond the point where the bubble had reached it maximum size.

Figure 4.7 presents the movement of the upstream stagnation point for the main vortex breakdown bubble as the rotating endwall Reynolds number increases. The normalised height of this stagnation point is represented by h_u* *(*% of $H = 2R$*)*. The cases for which the results are shown corresponded to the no-control, co-rotation and counter-rotation when the control disk Reynolds number (Re_r) was 31. To put in perspective, this Reynolds number corresponds to a rotation ratio $\varepsilon = \pm 0.92$ when the rotating endwall Reynolds number is 1440 (that is at the onset of vortex breakdown for the no-control case). Fujimura *et al.* (1997) data for the same aspect ratio, and no-control case, are included to compare with the current results. For the no-control case, Figure 4.7 shows that the height of the upstream stagnation point decreases as the Reynolds number is increased. Eventually, h_u* reaches an apparent asymptotic level of about 13% of the tank height ($2R$). The effect of co-rotation on the axial position of the upstream stagnation point was to shift it further upstream, getting closer to the bottom endwall. On the other hand, counter-rotation tended to move the upstream stagnation point in the downstream direction, or closer to the rotating endwall. Other results not reproduced here showed that the higher the absolute magnitude of the rotation ratio the more significant the shift appeared to be.

(iii) Effects of Co- and Counter-Rotation with Different Endwall Reynolds numbers (Re)

The next results assess the effect of co-rotation and counter-rotation on the vortex breakdown bubble when the rotating endwall was spun with three different angular velocities (corresponding to *Re*1, *Re*2 and *Re*3). Flow visualization pictures and graphs are presented to facilitate the examination. Two control disks were utilised for this set of experiments, d2 and d3.

(a) Flow Visualization

Flow visualization pictures shown in Figures 4.8 and 4.9 are for both co-rotation and

counter-rotation of d2 and d3 respectively; and the three different Reynolds numbers employed were $Re1 = 1550$, $Re2 = 1660$ and $Re3 = 1835$. Vortex breakdown bubbles generated without control (Figures 4.8 & 4.9 (a), (d) and (g)) served as the basis of comparison to assess the effectiveness of the control disk rotation. Co-rotation cases are shown in Figures 4.8 & 4.9 (b), (e) and (h), while counter-rotation cases are represented in Figures 4.8 & 4.9 (c), (f) and (i).

Using the control disk d2 in co-rotation and counter-rotation, the findings were that the breakdown bubble underwent only marginal changes when the endwall Reynolds number was $Re1$. The effect of the control disk on the vortex breakdown became even less apparent when the Reynolds numbers increased to $Re2 = 1660$ and $Re3 = 1835$. On the other hand, when the control disk size increased, from d2 to d3, the effects of co-rotation and counter-rotation on the breakdown bubble became clearly visible as illustrated in Figures 4.9 (a) through to (i). From the above figures, it can be seen that the breakdown bubble has the tendency to migrate upstream when under the influence of co-rotation, and downstream when subjected to counter-rotation.

(a) (b) (c)

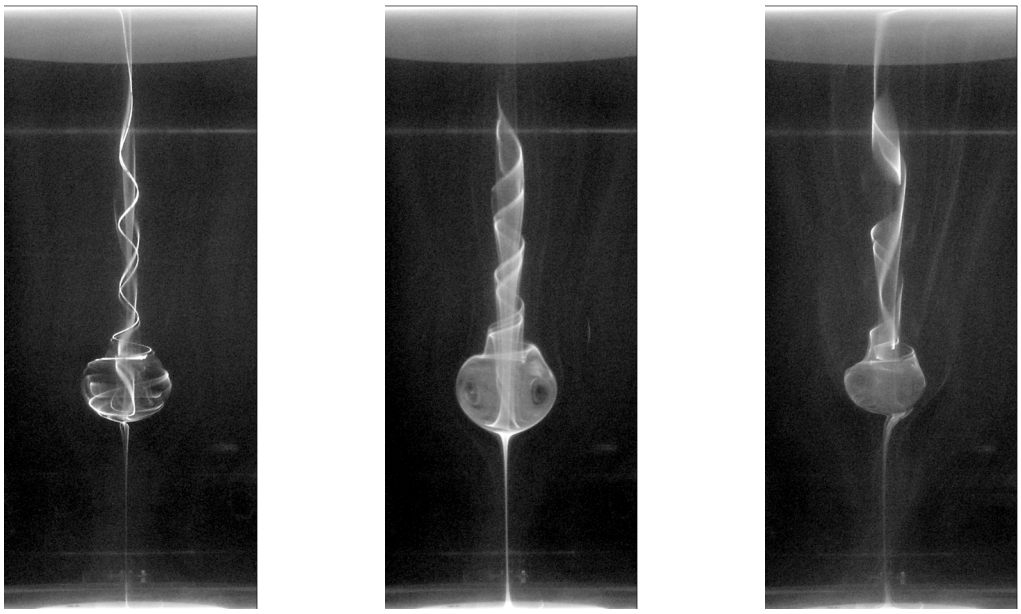

(d) (e) (f)

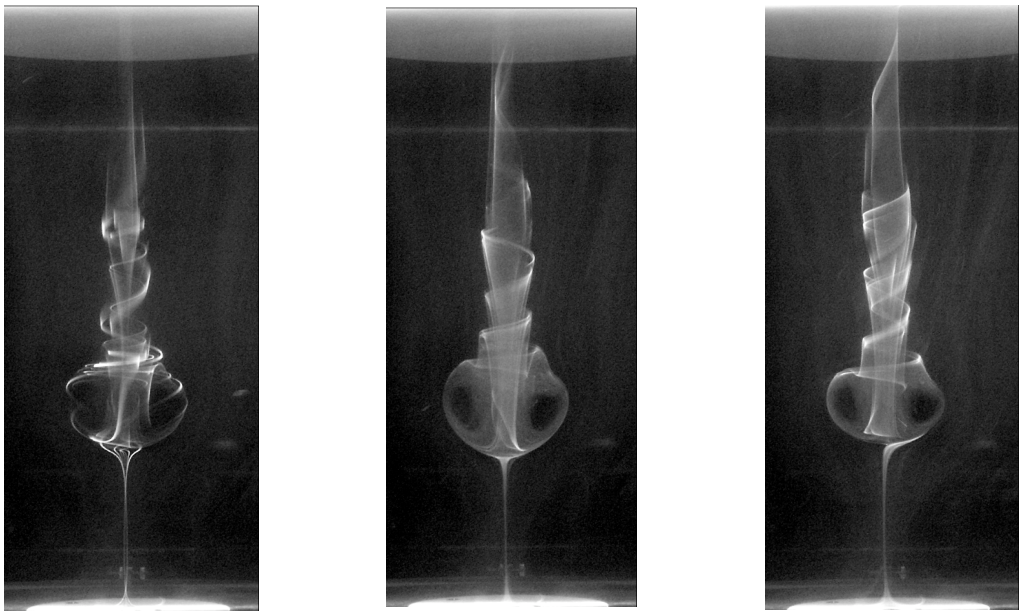

(g) (h) (i)

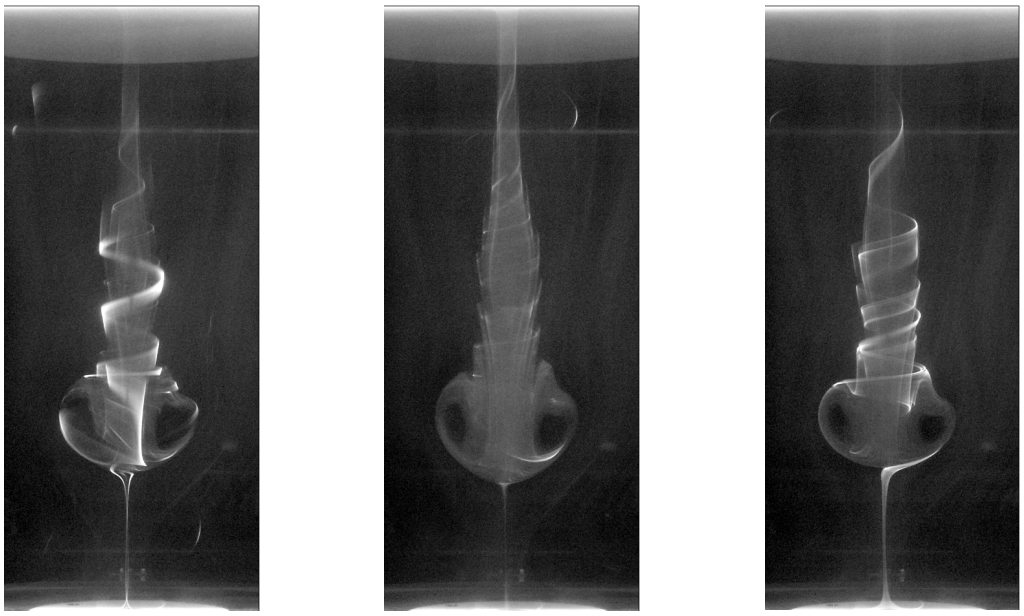

Figure 4.8 Flow visualization of vortex breakdown due to the rotation of the top endwall at three different Reynolds numbers. The effect of co-rotating and counter-rotating the disk d2 is revealed: Re = 1550 (a) no-control, (b) ε = 0.88, (c) ε = -0.88; Re = 1660 (d) no-control, (e) ε = 0.82, (f) ε = -0.82; Re = 1835 (g) no-control, (h) ε = 0.76, (i) ε = -0.76.

(a) (b) (c)

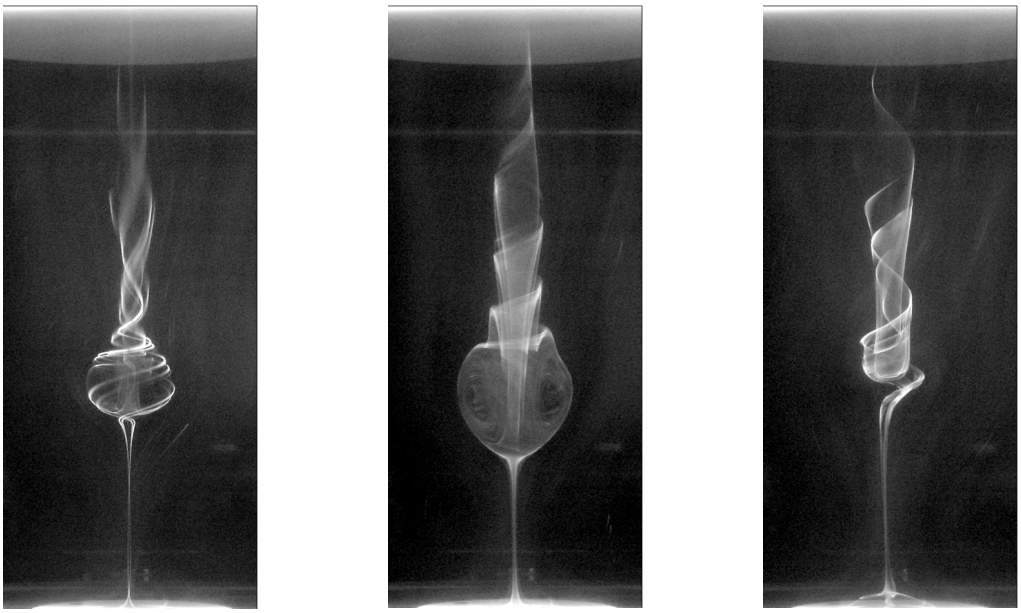

(d) (e) (f)

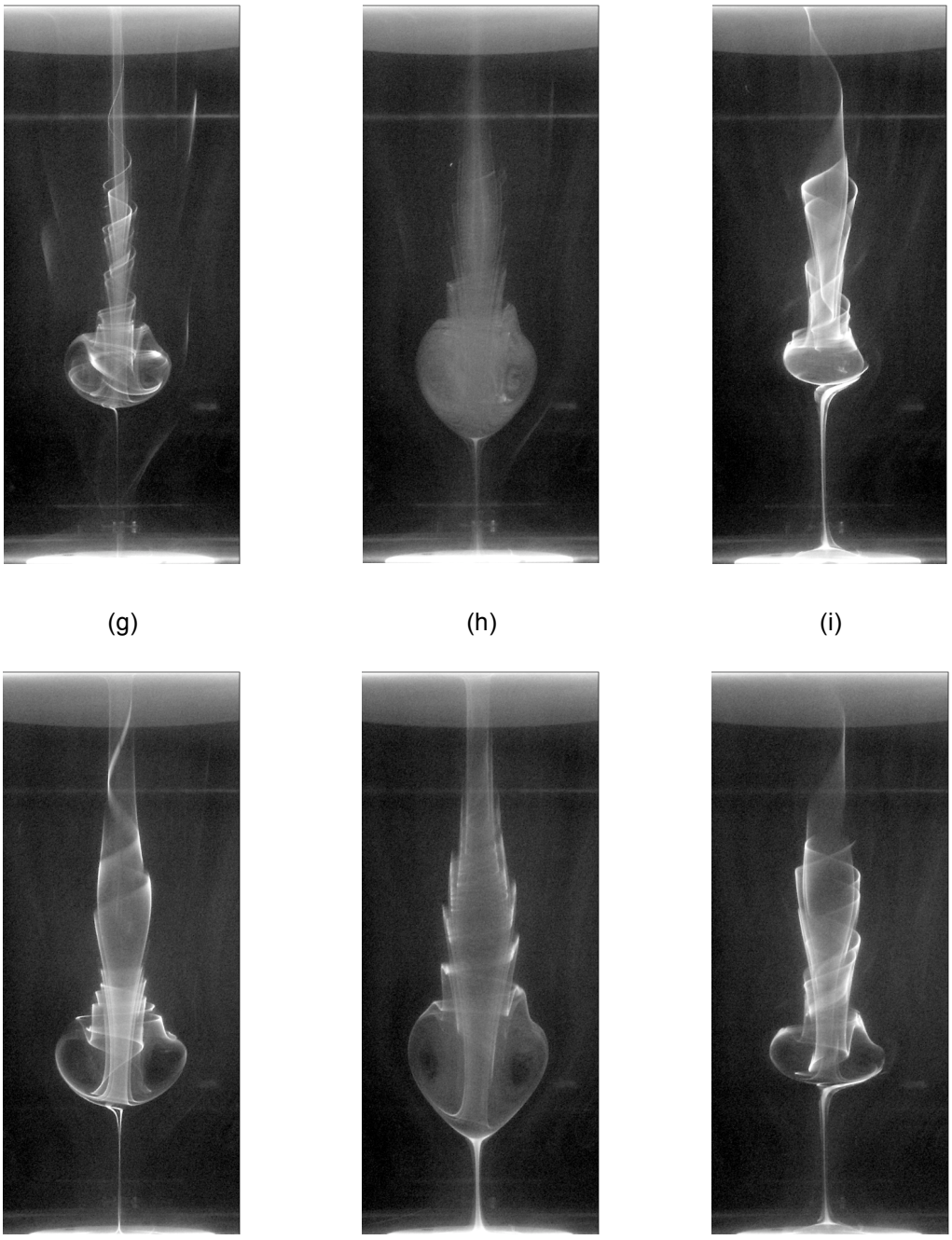

Figure 4.9 Flow visualization of vortex breakdown due to the rotation of the top endwall at three different Reynolds numbers. The effect of co-rotating and counter-rotating the disk d3 is revealed: Re = 1550 (a) no-control, (b) ε = 0.88, (c) ε = -0.88; Re = 1660 (d) no-control, (e) ε = 0.82, (f) ε = -0.82; Re = 1835 (g) no-control, (h) ε = 0.76, (i) ε = -0.76.

(b) Main Bubble Radial Size

In the next three graphs (Figures 4.10-12), experimental results show the dependence of the main breakdown bubble on the rotation ratio and also the effect of the rotating endwall Reynolds number is depicted. To vary the rotation ratio ε, the control disk was co-rotated and counter-rotated with increasing and decreasing angular velocities while maintaining the angular velocity of the endwall constant (*Re*1, *Re*2 or *Re*3). The bubble radius is described in Figure 4.10 using its normalised radius r^* (expressed as percentage of the cylinder radius *R*).

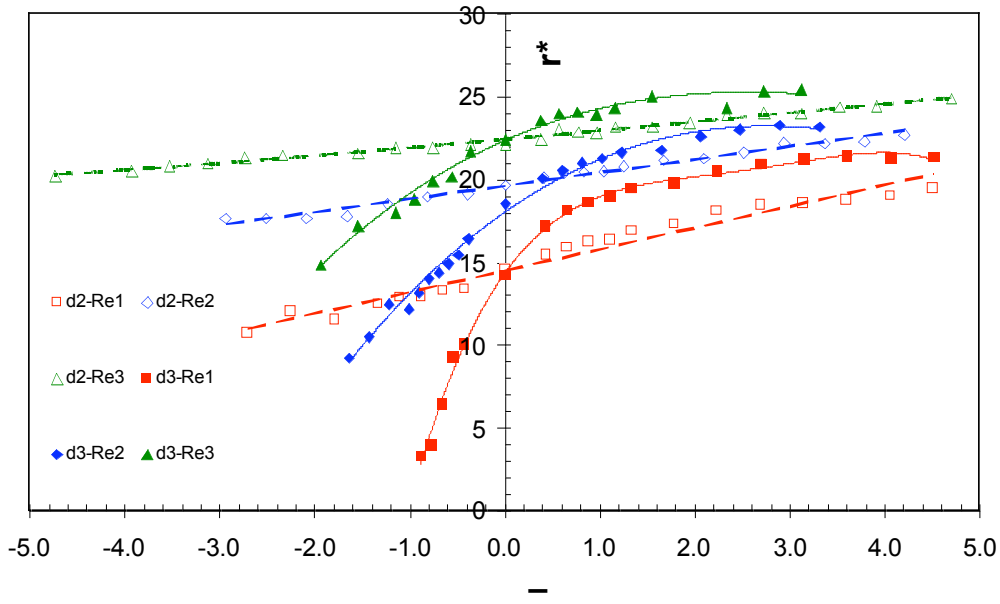

Figure 4.10 Variation of the breakdown bubble radius with rotation ratio (co-rotation and counter-rotation). Two disk sizes, d2 and d3 are compared at three Reynolds numbers (Re1 – Re3).

The experiments of Figure 4.10 were performed using two different control disks d2 and d3. Three rotating endwall Reynolds numbers were tested for each of the two control disks. Also the investigation covered both co-rotation and counter-rotation within the interval $-5.0 < \varepsilon < 5.0$. For the control disk d2, the experimental results revealed that there was a direct correlation between the bubble radius and the angular velocity ratio (ε). This is represented by the three straight lines with positive slopes (Figure 4. 10).

This seemingly linear relationship indicates that the bubble radius increases as the control disk is co-rotated with respect to the rotating endwall, but it decreases at the same rate with increasing rates of counter-rotation. The bubbles generated were found to be larger when the endwall Reynolds number was higher as illustrated in Figure 4.10. Furthermore, the rate of increase of the bubble radius with the rotation rate was found to be higher when the endwall Reynolds number was smaller ($Re1$). This is depicted in Figure 4.10 by three lines of decreasing order slope magnitude representing $Re1$, $Re2$ and $Re3$.

For the control disk d3, it was observed that the bubble radius was not linearly related to the angular velocity ratio (Figure 4.10). The relationship is represented by three curves rather than straight lines as in the case of control disk d2. Like in the case of control disk d2, it was observed that a higher endwall Reynolds number generated bubbles with larger radii throughout the entire rotation ratio range. Also, the rate of decrease of the bubble radial size was higher for the slowest endwall rotation ($Re1$), as noted for the control disk d2. Another significant observation was that the radial shrinkage rate of the bubble size in counter-rotation was significantly higher than the rate of growth in co-rotation.

(c) Upstream Stagnation Point

In Figure 4.11, the variation of the normalised upstream stagnation point height (h_u*) with the rotation ratio for the control disks d2 and d3 is presented. As in Figure 4.10, three rotating endwall Reynolds numbers were tested for each of the two disks. It was generally observed that for co-rotating cases the stagnation point migrated in the upstream direction, away from the rotating endwall, as the rotation ratio increased. Whereas, for the counter-rotating cases the migration was in the opposite direction. Control with both disks exhibited almost linear relationships between the normalised height of the stagnation point and the rotation ratio for the endwall Reynolds number $Re1 = 1550$ and $Re2 = 1660$. However, for the highest Reynolds number $Re3 = 1835$ the rate of movement of the stagnation point was higher when in the co-rotation mode than in counter-rotation. In addition, faster rates of movement were observed for control with d3, a bigger disk, than with d2.

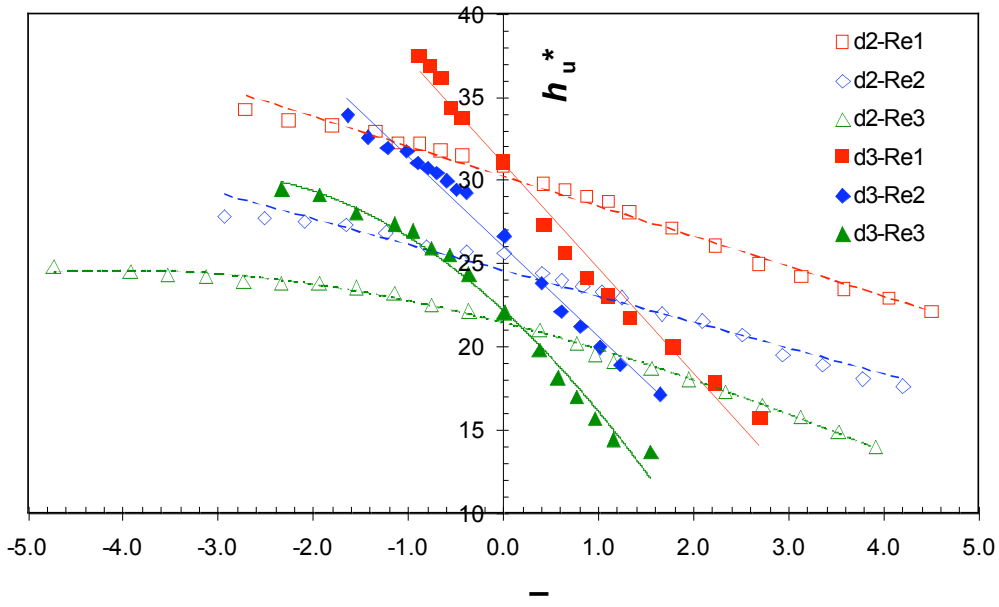

Figure 4.11 Variation of the breakdown bubble upstream stagnation point with rotation ratio (co-rotation and counter-rotation). Two disk sizes, d2 and d3 are compared at three Reynolds numbers (Re1 – Re3).

(d) Centre of the Breakdown Bubble

Figure 4.12 describes changes of the normalised height of the breakdown bubble centre with respect to variations of the rotation ratio. The results revealed that higher endwall Reynolds numbers tended to move the breakdown bubble centre in the upstream direction, as observed in the case of the upstream stagnation point. When control was effected using the control disk d2 and with *Re*2 the centre of the bubble was observed to maintain almost the same position. However, when the endwall Reynolds number was lowered, i.e. *Re*1, the bubble centre appeared to move away from the rotating endwall when in co-rotation mode but closer when in counter-rotation mode; in contrast, with *Re*3 it moved in the opposite direction as shown in Figure 4.12. When the bigger control disk was used the bubble centre was observed to migrate closer to the rotating endwall with increasing counter-rotating rates for all the three Reynolds numbers. Similarly, increasing co-rotation rates caused the centre to shift downstreamwise towards the rotating endwall. The bubble centre was seen to assume the closest position to the control disk at different rotation ratios depending on endwall Reynolds number as

shown in Figure 4.12. These corresponding rotation ratios tended to increase as the endwall Reynolds number decreased.

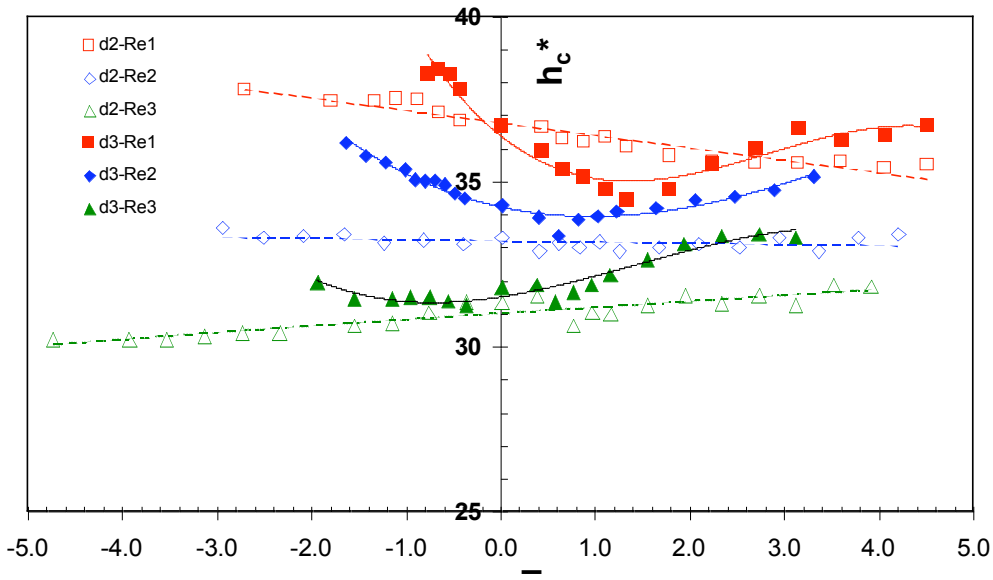

Figure 4.12 Variation of the breakdown bubble centre with rotation ratio (co-rotation and counter-rotation). Two disk sizes, d2 and d3 are compared at three Reynolds numbers (Re1 – Re3).

(iv) Effect of Control Disk Size with Constant Ω_r and Varying Ω

The size of the control disk was investigated to ascertain its effect on the location and size of the breakdown bubble. The results are presented as flow visualization pictures and graphs.

(a) Flow Visualization

Co-rotation

Figures 4.13 and 4.14 are presented to effectively show the effect of co-rotating control disks of different sizes (d2 and d4) on the breakdown bubble size and location along the swirl axis. In both cases, the initial state inside the cylinder was that corresponding to

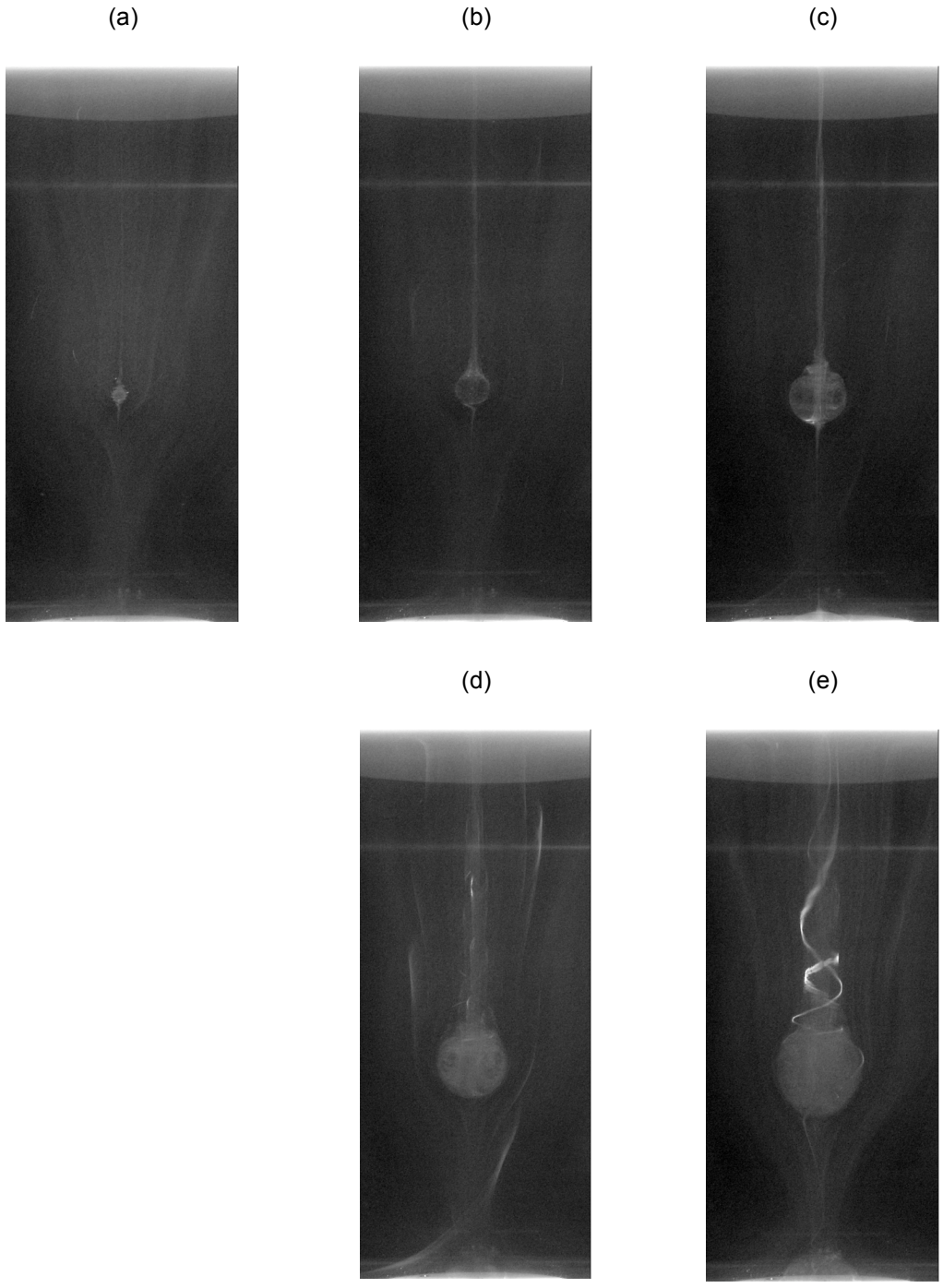

Figure 4.13 Flow visualization of vortex breakdown due to the rotation of the top endwall at Re = 1440 and the effect of co-rotating the disk d2 is depicted: (a) no-control, (b) ε = 0.45, (c) ε = 1.38; (d) ε = 2.32; (e) ε = 3.73.

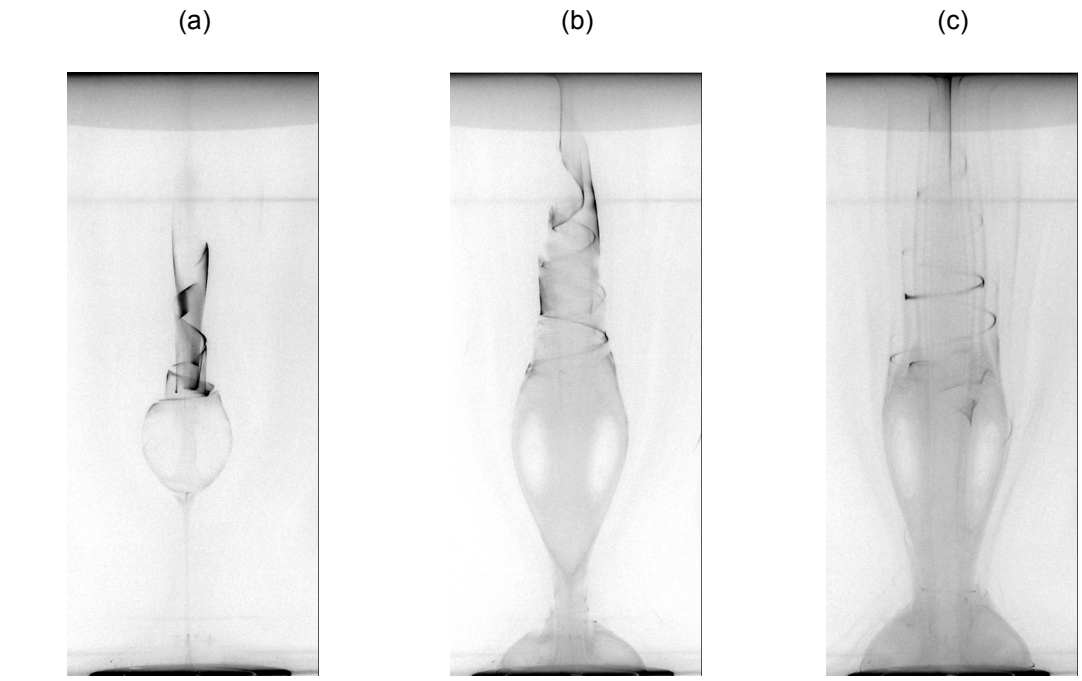

Figure 4.14 Flow visualization of vortex breakdown due to the rotation of the top endwall at Re = 1440 and the effect of co-rotating the disk d4 is depicted: (a) ε = 0.45, (b) ε = 1.38; (c) ε = 2.32. These breakdown bubbles were generated from the initial vortex breakdown onset as shown in figure 4.13(a).

the vortex breakdown onset as shown in Figure 4.13(a). In Figures 4.13(b-e), the control disk d2 was gradually co-rotated with increasing rates to manipulate the onset breakdown bubble. The breakdown bubbles illustrated in Figures 4.13(b-e) correspond to the rotation ratios: ε = 0.45, 1.38, 2.32 and 3.73 respectively; while those shown in Figures 4.14(a-c) correspond to the control disk d4 co-rotated at ε = 0.45, 1.38; 2.32 respectively.

It is important to note that with the same co-rotation ratios (ε = 0.45, 1.38 & 2.32) the bubbles generated using the larger control disk, d4 in this case, were significantly bigger than those obtained using the smaller control disk d2. To be specific, a comparison of the radii of the breakdown bubbles enhanced using d2 and d4 with the cylinder radius yielded the following ratios: 0.06, 0.10 and 0.133 (for d2) and 0.16, 0.20 and 0.21 (for

d4). It is also clear from Figures 4.13 and 4.14 that increasing rates of co-rotation shifted the bubble in the upstream direction.

The results depicted in Figure 4.13 indicate that the rate of increase of the breakdown bubble radius with co-rotation ratio was almost identical to the rate of increase of the axial size. In addition, the bubbles generated using d4 were observed to be very sensitive to co-rotation effect as the bubble radius tended to quickly reach a size close to saturation (maximum) as a result of only a minor rotation ratio (such as $\varepsilon = 0.45$) while progressively stretching in the axial direction. While the normalised radial size of the breakdown bubble varied from 0.16 to 0.20 (normalised by R) for a corresponding change in rotation ratio from 0.45 to 1.38, a significant change in the axial size was noted, from 0.21 to 0.38 (normalised by the cylinder height = $2R$). The development of the bottom bubble, as observed with both control disks, will be discussed later in this chapter.

Counter-rotation

Figures 4.15 and 4.16 illustrate the effect of counter-rotating control disks of different sizes on the breakdown bubble size and axial location. For the two figures, although the initial starting flow structures as well as the rotation ratios were different, the results clearly show the benefit of using a larger control disk to suppress vortex breakdown. Figures 4.15(a) and 4.16(a) represent the initial breakdown states with no-control and correspond to Re = 1660 and 1920 respectively. A higher starting Reynolds number for control disk d4 was employed to be able to sustain the breakdown state in the presence of slight counter-rotation. This goes to show how strong the effect of counter-rotating a disk the size of d4 is on the breakdown bubble. The breakdown conditions depicted in Figures 4.15(b-d) correspond to the rotation ratios ε = - 0.36, - 1.42 and - 2.84 respectively. While, the breakdown bubbles shown in figures 4.16(b-c) correspond to the control disk d4 counter-rotated at ε = - 0.33 and - 0.56 respectively.

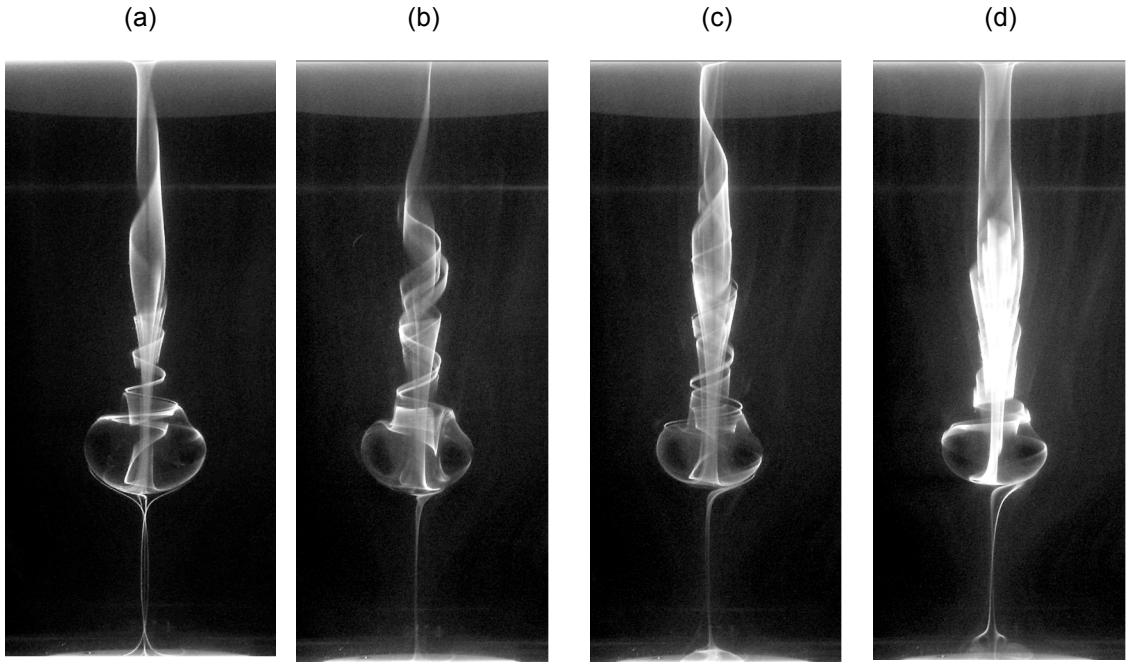

Figure 4.15 Flow visualization of vortex breakdown due to the rotation of the top endwall at Re = 1660 and the effect of counter-rotating d2 is depicted: (a) no-control, (b) ε = -0.36, (c) ε = -1.42; (d) ε = -2.84.

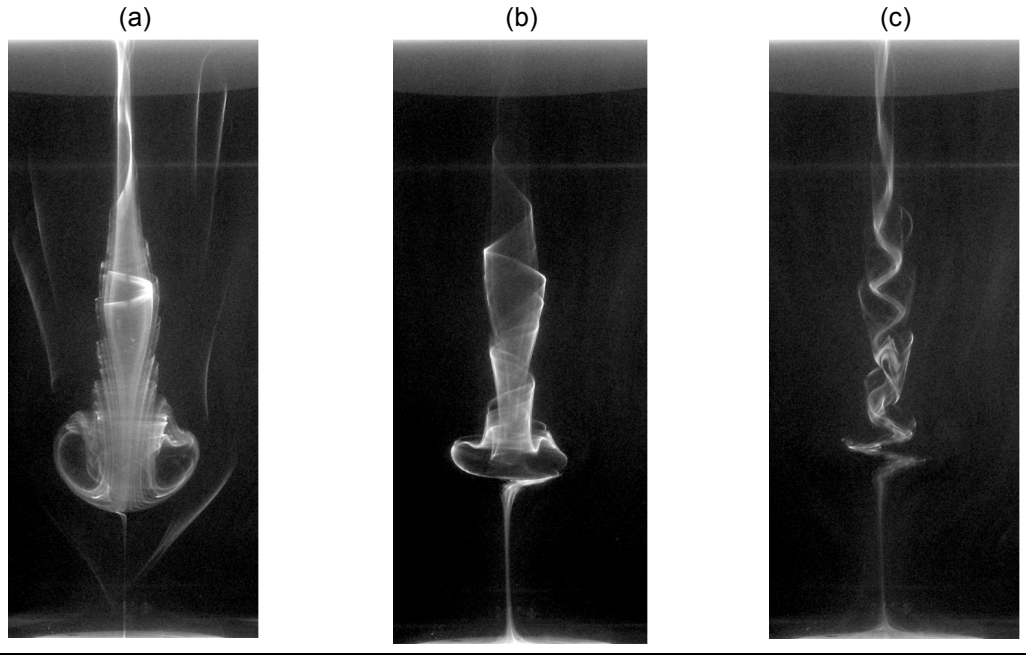

Figure 4.16 Flow visualization of vortex breakdown due to the rotation of the top endwall at Re = 1920 and the effect of counter-rotating d4 is depicted: (a) no-control, (b) ε = -0.33, (c) ε = -0.56.

A close analysis of Figures 4.15(a-d) reveals that the smaller control disk d2 changed the structure of the vortex breakdown only very marginally, this was true even with a higher value of counter-rotation ratio ε = - 2.84. In contrast, the larger control disk d4 was capable of completely suppressing the larger initial vortex breakdown bubble depicted in Figure 4.16(a) at a relatively slower counter-rotation ratio ε = - 0.56. The general tendency observed in both cases (i.e. counter-rotation with d2 and d4) was that the breakdown bubble appeared to be compressed in the radial direction and more so in the axial direction while the size of the downstream vortex core appeared to increase. In particular, a counter-rotation ratio of ε = - 0.33 using the control disk d4 caused a reduction in the axial size of the bubble from 0.19 to 0.095 (with respect to the cylinder height), whereas the compression due to d2 was insignificant for a similar rotation ratio. The change in the radius was again more marked for d4 than for d2. The results also showed that for higher counter-rotation ratio, the bottom bubble was generated.

(b) Main Bubble Radius and Axial Location

Figures 4.17-19 present the variation of the normalised radial size r^*, upstream stagnation point height h_u^*, and centre height $h_c^*$of the vortex breakdown bubble with the rotation ratio. The control disk was rotated at a constant angular velocity which would correspond to a rotation ratio $\varepsilon = \pm 0.45$ when the rotating endwall Reynolds number (Re) was 1440, which is at the vortex breakdown onset stage. Once the speed of the control disk was set and kept constant, the top endwall rotational velocity was adjusted in both directions to cover the range of rotation ratios $-0.5 < \varepsilon < 0.5$. In these experiments, five control disks were utilised and the results presented here intend to show the effect of the disk size on the vortex breakdown parameters r^*, h_u^* and h_c^*. It will be noted that in all the three figures there are no results for counter-rotation of the control disk d5. This was due to the fact that it was virtually impossible, given the speed limitation of the experimental facility, to sustain a vortex breakdown when d5 was counter-rotated even at the slowest angular speed we could achieve during the experiments. This constraint was one of the reasons that motivated the numerical work of vortex breakdown to be carried out. The results of this numerical investigation are presented in the next chapter.

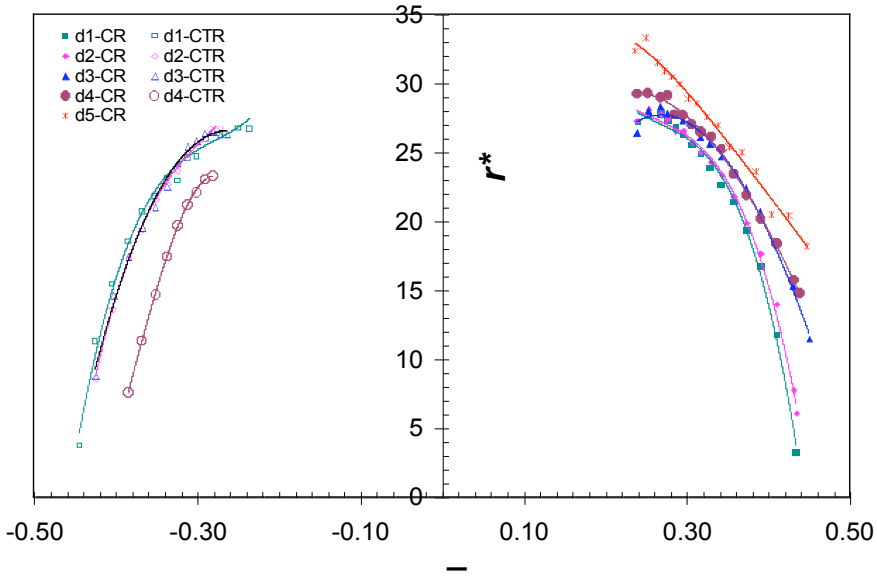

Figure 4.17 Variation of the normalised breakdown bubble radius with rotation ratio (co- and counter-rotation). The effect of control disk size is depicted (d1 – d5).

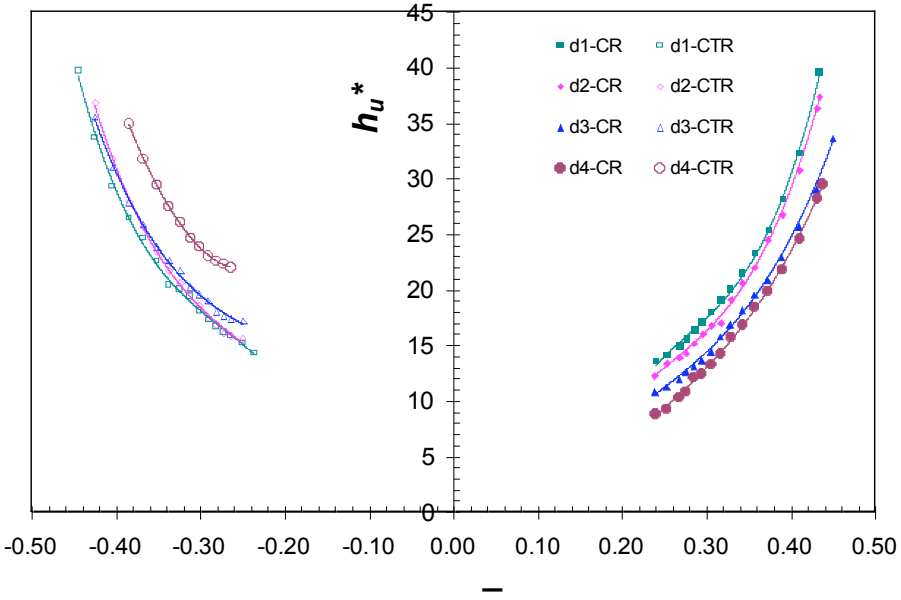

Figure 4.18 Variation of the normalised breakdown bubble upstream stagnation point height with rotation ratio (co- and counter-rotation). The effect of control disk size (d1 – d4) is shown.

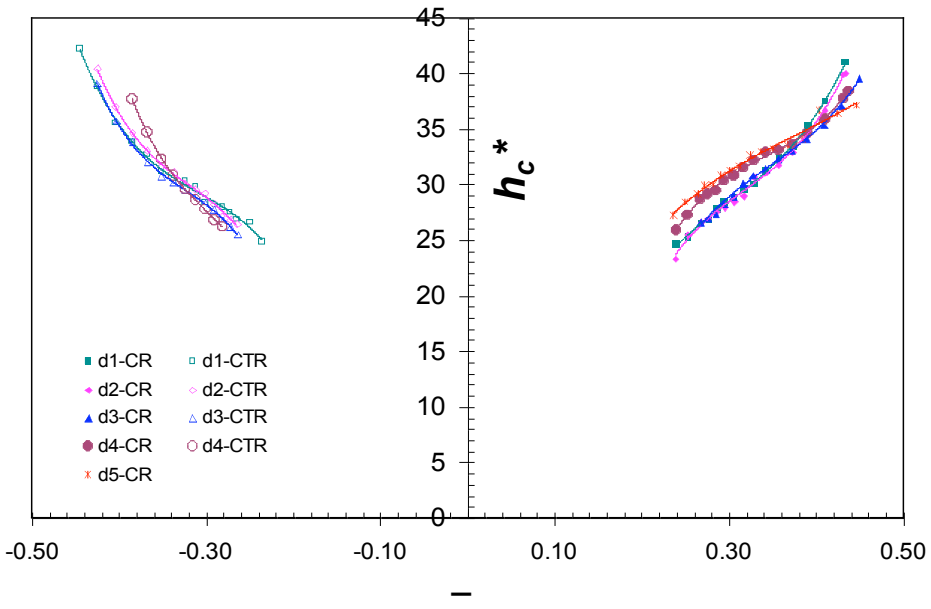

Figure 4.19 Variation of the normalised breakdown bubble centre height with rotation ratio (co- and counter-rotation). The effect of control disk size (d1-d5) is depicted.

From Figure 4.17, it is clear that in counter-rotation the breakdown bubble radius was almost unaltered except when the larger control disk was used. These figures show the importance of using a bigger disk size for the suppressing effect of counter-rotation to have a meaningful effect on the bubble radius, especially when using small rotation ratios. In co-rotation, however, the results revealed that the bigger the control disk size the more effective the enhancing effect on the bubble radius.

The normalised height of the breakdown bubble upstream stagnation point is illustrated in Figure 4.18 as it varies with corresponding changes in the rotation ratio. As expected for co-rotation, the extent of shift of the upstream stagnation point closer to the control disk was observed to be dependent on the size of the disk. Also in the case of counter-rotation, the amount of shift away from the control disk was seen to have a direct relationship with the size of the disk; the effect of the control disk d4 was obviously more significant than the effect of the other disks.. In summary, the results show that the larger the control disks the further away the stagnation point is from the rotating endwall, for co-rotation, or from the control disk, for counter-rotation.

Figure 4.19 illustrates the migration of the centre of the vortex breakdown bubble with changing rotation ratios. The normalised height h_c* was observed to have a crossing point in the co-rotation region at ε = 0.40 and in the counter-rotation region at ε = -0.35; the corresponding normalised height of the bubble centre were about 35% of the cylinder height for co-rotation and about 30% for counter-rotation. For co-rotation ratios less than the crossing value (0.40) the bubble centre was observed to shift in the downstream direction when a bigger disk was used, as opposed to the effect of the smaller disks. However, the reverse was true when the rotation ratio was more than the crossing point value. On the other hand, in the counter-rotating mode a larger control disk tended to shift the bubble centre in the upstream direction when the absolute value of the rotation ratio was less than the crossing point value (0.35). Beyond the crossing point value, the opposite effect was observed. However, in general the position of the centre of the breakdown bubble did not significantly vary with the size of the control disk.

(v) Effect of Control Disk Size with Varying Ω_r and Constant Ω

The next set of results presented in Figures 4.20 through to 4.22 show the effect of the control disk size on the normalised radius and heights of the upstream stagnation point and centre of the breakdown bubble. What differentiates these results from those presented earlier in (iv) is that this time the rotating endwall was spun with a constant angular velocity: in co-rotation Re = 1440 and in counter-rotation Re = 1660. In experiments involving co-rotation, the spinning of the control disks was the catalyst for vortex breakdown formation, from the initial onset state, shown in Figure 4.13(a), to its growth. For the counter-rotation cases, the initial flow structure inside the cylinder was characterised by the presence of a large bubble as depicted in Figure 4.15(a). Gradual increases of the counter-rotation rate caused the breakdown bubble to shrink as illustrated in the following graphs.

(a) Bubble Radius

In Figure 4.20, the normalised breakdown bubble radius is plotted against the rotation ratio and the effect of co-rotating and counter-rotating control disks of different sizes is

presented. The initial flow for counter-rotation was generated at Re = 1660. The smallest disk d1 appeared to have no noticeable effect on the size of the breakdown bubble even at a very high counter-rotation ration of ε = -6.50. While counter-rotation of control disk d2 appeared to cause some degree of shrinkage to the breakdown bubble, it is obvious that d3 had the biggest reduction effect on the bubble radius. To illustrate this, for a counter-rotation ratio of about – 1.60 the control disk d2 caused the bubble radius to shrink to only 92% of the original bubble size, whereas d3 caused a corresponding shrinkage to 42%.

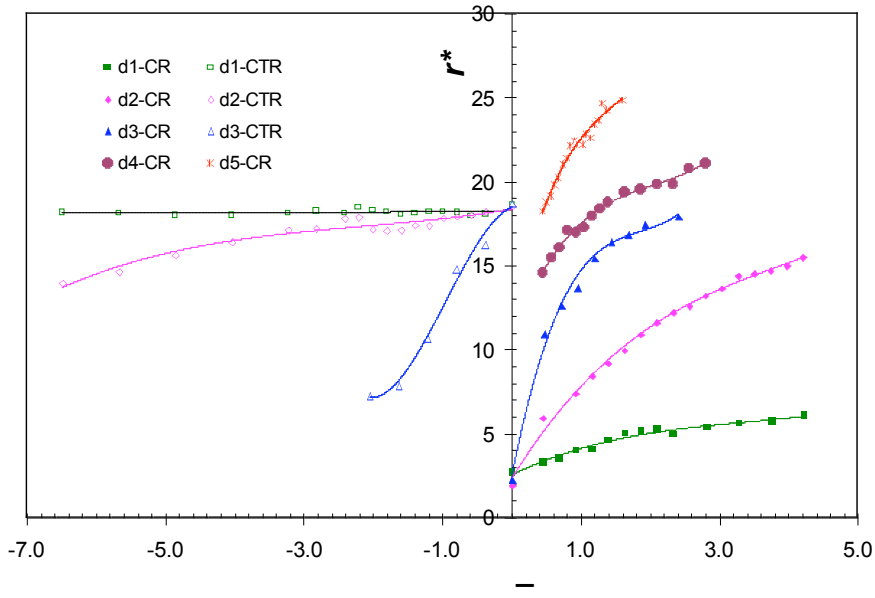

Figure 4.20 Variation of the breakdown bubble radius with rotation ratio. The effects of five control disks, d1 – d5, are compared. Co-rotation starts with Re = 1440 while counter-rotation starts with Re = 1660.

Co-rotation of the control disk with the base flow initially at the onset state was performed with all the five control disks. Looking at the results in Figure 4.20, it is clear that the size of the control disk has a significant effect on the size of the breakdown bubble. To demonstrate the effect of the different disks in co-rotation on the onset breakdown bubble (r* = 2.5% of the cylinder radius) we consider all disks rotating with ε ≈ 2.40. This yielded the following results in varying degrees of bubble radius enhancement factor: 2.0, 5.0, 7.2, and 8.0 for control disks d1, d2, d3 and d4

respectively. The control disk d5 caused a bubble radius increase by a factor of 10 when co-rotating at a relatively lower rotation ratio ε = 1.60. Again, these results clearly show that the size of the control disk has a significant bearing on the size of the breakdown bubble.

(b) Upstream Stagnation Point

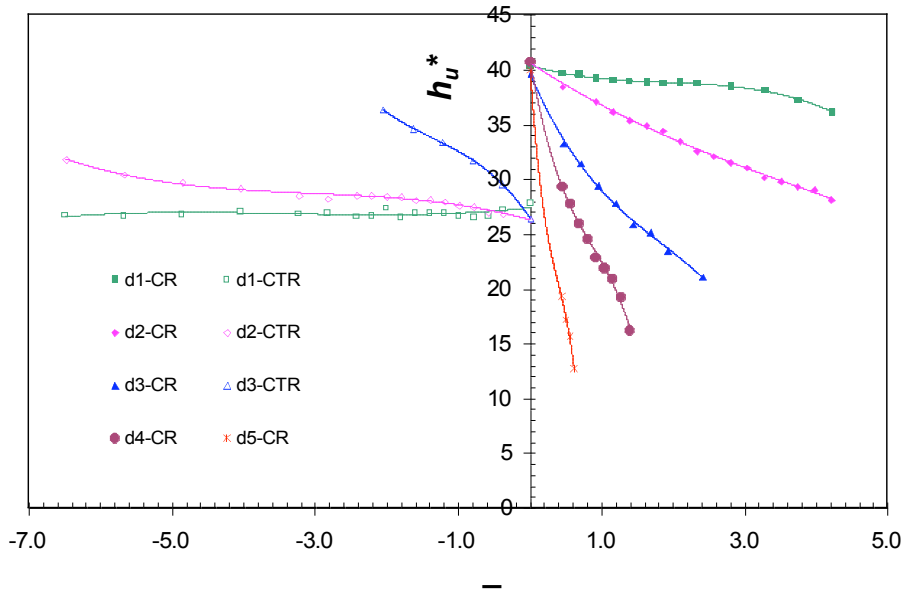

Figure 4.21 Variation of the breakdown bubble upstream stagnation point with rotation ratio. The effects of five control disks, d1 – d5, are compared. Co-rotation starts with Re = 1440 while counter-rotation starts with Re = 1660.

Figure 4.21 presents the variation of the normalised upstream stagnation point height with changes of rotation ratio. The results show that in counter-rotation the smallest control disk d1 did not affect the axial location of the bubble as illustrated by an almost horizontal line in the graph. Counter-rotation using d2 and d3 revealed a downstream shift of the upstream stagnation point, with d3 exhibiting the bigger movement. However, for co-rotation the general trend for all control disks was an upstream movement of the stagnation point. Again, the control disk d1 showed the least effect as opposed to the largest disk (d5) which only needed a slight rotation ratio ε = 0.61 to move the breakdown bubble from a normalised height of 0.40 to 0.13. Such a shift is by

all means highly significant considering the slight co-rotation ratio employed. On the other hand, the control disk d1 co-rotating with a much higher rotation ratio ε = 4.2 caused a shift of the upstream stagnation point from about 0.40 to only about 0.36.

(c) Bubble Centre

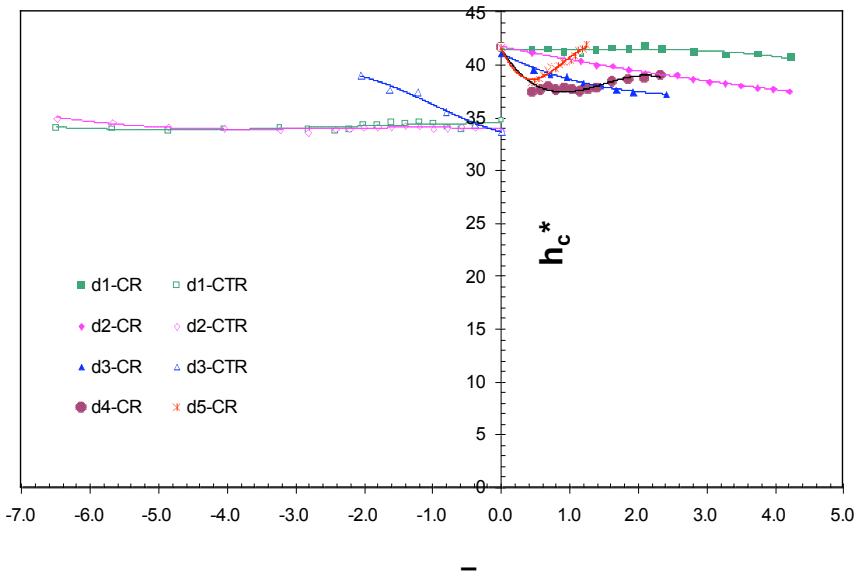

Figure 4.22 Variation of the breakdown bubble centre with rotation ratio. The effects of five control disks, d1 – d5, are compared. Co-rotation starts with Re = 1440 while counter-rotation starts with Re = 1660.

The movement of the breakdown bubble centre with changes in rotation ratio is depicted in Figure 4.22, which shows results from experiments using all the five control disks. It can be seen that counter-rotation with the smaller control disks, d1 and d2, did not move the centre of the breakdown bubble from its original normalised height of about 0.35. However, counter-rotation with the control disk d3 showed a marked shift in the axial position of the bubble centre in the downstream direction. In co-rotation, the bubble centre was seen to shift in the upstream direction depending on the size of the disk. Surprisingly, this was not true for control disks d4 and d5 which portrayed a downstream trend of the vortex breakdown bubble centre. This change of direction, starting with a sharp drop at the initial point of co-rotation (ε = 0.45), was a rather

strange phenomenon observed during the experiments. Apart from the control disk d5, the rate of movement of the breakdown bubble centre produced by the other control disks was fairly marginal, with control disk d1 seemingly showing no change in axial position.

(vi) Bottom Bubble

The results presented in this part of the chapter are concerned with the bubble which was observed to form on the active surface of the control disk as its rotation reached a threshold point. This bubble is referred to as the "bottom" bubble to differentiate it from the other bubble(s) that form in the space between the two endwalls. The first set of results describe the effect of changing the rotating endwall Reynolds number on the bottom bubble, while the next set show the effect of the control disk size.

(a) Effect of Endwall Reynolds Number

Figures 4.23 and 4.24 describe the variation of the normalised radius and height of the bottom bubble when the control disk was co- and counter-rotated while the endwall Reynolds number was varied at three different levels namely, $Re1 = 1550$, $Re2 = 1660$ and $Re3 = 1835$. In these experiments, two control disks (d2 and d3) were tested, which means that the effect of the disk size can also be examined. The present results and the ones described in section 1.3.2(iii) above are for the same experiments.

Bubble Radius

A close examination of Figure 4.23 reveals that the endwall rotation at the three different speeds corresponding to $Re1$, $Re2$ and $Re3$ did not seem to influence the radial size of the bottom bubble. Apart from some minor scattering of the data at low co-rotation ratio, the results show that the endwall Reynolds numbers did not affect the radius of the bottom bubble. This was true for both co-rotation and counter-rotation. However, it was evident that the size of the control disk played a major part in the radial size of the bottom bubble as shown in Figure 4.23. Furthermore, changes in the rotation ratio, realised by increasing the rotational speed of the control disk, resulted in magnification of the bottom bubble in the radial direction. For both co-rotation and

counter-rotation, the bubble radius was more sensitive to changes in rotation ratios when using the bigger control disk d3 than when using the smaller disk d2. It was also observed that the bottom bubble did not form until the rotation ratio $\varepsilon \approx \pm 1.00$ with the only exception of disk d3 in counter-rotation when it formed at $\varepsilon \approx -0.70$.

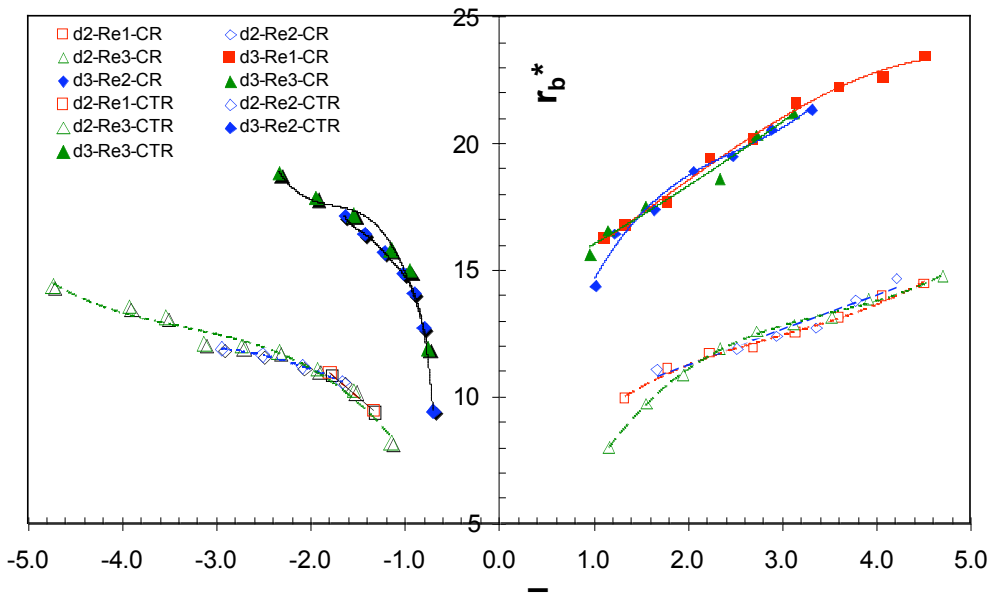

Figure 4.23 Variation of the control disk bubble radius with rotation ratio (co-rotation and counter-rotation). Two disk sizes, d2 and d3 are compared at three Reynolds numbers (Re1 – Re3).

Bubble Height

In Figure 4.24, the normalised height of the bottom bubble is plotted against the rotation ratio. As in the case of radius (Figure 4.23), the height of the bottom bubble does not seem to be greatly affected by the constant rotation rate of the rotating endwall. The only differences noted were for the cases of counter-rotation with the control disk d2 and co-rotation with d3. It was observed that a higher endwall Reynolds number tended to marginally increase the bubble height when co-rotating d3 while it tended to slightly reduce the height when counter-rotating d2. Again, the results generated using the control disk d3 showed greater sensitivity of the value of the normalised height h_b^* to changes in the rotation ratio than did the results for the control disk d2. The initial

occurrence of the bottom bubble, as seen in Figure 4.24, is as described earlier (Bubble Radius).

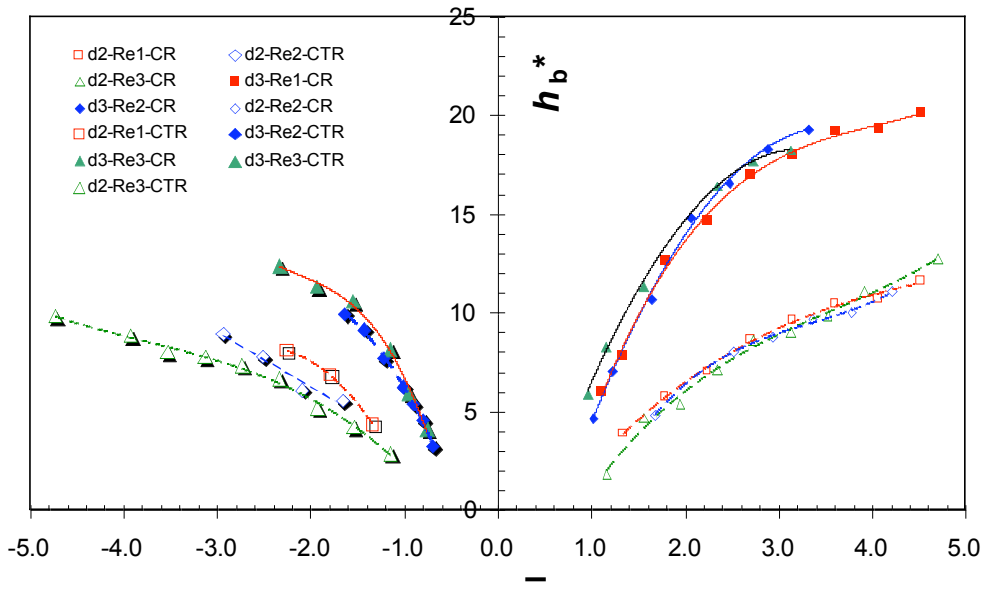

Figure 4.24 Variation of the control disk bubble height with rotation ratio (co-rotation and counter-rotation). Two disk sizes, d2 and d3 are compared at three Reynolds numbers (Re1 – Re3).

(b) Effect of Control Disk Size

Figures 4.25 and 4.26 illustrate the effect of the control disk size on the normalised radius and height of the bottom bubble when the disk was co- and counter-rotated whilst keeping the angular velocity of the rotating endwall constant (Re = 1440 for co-rotation and Re = 1660 for counter-rotation). Four control disk sizes were used in these experiments (d2 through to d5). These results are for the same experiments as the results presented in section 1.3.2(iv) above.

Bubble Radius

The evolution of the bottom bubble radius with changes of the rotation ratio is presented in Figure 4.25. Here, the results show a rapid growth in bubble radius as the diameter of the control disk increases. Control disk d5 generated bottom bubbles at very low value

of rotation ratio in co-rotation. As the disk size got smaller, the appearance of the bottom bubble was delayed until a sufficiently high rotation ratio, which was different for each disk, was attained. The rate of growth of the bottom bubble radius was the highest when using the control disk d5.

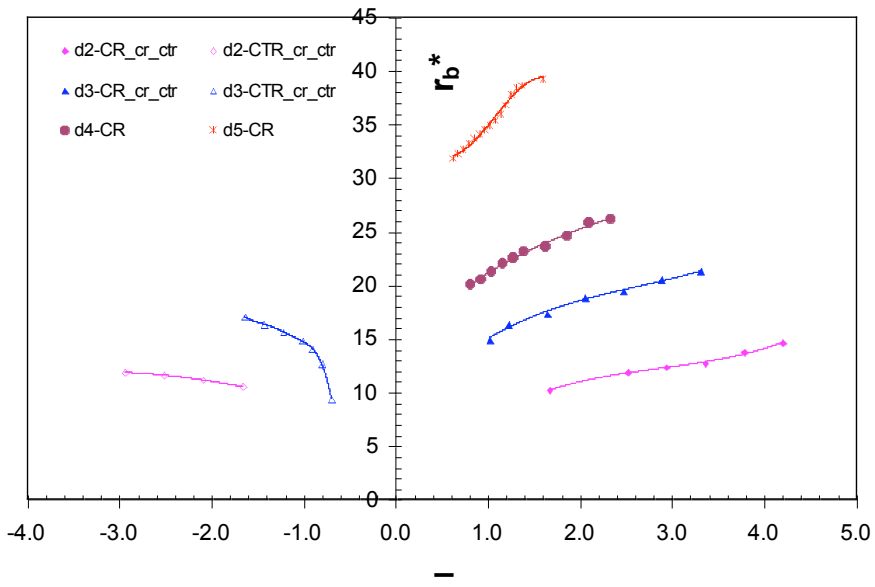

Figure 4.25 Variation of the control disk breakdown bubble radius with rotation ratio (co-rotation and counter-rotation). Four disk sizes, d2 – d5 are compared at Re = 1440 for co-rotation and Re = 1660 for counter-rotation.

Bubble Height

The results shown in Figure 4.26 describe how the height of the bottom bubble varied with the rotation ratio in co-rotation and counter-rotation. Of particular interest is the effect of the control disk size on the height of the bubble. Clearly, the findings indicate that a larger disk significantly increased the bottom bubble size in the axial direction. Also, the results reveal that the larger the control disk the faster the growth rate of the height with increasing rotation ratio. Moreover, when the control disk size was smaller the bottom disk formation was delayed; this is true for both co-rotation and counter-rotation. It was also observed that when the rotation ratio was sufficiently high, especially when the control disk was larger or equal to d3, the bottom bubble was seen to connect with the main breakdown bubble as shown in Figure 4.14(c).

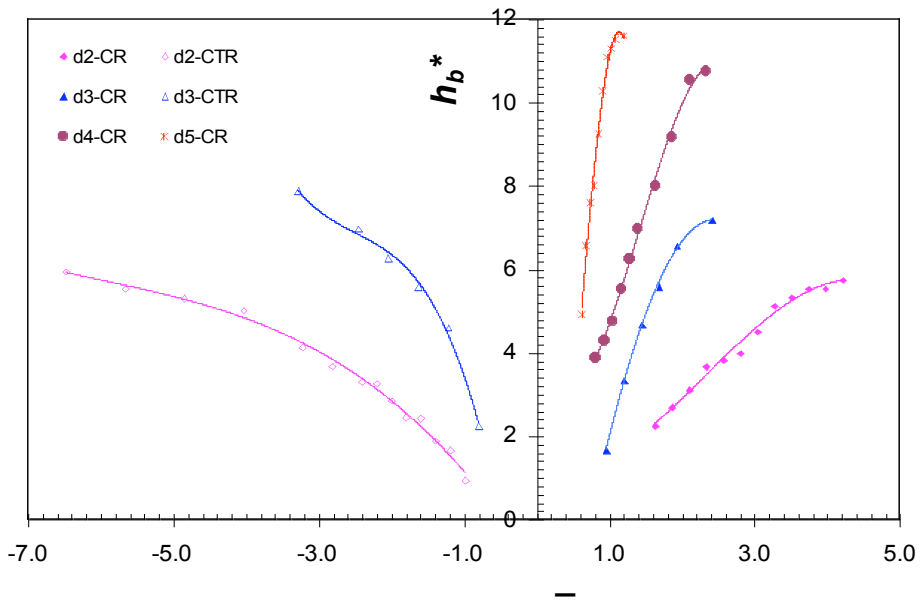

Figure 4.26 Variation of the control disk breakdown bubble height with rotation ratio (co-rotation and counter-rotation). Four disk sizes, d2 – d5 are compared at Re = 1440 for co-rotation and Re = 1660 for counter-rotation.

4.4 Summary

In this chapter, a new technique to control vortex breakdown in a closed cylinder has been proposed and experimentally implemented with success. The technique involved co-rotation and counter-rotation of a small control disk to manipulate the flow structure upstream of the vortex breakdown region.

Initial results involving vortex breakdown with no-control were compared with the data by Fujimura *et al.* (1997) and very good agreement was noted in terms of vortex breakdown state and upstream stagnation point height with respect to the rotating endwall Reynolds number variation. From these experiments, it was observed that the main bubble radius initially grew with increasing Reynolds number until it reached a maximum size in the second single bubble region. Further increases in the Reynolds number beyond this point led to a bubble size reduction and eventual disappearance.

The vortex breakdown control investigation comprised of the studies of vortex breakdown onset, effect of co- and counter-rotation, effect of control disk size and formation of the bottom bubble above the active surface of the control disk. Five control disks of different diameters were employed in this study.

The vortex breakdown onset study aimed to establish the effect of the direction of rotation, i.e. co- and counter-rotation, the rotation ratio and of the control disk size on the occurrence of the first sign of vortex breakdown along the axis of swirl. It was found that in general co-rotation precipitated the onset of vortex breakdown while counter-rotation retarded the process. Similarly, the critical Reynolds number associated with the onset of vortex breakdown was observed to be directly related to the magnitude of the rotation ratio. Such that, higher rotation ratios were conducive to lower critical Reynolds numbers for co-rotation cases, hence further precipitating the onset of vortex breakdown. However, higher rotation ratios were observed to further delay the onset of vortex breakdown in counter-rotation case by increasing the critical Reynolds number. In addition, the results showed that larger control disk sizes tended to significantly amplify the compound effect of the direction of rotation and rotation ratio just mentioned above.

The effect of co-rotation and counter-rotation on an existing vortex breakdown was found to be similar to what was discussed in the case of vortex breakdown onset. Generally, co-rotation was found to be favourable to vortex breakdown bubble growth, while counter-rotation tended to shrink the bubble size and in some cases completely suppress it. Furthermore, co-rotation was observed to generally cause the breakdown bubble to move in the upstream direction, whereas counter-rotation tended to shift it in the opposite direction. The amount of shift was found to be dependent on the rotation ratio.

Experiments were conducted in which the angular velocity of the control disks (d2 and d3) was varied while keeping the endwall Reynolds number fixed at three different levels ($Re1<Re2<Re3$). It was found that the bubble radius tended to grow faster with rotation ratio when the endwall Reynolds number was smallest ($Re1$). Also, the rate of change of the bubble radius was observed to have a linear relationship with the change

in rotation ratio for the smaller disks d2, whereas for d3 the relationship was more complex. On the other hand, the centre of the breakdown bubble was seen to be moving towards the rotating endwall as the rotation ratio increased for both co-rotation and counter-rotation. At a certain rotation ratio, the bubble centre was seen to be the closest to the control disk and the rotation ratio at which this occurred was the lowest when the highest endwall Reynolds ($Re3$) number was used.

In the next experiments, the rotation ratio was manipulated in two ways: first by varying the angular velocity of the rotating endwall while keeping that of the control disk constant and second by keeping constant the rotating endwall rotation rate while varying the control disk angular velocity. It was found that, for the first method the control disk size had some degree of influence on both the breakdown bubble size and location along the swirl axis. Bubbles generated by larger control disks tended to be more sensitive to the suppressing effect (for counter-rotation) and enhancing effect (for co-rotation). It was observed that the size of the control disk influenced the position of the breakdown bubble along the axis. Smaller disks tended to cause negligible shift while larger disks had tendency to impart significant movement to the upstream stagnation point away from the rotating endwall for co-rotation but closer for counter-rotation. In general, it was observed that the position of the centre of the breakdown bubble did not significantly vary with the size of the control disk.

For the case where the rotation ratio was manipulated by varying the control disk angular velocity while keeping that for the endwall constant, it was found that of the variations of the bubble radius and axial location with the rotation ratio were more pronounced when larger control disks were used compared to the first case. Larger control disk sizes significantly enhanced the size of the breakdown bubbles and also produced significantly bigger shifts of the upstream stagnation point along the swirl axis. Although generally the position of the bubble centre did seem to maintain its original height along the swirl axis when smaller control disks were used in counter-rotation mode, in general the centre appeared to move downstream for counter-rotation and upstream for co-rotation. However, when the control disks d4 and d5 were used in co-rotation the centre appeared to move in the opposite direction (downstream).

The study of the bottom bubble under the influence of three different endwall Reynolds numbers revealed that the overall size of the bubble was not affected in a significant way by the Reynolds number. The radius of the bottom bubble was the least affected by changes in the endwall Reynolds number. However, the size of the bottom bubble was observed to be largely dictated by size of the control disk. It was also shown that the bottom bubble formation occurred at a higher rotation ratio when using a smaller control disk than it did when using a larger disk.

Following this presentation of experimental results, the next chapter describes the results of numerical investigation.

Chapter 5
Numerical Modeling of Confined Flow Vortex Breakdown

This chapter describes the results of numerical simulations for the vortex breakdown investigation in a closed cylinder. The general methodology for these simulations was presented in chapter 3; therefore, only brief additional aspects of the methods will be presented here. The work is divided into five sections. Section 5.1 presents a brief introduction to the numerical investigation, section 5.2 deals with results of vortex breakdown without control. The flow generated by the top endwall (or rotating endwall) and the bottom disks are separately investigated. The results from the study concerned with the control of vortex breakdown are described in section 5.3. This section investigates in turn the effects of the size of the control disk, co- and counter-rotation of the control disk and the bottom endwall on the vortex breakdown. Section 5.4 focuses on the relative viscous power expended due to the rotation of the top endwall, bottom endwall and control disks. The chapter ends with a summary of the main results.

5.1 Introduction

The background presentation in chapter 1 and the review of the literature in chapter 2 show that vortex breakdown can be beneficial in some industrial applications and detrimental in other situations. It was also established that vortex breakdown control in closed cylinders has not been sufficiently researched. Among the few publications on vortex breakdown control are the studies of Bhattacharyya and Pal (1998), Husain *et al.* (2003) and Herrada and Shtern (2003a). In these studies, vortex breakdown was controlled using the rotation of the second endwall mainly in co-rotation, the rotation of a small centrally located rod along the swirl axis, and temperature gradient. In the current study, the control of vortex breakdown was achieved by co- and counter-rotating a control disk located at the opposite end of the rotating endwall. As an extension to the control disk method, the bottom endwall was also co- and counter-rotated to achieve the same results.

It has been shown that when the small disk, flash mounted concentrically with the bottom endwall, is co-rotated with respect to the rotating endwall the vortex breakdown phenomenon is enhanced; whereas, when it is counter-rotated the flow inside the cylinder is conducive to suppressing vortex breakdown.

The main objectives of this numerical study of vortex breakdown were:

- To compare some of the current results with existing experimental results in order to assess the validity of the current results.
- To provide further support to the effectiveness of this new method, besides the results of chapter 4, to enhance and suppress vortex breakdown.
- To provide more details about the upstream flow, with a view to better understand the flow conditions that are conducive to the vortex breakdown phenomenon.
- To examine the relative viscous power needed to generate and control vortex breakdown.

The last two aspects form the basis of what could be an important contribution to the

field of vortex breakdown. The numerical results presented here have provided far better and diverse insight into the capability of the proposed control methods.

5.2 Vortex Breakdown without Control

In this section, numerical predictions of vortex breakdown due to the rotation of only the top endwall and the control disks are presented separately. The results are presented as flow visualization of streamlines; the variation of swirl number, swirl and axial velocities with the normalised height along the swirl axis and the global Reynolds number (Re); the variation of axial Reynolds number (Re_a) with global Reynolds number.

5.2.1 Endwall Rotation

The results in this section are for simulations in which only the top endwall was rotated at different rotation rates corresponding to Reynolds numbers selected within the range $1350 < Re < 3100$. This Reynolds number (Equation 3.13), based on the radius of the top endwall, is also referred to as the global Reynolds number to differentiate it from the axial Reynolds number (Equation 3.16).

(i) Flow Visualization

Figure 5.1 depicts flow visualization of streamlines of the right hand side of the closed cylinder. The vertical left side represents the swirl axis while the right side represents the vertical cylindrical wall. The horizontal top is the rotating endwall and the bottom is the bottom endwall. The six flow conditions illustrated in Figure 5.1 cover all the possible flow regimes as far as vortex breakdown is concerned. General good agreement was noted between the current results and those from experiments in chapter 4 as well as the now-famous data of Escudier (1984) reproduced in chapter 3 (Figure 3.5). For instance, at $Re = 1430$ (Figure 5.1(a)) the current predicted results show that there is no vortex breakdown and at $Re = 1440$ Figure 5.1(b)) a very small vortex breakdown bubble is observed for the first time, marking the onset of vortex breakdown.

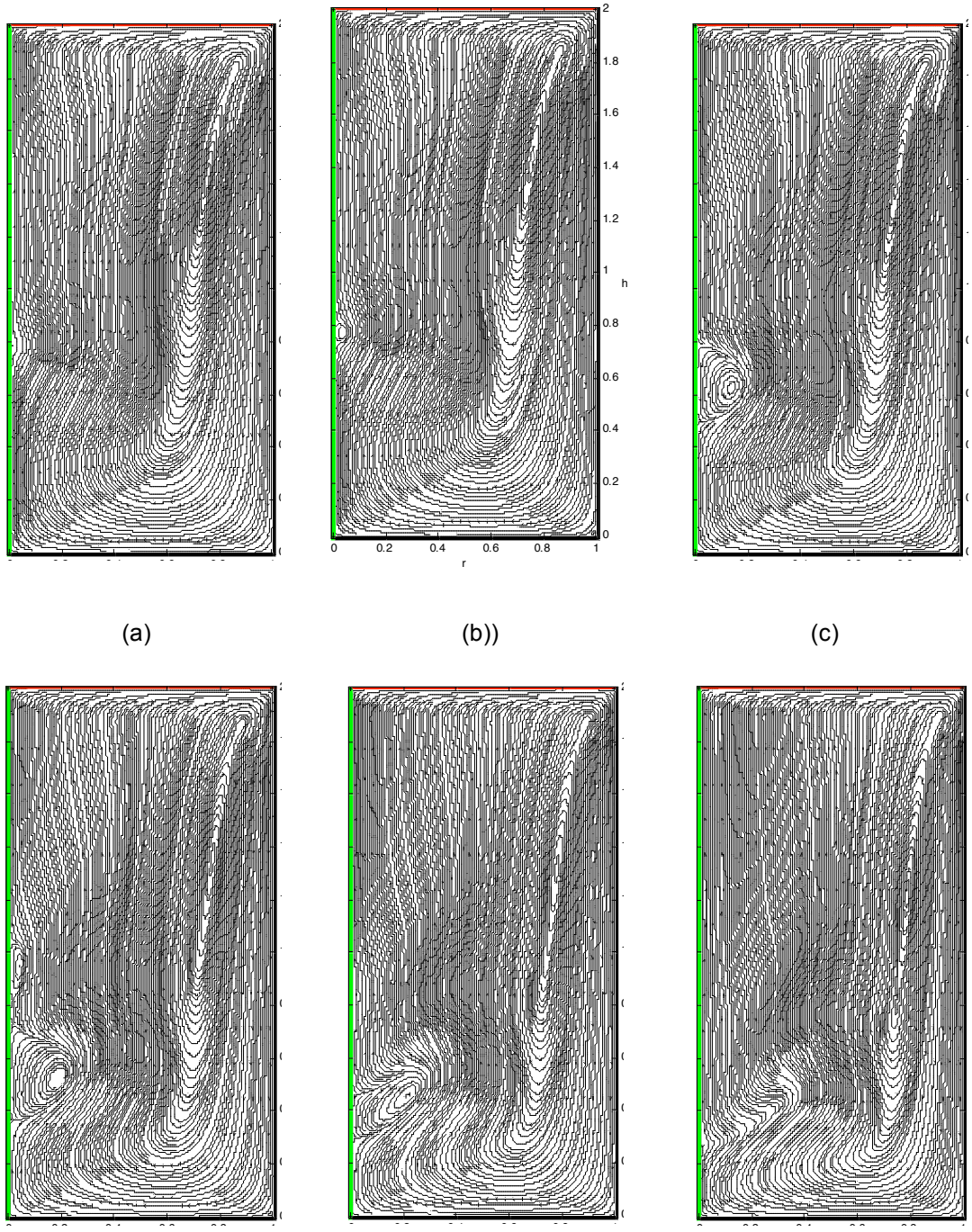

Figure 5.1 Streamlines flow visualization of confined swirling flow in a cylinder with the top endwall rotating at different rates: Re = (a) 1430; (b)1440; (c) 1660; (d) 2000; (e) 2400; (f) 3100.

As the Reynolds number increases, the flow topology within the cylinder is seen to be changing: at Re = 1660 (Figure 5.1(c)) the breakdown bubble grows in size and also appears to shift towards the non-rotating endwall at the bottom of the cylinder; at Re = 2000 a second breakdown bubble appears downstream of the first bubble. This second bubble was observed to be always smaller than the first one; at Re = 2400 the second breakdown bubble disappears while the first bubble undergoes a deformation as if it is being compressed in the vertical direction but its vertical location along the swirl axis appeared to be unchanged; at Re = 3100 there is no sign of vortex breakdown. These predictions are consistent with the data of Escudier (1984) and current experimental results.

(ii) Upstream Flow Characteristics

This study has identified that the flow upstream of the vortex breakdown is crucially important to the formation and sustenance of the vortex breakdown bubble. To evaluate the state of this upstream flow a couple of non dimensional parameters were defined, namely the swirl number (Equation 3.17) and the axial Reynolds number (Equation 3.16). The results in this section are concerned with the variation of these non-dimensional parameters with the height along the swirl axis and the global Reynolds number.

By definition, the swirl number is the ratio between the swirl velocity and the axial velocity along the swirl axis, both measured at the same vertical height. As such, it is necessary to specify the location at which the swirl number is computed from. Figure 5.2 is a good representation of how the swirl number varies along the swirl axis. Here, only the region upstream of the vortex breakdown is considered ($h/H < \approx 0.30$), whereas in Table 5.1 the region slightly beyond the upstream stagnation point is also included ($h/H < \approx 0.45$).

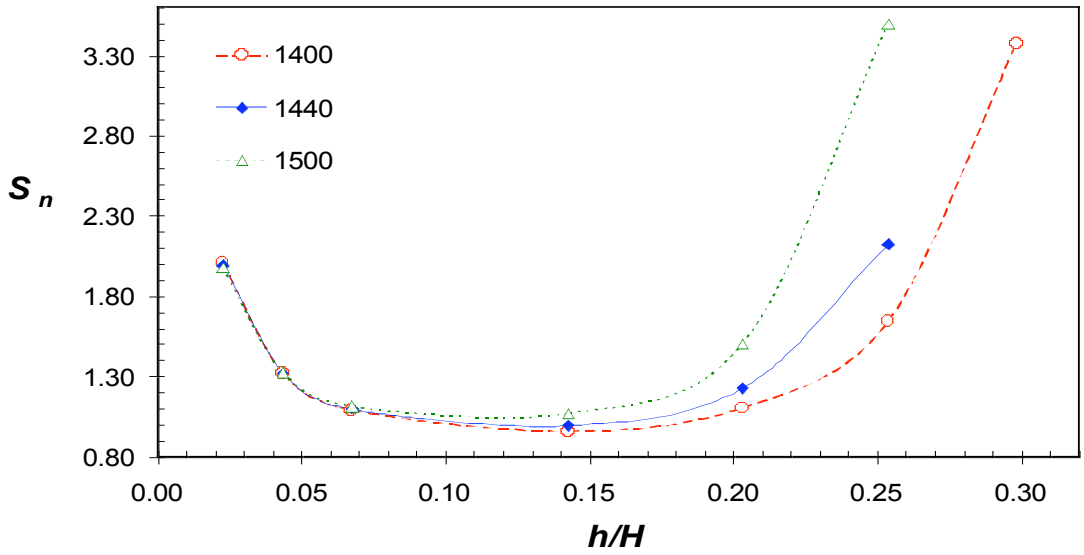

Figure 5.2 Variation of swirl number with normalised height along the swirl axis. Three different Reynolds numbers are considered: Re = 1400, 1440 and 1500.

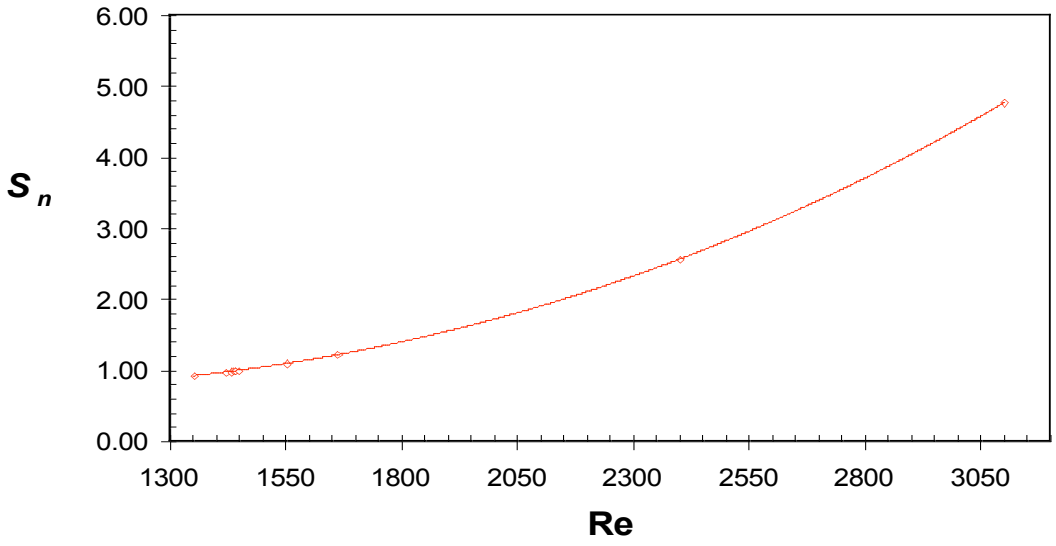

Figure 5.3 Variation of swirl number with Reynolds number for a flow driven by the top endwall.

Table 5.1 Variation of swirl number with normalised vertical height for three Reynolds numbers. Only the bottom half of the vessel is considered.

h/H	1400	1440	1500
0.022	2.02	2.00	1.98
0.043	1.33	1.33	1.33
0.067	1.10	1.10	1.12
0.1423	0.96	1.00	1.08
0.203	1.11	1.23	1.51
0.253	1.65	2.13	3.50
0.298	3.38	5.58	19.35
0.387	42.49	-211.85	-54.17
0.452	37.02	40.12	36.73

The swirl number is clearly seen to vary along the axis of rotation, with its value initially decreasing with increasing height until it reaches a minimum value at approximately $h/H = 0.1423$. This minimum value is the critical swirl number that was observed to occur at an axial location where the axial velocity along the swirl axis was maximum (V_{a_max}). Above this critical height the swirl number was observed to increase. A rapid rate of increase was noted for $h/H > 0.20$. More detailed data on the variation of the swirl number are shown in Table 5.1, where negative swirl numbers indicate regions of reversed flow within the vortex breakdown bubble.

The swirl number represented in Figure 5.3 corresponds to the critical value described above and from this point onwards will be referred to simply as swirl number (S_n). In Figure 5.3, the S_n is seen to increase as the Reynolds number grows. However, the axial Reynolds number Re_a (Figure 5.4) tends to decline as the global Reynolds number increases. These opposing trends are due to the fact that the S_n and the Re_a are inversely and directly proportional, respectively, to the maximum axial velocity which in turn tends to decrease as the Reynolds number increases. The Re_a, unlike Re is a better indicator of the flow within the core vortex around the swirl axis.

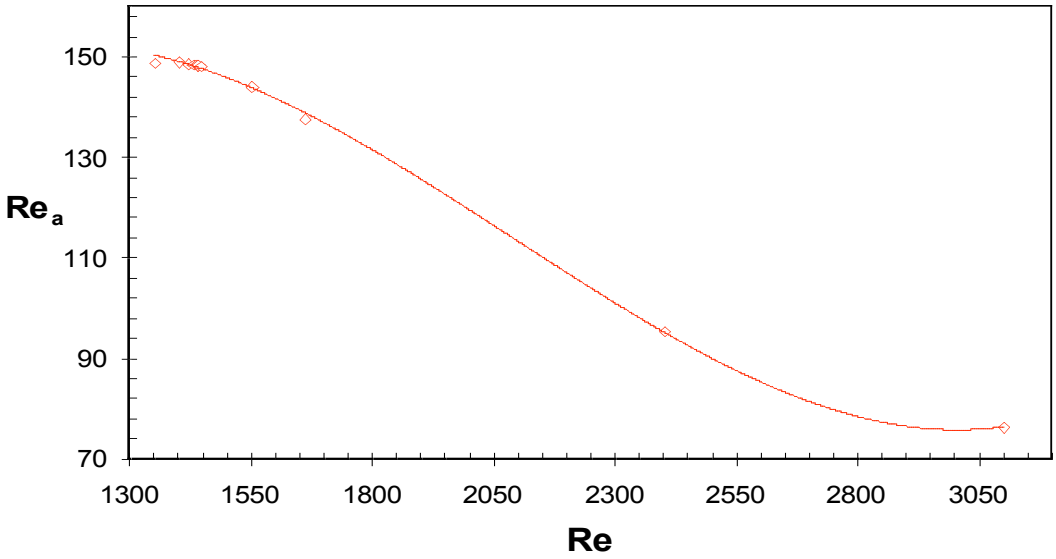

Figure 5.4 Variation of axial Reynolds number with global Reynolds number for a flow driven by the top endwall.

(iii) Onset of Vortex Breakdown

Determining the exact point at which vortex breakdown just appears has always been a difficult test especially in laboratory experiments where the decision is generally thought to be dependent on the experimentalist's skill and experience. However, this task is made relatively easier by the use of CFD. In this work, the first appearance of vortex breakdown was determined by axial flow reversal along the swirl axis; in other words, the onset of vortex breakdown was achieved at the first appearance of a negative

axial velocity along the axis of swirl. This ensured that the onset of vortex breakdown was determined with a lot more accuracy and confidence.

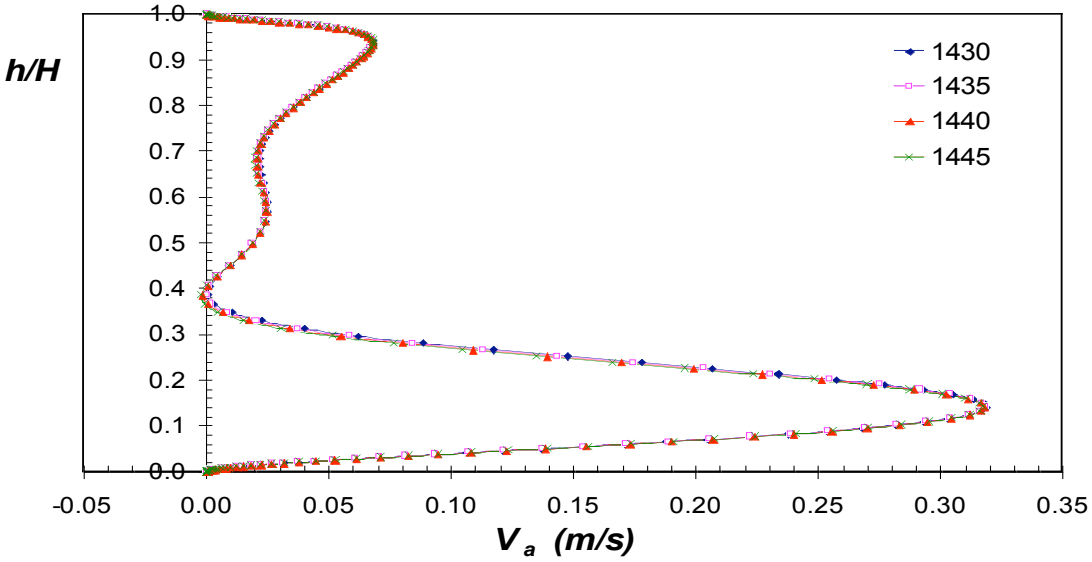

(a)

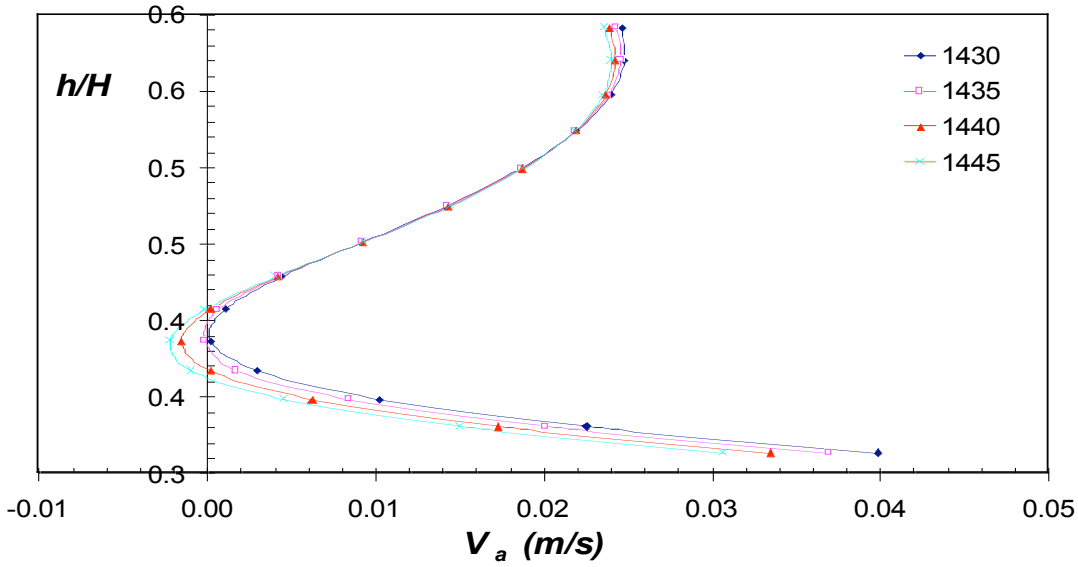

(b)

Figure 5.5 Axial velocity along the swirl axis for a flow generated by the rotation of the top endwall at Reynolds numbers closer to the vortex breakdown formation: (a) The entire tank height is covered; (b) the region around the breakdown bubble is shown.

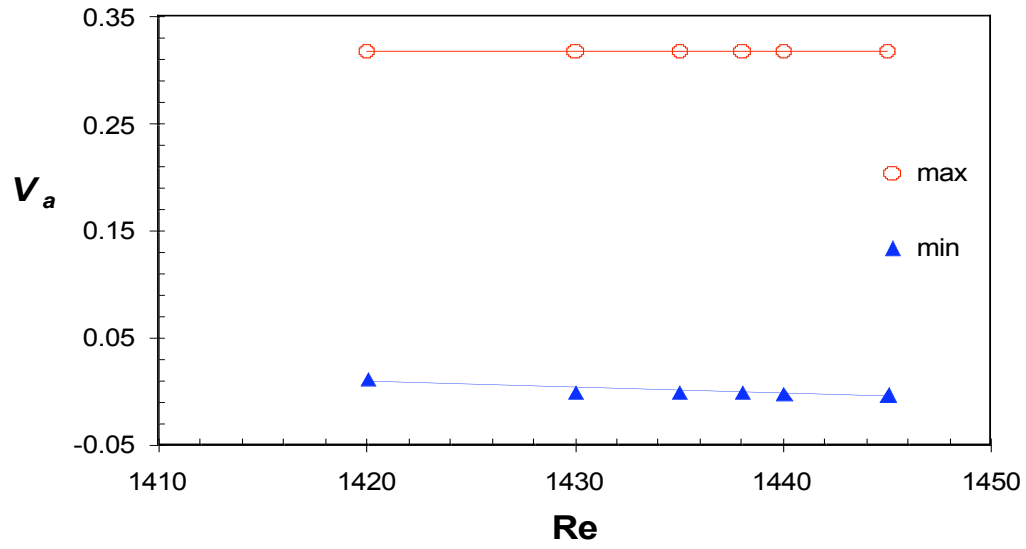

(a)

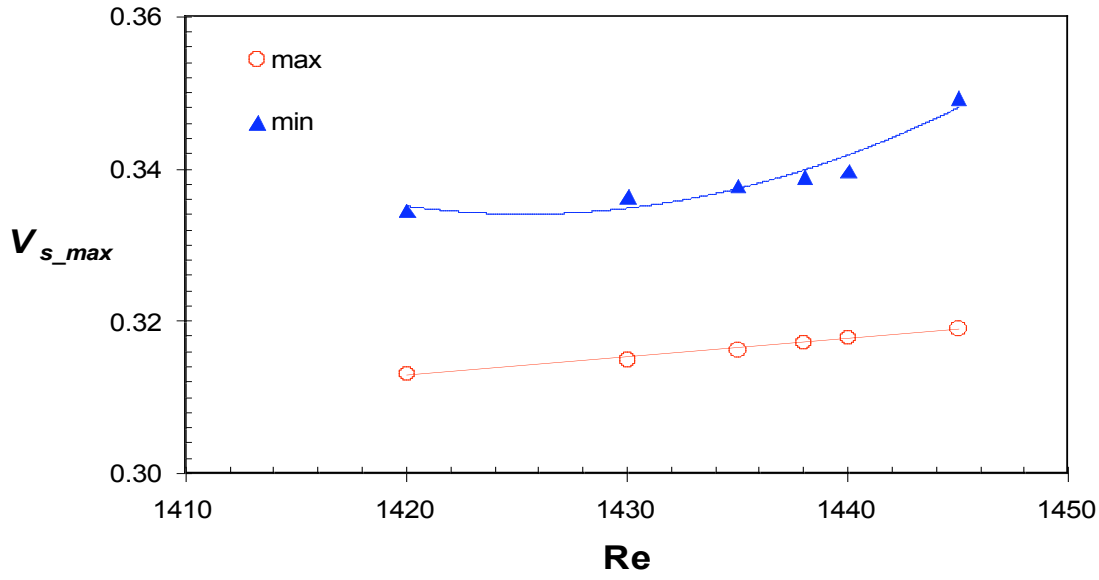

(b)

Figure 5.6 The maximum and minimum axial velocities and their corresponding maximum swirl velocities in the proximity of vortex breakdown onset: (a) maximum and minimum axial velocities; (b) maximum swirl velocities.

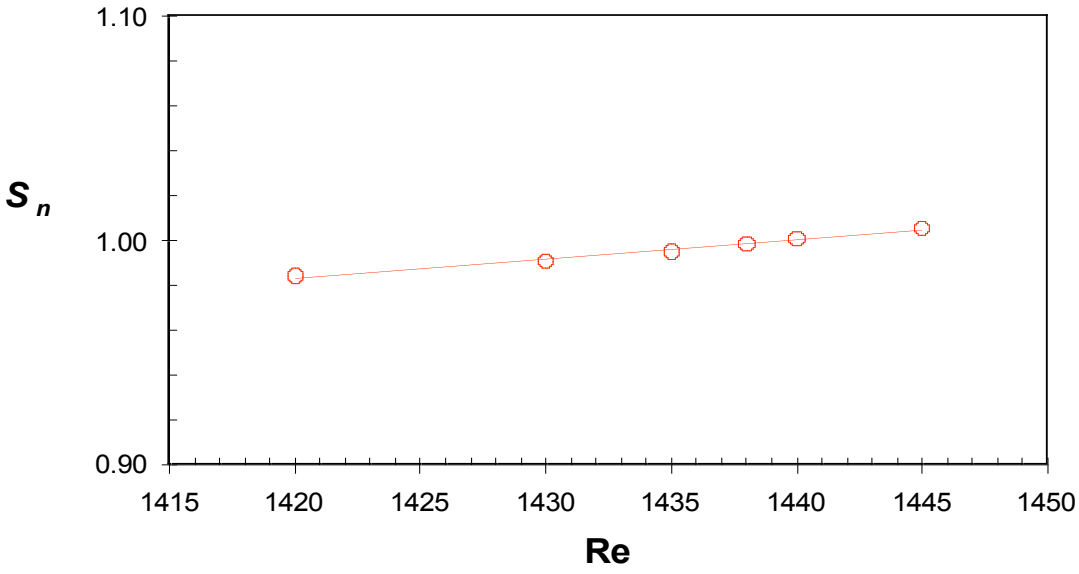

(a)

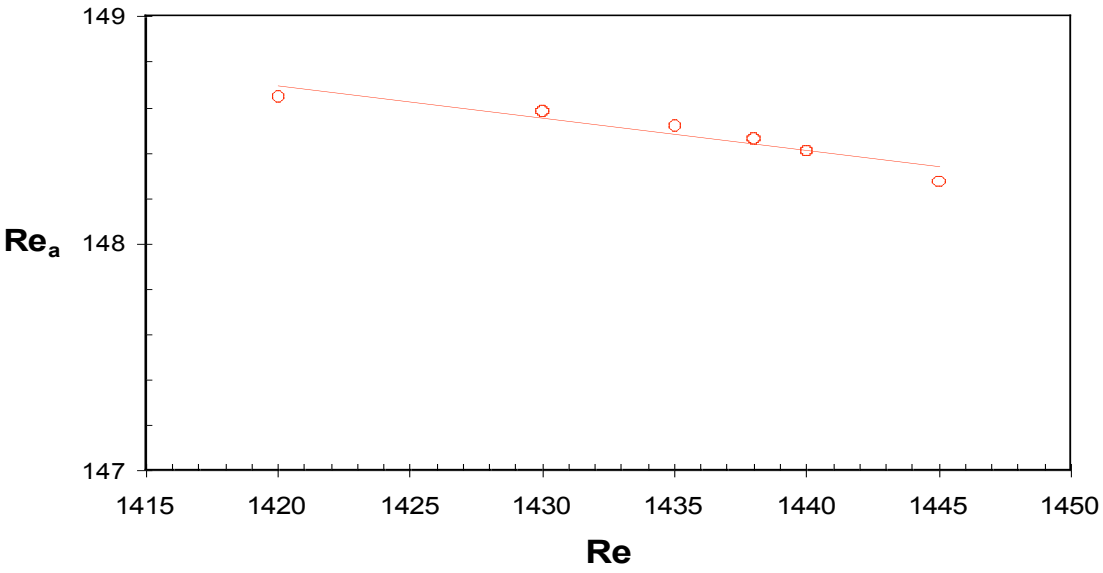

(b)

Figure 5.7 The variations of swirl number and axial Reynolds number in the proximity of vortex breakdown onset.

Figure 5.5 presents the variation of the axial velocity with the normalised height along the axis of rotation. Four Reynolds numbers (Re = 1430, 1435, 1440 and 1445) were tested for vortex breakdown onset. From the plotted curves in Figure 5.5(b), at Re = 1440 the first sign of a recirculation zone along the axis emerges to signify the onset of vortex breakdown. The resulting vortex breakdown bubble is clearly illustrated by the streamlines flow visualization.

In Figure 5.6(a), the maximum and minimum values of the axial velocity along the axis of rotation are shown, while their corresponding maximum swirl velocities are plotted in Figure 5.6(b). These maximum swirl velocities were determined from the swirl velocity profile plotted at the vertical location corresponding to the maximum and minimum axial velocities along the axis of rotation. A striking observation from the result in Figure 5.6(b) is that the maximum swirl velocity corresponding to the minimum axial velocity is always higher than the one related to the maximum axial velocity. It is also noted that in the vicinity of the onset of vortex breakdown (i.e. $Re \approx$ 1440) the maximum axial velocity tended to assume almost a constant value while the minimum axial velocity underwent a marginally slow reduction. This reduction of the minimum axial velocity continued until it attained a negative value to give rise to a recirculation bubble. However, the maximum swirl velocities were observed to progressively increase as the central vortex changed it structure to give rise to a vortex breakdown along the swirl axis.

The tendency of the maximum swirl velocity to gradually increase as the global Reynolds number was incremented near the vortex breakdown onset region is also reflected by the steady increase in the swirl number (Figure 5.7(a)). Perhaps one of the most notable findings of this study is that the critical swirl number corresponding to the onset of vortex breakdown was equal to *unity* (S_n = 1). This critical S_n value for the case where vortex breakdown onset was solely caused by the rotation of the top endwall was investigated in great detail to ensure that it was reliable. Also, it is evident from the results (Figure 5.7(b)) that the axial Reynolds number Re_a, unlike the S_n, gradually decreased as the global Reynolds number was incremented near the vortex breakdown onset region. The vortex breakdown onset value for the axial Reynolds number was found to Re_a = 148.4.

(iv) Stagnation Points

To determine the appearance and the axial extent of the vortex breakdown bubble, axial velocity profiles along the swirl axis were examined. Figure 5.8 illustrates axial velocity profiles along the axis for flow conditions corresponding to six Reynolds numbers (Re = 1430, 1440, 1660, 2000, 2400 and 3100). The flow structures at these Reynolds numbers are shown in Figure 5.1. A careful examination of Figure 5.8 reveals, as shown in section 5.2.1, six different flow regimes namely: no vortex breakdown, vortex breakdown onset, one large vortex breakdown bubble, two vortex breakdown bubbles, back to one vortex breakdown bubble and no vortex breakdown bubble. As before, the presence of a vortex breakdown, in Figure 5.8, is noted by the appearance of negative axial velocity. The size of the bubble in the axial direction is represented by the distance between the two corresponding stagnation points along the axis of rotation. These stagnation points also indicate the axial location of the breakdown bubbles; from which it is evident that the bubble tends to migrate towards the non-rotating endwall as the global Reynolds number increases.

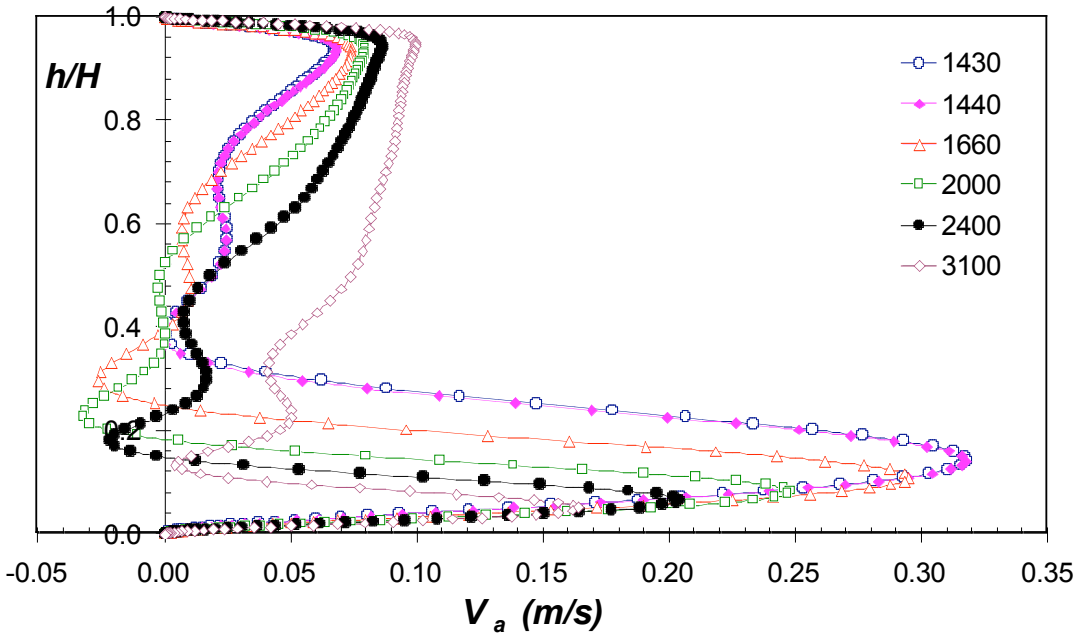

Figure 5.8 Variation of the axial velocity along the swirl axis for flow generated by the rotation of the top endwall at various Reynolds numbers.

5.2.2 Small Control Disk Rotation

The method of controlling vortex breakdown proposed here involves co- and counter-rotating a small control disk concentrically located in the bottom endwall. In this section, the flow generated by rotating this small control disk is briefly investigated.

(i) Flow Visualization

The flow visualization of streamlines shown in Figure 5.9 represents the different flow topologies inside the closed cylinder driven by the rotation of a small control disk. The five different flow structures shown in Figure 5.9 correspond to flows generated by the five control disks employed in this study (d1 through to d5). These disks are in increasing order of size from 5.1 to 30.7% of the cylinder diameter as described in Table 3.1. It was observed that irrespective of the direction of rotation the circulation loops in the vertical plane generated by the rotation of the control disk was always counter-clockwise, for the right hand side half of the cylinder. Such meridional flow always gives rise to downwards axial flow along the axis of rotation, which is in the opposite direction to the axial flow resulting from the top endwall rotation.

Figure 5.9 reveals the increasing strength of the recirculation region with corresponding increases in the control disk diameter. In all these cases (a-e), the rotation of the control disk was kept constant at 90.54 rad/s even though the disk size was varied. To put this rotation into perspective, it is about seven times faster than the top endwall rotation equivalent to Re = 1440 (at the onset of vortex breakdown). As the disk size increases, the centre of recirculation is seen to move away from the swirl axis and the control disk.

(ii) Axial Velocity along the Swirl Axis

The axial velocity profile along the swirl axis is shown in Figure 5.10. The profiles generated by the rotation of the control disk d3 at different rotation rates are illustrated in Figure 5.10(a), while Figure 5.10(b) represents the profiles for the flow developed by the control disk d5. It is evident that the active flow produced by the smaller disk (d3), even at this higher rotation rate of 90.54 rad/s, barely extends up to 70% of the cylinder height; whereas the larger control disk (d5) affects nearly the entire cylinder.

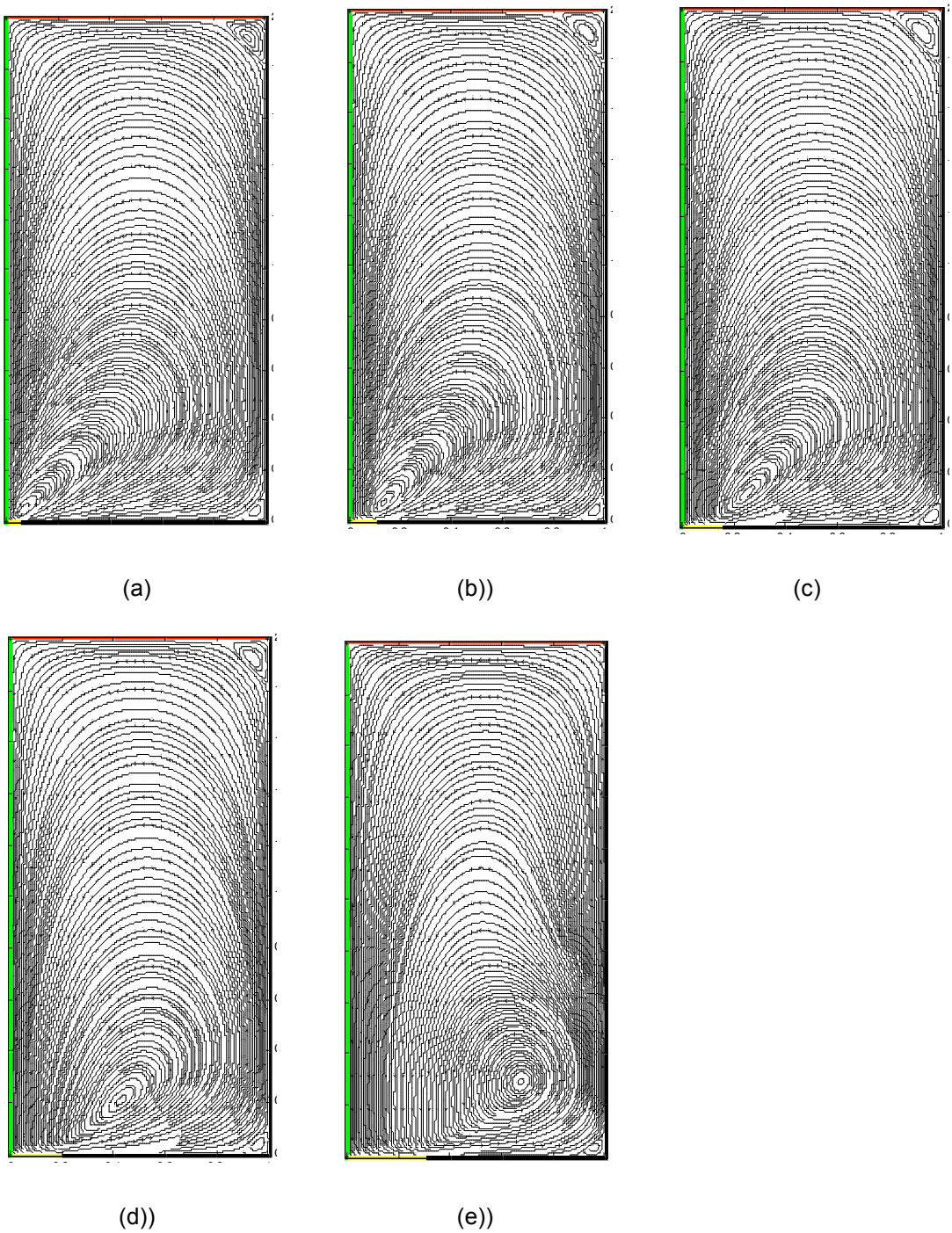

Figure 5.9 Streamlines flow visualization for a flow generated by the rotation of only the control disks: (a) d1; (b) d2; (c) d3; (d) d4 and (e) d5. All the disk are given an angular velocity of 90.54 rad/s.

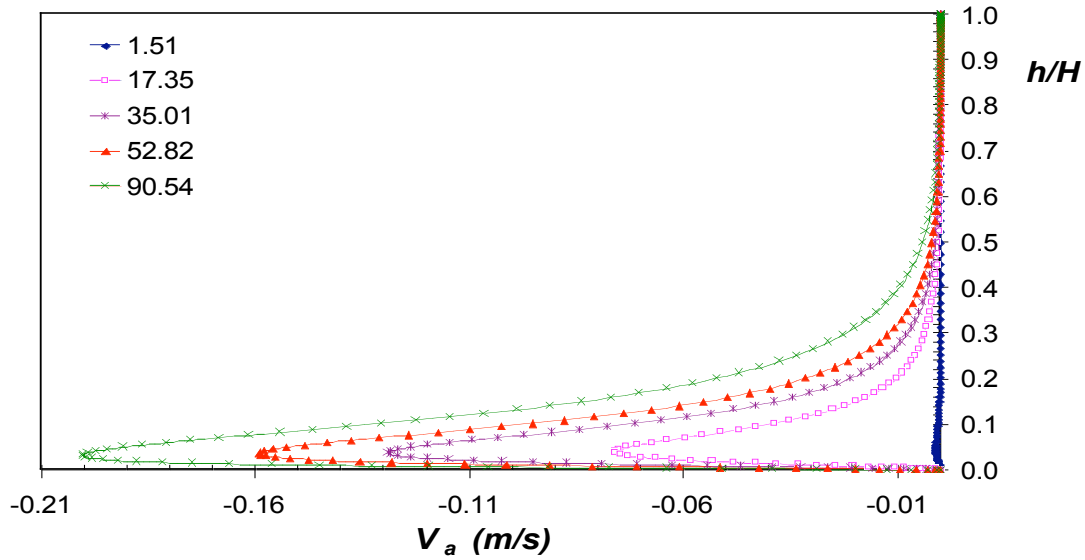

(a)

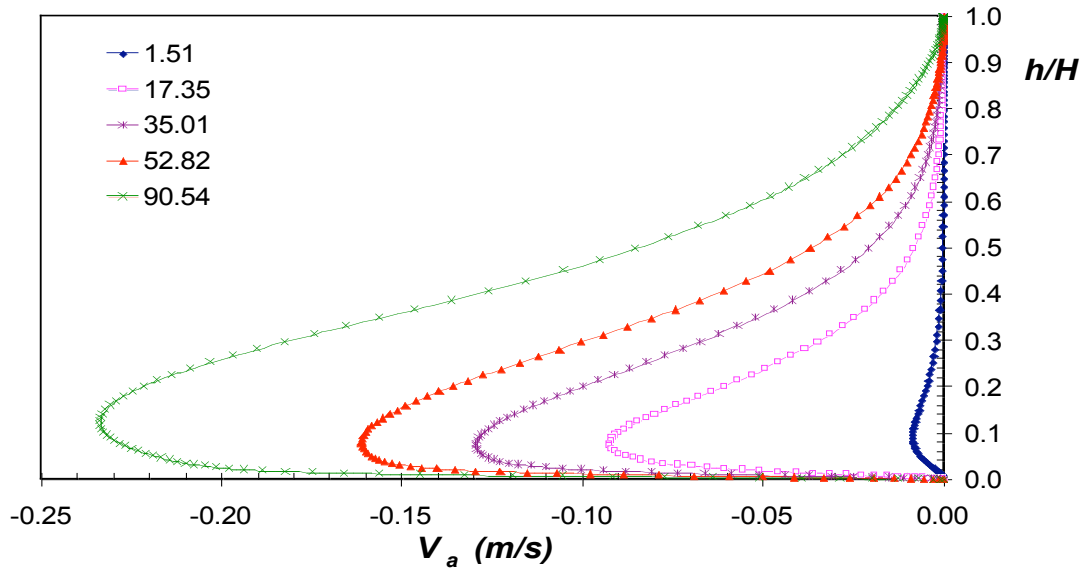

(b)

Figure 5.10 Axial velocity profiles along the swirl axis. The flow was generated by rotating a small control disk in the bottom endwall: (a) d3 and (b) d5.

5.3 Vortex Breakdown Control

To control vortex breakdown, a small control disk was used in both co-rotation and counter-rotation. In order to determine the effect of the disk size on the vortex breakdown bubble, five different sizes were used. However, in this section most of the results will only show data for a few disks at a time to ensure clarity and also that only the most informative results are presented. To the best knowledge of this author, the small control disk method employed here has not been investigated before by other researchers. Another method of controlling vortex breakdown that was examined here involved the use of the second endwall (the bottom endwall) in co- and counter rotation. Although the latter method has been used before by Bhattacharyya and Pal (1998), they only considered the case of co-rotation but here a more detailed investigation including counter-rotation and a wider range of rotation ratios is presented.

5.3.1 Rotation of a Control Disk

Results are presented as flow visualization of streamlines showing the effects of co- and counter-rotation as well as the disk size on the vortex breakdown bubble. Other aspects examined here include the flow upstream of the breakdown bubble and the stagnation points.

(i) Flow Visualization

Figure 5.11 presents streamlines of the flow structure generated by spinning the rotating endwall at Re = 1440, which corresponds to the onset of vortex breakdown, while co-rotating the control disks at $\varepsilon = 0.45$ (a-c) and $\varepsilon = 3.75$ (d-f). Three control disks were employed namely, d1 (a & d), d3 (b & e) & d5 (c & f). The results clearly illustrate that co-rotation of a control disk enhances the size of the breakdown bubble. In addition, a larger control disk has a more significant enhancing effect on the breakdown bubble than a smaller one. As the rotation ratio increases a small bubble emerged above the active surface of the control disk. The bottom bubble tends to grow as the size of the control disk increases. Figures 5.11(e) and (f) show the main breakdown bubble merged

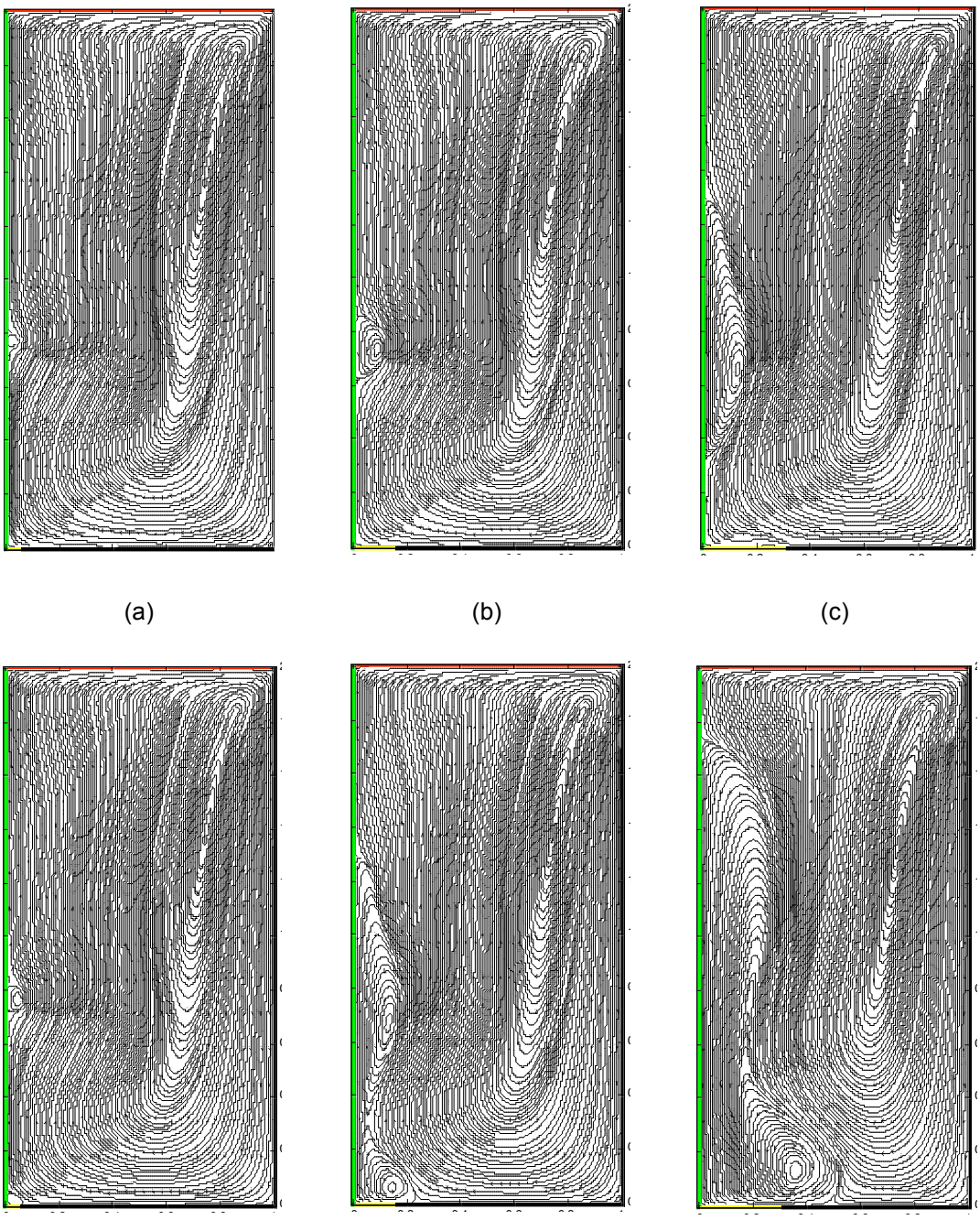

Figure 5.11 Streamlines flow visualization of confined swirling flow in a cylinder with a rotating top endwall and a co-rotating control disk. For all cases Re = 1440 but ε *= 0.45 (a-c) and* ε *= 3.75 (d-f); d1 is used in (a) & (d); d3 in (b) & (e); d5 in (c) & (f).*

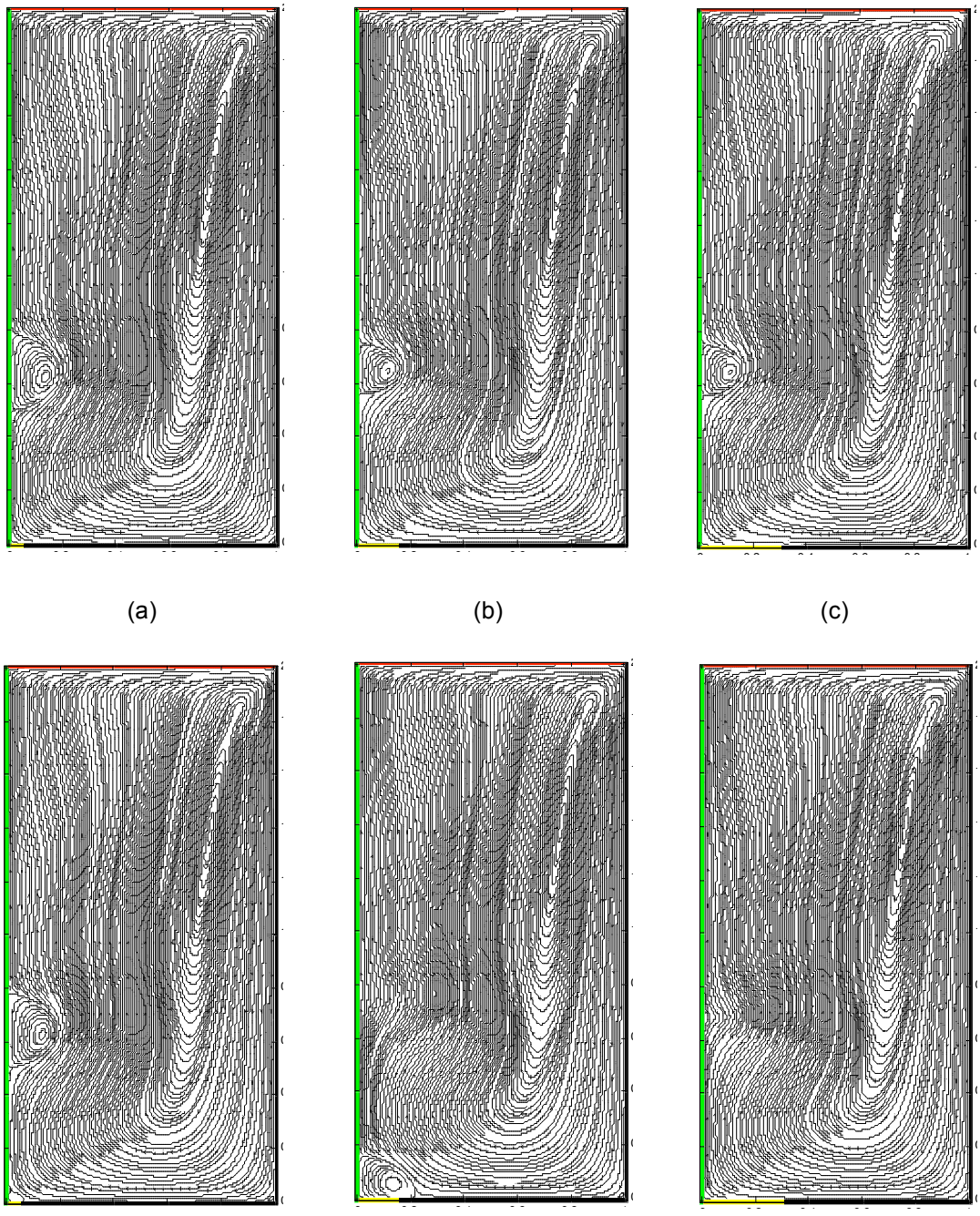

Figure 5.12 Streamlines flow visualization of confined swirling flow in a cylinder with a rotating top endwall and a counter-rotating control disk. For all cases Re = 1660 but ε = -0.45 (a) & (b) and ε = -3.75 (d) & (e); d1 is used in (a) & (d); d3 in (b) & (e); d5 in (c) with ε = -0.05 & (f) with ε = -0.10.

with the bottom bubble. Another effect of increased rate of co-rotation on the vortex breakdown bubble is to shift the breakdown bubble towards the control disk, in the upstream direction, eventually causing the main bubble to connect with the bottom bubble as the latter grows larger.

The effect of counter-rotating a control disk on the breakdown bubble is illustrated in Figures 5.12(a-f). Here, the initial flow topology included a fairly large vortex breakdown resulting from the top endwall at Re = 1660 (see Figure 5.1(c)). Three control disks were employed: d1 (a & d), d3 (b & e) and d5 (c & f). In Figures 5.12(a & b), ε = -0.45; (d & e) ε = -3.75; (c) ε = -0.05 and (f) ε = -0.10. A close examination of the results reveals that counter-rotation of the control disk has a suppressing effect on the vortex breakdown bubble. Also, the higher the counter-rotation rate the more pronounced the effect appears to be. Furthermore, the larger the control disk size the more significant the tendency to suppress the breakdown bubble.

(ii) Upstream Flow Characteristics

The flow upstream of the vortex breakdown bubble (or rather upstream stagnation point) has been known to be very critical to the formation and sustenance of the breakdown bubble. To investigate this flow, the maximum axial velocity (V_{a_max}) along the axis of rotation and its corresponding maximum swirl velocity (V_{s_max}) are plotted against the co- and counter-rotation ratios (ε). In addition, the variation of the swirl number and axial Reynolds number with the rotation ratio are examined. The control disks d1, d2 and d3 were used in co-rotation while disks d2, d3 and d4 were employed in counter-rotation. For all the cases considered here the initial flow was generated by the rotation of the rotating endwall at Re = 1660.

Figure 5.13 shows that in general co-rotation tends to reduce the maximum axial velocity along the swirl axis. Similarly, the larger the control disk size the more significant the reduction in maximum axial velocity. Counter-rotation, on the other hand tended to increase the maximum axial velocity. As in the case of co-rotation, larger control disks tended to amplify the effect of counter-rotating on the V_{a_max}.

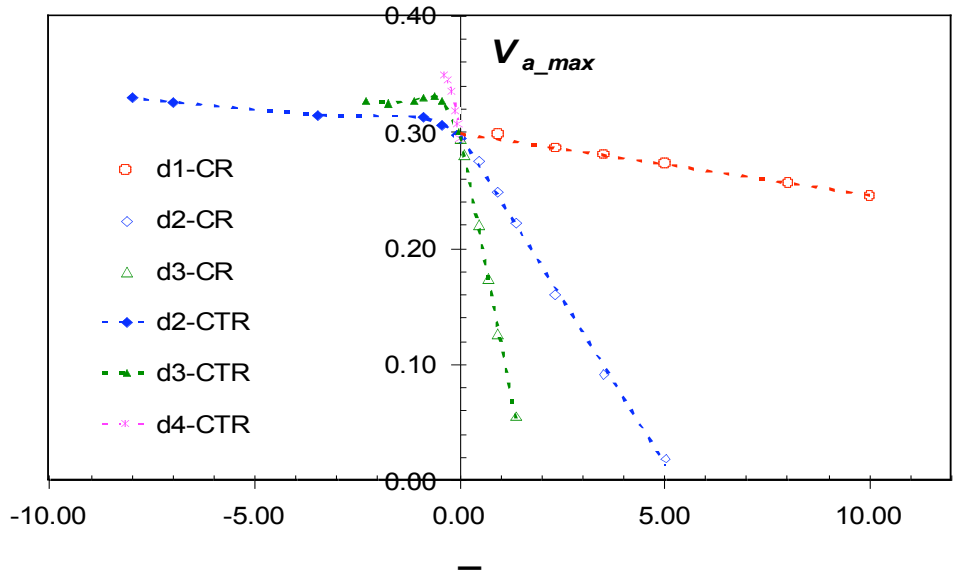

Figure 5.13 Effect of co- and counter- rotating a control disk on the V_{a_max}. Re = 1660 and for co-rotation d1, d2 & d3 are used; for counter-rotation d2, d3 & d4 are used.

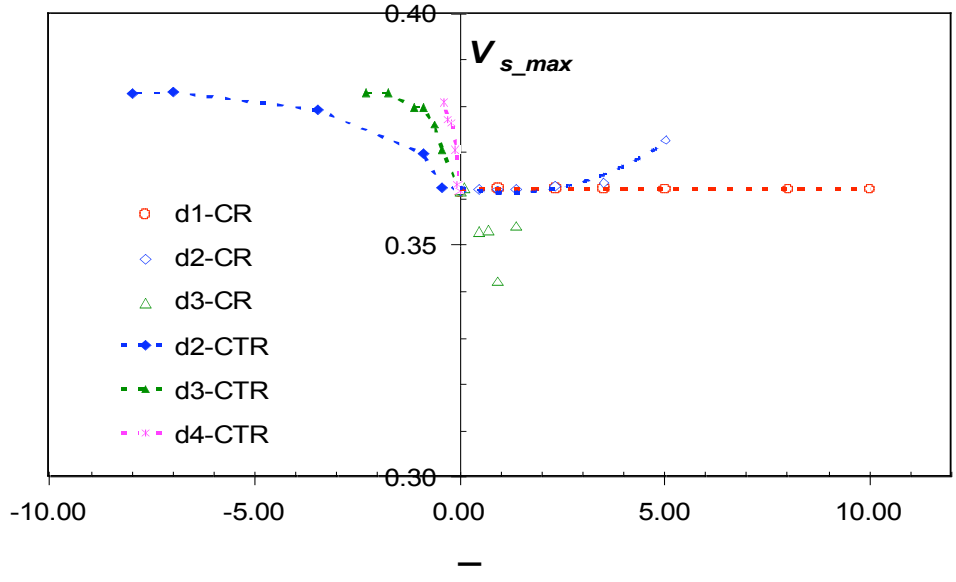

Figure 5.14 Effect of co- and counter-rotating a control disk on the V_{s_max} Re = 1660 and for co-rotation d1, d2 & d3 are used; for counter-rotation d2, d3 & d4 are used.

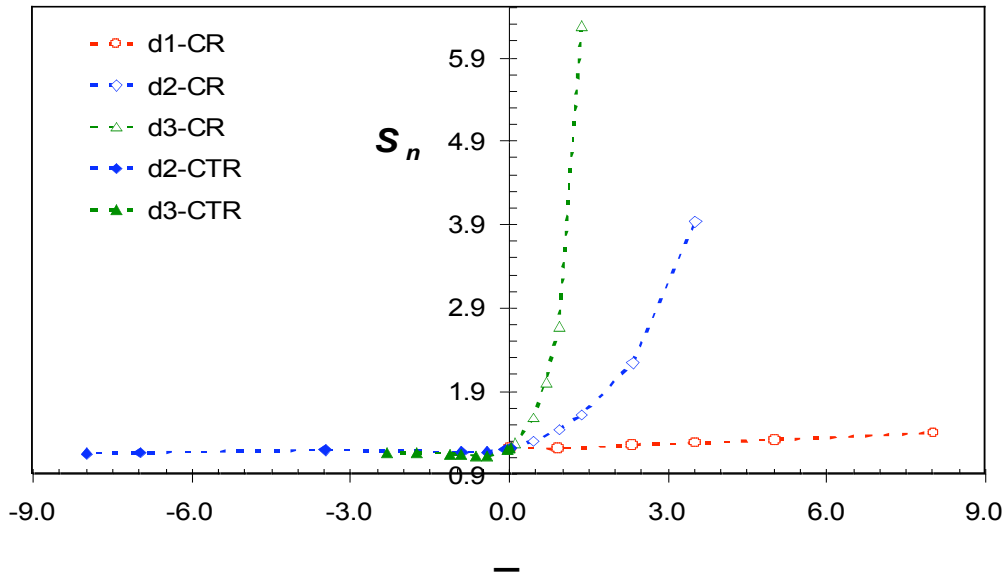

Figure 5.15 Effect of co- and counter-rotating a control disk on the S_n. Re = 1660 and for co-rotation d1, d2 & d3 are used; for counter-rotation d2 & d3 are used.

The results of Figure 5.14 show that in counter-rotation the resulting maximum swirl velocity tends to increase as the rotation rate increases. Rapid increases in V_{s_max} can be observed when the control disk size is relatively large. However, as the counter-rotation ratio increased further, V_{s_max} was seen to assume an almost constant value. In co-rotation, the V_{s_max} showed no variation when using the smallest control d1 ($V_{s\_max} \approx$ 0.36 m/s which is the initial value corresponding to the case with no-control). However, when the control disk d2 was employed, V_{s_max} appeared to maintain its initial constant value until $\varepsilon > \approx 3.5$ was reached where a sudden increase was recorded. In contrast V_{s_max} registered for different co-rotation ratio using the control disk d3 showed a sudden drop from the initial value. These two opposite trends, for d2 and d3, are irregular and seem to be caused by the fact that beyond the rotation ratio $\varepsilon = 5.00$ for d2 the growth of the main breakdown bubble in the axial direction was such that it merged with the growing bottom bubble, hence leading to a complex flow regime.

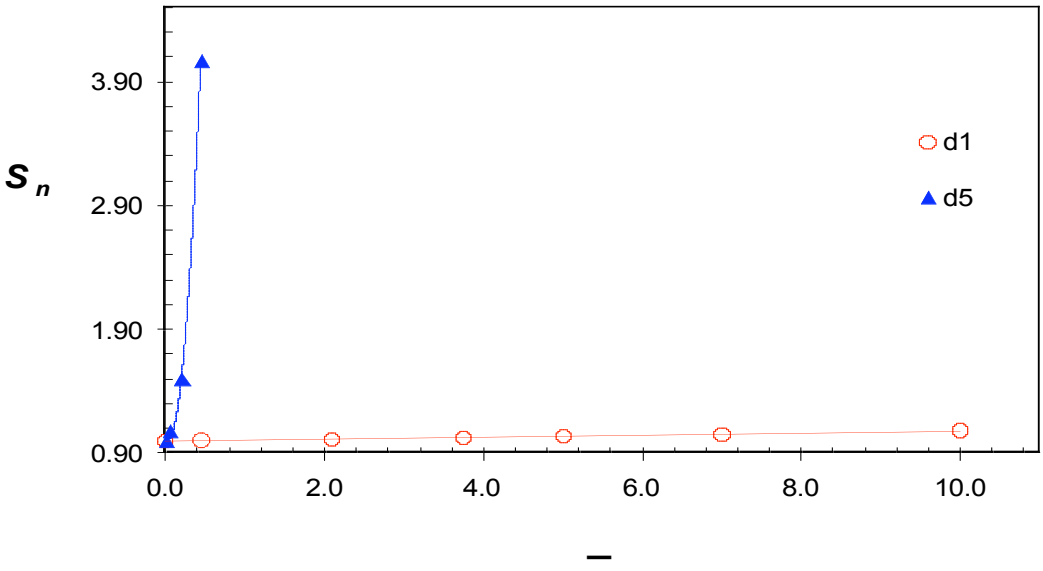

(a)

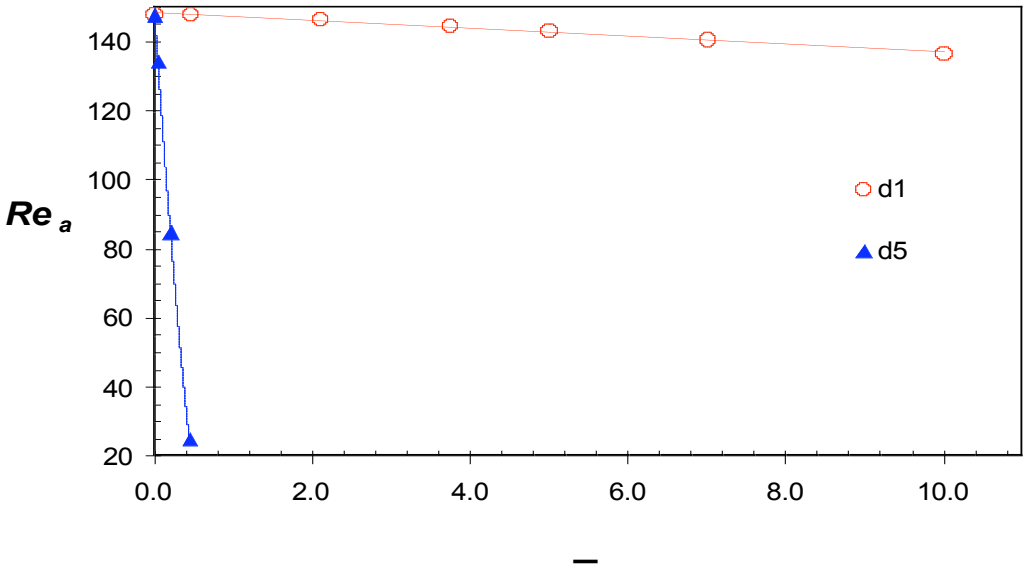

(b)

Figure 5.16 Variation of S_n (a) and Re_a (b) with co-rotation ratio using two control disks (d1 & d5).

In Figure 5.15, the variation of the swirl number with rotation ratio is presented for the same simulations as in Figures 5.13 and 5.14. One striking observation from the results is that in counter-rotation, the swirl number appears to assume almost a constant value close to the initial value S_n = 1.227 (for Re = 1660 without control). The constant value maintained for most of the counter-rotation ratios was noted to be only 5% lower than the initial value and did not seem to be affected by the size of the control disk (in this case d2 and d3). However, in co-rotation the swirl number was significantly affected by both the size of the control disk and the rotation ratio. Co-rotation with the smaller disk d1 registered only minor increases in S_n values over a wider range of rotation ratios; but d2 and d3 caused considerable growth in the value of S_n over smaller ranges of the rotation ratio. This could be mainly attributed to the considerable drop in the values of maximum axial velocity noted from increased co-rotation ratios (Figure 5. 13).

Perhaps the best way to assess the effect of co-rotation on vortex breakdown is to start with the rotating endwall rotating just fast enough to generate vortex breakdown onset. Then, by co-rotating the control disk, the resulting vortex breakdown is the strongest evidence of the enhancing effect. Having performed such experiments and shown the results in Figure 5.11 it is now convenient to present the effect of co-rotation on the swirl number and the axial Reynolds number.

Figures 5.16(a) and (b) depict the relationship between the swirl number and the axial Reynolds number, on the one hand, and the co-rotation ratio, on the other hand. Two control disks were tested: the smallest of the five disks was d1 and the largest was d5. When the largest disk d5 was used a sharp increase in the in the value of S_n was noted; at the same time a marked decrease in the value of Re_a also was recorded. As expected, when the smaller disk d1 co-rotated only marginal rates of increment and decline in the values S_n and Re_a respectively were observed.

(iii) Stagnation Points

The effects of co- and counter rotation and the control disk size on the vortex breakdown bubble are further examined by looking at the stagnation points along the swirl axis. In this way it is possible to determine the axial extent of the resulting breakdown bubble and also its location along the axis. To do so, profiles of axial

velocity along the axis of rotation are presented for three different control disks, d1, d2 and d3.

In Figure 5.17, only the lower part (about 42% of H) of the swirl axis is considered for the obvious reason that the small control disk d1 has only a minor effect on the flow structure even at high rotation ratios. Therefore, to clearly bring out differences in the V_{a_max} due to changes in rotation ratio, magnified plots of the region of interest along the axis are displayed in Figure 5.17. Despite a considerable increase in rotation ratio from ε = 0.92 to 8.00, the size of the initial breakdown bubble generated at Re = 1660 (without control) increased in the axial direction by only about 24%. In addition, the upstream stagnation point barely shifts towards the control disk by only about 8% of the cylinder height (H). By increasing the co-rotation ratio to ε = 2.32, a small bottom bubble appears above the control disk. This bottom bubble develops as the rotation ratio is increased further.

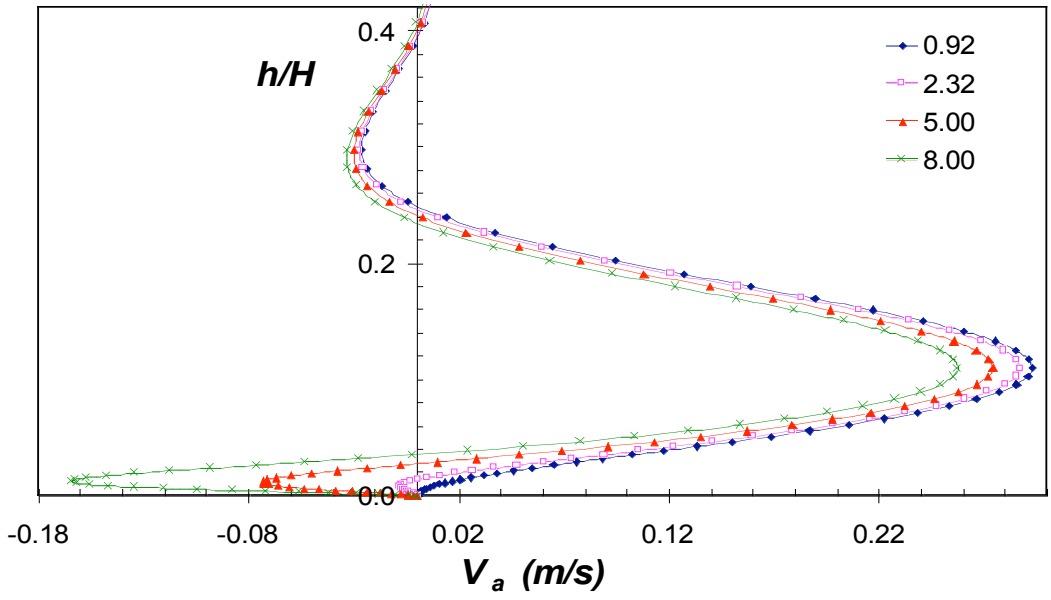

Figure 5.17 Axial velocity profiles along the swirl axis for co-rotation using the control disk d1: ε = 0.92; 2.32; 5.00 and 8.00. The initial flow was generated at Re = 1660.

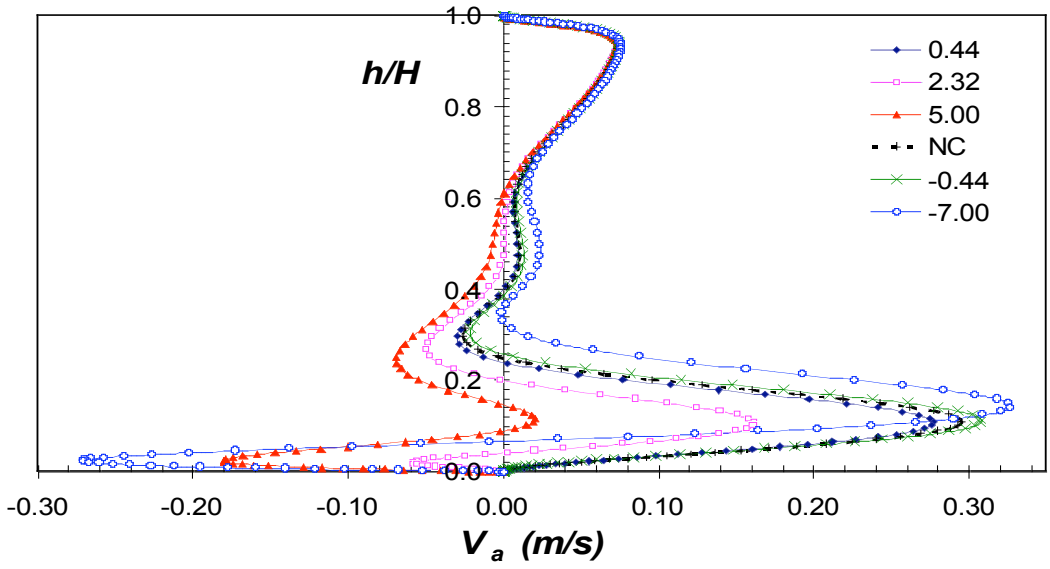

Figure 5.18 Axial velocity profiles along the swirl axis. Vortex breakdown is controlled using d2. Co-rotation: ε *= 0.44; 2.32; 5.00 and counter-rotation:* ε *= -0.44 and -7.00. The initial flow was generated at Re = 1660 (NC means without control).*

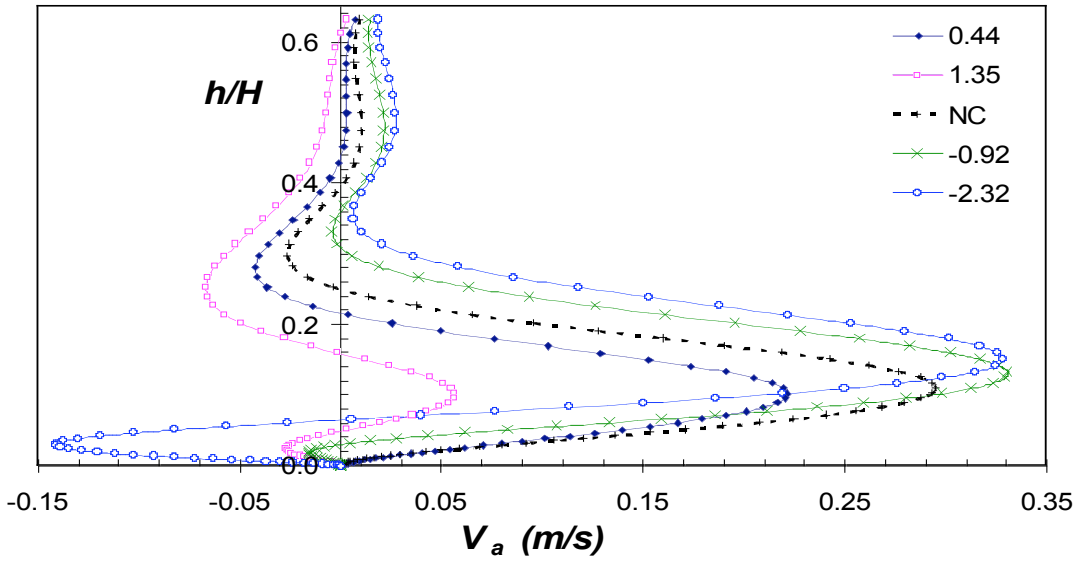

Figure 5.19 Axial velocity profiles along the swirl axis. Vortex breakdown is controlled using d3. Co-rotation: ε *= 0.44; 1.35 and counter-rotation:* ε *= -0.92 and -2.32. The initial flow was generated at Re = 1660 (NC means without control).*

Figure 5.18 illustrates the axial velocity profiles along the axis of rotation for the control disk d2 with the initial flow at *Re* = 1660 without control. The results show co-rotation cases (ε = 0.44, 2.32 & 5.00); no-control case and counter-rotation cases (ε = -0.44 & -7.00). The most obvious effect of co-rotation is the observed increase in the breakdown bubble size coupled with a tendency to shift it upstream. However, counter-rotation is seen to reduce the axial dimension of the breakdown bubble, at the same time dragging it in the downstream direction (i.e. closer to the rotating endwall). To quantify the effect of co-rotation using d2, an increase in the rotation ratio from ε = 0.00 (no-control) to 5.00 increases the size of the bubble by more than 2.5 times. Counter-rotation at the rate of ε = -7.00 results in almost complete suppression of the breakdown bubble.

As the size of the control disk increases from d2 to d3, the effects of co- and counter-rotation on the breakdown bubble becomes so pronounced that only smaller rotation ratios suffice to reveal resulting changes (Figure 5.19). The net results of co- and counter-rotation on the breakdown bubble remain the same as described above (for d2). In Figure 5.19, only about 62% of the swirl axis is considered, again for the sake of clarity. Using d3 as the control disk with a rotation ratio of only ε = 1.35 the axial dimension of the breakdown bubble is observed to increase threefold. In counter-rotation, a rotation ratio of ε = -2.32 results in complete suppression of the breakdown bubble. From the above data, it is very evident that co-rotation using a relatively small control disk is an effective way to enhance vortex breakdown, while counter-rotation effectively suppresses the main vortex breakdown.

(iv) Bottom Bubble Formation

Results from the investigation with a rotating control disk have revealed that there is a rotation ratio above which the bottom breakdown bubble appears on the active surface of the disk. Such findings for the case where *Re* = 1660 have been summarised in Table 5.2. The results show that the size of the control disk as well as the direction of rotation (co- or counter-rotation) do influence the formation of the bottom bubble. It follows that the larger the control disk size the lower the rotation ratio for which the bottom bubble appears. Furthermore, counter-rotation of the control disk appears to precipitate the formation of the bottom bubble.

Table 5.2 Rotation ratio values for which the bottom bubble forms on the active surface of the control disk when the rotating endwall has a Re = 1660.

d#	Co-rotation	Counter-rotation
d1	1.80	1.63
d2	1.35	0.92
d3	1.15	0.65
d4	0.92	0.60
d5	0.67	0.45

5.3.2 Rotation of Both Endwalls

The rotation of the second endwall, in this case the bottom endwall, is another possibility to control vortex breakdown in a closed cylinder. The merits of this technique, especially in terms of power required to achieve a preset goal compared to the use of a small control disk, will be discussed in chapter 6. Numerical predictions of the flow generated inside the cylinder using this method are presented next.

(i) Flow Visualization

Streamlines of flow visualization inside the cylinder driven by the rotation of the top endwall at *Re* = 1440 coupled with co-rotation of the bottom endwall are given in Figures 5.20(a-c), and at *Re* = 1660 with counter-rotation in Figures 5.20(e & f). Figure 5.20(d) represents the case where *Re* = 1660 without control.

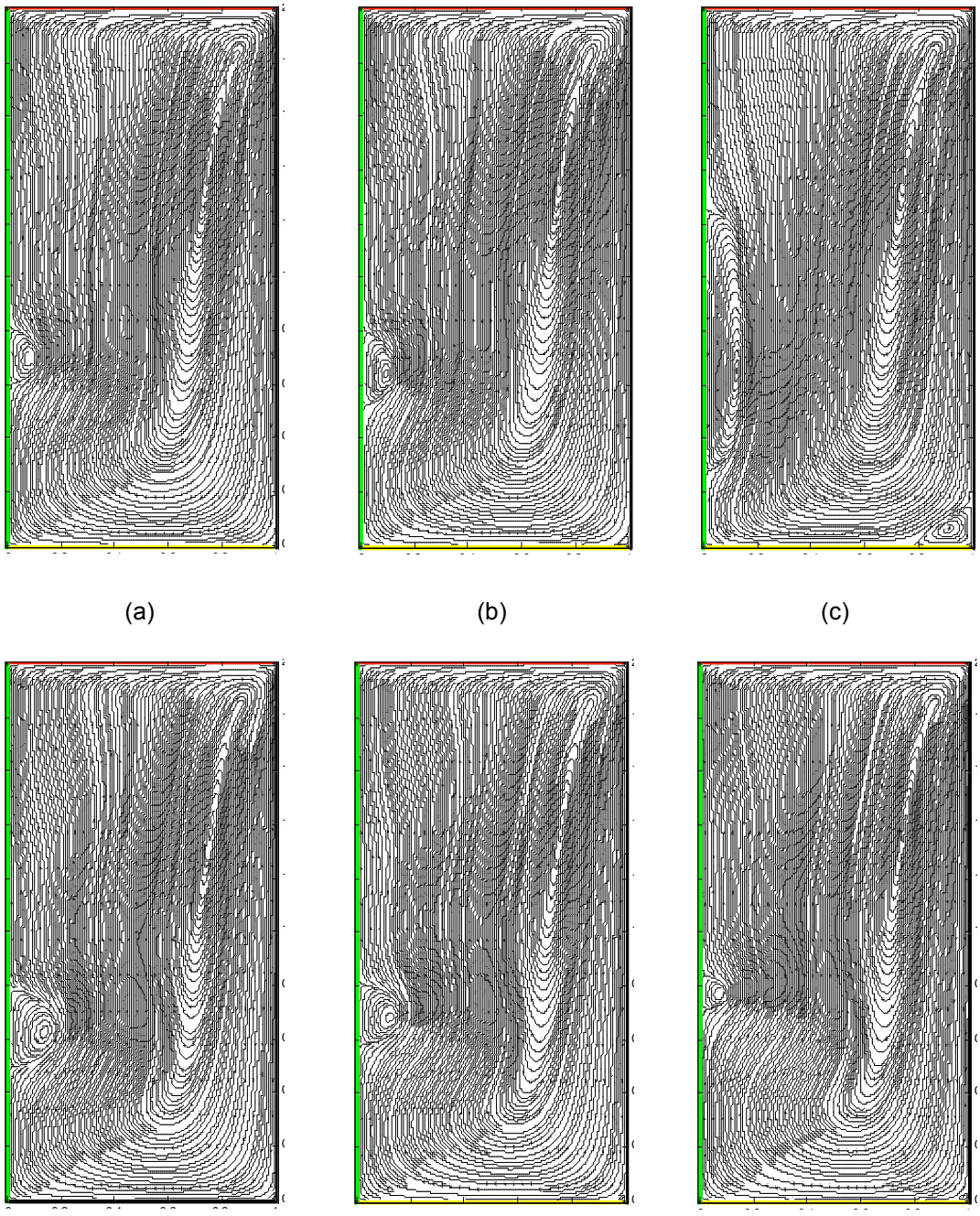

Figure 5.20 Flow visualization using streamlines. The bottom endwall is employed to control vortex breakdown; Re = 1440, co-rotation (a) ε *= 0.01, (b)* ε *= 0.02, (c)* ε *= 0.10; Re = 1660, (d)* ε *= 0.00, counter-rotation (e)* ε *= -0.01, (f)* ε *= -0.02.*

Co-rotation and counter-rotation cases in Figure 5.20 illustrate the immense capability of the bottom endwall as a control tool for the breakdown bubble. The results show that even slight co-rotation and counter-rotation can cause substantial geometrical changes to the vortex breakdown bubble. A rough estimate reveals that co-rotation ratios ε = 0.01, 0.02 and 0.10 induce the growth of the breakdown bubble from its smallest size at the onset (Re = 1440) to a fairly sizeable bubble at ε = 0.01, and to almost double this size (surface area) at ε = 0.02 and about eight times the size at ε = 0.1. The growth of the breakdown bubble seems to be proportional to the increase in the rotation ratio. For counter-rotation, the bubble generated by the top endwall rotation corresponding to Re = 1660 is approximately reduced to 70% when ε = -0.01 and further reduced to about 25% when ε = -0.02. Such reductions are significant considering that only slightly counter-rotations were implemented.

(ii) Upstream Flow Characteristics

Figure 5.21 shows the variation of the swirl number with changes in the rotation ratio between the two endwalls. For co-rotation, three global Reynolds numbers (Re = 1350, 1440 and 1660) were tested whereas for counter-rotation only Re = 1660 was examined. The results suggest that there is a direct correlation between the global Reynolds number and the swirl number. It can be observed in Figure 5.21 (a) that the S_n is always higher across the co-rotation ratio range when the value of Re is raised. Also, it is shown that for co-rotation the S_n increased with corresponding rise in the rotation ratio. However, increases in the values of the rotation ratio resulted in reductions of the swirl number when in counter-rotation mode. The behaviour of the axial Reynolds number is shown to be the exact opposite to that of the swirl number variation with respect to both the rotation ratio and the global Reynolds number. Figure 5.21(b) shows a progressive reduction of the Re_a as the co-rotation ratio increased while the opposite trend is noted for counter-rotation ratio. Furthermore, higher global Reynolds numbers are seen to yield lower values of the Re_a.

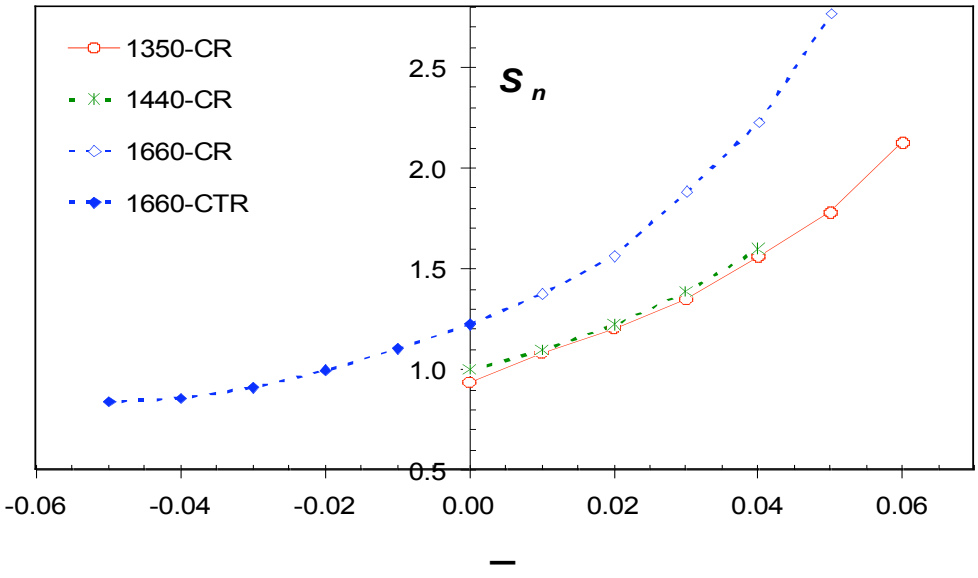

(a)

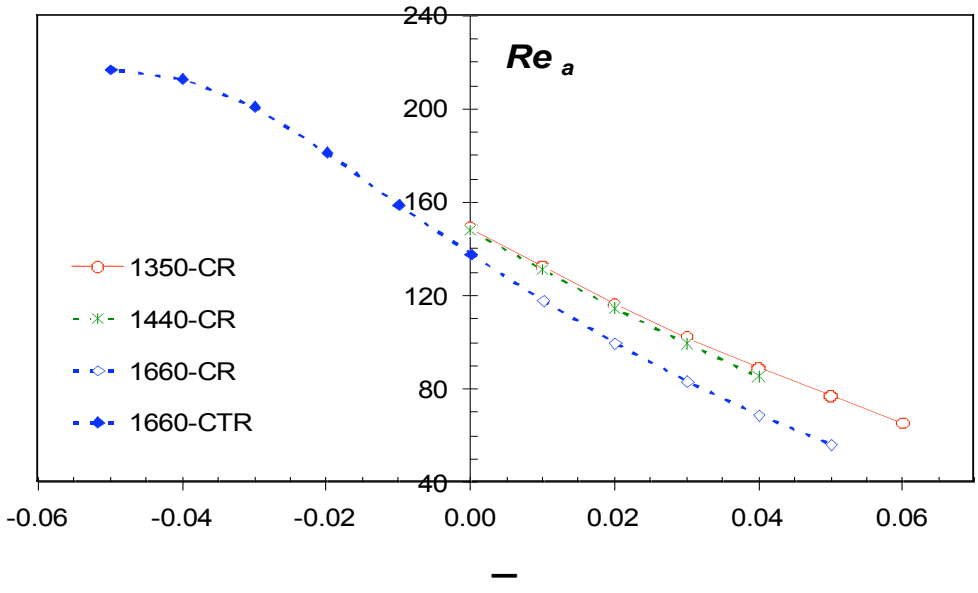

(b)

Figure 5.21 Variation of (a) swirl number and (b) axial Reynolds number with rotation ratio. The bottom endwall was used to control vortex breakdown: for co-rotation Re = 1350, 1440 & 1660 while counter-rotation Re = 1660.

(iii) Stagnation Points

In Figure 5.22, axial velocity profiles along the swirl axis are shown. These profiles are for flows generated by the top endwall rotation with *Re* = 1440, and co-rotation ratios of ε = 0.01, 0.05 and 0.10. The profile for the case without control (NC) is included to provide the basis for comparison, and therefore to assess the effectiveness of the control technique. A close examination of the results reveals that increasing the rate of co-rotation of the bottom endwall, even slightly, significantly enhances the breakdown bubble size in the axial direction as shown by the widening distance between the upstream and downstream stagnation points. The breakdown bubbles generated by co-rotation tend to move slightly in the upstream direction.

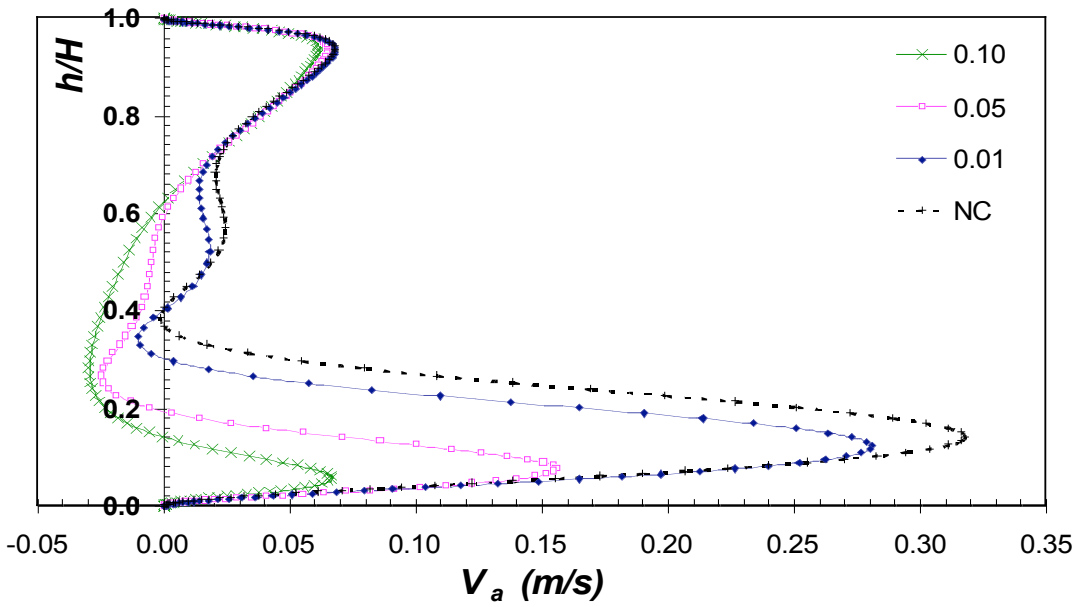

Figure 5.22 Axial velocity profiles along the swirl axis for vortex breakdown control using both endwalls with Re = 1440. NC is for the case without control and for co-rotation ε = 0.01, 0.05 & 0.10.

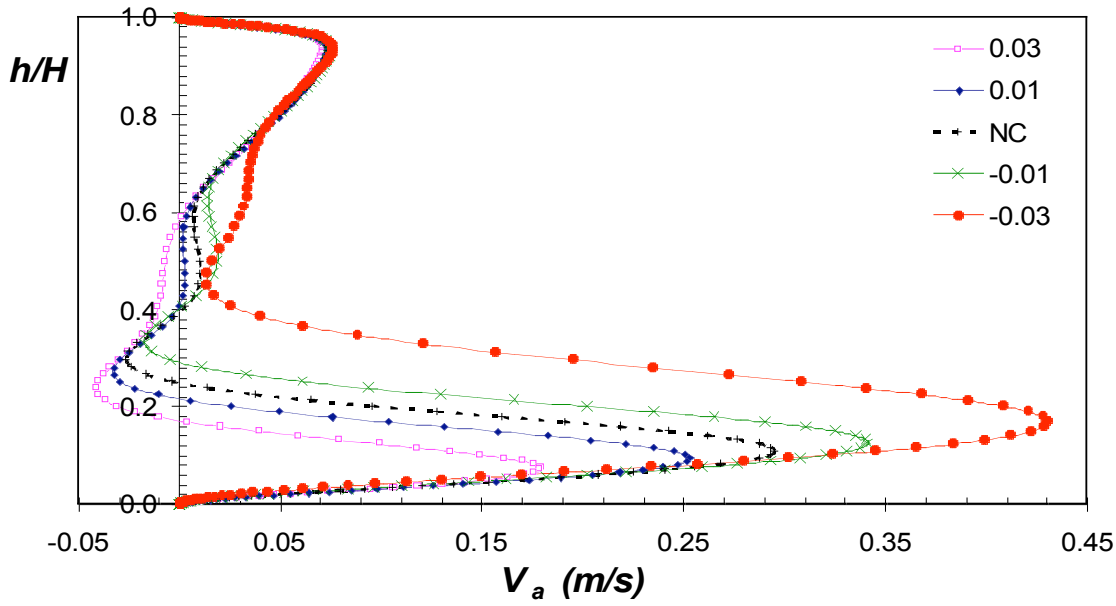

Figure 5.23 Axial velocity profiles along the swirl axis for vortex breakdown control using both endwalls with Re = 1660. NC is for the case without control and for co-rotation ε = 0.01 & 0.03 while for counter-rotation ε = -0.01 & -0.03.

A better assessment of the effect of co- and counter-rotation on the vortex breakdown bubble is carried out by examining the results shown in Figure 5.23. Here, the top endwall was spun so that *Re* = 1660, and the bottom endwall was co-rotated at ε = 0.01and 0.03 and counter-rotated at ε = -0.01 and -0.03. The net effect of co- and counter-rotating the bottom endwall on the vortex breakdown bubble is essentially the same as discussed in the cases involving small control disks. That effect is to enhance the bubble when in co-rotation and to suppress it when in counter-rotation. However, the main difference between the two systems is that for the bottom endwall rotation only slight rotation ratios are needed to achieve similar results. Perhaps what is more important is to assess the effectiveness of the two systems by evaluating the relative viscous power needed to perform the above tasks. This is the subject of investigation in the next section.

5.4 Viscous Power

The results in this last section of the chapter focus on determining the relative viscous power required to produce, enhance and suppress the vortex breakdown bubble. The viscous power being discuss here is effectively the input power to the fluid. This power is computed from the shear stress generated by the rotation of the endwalls and the control disks. Here, a comparative study of the effectiveness of each of the control disks is presented. The relative viscous power due to the rotation of the bottom endwall is also given. To the best knowledge of this author, a detailed power study such as is described in this section has not been presented by previous researchers.

5.4.1 Top Endwall Power

The variation of the relative viscous power expended by the rotation of the top endwall with the Reynolds number is shown in Figure 5.24. Here, there is no additional contribution of either the control disks or the bottom endwall,. This power denoted by P^* is normalised by the viscous power expended by the top endwall to just cause vortex breakdown onset (P_{vbo}). This normalising power (P_{vbo}) is computed at Re = 1440, which is the critical Reynolds number for the case where the top endwall rotates without any control. The results from Figure 5.24 clearly show, as expected, a direct correlation between the relative power P^* and the Reynolds number. However, this relationship is not linear as the rate of change of P^* with Re appears to increase as the Reynolds number rises.

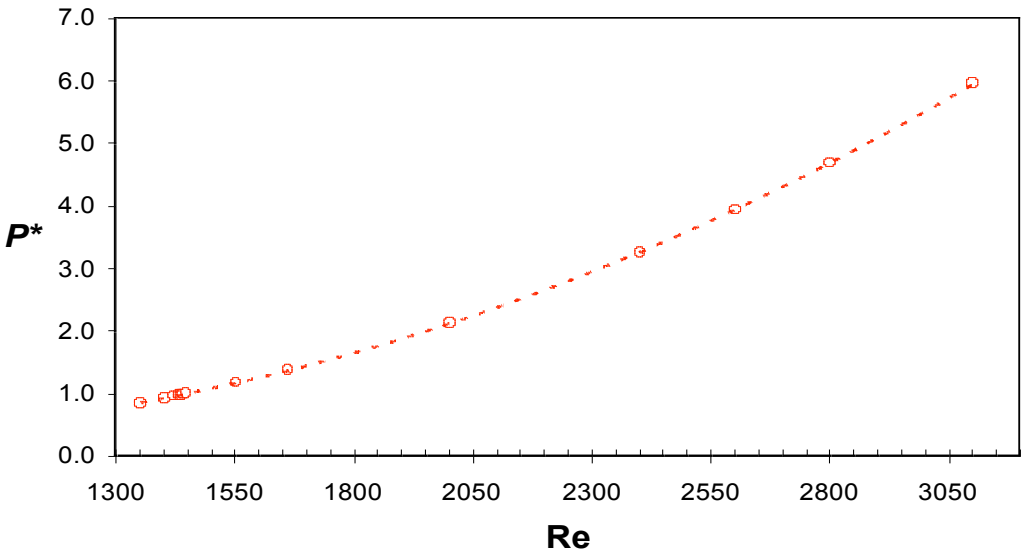

Figure 5.24 Relative viscous power as a function of Reynolds number. The shearing power is for the top endwall rotating without control.

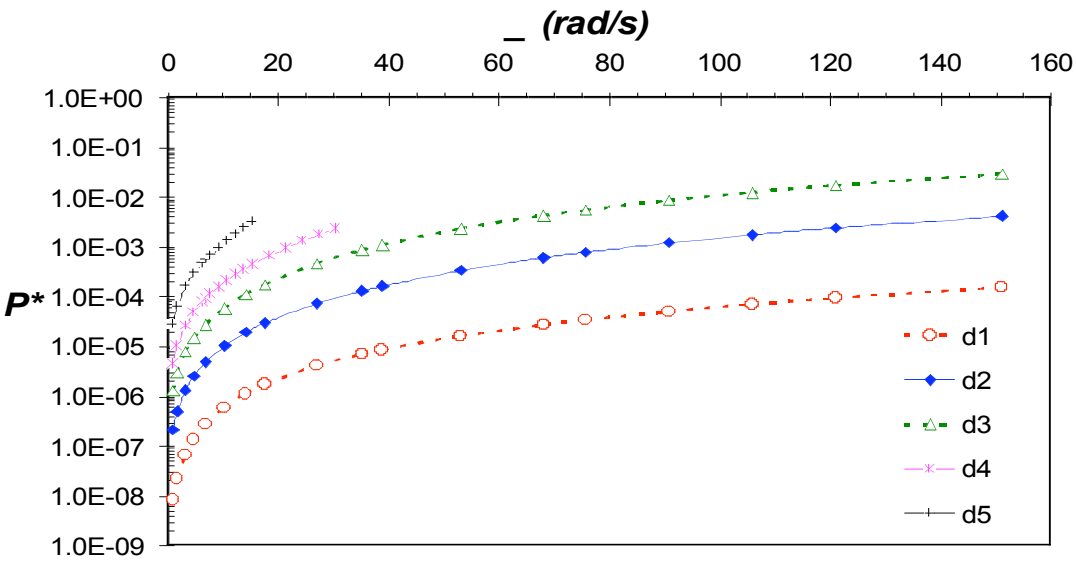

Figure 5.25 Relative viscous power as a function of rotation ratio. The relative shearing power curve for each of the five experimental control disks is plotted on a logarithmic scale.

5.4.2 Control Disk Power

Figure 5.25 illustrates the relationship between the relative viscous power and the rotation rate at which the different control disks were spun. The relative power is plotted on a logarithmic scale to accommodate the values for all the control disks as they were significantly disproportionate by up to four orders of magnitude. One general observation from the results is that the amount of power required to spin the control disks is far less than the power required to cause the vortex breakdown onset to occur (P_{vbo}). A close look at the actual data used to plot Figure 5.25 reveals that with all the control disks rotating at $\Omega \approx 10$ rad/s, for instance, the relative viscous power expended by the control disk d2 was found to be two orders of magnitude higher than that required for d1. Similarly, the viscous powers associated with d3 and d4 were estimated to be three orders of magnitude larger than that for d1, while the power for d5 was four orders of magnitude higher. Furthermore, the corresponding relative power for the control disk d4 was found to be 3.5 times bigger than that for d3. On the whole, the results show that the relative viscous power responded more sensitively to changes at lower rotational speeds than at higher speeds. In section 5.4.4 as well as the next chapter (discussion) a more relevant comparison of these relative powers will be presented.

5.4.3 Bottom Endwall Power

The variation of the relative viscous power expended by the bottom endwall operating in both co-rotation and counter-rotation is shown in Figure 5.26. Three Reynolds numbers were tested in the co-rotation mode (Re = 1350, 1440 and 1660), whereas only Re = 1660 was used in the counter-rotation mode. From the results, it follows that the relative viscous power expended by the bottom endwall is also affected by the rotation rate of the top endwall. Figure 5.26 clearly demonstrates that the bottom endwall requires more power to overcome viscous resistance when the global Reynolds number increases. Also, the relative viscous power shows a definite correlation, both in co- and counter-rotation, with the rotation ratio between the angular velocities of the two endwalls.

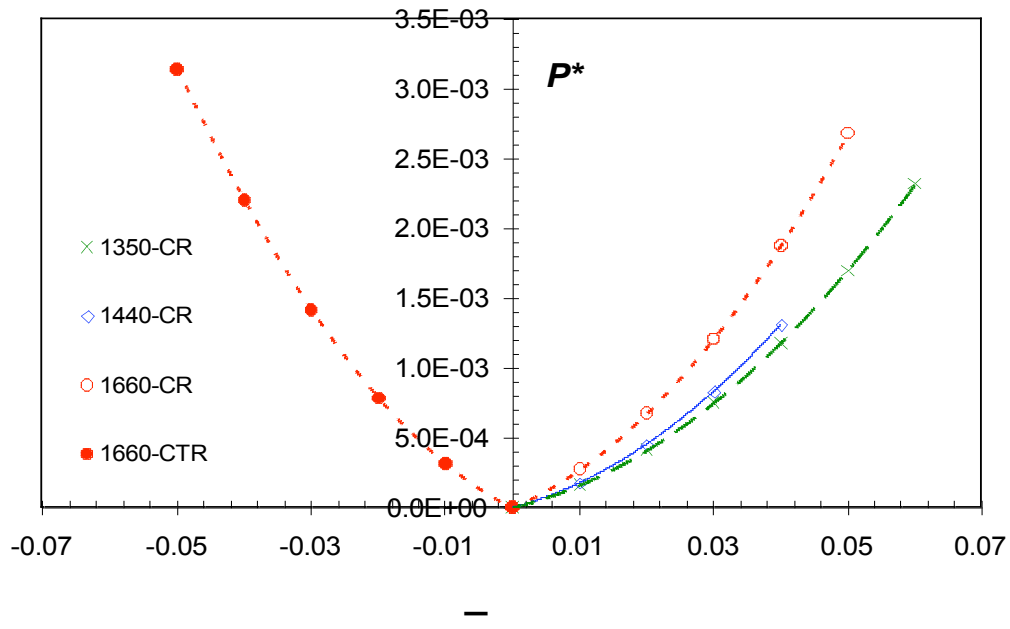

Figure 5.26 Relative viscous power as a function of rotation ratio for the case where vortex breakdown control is achieved by co- and counter-rotating both the top and bottom endwalls. For co-rotation Re = 1350, 1440 & 1660; for counter-rotation Re = 1660.

5.4.4 Comparison

More relevant power comparisons are carried out in the present section. Here, the objective is to quantify the effectiveness of the proposed method of controlling vortex breakdown compared with the conventional method of varying the rotational speed of the rotating endwall. In the conventional method the speed of the rotating endwall is generally increased (within reasonable limits) to enhance the size of the breakdown bubble, while speed reduction is used to achieve size reduction or suppression. In the current method, however, to enhance the breakdown bubble a control disk is co-rotated with respect to the rotating endwall; and to reduce the bubble size it is counter-rotated. It therefore follows that for the comparisons to be more meaningful, they have to take into account the similarity of the final results and also ensure that the initial conditions are identical. Only then can the corresponding viscous power levels spent to achieve those results be sensibly assessed.

(i) Power for Co-rotation

Table 5.3 displays data for the relative viscous power expended to enlarge the vortex breakdown bubble originally generated at the onset, when only the top endwall was rotating at Re = 1440 without employing any control methods. This means that the onset breakdown bubble is the starting point for all cases shown in the table. For the case without control the speed of the rotating endwall was increased such that Re = 1550, and the generated breakdown bubble was taken as the final result. The viscous power required to develop the vortex breakdown onset bubble (P_{vbo}), and that required to generate a breakdown bubble at Re = 1550 were separately computed.

For the other cases involving the co-rotation of control disks (d2 through to d5) and the bottom endwall (db), the starting point was the same as described for the case with no-control. However, the final result here was achieved by co-rotating the control disks and the bottom endwall such that the resulting breakdown bubble was approximately the same size (to within ±5%) as that for Re = 1550 (without control). The rotation ratio required to achieve the above final result using the control disk d1 was higher than the maximum speed of the experimental drive unit. That explains why the data for d1 are not shown in Table 5.3. The viscous powers spent to enlarge the onset breakdown bubble using each of the four control disks and the bottom endwall were then computed separately.

The above viscous powers were normalised by P_{vbo}, to obtain the "relative viscous power" P^*. The data in the second last column of Table 5.3 were also normalised by the difference between the relative viscous powers (P^*) at Re = 1550 and Re = 1440 for the cases without control (see the first column third data line, ΔNC). The second normalisation produced the ratios shown in the last column. This relative viscous power used for normalising is effectively what is required to enlarge the breakdown bubble from the onset size to the one at Re = 1550 without using control; the corresponding powers (P^*) for the cases involving co-rotation are displayed in the second last column.

From the results, it is clear that the use of control disks and also the bottom endwall to enhance the breakdown bubble is by far more power effective than the conventional technique of increasing the speed of the rotating endwall. It can also be seen that the

control disk d4 was the best performer in co-rotation.

Table 5.3 Relative viscous power expended to enlarge the vortex breakdown bubble from it size at the onset (Re = 1440 with no-control) to the size corresponding to Re = 1550 (with no-control, NC). The shearing power spent to enlarge the onset breakdown bubble using co-rotation (CR) of four control disks (d2 through to d5) and the bottom endwall (db) is also computed and compared with the above power for the cases without control.

	CR/NC	**Re**	ε	P^*	$\frac{P^*}{(P^*)_{\Delta NC}}$
NC	NC	1440	-	1.00E+00	-
NC	NC	1550	-	1.18E+00	-
ΔNC	NC	-	-	1.85E-01	1.00E+00
d2	CR	1440	2.09	7.62E-05	4.12E-04
d3	CR	1440	0.46	1.85E-05	1.00E-04
d4	CR	1440	0.20	1.48E-05	7.98E-05
d5	CR	1440	0.07	2.36E-05	1.27E-04
db	CR	1440	0.01	1.80E-04	9.75E-04

(ii) Power for Counter-rotation

In the case of counter-rotation, the viscous power was defined as the minimum power expended by counter-rotating the control disks and the bottom endwall to overcome shear resistance so as to be able to *just destroy* the breakdown bubble originally generated by the rotation of only the top endwall at *Re* = 1660. Here, as in the co-rotation case above, there is a common starting point, which is the breakdown bubble corresponding to *Re* = 1660 (for the case without control). The final result was the first indication of complete suppression of the breakdown bubble. The computed viscous powers corresponding to the control disks and the bottom endwall were normalised by P_{vbo} to yield the relative viscous power (P_{nv}^*), as in the case of co-rotation.

Table 5.4 Relative power expended to completely suppress a vortex breakdown bubble generated at Re = 1660 without any control. Suppression is achieved by counter-rotating control disks (d2 through to d5) and the bottom endwall (db).

d#	$\left(\frac{d}{D}\right)\times 100\%$	ε	$P_{nv}^{\ *}$	$\frac{\left(P_{nv}^{\ *}\right)_{d\#}}{\left(P_{nv}^{\ *}\right)_{db}}$
d2	10.1	8.00	0.00251	4.84
d3	15.2	1.78	0.00048	0.92
d4	20.2	0.40	0.000080	0.15
d5	30.7	0.10	0.000067	0.13
db	100.0	0.025	0.00053	1.00

The relative viscous powers are shown in the second last column of Table 5.4. A further normalisation is achieved by dividing the individual relative viscous powers by that for the bottom endwall (see the last column). From these results, it can be deduced that the control disks d4 and d5 are the most power efficient in counter-rotation as they require about one-seventh of the power of the bottom endwall to just destroy the vortex breakdown generated by the rotation of only the top endwall at Re = 1660. The control disks d3 and d2 were found to be about six and thirty five times more power demanding, respectively, than both d4 and d5.

5.5 Summary

In this chapter, results from numerical simulations of vortex breakdown in a closed cylinder with a rotating top endwall, control disks and a bottom endwall have been presented. These results were presented in three separate parts, namely: vortex breakdown without control, vortex breakdown control and viscous power.

The section on vortex breakdown without control was concerned with the flow generated by the rotation of either the top endwall or the control disks acting individually. In the case involving the top endwall rotation, flow visualization results

have shown good agreement with previously published experimental data, especially the classic results of Escudier (1984), and also this work's experimental results described in chapter 4.

It has also been established that the swirl number varies along the axis of rotation and that the minimum value is found to occur at the same axial location as the maximum axial velocity. This minimum swirl number is the critical value that was simply referred to as the swirl number. In the case where only the top endwall was rotating, it has been found that a necessary condition for the onset of vortex breakdown is that the swirl number has to be equal to *unity* (i.e. $S_n = 1$).

Also, for the case of no-control with top endwall rotation, the maximum swirl velocity corresponding to the minimum axial velocity was found to be always higher than that for the maximum axial velocity along the swirl axis.

When only the control disk was rotated, the meridional plane circulation loop was always counter-clockwise in the right-hand half of the cylinder. In addition, the axial velocity near the swirl axis was always in the upstream direction, which is opposite to the axial flow resulting from the top endwall rotation.

It was found that co-rotating a control disk significantly enhances the breakdown bubble, while counter-rotation tends to suppress it. Furthermore, co-rotation was observed to shift the breakdown bubble in the upstream direction whereas counter-rotation caused the bubble to migrate in the opposite direction.

Co-rotation of a control disk caused a considerable reduction of the maximum axial velocity in the upstream region of the axis; but counter-rotation had the opposite effect. Moreover, in co-rotation the swirl number was significantly affected by both the size and direction of rotation of the control disk. Larger control disk sizes and higher co-rotation ratios were observed to be responsible for increases in the swirl number. However, in counter-rotation the swirl number was noted to be almost constant; slightly lower by about 5% than its initial value of 1.227 (for $Re = 1660$ without control).

From the above data, it is evident that co-rotation using a relatively small control disk is a very effective way to enhance vortex breakdown, while counter-rotation effectively

suppresses the main vortex breakdown.

The results have shown that the size of the control disk as well as the direction of rotation (co- or counter-rotation) influence the formation of the bottom bubble. It follows that as the size of the control disk grows, the rotation ratio for which the bottom bubble forms becomes lower. Also, counter-rotation tends to precipitate the formation of the bottom bubble.

It has been shown that with increasing rotation ratios, the main vortex breakdown bubble grows bigger until it merges with the bottom bubble (above the control disk) giving rise to a very complex flow.

The new method of controlling vortex breakdown, presented in this thesis, was extended to simulate control using the bottom endwall in both co- and counter-rotation to enable a more extensive investigation.

The use of the bottom endwall as a control tool has shown that it is possible to achieve vortex breakdown enhancement and suppression by applying *slight* co-rotation and slow counter-rotation respectively. Encouraging results have been recorded using the rotation of both endwalls; typically, starting with a bubble generated at Re = 1660, slow counter-rotation at ε = -0.01 caused a 30% size reduction (in terms of area covered by the bubble), and ε = -0.02 caused a 75% reduction.

For co-rotation, the swirl number S_n was observed to increase as the ε and the global Reynolds number increased but for counter-rotation the S_n decreased only marginally as the ε increased. As the counter-rotation ratio increased further, the S_n was almost constant with values approaching about 0.84. However, the axial Reynolds number Re_a behaved in the opposite manner compared to the S_n.

The input power required to overcome viscous resistance when rotating a small control disk has been found to be considerably smaller, by orders of magnitude, than the power required to produce the vortex breakdown onset (P_{vbo}). Furthermore, the viscous power required to control vortex breakdown using the bottom endwall was noted to increase as the global Reynolds number rose.

In general, it was noted that the use of control disks and also the bottom endwall was more power efficient, both in enhancing and suppressing the breakdown bubble than the conventional method (varying the rotating endwall speed). For co-rotation the control disk d4 was found to be the most efficient, whereas for counter-rotation d5 was the best performer.

Chapter 6
Discussion and Conclusions

The results of experiments and numerical investigations have been presented in chapters 4 and 5. This chapter is devoted to the discussion of those results. The discussion is structured in three main parts: (i) vortex breakdown without control, (ii) vortex breakdown with control and (iii) viscous power. Each of the above parts ends with an outline of the conclusions drawn from the observed results and their discussion. Section 6.2 presents a discussion of the study on vortex breakdown without control. Here, the onset of vortex breakdown, the size of the breakdown bubble and its location are discussed. In section 6.3, the results of vortex breakdown with control are debated following an approach similar to the one described in section 6.2. In addition, the effects of control disks and the bottom endwall rotation on the breakdown bubble are investigated. In section 6.4, the discussion centres on the viscous power required to rotate the two endwalls and the control disks. The last part of the chapter presents a number of suggestions to guide future researchers in their pursuit for answers to some of the issues still unresolved.

6.1 Introduction

As mentioned earlier, vortex breakdown investigations were conducted experimentally and numerically. The underlying goals for conducting such a twofold study were:

- To present a more detailed investigation of the vortex breakdown in a closed cylinder with only the top endwall rotating and
- To test the effectiveness of a new method of controlling vortex breakdown.

The experimental data were also used to validate the accuracy of numerical predictions. Moreover, there were a number of issues that could not be investigated experimentally, partly due to limitations in the experimental facility that was available. Therefore, it was appropriate to complement these experimental results with carefully selected numerical predictions.

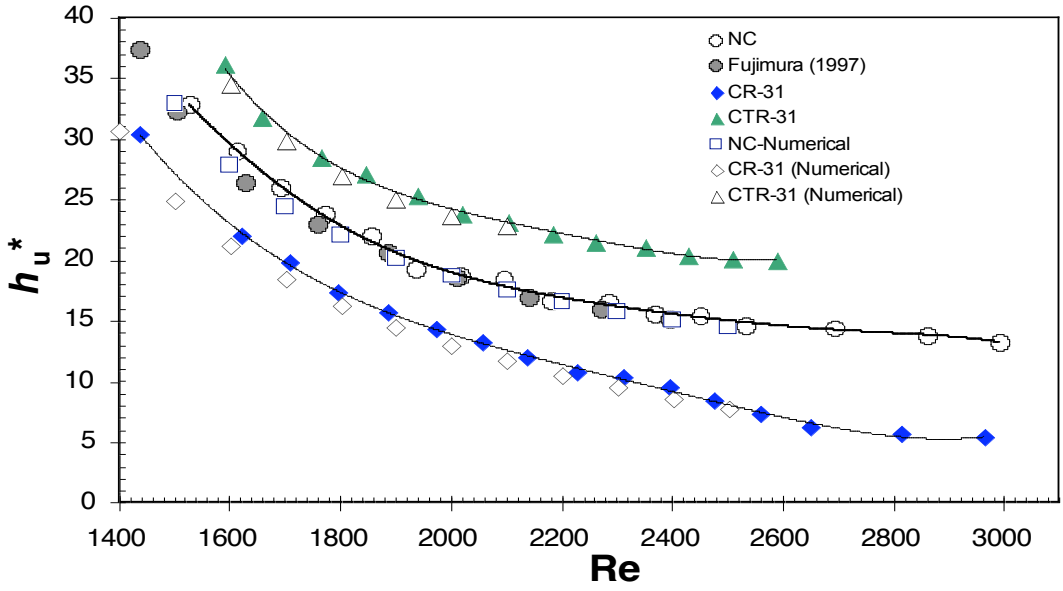

Figure 6.1 Variation of the normalised upstream stagnation height with Reynolds number. Currents results are compared with those of Fujimura et al. (1997) for the no-control (NC) case, experimental results for the co- and counter-rotation cases at Re_r = 31 are compared with numerical predictions. The control disk used here was d3.

Figure 6.1 consists of the current numerical and experimental results and the experimental data of Fujimura *et al.* (1997) for the case without control. The current results show the data for the case without control as well as some cases with co- and counter-rotation corresponding to Re_r = 31. The results show the variation of the normalised height of the upstream stagnation point above the bottom endwall with Reynolds number (*Re*). The purpose of presenting these results is to demonstrate the general agreement between the above three sets of data. The predictions from numerical simulations appear to be in good agreement with both current experimental and Fujimura's data (see also Mununga *et al.* (2004a)). Such level of accuracy in the numerical results yielded some degree of confidence in the numerical methods employed.

6.2 Vortex Breakdown without Control

The results from experiments and numerical simulations for the case of vortex breakdown with only the top endwall rotating, as presented in this thesis, has consistently shown good qualitative agreement with previously published data. In particular, the current results compare favourably with the data of Escudier (1984) for an aspect ratio *H/R* = 2.0 as depicted in the parameter space of Reynolds number and aspect ratio (*H/R*) reproduced in chapter 3 (Figure 3.5). The evidence of such agreement is reflected by Figure 4.1 (experimental results) and Figure 5.1 (numerical results) when compared with the data of Figure 3.5 (Escudier's). Of particular importance is the onset of vortex breakdown which is observed to occur at *Re* = 1440. Both experimental and numerical results have confirmed that the onset of the breakdown occurs at about that critical Reynolds number, which is in general agreement with most previously published data. The onset of vortex breakdown is usually a very crucial and stringent test for both experimental and numerical results. It is therefore gratifying to note that the current work satisfied this important test.

Closer examination of the flow structure revealed that the breakdown bubble underwent some transformation as the rotating endwall was gradually made to rotate at increasing rates. One such transformation was the loss of symmetry which was clearly visible, especially in experimental results depicted in Figure 4.1 and in particular (d) and (e).

This loss of symmetry could be attributed to minor imperfections in the geometry of the experimental rig as demonstrated by Thompson and Hourigan (2003). However, for larger Reynolds numbers such as $Re > 2600$, flow unsteadiness could also contribute to the loss of symmetry observed in the flow structure.

6.2.1 Vortex Breakdown Onset

The determination of the onset of vortex breakdown is one of the tasks that underscore the advantage of using numerical simulations over physical experiments. In the case of experiments, the task of detecting the first occurrence of vortex breakdown is largely dependent on the experimentalist's skill. However, the use of CFD makes the process not only easier but also more accurate.

One of the most important numerical results in this study was the establishment of a necessary condition for the onset of vortex breakdown without control. The condition is for the swirl number to be unity (i.e. $S_n = 1$). This result is very important as it establishes a necessary condition for vortex breakdown to occur. The condition is to be tested at an upstream location where the axial velocity along the swirl axis is maximum, as described in chapter 5. This test is more straightforward compared with a similar test proposed by Nakamura and Uchida (1980). In their study they found that a necessary condition for vortex breakdown to occur was for a non-dimensional angular velocity to be one (1) (see Equation 2.6). The difficulty with their condition is that the angular velocity was based on a vortex core radius which was not clearly defined. Moreover, the swirl velocity in Equation 2.6 was determined based on the axial location corresponding to the same vortex core. Although the method of testing the onset of breakdown proposed in this study appears to be similar to the one suggested by Nakamura and Uchida, the two conditions are different in the way they define the non-dimensional parameter (refer to Equations 3.17 and 2.6). This condition for the onset of vortex breakdown can also be useful in experimental work; especially to reduce or eliminate the subjectivity involved in the process of detecting the first occurrence of vortex breakdown.

At the onset of vortex breakdown, the axial Reynolds number (Re_a) was observed to be about 148.4. As the speed of rotation of the top endwall increased, the Re_a was observed

to decrease; this trend was contrary to that exhibited by the S_n. These opposing trends can be explained by the fact that while the maximum swirl velocity (V_{s_max}) increases gradually as the Reynolds number increases, the maximum axial velocity (V_{a_max}) decreases. The S_n and Re_a are thought to be more relevant parameters to describe vortex breakdown than the global Reynolds number because they take into account velocities associated with the flow in the vortex core upstream of the vortex breakdown. Furthermore, the state of this upstream flow has been known to be critical to the formation of breakdown.

6.2.2 Main Bubble Radius

This study has shown that as the Reynolds number increases the flow inside a closed cylinder with a rotating top endwall undergoes structural changes leading to the formation of a vortex breakdown (at Re = 1440) along the axis of rotation. Further increases in the Re result in the growth of the breakdown bubble in the radial and axial directions (see section 6.2.3). The size of the main bubble (the lower one which appears first) reaches its peak just before the flow becomes unsteady (Re > 2600). Whether the shrinkage of the bubble in the radial direction can be attributed to the change of flow from steady to unsteady is debatable.

The above observations are in good agreement with the findings of other researchers (Liu *et al.* (2003a)). Escudier (1984) observed significant changes in the structure of the bubble, especially the radial size, as the Reynolds number was increased. He further noted that his findings about the size of the breakdown bubble conformed with the observations of Vogel (1968). All these studies and the present investigation have shown that the size of the breakdown bubble increases monotonically until it reaches its peak. As the Reynolds number continues to increase the bubble shrinks progressively until it disappears. The implication of such results is that for a particular cylinder size and aspect ratio one can realistically predict the size the breakdown bubble depending on the Reynolds number.

6.2.3 Main Bubble Stagnation Points

Determining the location of the two stagnation points (upstream and downstream) is a

task better performed numerically than experimentally. With experiments, it was easier to spot the upstream stagnation point while it was virtually impossible to locate the one downstream, especially after the appearance of the second breakdown bubble downstream of the first bubble. The main purpose in establishing the position of the stagnation points is to know the location of the breakdown bubble along the axis of rotation. As mentioned in section 5.2.1 (iv) the axial extent of the breakdown bubble was determined by locating the region of negative axial velocity along the axis of swirl (Figure 5.8). The actual size of the bubble in the axial direction was represented by the distance between the two corresponding stagnation points along the axis of rotation.

The data of Fujimura *et al.* (1997) for the height of the upstream stagnation point above the bottom endwall were found to be consistent with the current results as shown in Figure 4.3 & Figure 6.1 (see also Mununga *et al.* (2004b)). The general motion of the breakdown bubble was to migrate towards the non-rotating endwall (upstream) as the Reynolds number increased. The appearance of two additional stagnation points downstream was an indication of the second breakdown. The region characterised by the presence of two breakdown bubbles is $1850 < Re < 2270$ in accordance with the findings of Escudier (1984). As the Reynolds number continued to increase, i.e. $Re > 2270$, the second set of stagnation points disappear leaving only the main breakdown bubble seemingly open at the downstream end. Although Liu *et al.* (2001) suggested that the bubble was still closed, based on the presence of a downstream stagnation point. However, careful laboratory examination of the bubble at such Reynolds numbers tended to suggest that the bubble was in fact open at the downstream end.

As the Reynolds number kept increasing, the behaviour of the main bubble was characterised by the upstream movement of the downstream stagnation point at a much faster rate than the motion of the upstream stagnation point. Such a combined migration eventually led to the complete disappearance of the main bubble.

The above observations support the findings of Lugt and Haussling (1982) that the axial size of the breakdown bubble initially increases until it reaches a maximum and eventually shrinks. Vogel (1968) and Ronnenberg (1977) also came to the same conclusion. The shrinkage and eventual disappearance of the breakdown could be partly

attributed to the increasing adverse pressure gradient as the Reynolds number increased. The same increase in adverse pressure gradient is thought to be responsible for the upstream motion of the breakdown bubble as also suggested by Berger and Erlebacher (1995).

6.2.4 Flow Generated by Control Disks

The flow generated by the rotation of a control disk was investigated and the results are shown in Figures 5.9-10. It was observed that irrespective of the direction of rotation the circulation loops in the meridional plane generated by the rotation of the control disk was always counter-clockwise, in the right-hand half of the cylinder. Such meridional flow always gives rise to a downwards axial flow which would oppose the upward moving flow developed by the rotation of the top endwall (see section 6.3).

The meridional flow is generated by the Ekman pumping effect from the boundary layer, above the active surface control disk, which drives the fluid outwards. Upon reaching the vertical cylindrical wall the fluid motion is forced to move parallel to it. The vertical distance travelled by fluid depends on the size and the rate of rotation of the disk. It was observed that the larger the disk diameter the bigger the height of the active volume developed by the control disk. Upon reaching an axial velocity of zero or the top endwall, the centrifugal velocity of the fluid is greatly reduced giving rise to an increase in the radial pressure gradient. This radial pressure gradient is responsible for the radial fluid motion towards the swirl axis. To complete the cycle, the fluid is forced to move along the axis and return to the boundary layer next to the control disk.

Naturally, the azimuthal flow developed by the rotation of the control disk assumes the same direction of rotation as the disk. In section 6.3.2, the effect of the control disk rotation on the breakdown bubble is investigated.

6.2.5 Conclusions

The following are the main results and conclusions:

- Experimental results and numerical predictions presented in this thesis have shown general agreement with previously published data.

- A condition for the onset of vortex breakdown without control has been established. This condition is that the swirl number Sn should be equal to unity. This condition can also be useful to experimentalists as a way of confirming their data related to the onset of vortex breakdown.

- The size of the breakdown bubble increases with the Reynolds number. There is, however, a limit beyond which further increases in Re lead to size reduction and eventual disappearance of the breakdown bubble.

- The breakdown bubble migrates upstream, away from the rotating endwall as a result of increased Reynolds number.

- The flow generated by the small control disk develops an anticlockwise meridional plane circulation loop in the right-hand half of the cylinder. This circulation loop gives rise to an upstream axial flow near the axis of rotation.

6.3 Vortex Breakdown Control

Results from the study of vortex breakdown control were presented in sections 4.3.2, for experimental investigations, and 5.3, for numerical investigations. The main goal of these investigations was to determine the effects of the size, direction and rate of rotation of the control disk on the vortex breakdown bubble. The other aspects investigated were the onset of vortex breakdown and the formation of the bottom bubble above the control disk.

6.3.1 Vortex Breakdown Onset

Co-rotation of all the control disks tested in this study tended to precipitate the onset of vortex breakdown. However, counter-rotation delayed the onset of breakdown. Precipitating vortex breakdown onset means that the critical Reynolds number (Re_c) at which the first occurrence of a breakdown is observed is lower than the Re_c corresponding to vortex breakdown without control. Whereas, delaying implies that the

Re_c is higher than the no-control one (Mununga *et al.* (2004a)).

It was also established that there was a correlation between the size of the control disk and the critical Reynolds number. The larger the control disk size, the smaller the critical Reynolds number for co-rotation in contrast to higher Re_c for counter-rotation.

For counter-rotation, the implication of the above results is that in applications where vortex breakdown is detrimental, a large control disk can be employed to delay the occurrence of breakdown. Conversely, when vortex breakdown is desirable its onset can be accelerated by co-rotating a large control disk. However, care must be taken on both the size and the rotation ratios of the control disk to ensure that the desired results are achieved.

Table 6.1 Swirl number corresponding to "Vortex Breakdown Onset" from the flow structure generated at Re = 1350 and 1400 without any control. The onset is caused by co-rotating control disks (d3 and d5) and the bottom endwall (db).

d#	Re	ε	Sn
d3	1350	0.63	1.09
d5	1350	0.08	1.03
db	1350	0.017	1.03
d5	1400	0.03	1.00

Since a necessary condition for the onset of vortex breakdown without control was determined as $S_n = 1$, it became logical to find out if this condition was affected by the use of a control disk. Two control disks, d3 and d5, and the bottom endwall were tested for onset of vortex breakdown, starting with a flow generated by rotating the top

endwall at Re = 1350 and 1400 in turn. The results in Table 6.1 reveal that the condition for vortex breakdown onset was $S_n \approx 1$. Except for the case where d3 was co-rotated starting from a flow with Re = 1350 the swirl number was very close to the no-control value of unity. The identity of this breakdown onset condition, S_n being approximately unity, for both controlled and non-controlled flows represents one of the important findings from this study.

6.3.2 Effect of Control Disk Rotation

The focus of the discussion here will be to determine the effect of both the direction of rotation and the size of the control disk on the vortex breakdown.

(i) Direction of Rotation

Results from experiments and numerical simulations have all confirmed the following observations:

- Co-rotation of a control disk tends to increase the size of the breakdown bubble. Also, in co-rotation the upstream stagnation bubble tends to shift away from the rotating endwall. Figure 6.1 presents the migration of the upstream stagnation point. The effect of co-rotation is clearly reflected as the bubble shifts in the upstream direction.

- Counter-rotation of a control disk is conducive to reducing the size of the bubble, with a possibility of completely suppressing it when the rotation ratio is high enough. Furthermore, counter-rotation causes the upstream stagnation point to move downstream.

In addition, co-rotation resulted in axially stretched breakdown bubbles. This may be thought to be a consequence of the additional axial velocity generated by the control disk and directed upstream, opposing the main axial velocity due to the rotating endwall (see section 6.2.4). One would imagine that the axial flow due to the rotation of the top endwall was pulling the bubble upwards while the one due to the rotation of the control disk acted in the opposite direction, hence stretching the bubble in both directions. In

counter-rotation, although the additional axial flow was still in the same direction the bubble seemed to shrink in both the axial and radial directions. This shrinkage in counter-rotation may be due to the action of the azimuthal velocities acting in opposite direction (one due to the rotating endwall and the other due to the control disk). This reasoning is further supported by the fact that the swirl number in co-rotation tends to increase as the rotation ratio increases while in counter-rotation it appears to maintain a constant level. The same combined effects can explain the radial size increase for co-rotation and size decrease for counter-rotation.

(ii) Size of the Control Disk

The growth of the bubble radius and the rotation ratio were found to be linearly correlated when the smaller disk d2 was either co-rotated or counter-rotated (Figure 4.10). However, when the larger disk d3 was employed it was observed that the bubble radius experienced significant reduction rates, in counter-rotation, compared to the rate of increase it experienced in co-rotation. The counter-rotation result signifies that a larger control disk is more effective in suppressing the breakdown bubble than a smaller one. In co-rotation, the enhancing effects of the two control disks were almost similar. This perhaps is due to the fact that the two disks were almost the same size.

Figure 4.11 reveals that when the larger control disk (d3) is co-rotated, the upstream stagnation point experiences a considerable upstream shift. Similarly, in counter-rotation, the bubble upstream stagnation point appeared to significantly move downstream.

Co-rotation with the smaller disk d1 registered only minor increases in S_n values over a wider range of rotation ratios; however, d2 and d3 caused a significant growth in the value of S_n over smaller ranges of rotation ratio (Figure 5.16). This could be mainly attributed to the considerable drop in the values of maximum axial velocity noted from increased co-rotation ratios in the case of the control disk d3.

The axial dimension of the breakdown bubble was also observed to be considerably affected by increases in the size of the control disk. Effectively, the size of the control disk can only amplify, when increased, or attenuate, when decreased, the already known

effects of co-rotation and counter-rotation on the breakdown bubble.

6.3.3 Effect of Bottom Endwall Rotation

The use of the second endwall, the bottom endwall in this case, to control vortex breakdown was investigated only numerically since the experimental facility did not have provision for this kind of investigation. This method has been employed by other researchers in the past (Hyun (1985b); Roesner (1990); Valentine and Jahnke (1994); Bhattacharyya and Pal (1998)). Given the similarity between this method and the newly proposed method of this thesis (using a small control disk), it was decided to further explore the possibility of using the second end wall in both co-rotation and counter-rotation as a means to control vortex breakdown. The other objective for carrying out this investigation was to compute the viscous power required by the bottom endwall (section 6.4.2) and compare it with the corresponding power for the control disks (section 6.4.1). A comparison to establish the effectiveness of each of the above methods is presented in section 6.4.3.

Flow visualization results (Figure 2.20) clearly display the effectiveness of using the bottom endwall as a control tool for vortex breakdown. The results show that the vortex breakdown undergoes significant structural and dimensional changes as a result of only slight co-rotation and counter-rotation ratios of the bottom endwall. It is interesting to point out that for the same rotation ratio (from $|\varepsilon| = 0.01$ to 0.02), counter-rotation generated a bubble radial size reduction ratio of about 2.8 while co-rotation caused a size increase ratio of about 2.0. This shows that counter-rotation of the bottom endwall has slightly more impact on the bubble than co-rotation. The radial size changes observed on the breakdown bubbles were almost similar to the corresponding changes in the axial size.

In a similar study, Roesner (1990) observed that a slight co-rotation of the bottom endwall was favourable to the onset of vortex breakdown even though the Reynolds number of the top lid was slightly below the critical value where the first vortex breakdown bubble is normally expected. He further noted that when the Reynolds number was slightly above the critical value, a slow counter-rotation of the bottom

endwall caused the recirculation region along the axis to disappear. These findings are in agreement with the current numerical predictions. The findings of Roesner (1990) were in complete agreement with those of Bhattacharyya and Pal (1998) for a similar study, although the latter investigation was restricted to co-rotation. Corresponding investigations by Valentine and Jahnke (1994) and Okulov *et al.* (2004) also concluded that co-rotation of the two endwalls, rotating at the same speed, was conducive to vortex breakdown formation.

Another important result reported by Bhattacharyya and Pal (1998) was that the vortex breakdown bubble appeared near the faster moving endwall, which in their case was the bottom endwall. That finding contradicts the observations by this author. This study's observations were that slight co-rotation caused the bubble to move away from the faster rotating endwall, whereas slow counter-rotation tended to push the bubble closer to it. These observations are similar to the ones made in the case of a small control disk (section 6.3.2). Moreover, even in studies with only one endwall rotating, the breakdown bubble always tends to move away from the rotating endwall as the Reynolds number increases (Lugt and Haussling (1982); Escudier (1984); Fujimura and Koyama (2002); Mununga *et al.* (2004b)).

6.3.4 Bottom Bubble

Vortex breakdown control has shown that continued increases in the rotation ratio lead to the formation of a breakdown bubble on the active surface of the control disk (top surface). Table 5.2 shows that the bottom bubble formation occurred in both co- and counter-rotation. However, it is evident from those results that in counter-rotation, the bottom bubble tended to form at a slightly lower rotation ratio than in co-rotation. This observation is also supported by the experimental data in Figure 4.23. It would appear that the generally lower swirl numbers obtained in counter-rotation are more favourable to the bottom bubble formation than the high swirl numbers observed in co-rotation.

Depending on the speed of rotation of the top endwall (or the *Re*), the size of the control disk and the rotation ratio, the bottom bubble and the main breakdown bubble end up merging. This leads to a combined bubble covering the central region around the axis of rotation. For the case where the control disk d5 was co-rotated at $\varepsilon = 3.75$, the

combined bubble occupied almost 90% and 30% of the cylinder height and diameter, respectively. Such an enhanced breakdown bubble will be of interest in real life applications involving cell or tissue growth in bioreactors. The large breakdown bubble is a controlled region conducive to cell growth. As mentioned in chapter 1, cell growth is an area of increasing interest which is the subject of many current studies.

6.3.5 Conclusions

The main results and conclusions are outlined as follows:

- A condition for the onset of vortex breakdown in the presence of co-rotation has been established. This condition is that the swirl number Sn should be approximately equal to unity.

- Co-rotation of a control disk and the bottom endwall tend to precipitate the onset of vortex breakdown as well as enhancing breakdown. However, counter-rotation delays the onset of vortex breakdown and also tends to suppress the breakdown bubble.

- Increasing the rotation ratio in co-rotation mode tends to move the breakdown bubble upstream, while in counter-rotation mode the bubble moves closer to the top endwall.

- Increases in the size of the control disk amplify the already known effects of co-rotation and counter-rotation (as described above).

- In general, counter-rotation was found to have relatively more effect on the breakdown bubble than co-rotation. This observation was true for control disks, especially large ones, and the bottom endwall operating in both modes with the same absolute rotation ratio.

- When the bottom endwall is used to control vortex breakdown only slight co-rotations and slow counter-rotations are needed to achieve enhancement and suppression of the breakdown bubble.

- Increased rotation ratios tend to generate a bottom bubble above the active surface of the control disk. It was observed that counter-rotation caused the formation of the bottom bubble at a lower rotation ratio compared with co-rotation.

- Higher co-rotation ratios lead to a merger between the main bubble and the bottom bubble. Such a large combined bubble is attractive to researchers involved in applications related to cell or tissue growth in bioreactors.

6.4 Viscous Power

The results for the power required by the control disks, the top and bottom endwalls to overcome viscous resistance were given in chapter 5; hence, this section is entirely devoted to discussing them. The viscous power considered here is the input power to the fluid required to produce, enhance and suppress the vortex breakdown bubble. The viscous power investigation, as presented in this thesis, constitutes one major contribution of this work to the field of vortex breakdown.

6.4.1 Individually Rotating Top Endwall and Control Disk

The relative power expended by the top endwall rotating in a system without control was observed to have a direct correlation with the Reynolds number. As noted in chapter 5, this correlation is not linear as the power tends to increase at a faster rate when the Reynolds number is continuously raised. For instance, an increase from Re = 1400 to 2800, which represents an increment of a 100%, yielded a corresponding increase in the relative viscous power from P^* = 0.94 to 4.70, which is five times higher. This kind of variation can easily be understood by using dimensional analysis, whereby, the Reynolds number is proportional to velocity while the power is proportional to velocity raised to the power three (3).

The viscous power expended by the control disks rotation, while the top endwall is stationary, has been shown to be orders of magnitude smaller than the power needed by the top endwall to generate vortex breakdown onset. This low power characteristic associated with the control disks is in fact their greatest asset, as will be shown in section 6.4.3. The numerical results of section 5.4.2 show that the size of the control

disk has a significant influence on the viscous power. For instance, at a very high rotation ratio of Ω = 140 rad/s, the relative viscous power corresponding to d2 and d3 were one and two orders of magnitude higher than the equivalent power for d1.

6.4.2 Power due to the Bottom Endwall Rotation

When the bottom endwall was used to control vortex breakdown, enhancement was easily achieved through slight co-rotation and suppression through slow counter-rotation. The viscous power associated with such slow rates of rotation was shown to be about three orders of magnitude smaller that for the top endwall at the point of vortex breakdown onset. This is an indication that only a very small amount of viscous power is required for the bottom endwall to produce significant structural changes to the vortex breakdown. A more realistic comparison is presented in the next section.

The Reynolds number of the top endwall was observed to influence the relative viscous power of the bottom endwall. In co-rotation mode, higher Reynolds numbers caused the relative viscous power to increase for the same rotation ratio. These increases in power were attributed to relative increases in rotation rate of the bottom endwall to maintain the same rotation ratio.

It was also established that the viscous power of the bottom endwall was affected by the direction of rotation. In counter-rotation mode, the relative viscous power was slightly higher than in co-rotation. This finding was an unexpected result considering that the resulting swirl velocity, especially near the bottom endwall, in a counter-rotation situation is always less than in a co-rotation scenario as depicted in Figure 6.2(a). Perhaps Figure 6.2(b) provides the answer to this surprising result. The radial velocity profile along the line close to the bottom endwall shows that the counter-rotation produces higher velocities than co-rotation. These larger radial velocities can explain the higher relative viscous power values recorded for counter-rotation.

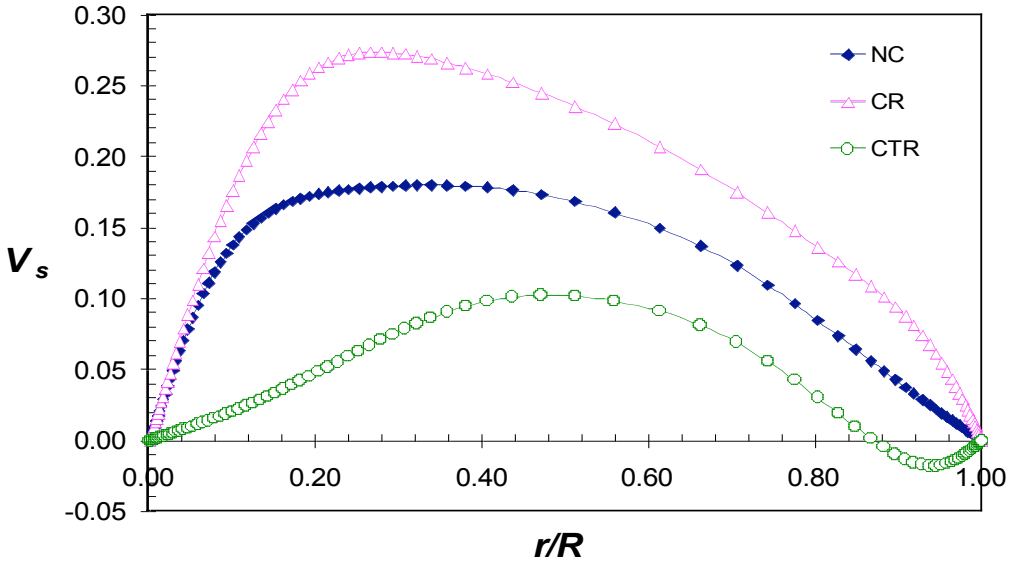

(a)

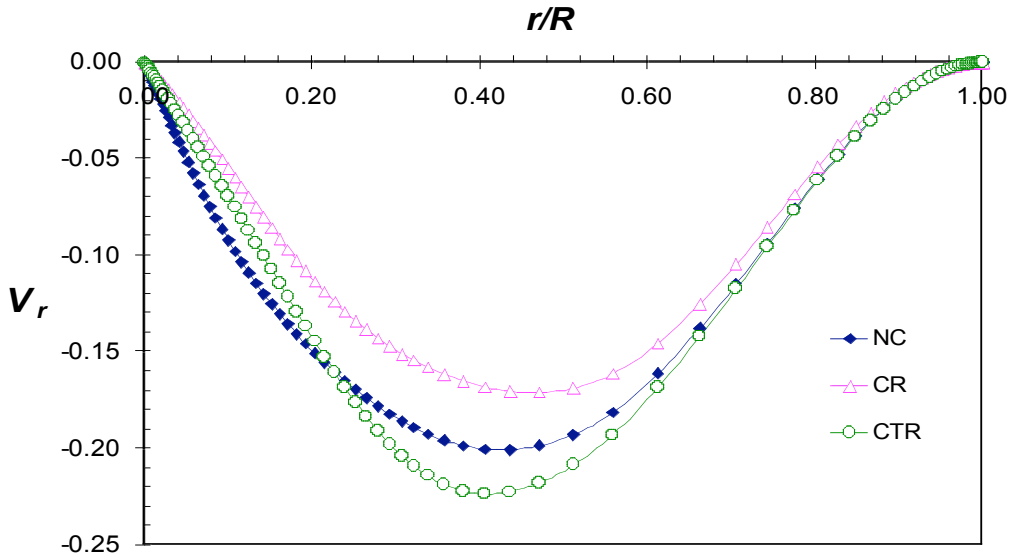

(b)

Figure 6.2 Velocity profiles along a horizontal line located at h = 0.04H above the bottom endwall. (a) Swirl velocity and (b) Radial velocity. The profiles are plotted for the case without control, co-rotation and counter-rotation.*

6.4.3 Performance Assessment

A comparative study to assess the effectiveness of the top endwall, the various control disks and the bottom endwall, in terms of viscous power expended, is discussed. The main idea is to establish which of the above methods is more power efficient than the others. Different scenarios are examined.

To generate the onset of vortex breakdown with the top endwall rotating at a Reynolds number below its critical value of $Re = 1440$ by using:

- Co-rotation of control disks.
- Co-rotation of the bottom endwall.

To enhance the size of the breakdown bubble by:

- Increasing the rotation rate of the rotating endwall (this is the conventional method).
- Using co-rotation of control disks.
- Using co-rotation of the bottom endwall.

To reduce the size of the breakdown bubble by:

- Reducing the rotation rate of the rotating endwall.
- Using counter-rotation of control disks.
- Using counter-rotation of the bottom endwall.

In the following sections the above scenarios are discussed in turn.

(i) Power for Vortex Breakdown Onset

The results of the relative viscous power to just cause the onset of vortex breakdown are presented in Table 6.2 for the control disks d3 and d5 and also the bottom endwall. These results are used to compare the effectiveness of the above control disks and the

bottom endwall to precipitate the onset of vortex breakdown when the top endwall was rotating at a speed associated with a Reynolds number below the critical value. In this case, the Reynolds numbers involved were *Re* = 1350 and 1400. The bottom endwall and the control disks, d3 and d5, were co-rotated at different speeds so as to be able to just generate the onset of vortex breakdown while to top endwall was spun with a constant *Re* = 1350 and 1440 in turn. As expected, the rotation ratio required to achieve this goal was the lowest (ε = 0.017) when using the bottom endwall and the highest when using the smaller control disk, d3, (ε = 0.63).

Table 6.2 Relative viscous power to precipitate vortex breakdown onset from the flow structure generated at Re = 1350 and 1400 without any control. The onset is produced by co-rotating the control disks d3 and d5 and the bottom endwall (db).

d#	$\left(\frac{d}{D}\right)\times 100\%$	ε	P_{VBO}	$\frac{\left(P_{VBO}^{*}\right)_{d\#}}{\left(P_{VBO}^{*}\right)_{db}}$	**Re**
d3	15.2	0.63	2.97e-05	0.10	1350
d5	30.7	0.08	2.27e-05	0.08	1350
db	100.0	0.017	3.01e-04	1.00	1350
d5	30.7	0.03	8.95e-06	-	1400

The computed viscous power (P_{VBO}), sufficient for vortex breakdown onset, is normalised by the power corresponding to the bottom endwall to yield the values shown in the second last column of Table 6.2. This relative viscous power provides the best way to compare the amount of viscous power expended by each of the above control systems. It is obvious from the results that the control disk d5 (the largest) is the most efficient followed by d3. It is also shown that the bottom endwall requires about ten times more viscous power to generate the onset of vortex breakdown than both d5 and

d3. This finding shows that the optimum control disk size to generate the onset of vortex breakdown is not necessarily the smallest one but d5 in this case. It is therefore important to carefully select the right size of the control disk in order to minimize the power expended to achieve the intended result, which in this case is the formation of vortex breakdown onset.

(ii) Power for Co-rotation

Table 5.3 summarises the findings from the comparative study carried out to assess the effectiveness of using co-rotation of the control disks, d2 through to d5, and the bottom endwall as an alternative to the conventional method of increasing the speed of the top endwall. In all cases the initial breakdown bubble was the onset size (i.e. at Re = 1440) and the final bubble was approximately the same size as the one generated at Re = 1550 (without using control). The results of Table 5.3 are discussed in tandem with Figure 6.3.

From the results, it is clear that the use of control disks and also the bottom endwall to enhance the breakdown bubble is by far more energy effective than the conventional technique of increasing the speed of the rotating endwall. In addition, the control disk method proposed in this study is more efficient in terms of viscous power requirement than the method that uses co-rotation of the two endwalls (as clearly depicted in Figure 6.3 and Table 5.3). The results have shown that co-rotation of small control disks tends to use less power, by about an order of magnitude, to achieve the same goal as the technique that employs co-rotation of both endwalls. It has also emerged that the most power efficient of the four disks in co-rotation is d4; the control disk d3 appeared to be the second best performer. Once again, the findings highlight the importance of carrying out such comparative investigations to determine the optimum size of the control disk to use for co-rotation.

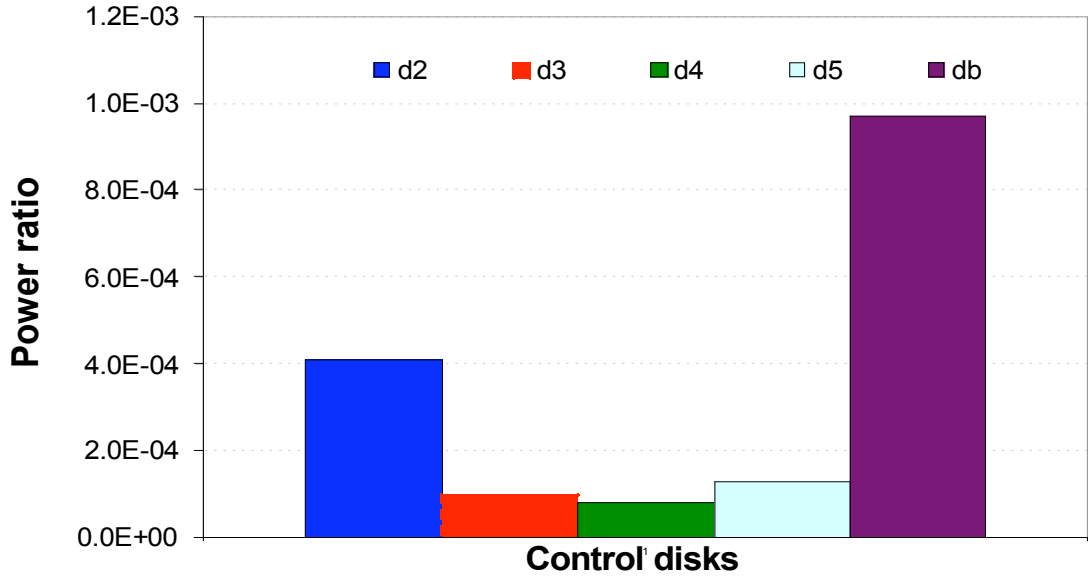

Figure 6.3 Proportional relative viscous power required to enlarge the vortex breakdown bubble generated at Re = 1440 (without control) using co-rotation of the four control disks (d2 through to d5) and the bottom endwall. The resulting bubble corresponds to Re = 1550 (without control). Refer to Table 5.3.

(iii) Power for Counter-Rotation

The viscous power of interest, for the case of counter-rotation, was defined as the minimum power expended by counter-rotating the control disks and the bottom endwall to overcome shear resistance so as to be able to *just destroy* the breakdown bubble originally generated by the rotation of the top endwall at Re = 1660. The results being discussed here are illustrated in Table 5.4 and Figure 6.4. Here, as in the co-rotation case, there is a common initial breakdown bubble size, which is the breakdown bubble corresponding to Re = 1660 (for the case without control). The viscous powers required to counter-rotate the control disks (d2 through to d5) and the bottom endwall to just suppress the initial breakdown bubble was normalised by P_{vbo} to yield what was referred to in the previous section as the relative viscous power.

Figure 6.4 shows the normalised values the relative viscous power for four of the five control disks and the bottom endwall (db). These data were further normalised by the

relative viscous power corresponding to the bottom endwall. From these results, it can be deduced that the control disk d5 was the most energy efficient in counter-rotation as it required about seven times less power than the bottom endwall to just destroy the vortex breakdown generated by the rotation of only the top endwall at Re = 1660. Also, the control disk d4 was the second best performer while d3 and d2 were found to be about six and thirty five times respectively more power demanding than both d4 and d5.

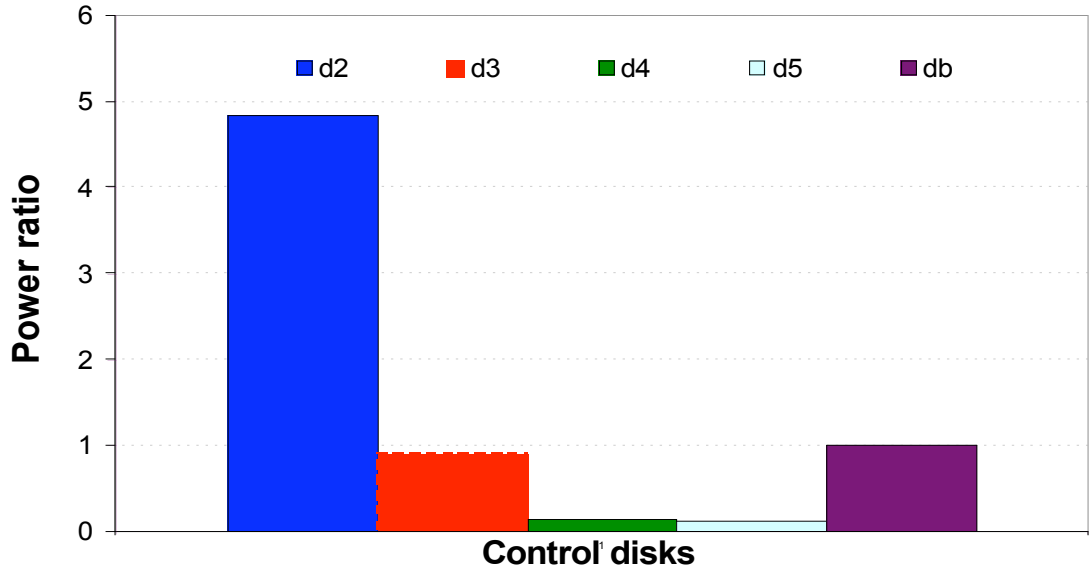

Figure 6.4 Relative viscous power ratios for four control disks (d2 through to d5) and the bottom endwall. These powers are computed such that they are just enough to completely suppress the vortex breakdown bubble generated at Re = 1660 (without control) using counter-rotation. Refer to Table 5.4.

6.4.4 Conclusions

The following conclusions can be drawn from the experimental and numerical investigations of vortex breakdown and its control:

- The viscous power associated with the rotation of the small control disks, even at high rotation rates, is still smaller than that required to rotate the top endwall to

generate the onset of vortex breakdown. The ratio was noted to be between two and five orders of magnitude depending on the size of the control disk.

- When using the bottom endwall to control vortex breakdown with slight co-rotations and slow counter-rotation, the evaluated viscous powers were about three orders of magnitude smaller than the power needed for the top endwall to generate the onset of vortex breakdown.

- Counter-rotation of the bottom endwall produces a slightly higher viscous power than co-rotation. This is thought to be related to the higher radial velocities generated by counter-rotation in the region next to the bottom endwall.

- The control disk d5 was found to be the most efficient in generating the onset of vortex breakdown compared to d3 and the bottom endwall.

- Co-rotation of the control disks to enhance the breakdown bubble from the onset size to the size at Re = 1550 (without control) has shown that the small disks are more power efficient than the bottom endwall. The use of the conventional method, by simply increasing the speed of the top endwall is the least efficient of all. On the whole, the control disk d4 was found to be the most efficient.

- While, in general, counter-rotation of the control disks and the bottom endwall were more efficient at suppressing vortex breakdown bubble, the control disk d2 was noted to be the least efficient of the control systems. The control disk d5 emerged as the least power demanding of all.

- Although the control disks d4 and d5 were found to be better performers in this study, it is clear that no single control disk was the most suitable in the three different scenarios investigated in this chapter. Therefore, a comparative study such as the one described in this thesis is essential to determine the most efficient size of control disk to use for a specific application; depending on whether vortex breakdown enhancement or suppression is the intended goal.

6.5 Suggestions for Future Research

The following suggestions are intended to be a guide for future research on vortex breakdown in a closed cylinder. Although this work has attempted to fill some gaps identified in the literature review, it has also raised a number of questions that require further investigation. The following are some of the issues that need further examination:

- The shrinkage of the breakdown bubble that was observed after the bubble had reached its peak size appeared to coincide with the beginning of unsteadiness in the flow (Re > 2600) as noted by Escudier (1984). Further investigation is needed to establish whether there is a link between the shrinkage of the breakdown bubble and the unsteadiness of the flow inside the cylinder.

- Investigation into the reasons why counter-rotation tends to promote the formation of the bottom bubble at a lower rotation ratio compared to co-rotation is required.

- Further work to determine the most power efficient control disk size for the three scenarios discussed here is needed. The study should extend the range of control disk sizes to $0.31 < d/D < 1.00$ and follow a comparative approach similar to what has been presented here.

Chapter 7
Numerical Modeling of Mixing in a Stirred Vessel

7.1 Prelude

Although this chapter is placed towards the end of the thesis, part of the work presented here provided the inspiration to conduct investigations of vortex breakdown, which forms the bulk of this publication. That part of the study involved mixing using a plain disk. When the plain disk diameter was increased to equal that of the cylinder and its location along the axis of rotation made to coincide with that of the top lid, such a mixing configuration was essentially a closed cylinder with a rotating endwall. This configuration was the subject of the first six chapters.

In this chapter investigations of flow mixing in an unbaffled vessel equipped first with a plain disk agitator and second with a paddle impeller are presented. A brief introduction to mixing is given in section 7.2 followed by section 7.3 which deals with the theoretical background of the mixing process in agitated vessels. In this section important previous studies are discussed to establish the context of the present study. In section 7.4, the methods employed in this study are described; this includes pre-processing, processing and post-processing of numerical results. Section 7.5 focuses on the description and discussion of the two sets of results. This section also shows a link between the vortex breakdown and mixing studies. The chapter ends with a presentation of conclusions and recommendation for further investigations.

7.2 Introduction

It is appropriate to begin the study of mixing by defining what a mixing operation is. The generally accepted working definition of mixing describes it as an operation that is designed to reduce inhomogeneity in concentration, phase or temperature so as to achieve an intended process result. Mass transfer, reaction, and product properties are some of the critical factors that determine the success of a mixing operation. The above task can be accomplished by moving a bulk material which can be solid, liquid or gas within a mixing vessel using an agitator of some kind. While in most industrial applications mixing is generally a multi-phase process there are also cases where only a single phase is used. In this study a single phase liquid is employed as the experimental fluid as it suits the nature of the investigation.

Mixing has evolved since its early days dating from as far back as the 1950s. It was only until a decade later that the first publication by Uhl and Gray (1966) came into being. A decade later, yet again, another significant publication by Nagata came out; these publications as well as other early works helped to establish mixing as worthwhile branch of Fluid Mechanics. It is interesting to note that, over the years, despite the significant level of technological advancement, with experiments and Computational Fluid Dynamics (CFD), one can not claim with confidence to have a complete understanding of mixing processes, especially those involving turbulent flow. For this reason, the study of mixing is very topical.

Mixing is of fundamental importance in a wide range of industries such as: petrochemicals, agrichemicals, pharmaceuticals, biotechnology, polymer processing, cosmetics, food, drinking water and water treatment, pulp and paper and mineral processing. The above list is by no means exhaustive but only representative. The range of applications is diverse and includes the following: blending of two liquids, solid suspension accompanied by another process such as leaching and flotation, gas dispersion into a liquid followed by absorption and/or chemical reaction between liquid and gas, fermentation or crystallisation.

In the process industry, there is an increasing need for properly designed mixing vessels so as to reduce production losses and maintenance costs. The efficiency of many

industrial processes greatly depends on optimization of the relevant mixing parameters. It is thus important to investigate flow generated in mixing vessels to enable the design of systems with improved efficiencies. For instance, using CFD, Bakker and Fasano (1994) were able to study the effects of flow pattern on the solids distribution in a stirred vessel and found that the solids distribution was strongly affected by certain flow transitions.

The significance of research in the field of mixing cannot be over-emphasised neither should it be taken for granted. For instance, in the U.S. chemical industry alone it was estimated that the cost to their process industries due to an inadequate understanding of mixing was of the order of U.S. $1 to 10 billion during the year 1989 (Paul *et al.* (2004)). Tatterson (1994) also stated that the design of stirred reactors, which had often been based on empirical knowledge and "rules of thumb" resulting in approximations and uncertainties, caused financial losses estimated in the region of US $1 billion per annum in the USA alone.

There is also enough evidence in the literature to suggest that a well-designed mixing vessel contributes significantly to energy efficiency (Khang and Levenspiel (1976); Ruszkowski and Muskett (1985)). It is worth noting that vessels are designed with a view to optimising specific process results, such as solids suspension, so that appreciable energy saving can be achieved.

7.3 Theoretical Background

Background theoretical aspects of the mixing process in a cylindrical mixing vessel without baffles are discussed. These include descriptions of the mixing vessel configuration, the role of CFD in mixing, a look at flow regimes and patterns and the definitions of global mixing parameters used in this study.

7.3.1 Mixing Vessel Configuration

The system shown in Figure 7.1 is a basic mixing configuration. The main parts of a mixing vessel configuration include a cylindrical vessel, which can be baffled or unbaffled (as is the case here), covered with a top lid or open; and an agitator that is

responsible for providing the energy to move the material being mixed from one region of the vessel to another. The flow so generated inside the vessel begins as a radial jet emanating from the impeller and directed towards the vessel vertical wall. Upon approaching the wall this radial jet is deflected, producing two streams, one moving vertically upwards and the other in the opposite direction towards the vessel bottom surface. The presence of the two solid surfaces, the vessel bottom and top lid, causes the jets to turn towards the axis of rotation before returning to the impeller region along the swirl axis hence completing a circulation loop. The above fluid motion is responsible for the two circulation loops. The absence of a free surface prevented the formation of a vortex. The flow is predominantly circumferential, with the region near the impeller shaft having the mean tangential velocity directly proportional to the radius (i.e. solid body rotation) and decreasing towards the vessel wall in the outer region.

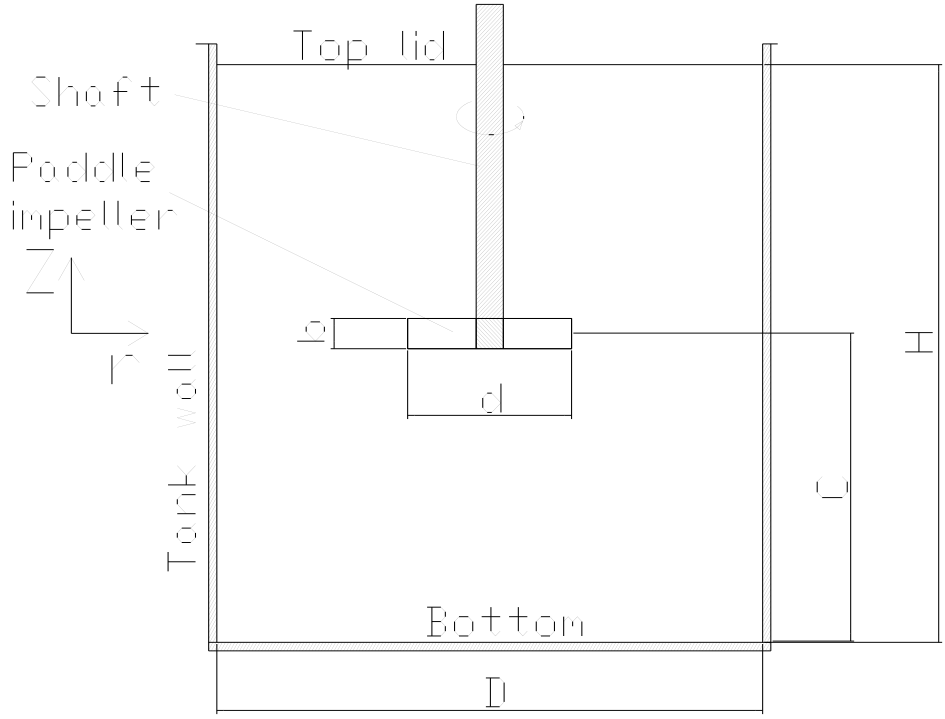

***Figure** 7.1 Mixing system configuration.*

(i) Unbaffled Tank

The number of research papers related to flow in mixing vessels with baffles (Kresta and Wood (1991); Ranade *et al.* (1989); Luo *et al.* (1993); Armenante and Chou (1996)) is by far larger than the number of papers dealing with unbaffled vessels. It is, however, encouraging to note that in the mid 1990s a few studies devoted to investigating flow in unbaffled vessels started to emerge (Dong *et al.* (1994a, b); Ciofalo *et al.* (1996); Armenante and Chou (1994)).

The absence of baffles in a mixing vessel causes the liquid to move mainly along circular trajectories, which results in small relative velocities between impeller and fluid and weaker radial flows impinging onto the vessel walls Ciofalo *et al.* (1996). This results in small axial velocity components leading to poor axial mixing and also the formation of a vortex on the free surface of the liquid. The depth of this free vortex depends on the rotational speed of the agitator.

On the other hand, in baffled vessels, the presence of baffles inhibits the formation of the vortex by destroying the circular motion of the liquid, leaving the liquid's free surface flat. This means that in unbaffled vessels the flow is essentially two-dimensional and is dominated by swirling action like in a solid body rotation. Moreover, axial flow becomes more pronounced, giving rise to a much-improved mixing rate. It is not surprising, therefore, that baffled vessels are more widely used in industrial applications, and have attracted much more interest in both experimental and numerical studies.

Wall baffles are often used when the flow regime is either transitional or turbulent but certainly not in cases prone to severe fouling, where frequent cleaning of vessel internals is required. Baffles are solid surfaces equally spaced around the inner surface of the cylinder. To minimize dead zones a small gap is left between the baffles and the inner cylinder surface. Wall baffles do increase the power consumption of the mixer but lead to better process results as mentioned above.

There are, however, many other cases in which the use of unbaffled vessels may be desirable, namely:

- Baffles are usually omitted in processing of very viscous fluids (Re < 20), where they worsen the mixer performance by giving rise to dead zones.

- Applications involving low rotational speed (laminar flow) and high friction on the vessel cylindrical wall are not prone to vortex formation (Nagata (1975)).

- In crystallisers, where the presence of baffles may cause particle attrition phenomenon (Mazzarotta (1993)).

- In a number of other processes it may be preferable to use unbaffled vessels since they generate higher fluid-particle mass transfer rates for a given power consumption. Medek and Fort (1994) found that the value of the power number in a closed fully filled unbaffled vessel was approximately half of the value obtained from a baffled vessel with a free liquid surface. This low power requirement makes unbaffled mixing vessels an attractive option yet to be explored.

- The generally undesirable central vortex, in free-surface unbaffled vessels, may prove to be an advantage in some cases. For instance, the central vortex is effective in drawing down floating solid particles or in removing gas bubbles from the liquid, hence reducing foam formation.

It is known that the absence of baffles in a mixing vessel typically results in the generation of a central vortex and a swirling flow (Rieger *et al.* (1979); Markopoulos and Kontogeorgaki (1995); Ciofalo *et al.* (1996). However, if the vessel is completely filled with liquid and provided with a top lid no vortex forms. This helps in simplifying the mathematical modeling and simulation of flow in unbaffled systems, while retaining the complexity of the swirl dominated flow (Armenante and Chou (1994); Armenante *et al.* (1994); Ciofalo *et al.* (1996). It is for this reason that the present work modeled the vessel with a top lid.

High profile studies amongst the few studies about the hydrodynamics of fluid flow in unbaffled mixing vessels include the following: Nagata *et al.*, 1958; Dong *et al.* (1994a, b); Lamberto *et al.* (1996); Armenante *et al.* (1997).

Armenante *et al.* (1997) investigated velocity profiles in a closed unbaffled vessel

agitated by a 6-PBT (Pitched Blade Turbine) with 45º blade angle and d/D = 0.3 and C/D = 0.25, using both experimental and numerical simulations. They observed that dimensionless velocity and turbulent kinetic energy profiles were nearly independent of agitation intensity. They also found that the flow number (N_{qp}) was almost constant and independent of the speed whereas the power number decreased with increasing impeller agitation speed. However, N_{qp} and N_p values calculated from numerical predictions were not in good agreement with experimental data.

A number of studies have shown that the laminar flow structure in unbaffled stirred vessels is characterised by ring vortices that are distinctly separated from the bulk flow. In a recent study Lamberto *et al.* (1999) observed torus-shaped segregated regions above and below the 6-blade radial flow impeller in the laminar flow regime. They observed that these regions of poor mixing exchanged material with the bulk flow through diffusion as a result of concentration gradients. The segregated regions were seen to persist for several hours, and in practice this would cause extended run times and also excessive generation of unwanted side products in reactive applications. CFD simulations and validation with PIV revealed that the centres of the segregated regions not only depended on the Reynolds number but also on the impeller blade position Lamberto *et al.* (1996).

Lamberto *et al.* (1999) investigated the extent of laminar flow within the secondary circulation regions and found that circulation flow rates were about four times higher than the pumping capacity. The finding is in agreement with the finding of Costes and Couderc (1988) from similar studies in a baffled mixing vessel operating in the turbulent flow regime.

(ii) Agitator

One of the most important parts of a mixing vessel system (Figure7.1) is the agitator, also known as the turbine or impeller. Impellers are classified, on the basis of flow pattern, applications and special geometries. Classified according to flow pattern there are two main types, namely axial and radial flow impellers. Axial flow impellers are often used in liquid blending and solid suspension applications; whereas, radial flow impellers are popular in applications involving gas dispersion.

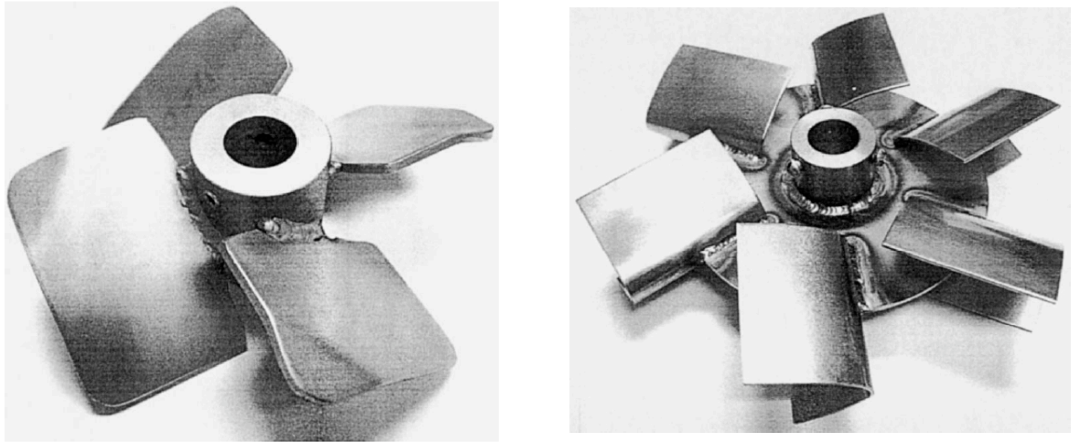

(c) (d)

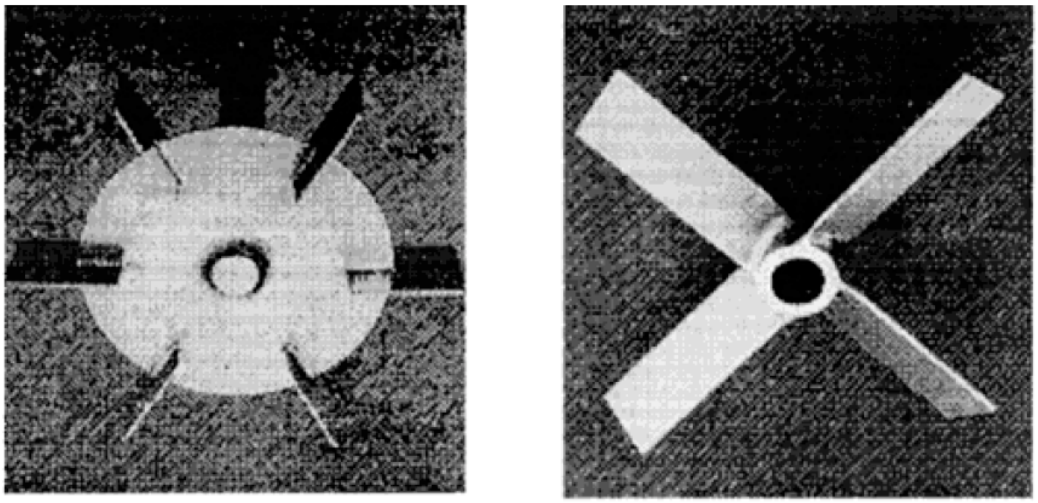

(a) (b)

Figure 7.2 Impeller classification: (a) Radial flow impeller (Rushton turbine); (b) Pitched blade turbine (PBT); (C) Lightnin A315 impeller; (d) Chemineer BT-6 impeller.

Among axial flow impellers are: the propeller, which is the oldest design in this category; the PBT or pitched blade turbine (Figure 7.2(b)) also known as the mixed flow impeller because the flow discharge has components of axial and radial flow velocity; and the retreat blade impeller (Li *et al.* (2004)) developed by the Pfaudler Company. On the other hand, radial flow impellers can have either a disk (Rushton turbine shown in Figure 7.2(a)) or be open (Flat blade turbine or paddle impeller). Sometimes the blades may be curved (backswept turbine). Compared to axial flow impellers, radial flow impellers generate higher shear and turbulence levels but lower pumping. Other agitators are classified as hydrofoil impellers; they are used when axial flow is desirable coupled with low shear. Lightnin A310 (Bouyer *et al.* (2004)) and Chenineer HE3 fall under the hydrofoil group (variants of these models are shown in Figures 7.2(c-d).

A variety of impeller designs exists but there are still efforts to make further improvements so as to achieve energy efficient designs. In terms of application, no single impeller is sufficiently versatile to perform all the functions of mechanical agitation; therefore, in practice impellers are selected and designed to generate a flow pattern that enhances performance for a specific function (Mishra and Joshi (1993)).

Until recently, Rushton turbines agitated most industrial-scale bioreactors (named in recognition of the extensive research on mixing and agitators by J. H. Rushton and co-workers). Rushton *et al.* (1946) pioneered work on the study of fluid flow in turbine impeller agitated systems. Angled blade agitators (45º pitch angle), also known as Pitched Blade Turbines (Figure 7.2(b)), were occasionally used as upper agitator in earlier work especially for more viscous fermentations because of their higher pumping capacity. In recent years, it is becoming increasingly popular to use high flow number and low power number agitators such as the Ekato Intermig, the Lightnin A315 (Figure 7.2(c)), the Prochem Maxflo T and Chemineer CD6 (Nienow (1998)). There are now a wide variety of agitators in use but the plain disk is not among the favourites. The present research study investigates the flow characteristics and usefulness of both the plain disk and the bladed paddle impellers.

A plain disk is the simplest of all mixing vessel agitators in terms of design and

manufacture. It is classified as a high velocity and low flow impeller. The type of flow generated by the plain disk is axisymetric unless the Reynolds number is extremely high. It can be operated at high peripheral speeds with relatively low power consumption, but has poor circulating capacity and can be expected to perform well only at very low viscosities. This type of agitator is not popular because most industrial applications involve turbulent mixing and as a result only a limited number of publications have reported about its performance. Although it is generally perceived that turbulent mixing is the most efficient, there are several industrial applications for which it is detrimental. For instance in mixing processes where the fluid is very viscous or contains substances that are shear sensitive, turbulent agitation can lead to unfavourable mixing conditions. The research in this thesis has been motivated by the fact that in some applications, as described above, a plain disk rotor is more relevant than a bladed impeller. Bladed impellers represent too rapid a change of geometry in the flow, which leads to turbulence and higher shear rates. A plain disk rotor is thought to have the ability of producing a smoother mixing laminar flow at much higher Reynolds numbers (*Re*) compared to a bladed impeller.

7.3.2 CFD in Mixing

The main difficulty facing designers of mixing vessels is that it is difficult to establish robust "scale-up" criteria. In many cases the design of reactors used in process industry has been based not on rational design procedures but on empirical correlations, work experience, and intuitive knowledge of experienced workers in the field. Even so, over the years, there have been continuous efforts to develop rational design procedures. In recent years, the development of fast computers has been a great catalyst behind the progress recorded in recent years in CFD simulation of mixing vessels.

The application of CFD to fluid flow investigations in stirred reactors dates back to the late 1970's (Harris *et al.* (1996)), but it is only in the last decade that CFD has taken a major role following increased development of simulation techniques. Perhaps the first detailed CFD investigation of flow in mixing vessels is the work of Harvey and Greaves (1982). Middleton *et al.* (1986) are credited for being the first to simulate 3D flow in a stirred vessel reactor. It took several years after the pioneering work of Middleton *et al.*

before CFD simulation of stirred vessels could resolve both the baffles and the motion of the vessel. Before then, predictions of flow in the impeller region were very poor.

The next stage saw the publication of papers reporting the use of "impeller boundary conditions", acquired from experimental data (Ranade and Joshi (1990b); Brucato *et al.* (1990); Kresta and Wood (1991)). The setting of "steady" impeller boundary conditions presented some disadvantages namely: it neglected the transient coherent structures such as eddies shed by the trailing edges of the impeller blades as they move through the fluid; and the need for experimental data input. There arose the need to find a simulation technique that did not require empirical data input. Dong *et al.* (1994b) were the first researchers to carry out simulations in a frame that was rotating with the impeller.

In the early days of research on mixing and agitators, investigations were mainly theoretical and experimental. These investigations used relatively crude techniques such as Pitot tubes for velocity measurements as opposed to recent sophisticated experimental methods involving the use of techniques such as stereoscopic PIV (Prasad and Adrian (1993)).

Over the years, researchers have employed two approaches to investigate flow in mixing vessels namely, experimental measurements (Calabrese and Stoots (1989); Rutherford *et al.* (1996b); Sharp and Adrian (2001)); and numerical simulations (Kresta and Wood (1991); Bakker *et al.* (1997); Syrjanen and Maninnen (2000)). Although experimental investigations have been more widely used than their numerical counterparts they do present some shortcomings. Laboratory experiments can be expensive and time-consuming, and can not cover all relevant parameters. In addition, the scale-up to large industrial scale units is neither straight forward nor well established, since most mixing systems have to perform simultaneously several functions (such as dispersion, reaction and heat transfer) which do not scale-up in the same manner. It is difficult to optimise a configuration for a particular process because of the semi-empirical nature of the correlations, which limits the design to geometric similarity with small-scale work.

In view of the demerits of experimental investigation, CFD is seen to have an enormous

potential and might provide a means for understanding the details of flows, and possibly give insights required for design and scale-up. CFD is a tool that is increasingly becoming popular in the study of complex fluid flows such as those typically encountered in mixing vessels. Nienow (1998) observed that although in recent years there has been substantial increase in the understanding of stirred bioreactor hydrodynamics, further understanding would largely depend on the progress of CFD techniques. Ironically, because of the difficulty in modeling the exact physics of these complex flows, CFD predictions require validation by comparison with empirical data.

One other advantage of CFD over laboratory experiments is that the amount of information which can be generated by numerical calculations is immensely larger. As an alternative to experimental investigation, CFD constitutes not only a useful tool but also a cost effective means in the design of mixing systems. However, the development of modeling methods is a continuing process, which necessitates validation of predicted results against experimental data (Ng *et al.* (1998); Montante *et al.* (2001b)). For this reason, CFD will continue to complement laboratory investigations because of the huge financial benefit it offers; it is therefore not surprising that numerical work in the area of mixing has been on the increase especially in the last decade. Continual development of numerical simulation techniques is bound to lead to significant improvements in the design capability and reliability of stirred reactors.

7.3.3 Flow regimes

Uhl and Gray (1966) suggested that fluid mixing occurs by a combination of the following mechanisms:

- In laminar mixing such as stirring a coloured pigment in a bucket of paint, layers of pigment are thinned, lumps flattened, and threads elongated by laminar bulk flow followed by molecular diffusion.
- In turbulent mixing such as stirring of cream in a cup of coffee, the process begins with turbulent bulk flow, eddy diffusion and ends with molecular diffusion.

Turbulence is vital to the majority of mixing operations. Such operations involve

reaction, mass transfer, dispersion and blending. Although a considerable number of publications have been devoted to the study of turbulence in mixing, the nature of turbulence is still not yet fully understood. Therefore, it is still not easy to comprehend all aspects of turbulent fluctuations in mixing processes. The flow in stirred vessels is complicated further by strong swirling flows, difficult geometries, and the presence of instabilities. Although laminar flow is thought to be easier to understand than turbulent flow, it has not been researched as extensively. Szalai *et al.* (in Paul *et al.* (2004)) noted that our scanty understanding of the dynamics of laminar mixing processes is a major limitation in the effective design of mixing equipment. The present study attempts to address some of these issues that hopefully will lead to better understanding of mixing processes under different flow regimes.

The classical definition of laminar flow regime is the region where the product N_p x Re = A; where A is a constant value between 22.3 and 260 according to Nagata (1975), Re is the Reynolds number defined by Equation 7.1 and N_p is the power number defined by Equation 7.11. In this region, usually identified by $Re < 10$ (for mixing using a bladed impeller), the slope of the curve N_p as a function of Re is negative. The fully turbulent region is normally considered to be where $Re \geq 10^4$ and the flow associated with the region between the above two is considered to be in the transitional regime. The Reynolds number for a mixing process in a cylindrical vessel is defined by Equation 7.1,

$$\mathrm{Re} = \frac{\rho N D^2}{\mu} \ , \tag{7.1}$$

where N is the impeller rotational speed, in revolutions per second (rps), D is the impeller diameter, ρ is the fluid density and μ is the molecular or dynamic viscosity of the fluid.

7.3.4 Flow Patterns

Stirred vessels have been widely used in the process industry for different purposes such as blending liquids, gas or solid dispersion in a liquid. In some applications a chemical

reaction follows later. In these processes, the end product depends not only on the physiochemical aspects of the particular process but also on the flow patterns of the different species. The distribution of solid particles and the dispersion of gas in a liquid largely depend on the type of flow patterns that a particular agitator can produce in a given mixing vessel.

Generally, flow patterns induced by an agitator are the first indication of its suitability for a particular process. The study of flow patterns in mixing vessels has perhaps been the most investigated aspect of this research area, mainly due to its basic importance (Nagata *et al.* (1958); Nagata *et al.* (1960); Ranade and Joshi (1990a); Mishra and Joshi (1993); Montante *et al.* (2001a)).

(i) Flow Visualization Techniques

Recently, Mavros *et al.* (2001) reviewed the experimental techniques employed to establish the flow patterns of various mixing configurations. He discussed both the old and simpler flow mapping techniques, as well as the current more sophisticated ones. He grouped them into two categories: single-point measuring techniques and ensemble-measuring techniques,

Single-point techniques determine velocity (or one of its components) at a set point within the vessel. These techniques include Pitot tubes, originally developed by Henri de Pitot (1695-1771), which have been used in the past to measure velocities in stirred vessels (Wolf and Manning (1966); Nagata (1975)); Hot-wire Anemometry (Wong and Huang (1988)) and Laser Doppler Velocimetry (Bakker and Van den Akker (1994); Armenante *et al.* (1997).

Ensemble-measuring techniques determine the flow field simultaneously (2D velocity field) in a wider region of the bulk fluid. These techniques include simple imaging using still pictures and streak lines (Yianneskis (1991); Ju *et al.* (2000)); Laser-Induced Fluorescence (Houcine *et al.* (1994)); Particle Image Velocimetry, PIV, (Cheng *et al.* (1997); Grant (1997); Sheng *et al.* (1998)) and holographic PIV (Zhang *et al.* (1997)).

(ii) Effect of Reynolds Number

Reynolds number (*Re*) based on the speed of the impeller or agitator may affect circulation patterns in stirred vessels and many researchers have reported variations in flow patterns caused by changes in *Re*. For axial flow impellers, such as pitched blade turbines (PBT), Nouri and Whitelaw (1990), and Hockey and Nouri (1996) reported that the impeller stream with 45º and 60º PBTs changed direction with increasing *Re* from mainly radial (at *Re* = 490) to mainly axial flow (at *Re* = 650).

One of the major problems associated with stirred vessels is the presence of segregated regions where the degree of mixing of the fluid with the bulk flow is not satisfactory. Both laboratory experimentation (Metzner and Taylor (1960); Dong *et al.* (1994a)) and computation (Desouza and Pike (1972); Kuncewicz (1992)) have revealed the existence of segregated regions in stirred vessels especially for $Re < 500$. These segregated regions, or torii of recirculating flow, act as barriers to mixing, hence they increase mixing time. Lamberto *et al.* (1996) observed that the size and position of the segregated regions depended on the impeller rotational speed or *Re*. Therefore, in order to improve mixing efficiency, they proposed the use of time-dependent RPM, which relies on continuous perturbation of flow to prevent the formation of stable and coherent segregation regions.

At low *Re*, because the flow generated by PBTs is predominantly radial (hence directed towards the vessel wall), many researchers have observed the formation of a counter-rotating secondary recirculation region near the base of the vessel. Nouri and Whitelaw (1990) reported the presence of a secondary loop along the vessel base near the impeller axis of rotation. Their results indicated that this loop experienced a reduction in size and strength with increasing *Re*.

Bakker *et al.* (1997) found that a baffled vessel agitated with a PBT at low speed ($Re = 40$) created a mainly radial flow pattern with two circulation loops, one above and the other below the impeller, instead of the expected single-loop. In their investigation, they observed that the jet coming from the impeller hit the vessel bottom rather than the wall, becoming more axial, at $Re > 400$. This transitional *Re* is slightly lower than reported by other investigators ($490 < Re < 650$). The above difference could possibly be attributed

to different blade pitch angles, and perhaps more importantly, different off-bottom clearances used in the various studies. Therefore, in the next section the effect of the impeller off-bottom on flow patterns is considered.

(iii) Effect of Off-bottom Clearance

The impeller clearance (C) measured from the bottom of the vessel has been known to have a major effect on the flow patterns and this phenomenon has been studied quite extensively. In the early stages of mixing research Nienow (1968) had already noted the dependence of flow pattern on impeller location. Yianneskis *et al.* (1987) and Rutherford *et al.* (1996a) studied single and dual Rushton turbine configurations while Jaworski *et al.* (1991) and Kresta and Wood (1993), and Mao *et al.* (1997) investigated single PBTs configurations. In all these studies it was found that the impeller off-bottom clearance had a critical, perhaps the most significant, effect on the hydrodynamics of flow in a mixing vessel.

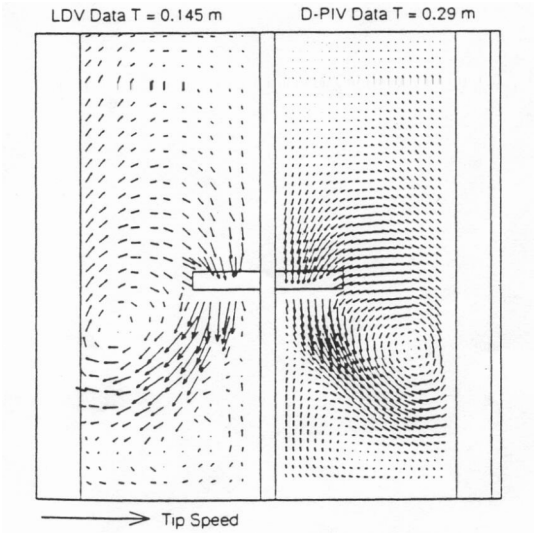

Figure 7.3 Turbulent flow patterns for an axial flow impeller operating with high clearance (Bakker et al. (1996)).

In another study, Bakker *et al.* (1996) investigated laminar and turbulent flow generated by a PBT in a baffled vessel using laser Doppler velocimetry (LDV) and digital particle image velocimetry (DPIV) experimental techniques. For high off-bottom impeller

clearances, they reported that the discharge flow impinged on the vessel wall and the flow at the base of the vessel was directed radially inwards. This radial flow was responsible for the reversed flow observed at the vessel base near the impeller axis of rotation as shown in Figure 7.3.

Circulation pattern changes were measured by Jaworski *et al.* (2001) using a $d = D/3$ PBT at $C = D/2$ and $D/4$ clearances. Kresta and Wood (1993) used two PBTs agitators ($d = D/2$ and $D/3$) with C systematically varied between $D/20$ and $D/2$. In both studies they observed that as the off-bottom clearance was increased the angle of the flow discharge with respect to the horizontal (or the vessel base) decreased. In other words, as the clearance (C) was increased the discharge flow from the impeller changed from a mainly axial to a mainly radial direction. In line with the above findings, Mao *et al.* (1997) concluded that the downward flowing jet from a PBT depended strongly on the impeller location. The single recirculation loop was evident at low C values and a second loop formed as the impeller clearance increased. The above findings show that although PBTs have been associated with single loop circulation the flow pattern changes with impeller off-bottom clearance.

When the discharge flow from an axial flow impeller is directed such that it impinges on the bottom of the vessel, it is redirected in the outward radial direction. This leads to suspension of the solid particles at the periphery of the vessel. However, if the impeller is sufficiently far away from the bottom its discharge flow will impinge on the wall of the vessel instead of the base (Jaworski *et al.* (1991)). With the discharge flow impinging against the wall, a double loop flow structure forms in the vessel and this causes flow reversal. This is independently corroborated by CFD simulations results of Yianneskis *et al.* (1987) and Bakker and Fasano (1994).

As noted above for axial flow impellers the dependence of flow pattern on the off-bottom impeller clearance has also been observed by other researchers using radial flow turbines. Yianneskis *et al.* (1987) noted that in a single impeller configuration using a Rushton turbine with $d = D/3$ the inclination of the impeller stream to the horizontal increased with decreasing impeller clearance. Typically, inclinations of 2.5°, 4.5° and 7.5° were observed for $C = D/2$, $D/3$ and $D/4$ respectively, which shows a trend similar

to the axial flow cases. Montante *et al.* (1999) observed the Rushton turbine streams inclined at angles between 25° to 30° to the horizontal when the off-bottom clearance was about 0.2*D*, which also corresponded to the transition point from double-loop to a single loop. The discharge flow inclination is thought to be responsible for the flow transition in mixing vessels.

Flow pattern transition from double to single loop was first reported by Nienow (1968) who observed that reducing *C* to *D*/6 (or $C = 0.17D$) caused the impeller jet to dip towards the vessel corner. Armenante *et al.* (1998) found that the transition took place between $0.15 < C/D < 0.20$ for vessels agitated by Rushton turbines of various sizes. Recently, this same phenomenon was investigated by Montante *et al.* (1999) using Laser Doppler Anemometry (LDA) to characterise the flow pattern transition where they observed the single-loop flow field structure at $C/D = 0.15$.

Very recently, Galletti *et al.* (2003) used a Rushton turbine located at an off-bottom clearance $C = 0.33D$. They showed that the radially discharged impeller stream was divided near the vessel walls into two axial streams, one directed downwards and the other upwards, forming two circulation loops as shown in Figure 7.3(a). They further observed a complete change in the flow pattern as the clearance was reduced to $C = 0.15D$ (Figure 7.4(b)). This time, the flow was characterised by the presence of a very small secondary low intensity circulation loop below the impeller. This, they observed, was the transition from a double-loop to a single-loop as reported by previous researchers (Nienow (1968); Montante *et al.* (1999)).

Using an 8-blade disk turbine, Conti *et al.* (1981) found that when the ratio between impeller clearance and vessel diameter was about 0.22 ($C = 0.22D$) flow transition was noticed as the impeller power exhibited a marked jump with two distinct flow regimes. The rise in power number was associated with the flow transition from double-loop to single-loop. The results by Conti and co-workers revealed that this critical C/D value of 0.22 was independent of either *N* or d/D for the range of geometries considered ($0.22 < d/D < 0.37$).

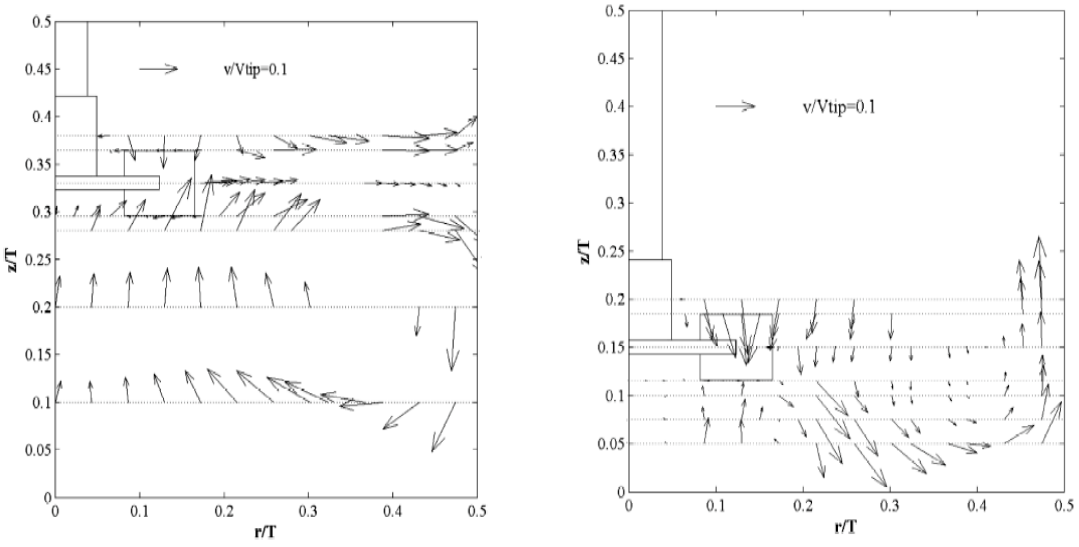

(a) (b)

Figure 7.4 Axial and radial velocity fields measured with the impeller located at (a) C = 0.33D and (b) C = 0.15D (Galletti et al. (2003)). The velocities are normalised with the blade tip velocity Vtip.

A similar critical value of impeller clearance was also obtained by Myers *et al.* (1996) in their study with a straight-blade turbine (S-4). They observed flow reversal for impeller off-bottom clearances greater than 20% of the vessel diameter ($C/D > 0.20$) for small impellers ($d/D < 0.35$) within the same range as Conti *et al.*'s.

Although most of the above studies found that the size of the impeller did not affect the flow transition clearance, other researchers have found a link between impeller size and flow pattern. Myers *et al.* (1996) found that the impeller diameter also affected the flow pattern. This view supports of the finding by Abid *et al.* (1994) that the impeller diameter and blade size play a significant role on flow structure. Abid *et al*. observed that in order to create an axial circulation in the volume of the vessel, the paddle blade height had to be decreased. This last aspect has not been fully investigated. It is for this reason that the present research examined the effect of the blade size on some important mixing global parameters. These important mixing global parameters are described next.

7.3.5 Important Global Quantities

The global parameters discussed here are non-dimensional numbers associated with mixing process. They include: pumping flow number N_{qp}, circulation flow number N_{qc}, power number N_p, pumping effectiveness η_e and pumping efficiency λ_p.

(i) Pumping and Circulation Flow Numbers

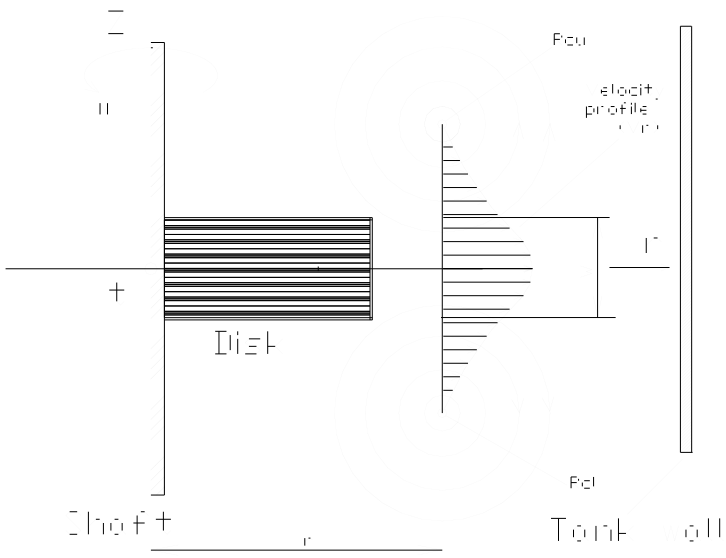

Figure 7.5 Radial velocity profile and circulation flow.

Some of the important factors that dictate the quality of mixing are primary and secondary circulation flow rates and impeller volumetric flow rate. Rushton *et al.* (1946) were among the first investigators to publish data on the actual discharge flow of impellers in mixing vessels. Later, Sachs and Rushton (1954) published data on discharge flow for turbine type impellers in baffled vessels. Since then, a number of researchers have studied both circulation and impeller stream discharge flow rates (Costes and Couderc (1988); Kresta and Wood (1993); Dong *et al.* (1994a); Lamberto *et al.* (1999)). In these studies, some aspects have interested researchers and among them is the relationship between circulation flow number N_{qc} (Equation 7.4) and discharge flow number N_{qp} (Equation 7.2). The vast majority of published data is concerned with mixing in baffled vessels; as a result the study of circulation and

discharge flow rates in unbaffled vessels has received less attention.

$$N_{qp} = \frac{Q_p}{ND^3} \tag{7.2}$$

$$\text{where, } Q_P = 2\pi r \int_{-w/2}^{w/2} V_r dz, \tag{7.3}$$

$$N_{qc} = \frac{Q_c}{ND^3}, \tag{7.4}$$

$$Q_c = Q_{c1} + Q_{c2}, \tag{7.5}$$

$$Q_{c1} = 2\pi \int_{rs}^{rc} r V_z dz, \tag{7.6}$$

$$\text{and, } Q_{c2} = 2\pi \int_{rc}^{T/2} r V_z dz. \tag{7.7}$$

From the above equations, V_z and V_r are the axial and radial components of velocity respectively and w is the blade width.

Costes and Couderc (1988) found that the pumping coefficient for a Rushton turbine (d/D = 0.33 and $C = D/2$) was constant in all cases with the mean value independent of the stirrer rotational speed or the size of the unit, and equal to 0.73. They also found that the circulation flow rate near the wall of the vessel, Q_{c2}, was always slightly lower by between 10 and 20%, than the one calculated in the centre of the vessel, Q_{c1} (Figure 7.5). They attributed this difference to experimental errors and also established that the circulation flow rate appeared to be proportional to the rotational speed of the turbine. Furthermore, the circulation number, N_{qc}, was observed to be independent of the rotational speed and size of the impeller, with an average value of 3.4 ± 0.4, which was found to be about four times greater than the discharge number, N_{qp}.

A similar study conducted by Nagata (1975) found that the ratio between circulation number and pumping number was within the range 1.8 and 1.9, which is almost half the value obtained by Costes and Couderc (1988). They attributed the disparity to the use of different experimental methods for measuring velocities. The results of Costes and Couderc could be more reliable than Nagata's because they used the more accurate

LDA measurements. Recently, Lamberto *et al.* (1999) reported a similar ratio ($N_{qc}/N_{qp} \approx$ 4) from their study of laminar flow structure in a stirred vessel agitated by a radial flow impeller.

Dong *et al.* (1994a) used LDA to study turbulent flow in an unbaffled vessel agitated by a paddle impeller (radial flow). In particular, they investigated the effects of the impeller rotational speed and clearance to vessel bottom on flow characteristics. They found that N_{qp} was independent of the impeller speed but was strongly affected by the impeller clearance and was about 0.62. They also reported N_{qc} = 2.0, which was found to be independent of impeller speed and off-bottom clearance. From the above findings the ratio N_{qc}/N_{qp} was about 3.2, which is lower than the value of 4 reported by other researchers. A good comparison, though, would require that the same type of agitator and vessel be used in all the studies, which was not the case. The main finding of Dong and co-workers was that the impeller clearance to the vessel bottom had an effect on the pumping capacity; however it did not influence the circulation capacity.

A plain disk agitator has been found to function like a radial flow impeller, at least from the flow pattern point of view (Mununga *et al.* (2001); Mununga *et al.* (2003)). Nagata *et al.* (1958) used a rotating disk (d/D = 0.513 and b/D = 0.1) in an unbaffled vessel and found that N_{qp} = 0.031, which was very close to theoretical value of 0.027. The above impeller performance values for a plain disk are of an order of magnitude smaller than that for a typical radial flow impeller.

(ii) Power Number

The power supplied to the mixing system through the agitator generates circulating capacity and a velocity head. During the mixing operation the velocity head provides the shearing action as kinetic energy that generates shear through pulsating fluid motion. Mathematically the power consumed by a mixer, which is essentially the power generated by the impeller can be expressed as

$$P = FV\,, \tag{7.8}$$

where F is the drag force and V the impeller velocity. Because of the uncertainty on the

drag coefficient Equation 7.8 can also be numerically evaluated by

$$P = 2\pi N n T \,, \tag{7.9}$$

where T is the torque exerted on a single impeller blade as shown in Equation 7.10, N is the rotational speed of the impeller and n is the number of blades on the impeller and

$$T = \sum_i (\Delta p)_i A_i r_i \,, \tag{7.10}$$

where A_i is the projected area of an elemental blade surface denoted by 'i' on the leading or trailing faces of the blade, r_i is the corresponding radial location and $(\Delta p)_i$ is the element's pressure difference between the leading and trailing faces. It follows then that the power number is defined by Equation 7.11:

$$N_p = \frac{P}{\rho N^3 D^5}, \tag{7.11}$$

(iii) Pumping Effectiveness

Mixing effectiveness (Aubin *et al.* (2001)) is a performance factor that relates to the quality of mixing. It is the rate of pumping of an impeller per unit power consumption, which is an indication of how effective the impeller is in providing the main flow responsible for mixing. Mixing effectiveness sometimes known as pumping effectiveness is expressed as:

$$\eta_e = \frac{N_q}{N_p}. \tag{7.12}$$

N_q or N_{qp} is the pumping flow number defined by Equation 7.4. Pumping effectiveness η_e is an important selection factor for impellers. When its value is low the impeller is classified as a shearing type and when it is high the impeller is referred to as a circulation type.

(iv) Pumping Efficiency

Another useful index often used to characterise the quality of mixing process is the pumping efficiency λ_p defined by Equation 7.13, which was previously employed by Wu *et al.* (2001b):

$$\lambda_p = \frac{N_q}{(N_p)^{1/3}}. \tag{7.13}$$

7.3.6 Aims of the Study

The literature has shown that unbaffled mixing vessels present advantages such as suitability for very viscous flow and low speed applications, and high fluid-particle mass transfer rate given the same power as baffled vessels. Medek and Fort (1994) showed that the power number in a closed fully filled unbaffled vessel was approximately half of the value obtained from a baffled vessel with a free liquid surface. However, from the review of previous studies presented above, it can be seen that not many studies have been conducted on mixing unbaffled vessels.

The study of mixing presented in this thesis is concerned with an unbaffled vessel. The investigation is divided into two main parts. The first is deals with mixing agitated by a plain disk. The second part deals with agitation using a bladed paddle impeller. The objectives of each part of the study are presented next.

(i) Plain Disk

Of all agitators, the plain disk is the simplest in terms of design and construction. It also presents other advantages such as low power consumption even at high Reynolds numbers and suitability for laminar flow applications. In spite of all these benefits, the review of previous studies has shown that the plain disk agitator has not been researched very much. Therefore, the present study investigates some performance characteristics of the plain disk agitator. The major objectives of this first part of mixing investigations are:

- To describe the locus of the centre of recirculation generated by a plain disk located half way between the top lid and the bottom surface of the vessel, as well as at an off-centre position. No previous study has provided a detailed study to predict the movement of the recirculation centres or Isolated Mixing Regions (IMRs) within the mixing vessel agitated by a plain disk.

- To examine the effect of varying the off-bottom axial location of the agitator on global mixing parameters such as circulation and pumping flow rates, as well as their non-dimensional numbers.

- To investigate whether there is a transition of flow pattern from a double-loop to a single-loop associated with a reduction in off-bottom clearance, as previously observed by other researchers using radial flow impellers.

(ii) Bladed Impeller

Most of the studies on flow number and power number in the literature are for vessels fitted with baffles (Nagata (1975); Tiljander and Theliander (1993); Myers and Bakker (1998); Wu *et al.* (2001b)). There is a need to investigate how the flow number, power number and pumping effectiveness are affected by the Reynolds number and the impeller width in an unbaffled vessel. Therefore, in the second part of the study, involving agitation with a bladed paddle impeller, the main aims are:

- To numerically predict the relationship between the impeller Reynolds number, on one hand, and the pumping number (Nq), the power number (Np), on the other hand.

- To establish the effect of varying the impeller blade width (b) on the pumping number (Nq), the power number (Np), the pumping effectiveness ηe and the pumping efficiency λ_p.

7.4 Methods

7.4.1 Procedure and Grid Construction

The general procedure adopted to build the two models, the plain disk and the bladed impeller, is presented followed by specific details related to the design of each model.

(i) General Procedure

Numerical solutions involved three main stages: pre-processing, processing and post-processing. The pre-processor software package Gambit was used to create a model ready for use in the CFD simulation environment. The creation of the model involved constructing the model geometry, meshing the model and specifying zone types on it. During the processing stage, the commercial software Fluent was used. Fluent's solution procedure involved importing the geometry and model grid, choosing the basic equations to be solved, specifying boundary conditions, specifying fluid properties, adjusting the solution control parameters (optional) and conducting the numerical solution. Once simulations were completed, post-processing involved examining the results. Depending on their quality, decisions had to be taken for further action. In most cases a revision of the numerical or physical model was effected until such time that a stable and fully converged solution was obtained. Post-processing was carried out using Fluent's post-processor primarily for qualitative examination of the flow patterns. Quantitative examination of simulated results was done both in the Fluent environment and using an in-house software based on the Matlab code and later converted to "C" code to accelerate processing speed. After initial simulations were found to be satisfactory, a grid resolution study was conducted before proceeding with the bulk of simulations.

(ii) Plain Disk

The modeled mixing vessel system was a laboratory configuration of which the diagram is shown in Figure 7.1. It consisted of a cylindrical vessel of inside diameter D = 0.486 m and with an aspect ratio H/D = 1.0. The agitator employed here was a plain disk with the following specifications: d = 0.325D, width b = 0.064D. Different models were

generated using this agitator by varying its axial location along the shaft (C = 0.50D, 0.35D, 0.25D and 0.15D). A bigger disk designed to correspond with the one used by Nagata *et al.* (1958) was used mainly to duplicate some of their results for validation purposes. The disk parameters were d = 0.513D, b = 0.10D and C = 0.50D.

Due to the model symmetrical shape only one half was modeled and meshed, the advantage being to simplify the computational effort. The original grid consisted of 77 grid points in the radial direction (r) and 150 grid points in the axial direction (z) resulting in a total of 11,130 cells. In the end, the grid was refined by adapting it based on velocity gradient to ensure that the solutions were grid independent and in the end a grid with 22,148 cells was used for simulations.

The simulation fluid used was Silicone Fluid with a viscosity of 500 centistokes and a density of 969 kg/m^3. The continuity and momentum transport equations were solved using Fluent's CFD versions 5.5.14 and 6.0.

(iii) Bladed Impeller

Since the mixing vessel was agitated by a 6 bladed impeller, only a 60˚ sector (Figure 7.6) was modeled to take advantage of the rotational symmetry of the geometry. Using the commercial software GAMBIT (version 2.0), different grids were constructed, first for grid resolution study (Table 7.1) and then for the different blade sizes investigated in this study (Table7.2). The task of generating so many models was made easier by the use of GAMBIT journal files, which automated the design of geometries and meshing. Table 7.1 shows the characteristics of the seven grids employed in this study. It can be seen that the grid density was varied from 112,358 to 553,348 structured hexahedral cells. The grids were compressed near the solid surfaces, especially rotating surfaces of the blade, to ensure adequate resolution. A grid resolution study was conducted using the grids shown in Table 7.1 by monitoring the mass flow rate through a circumferential surface located at the impeller tip radius and also the pressure difference between the leading and trailing faces of the blade. It was found that grid G6 (310,958 cells) was optimal and was therefore used in the computations. For laminar flow cases all the grids shown in Table 7.1 were sufficiently dense; however. However, for turbulent flow simulations, the grids were adapted in order to further resolve the flow near the wall

regions. The turbulent flow grids were adapted based on the "y+" value near the walls (this is discussed later in this chapter).

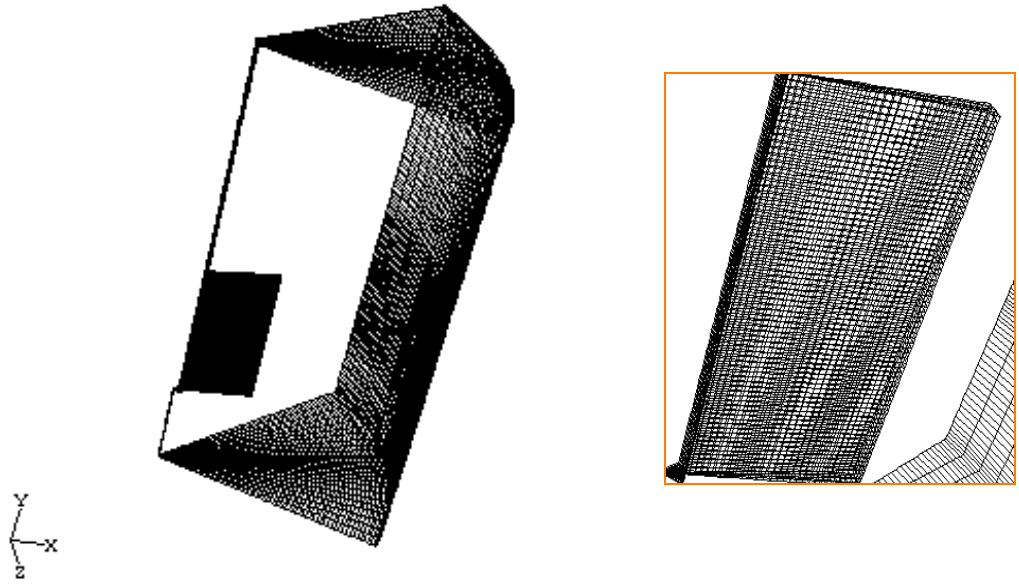

(a) (b)

Figure 7.6 The geometry and typical grid used in this study. (a) a 60 sector with a shaft and an impeller but without cyclic planes; (b) a close-up view of the meshed impeller.

The experimental fluid and the modeled mixing vessel system were as described in the case of the plain disk except for the agitator. This mixing system was equipped with a 6 bladed paddle impeller with a diameter d = 0.162 m (or $D/3$). The impeller was located with an off-bottom clearance $C = D/3$, which has previously been found to be an optimum impeller position (Kuncewicz (1992)). Kuncewicz found that at $C = D/3$ the total secondary circulation reached the highest value, which would imply that mixing time would be the lowest. In addition, Mishra and Joshi (1993) reported that $C = D/3$ and d = $D/3$ were associated with the maximum flow number for a disk turbine. The liquid height, H, was equal to the vessel diameter D, which implies that the aspect ratio H/D = 1.0. Seven impellers with different blade widths (b) but a constant blade thickness of 8 mm were employed in simulations and will be referred to as P1 through to P7. The different blade widths were normalised with respect to the vessel height (H)

and their respective values are shown in Table 7.2.

Table 7.1 Different grids used for the resolution study.

	Number of cells (60° sector)			
Grid #	**Axial**	**Radial**	**Azimuthal**	**Total**
G1	96	52	24	112,358
G2	104	58	26	148,984
G3	116	65	30	211,468
G4	131	70	32	283,904
G5	142	72	30	303,166
G6	133	81	30	310,958
G7	166	95	36	553,348

Table 7.2 Impellers used for modelling: seven blade sizes are described.

Impeller ID #	Blade width - b (mm)	b/b2	(b/H)x100%
P1	16.2	0.5	3.3
P2	32.4	1.0	6.7
P3	48.6	1.5	10.0
P4	64.8	2.0	13.3
P5	97.2	3.0	20.0
P6	145.8	4.5	30.0
P7	194.4	6.0	40.0

7.4.2 Governing Equations

(i) Plain Disk

The conservation equations used in simulating the mixing flow with agitation by the plain disk are identical to those employed for the vortex breakdown (see section 3.3.2).

(ii) Bladed Impeller

In the case of the bladed impeller the equations solved in the simulations are the standard conservation equations for mass and momentum, in addition to those associated with turbulence (section 7.4.7). As the impeller blades move through the fluid, to accurately describe such motion, the momentum equations for the entire domain are solved in a rotating reference frame (RRF). This means that the frame of reference is attached to the impeller, which appears to be stationary while the vessel wall, bottom and top ends appear to be moving at the same speed as that of the frame but in the opposite direction. The absence of baffles means that the RRF, rather than the Multiple Reference Frame (MRF), is the preferred option of treating this flow within the FLUENT environment. The distinction between the two solution methods will be elucidated in section 7.4.4.

Given that the fluid used is incompressible, the modified conservation equations take the form:

$$\nabla \cdot \mathbf{u} = 0\,, \tag{7.14}$$

$$\nabla \cdot (\rho \mathbf{u}\mathbf{u}) = -\nabla p + \nabla \hat{o} + s\,, \tag{7.15}$$

where **u** is the velocity relative to the frame of reference introduced by working in a non-inertial frame, τ is the stress tensor and s represents the source terms, i.e. the Coriolis and centrifugal forces,

$$\mathrm{s} = -2\rho \grave{U} \times u - \rho \grave{U} \times (\grave{U} \times r)\,, \tag{7.16}$$

where **Ω** is the angular velocity of the frame. Equations 7.14 and 7.15 are the vector

representations for the conservation of mass and momentum respectively.

7.4.3 Boundary Conditions

Gelfgat *et al.* (1996) found that a confined axisymmetric swirling flow in a closed circular cylinder with a rotating lid was still stable up to Re = 2000. In a related study, Hourigan *et al.* (1995) concluded that the apparent non-axisymmetry of the flow observed by other researchers was deceptive. Based on the above findings, the flow generated by the plain disk rotor was assumed to be symmetrical in the azimuthal direction. Therefore, only one half of the geometry was modeled. The shaft and disk surfaces were assigned a moving wall boundary condition with a defined absolute motion and no slip shear condition. The cylindrical vessel wall, the vessel bottom and top lid were treated as stationary walls with no slip shear condition.

In the bladed impeller set up, using the rotating reference frame (RRF) approach, the impeller and shaft were set to be stationary with respect to the rotating frame. The top, bottom and side walls were assigned a rotational velocity equal in magnitude but opposite in sign to the rotation of the frame of reference. All solid surfaces were given a no-slip velocity condition. As previously mentioned, due to the rotational symmetry of the geometry only $1/6^{th}$ of the vessel was modeled. Therefore, a periodic boundary condition was imposed at the two end surfaces in the azimuthal direction.

7.4.4 Solution Techniques

As mentioned earlier, most stirred vessel configurations are equipped with baffles attached to the inner surface of the cylindrical wall. In such a set up, flow is very unsteady and therefore, complicated to model numerically. In both baffled and unbaffled vessels the periodic motion of the blades through the solution domain is problematic. Because of these inherent complications, a number of approaches have been devised to approximate the motion of the impeller as it moves within the fluid. The most important of these techniques involve the use of:

- Experimental data,

- The rotating frame model,
- The multiple reference frames model and
- The sliding mesh model.

The first technique, using experimental data, models the motion of the impeller implicitly whereas the other techniques model the impeller directly or explicitly. These approaches are briefly described in the following sections:

(i) Experimental Data

With this method, the impeller is modeled using time-averaged velocity data and other experimental data to represent its motion. The experimental velocities are assigned to the outflow of the impeller leaving the CFD to solve the flow in the other parts of the mixing vessel. Here, the impeller is somehow treated like a "black box" with velocity data prescribed on one or two edges. In general, the three velocity components should be assigned to the relevant edges of the impeller. Quantitative as well as qualitative validation of velocity data and the well known double loop flow pattern have been presented by Bakker and Van den Akker (1994). When the flow is turbulent both the turbulent kinetic energy and dissipation rate must be prescribed. Normalization and interpolation of the experimental data including radial and axial locations is usually required since the experimental data is likely to have been generated from different flow conditions.

(ii) Rotating Reference Frame (RRF)

The single rotating frame option is normally used to model flows in mixing vessels when baffles or stators are not present, such as in unbaffled mixing vessels. This way, the flow is steady relative to the rotating (non-inertial) frame, which simplifies the analysis. The application of the rotating frame model in mixing entails that the momentum equations for the entire domain are solved in the non-inertia frame with the angular velocity of the impeller Ω also being that for the frame. This implies that the impeller is at rest in the rotating frame. However, the vessel and the two endwalls (i.e.

the bottom wall and the top lid) assume the angular velocity of the impeller but in the opposite direction (-Ω). This solution method suits unbaffled vessels with axisymmetric bottom walls.

Figure 7.7(a) depicts the configuration in the laboratory frame of reference. This is a non-accelerating coordinate system, whereas Figure 7.7(b) shows the same system in a transformed rotating frame, which represents the accelerating frame of reference. By having a coordinate system that experiences a constant acceleration in the radial direction like the impeller, the flow can be solved as if it was steady.

(a)

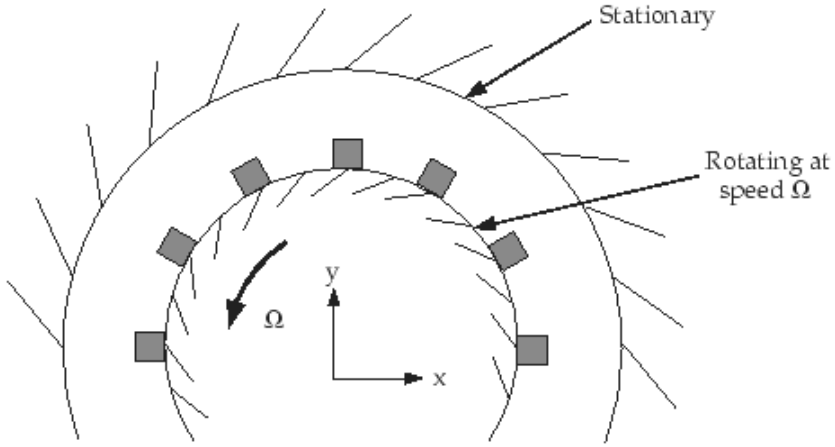

(b)

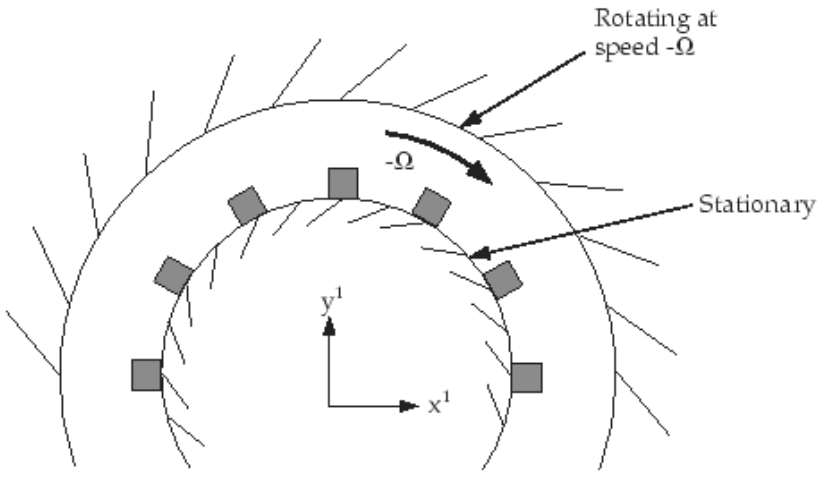

Figure 7.7 Transformation of coordinates: from (a) original inertia frame of reference to (b) rotating reference frame (Fluent 6.1.18 manual, 2003).

As mentioned above, the RRF technique was used for modeling, which meant that a single frame of reference attached to the impeller was considered in solving the equations of motion. The segregated solution algorithm with implicit solver formulation was employed as well as a relative velocity formulation.

The first attempt to simulate flow in an unbaffled vessel without recourse to empirical data was by Dong *et al.* (1994b). They predicted a 3D turbulent flow field in an unbaffled vessel agitated by an 8-blade paddle impeller using the RRF, which constituted a major step forward in the capability of CFD. By employing the RRF in the numerical model, they were able to calculate in a domain exactly as in the real agitation system. Hence, it allowed the entire 3D flow field to be fully predicted.

(iii) Multiple Reference Frames (MRF)

There are many cases where baffles and other complex internals are present in addition to a rotor or impeller. In such cases, it is not possible to render the computational problem steady by simply choosing a calculation domain that rotates together with the impeller. A typical example where this situation occurs is in turbomachinery applications where the interaction between the stator and the rotor is important, usually when they are in close proximity. This situation is resolved by employing either the MRF model or the sliding mesh model.

The MRF model is a modified version of the rotating frame model. This is also a steady state solution approach which uses more than one rotating (or non-rotating) reference frame in performing simulations. A rotating frame of reference is employed for the region that encloses the rotor or impeller, while a stationary frame is used in the regions with stationary components. As in the case of the rotating reference frame model, the impeller is considered at rest in the rotating frame and the vessel walls and baffles are at rest in the stationary frame. The computational domain is also divided according to the number of frames of reference. For the case of a baffled mixing vessel with one impeller, the grid region surrounding the impeller is assigned the rotating frame, whereas the stationary frame is attached to the remainder of the domain. The momentum equations are solved in the corresponding frames and a steady transfer of information is made at the interface between the two grid zones (moving and stationary)

while the solution process progresses. The MRF model is best suited to applications where the flow at the boundary between the adjacent zones that move at different speeds is nearly uniform. That is, when the interaction between the rotor and the stator is relatively weak.

Luo *et al.* (1994) developed the MRF approach, the solution of which assumes steady state conditions for the flow field simulation. This results in substantial savings in computational resources, especially time, when compared with the sliding mesh method (SM: is discussed in the next section). Both the SM and the MRF approaches are fully predictive methods that allow simulation of virtually any impeller and vessel geometry without recourse to experimental data. However, in applications where transient simulations are required (such as where there is a strong impeller-baffle interaction) the sliding mesh model should be used rather than the MRF model.

(iv) Sliding Mesh (SM)

The grid set up for the sliding mesh method is divided in two regions: the outer region mesh associated with the vessel and baffles remains stationary while the inner region surrounding the impeller physically rotates relative to the stationary mesh. This motion is not continuous but executed in small discrete steps while the solution progresses. The impeller is stationary with respect to the moving mesh region, as are the baffles and the walls with respect to the stationary region of the mesh. In doing so, the impeller is realistically modeled. For each step motion of the moving grid, conservation equations are iteratively solved until convergence is reached. Information is exchanged at the cylindrical interface between the two grids as they slide past each other in a time-dependent manner.

The sliding mesh model is used when a time-accurate solution (rather than a time-averaged one) is required for the interaction between the rotor and stator. This also means that an unsteady solution must be used. This method is more accurate than steady state calculations such as the MRF method, but with a corresponding penalty in the calculation time, which can be an order of magnitude higher. Quite often the solution from the MRF model is used as an initial condition to compute transient sliding mesh calculations. By doing so, there is no need for a startup calculation often required in the

SM approach, hence reducing the normally excessive computational time.

Luo *et al.* (1993) were the first to develop the sliding-mesh approach, where the transient simulations were conducted step by step for each relative position of the stirrer and the baffles. Their numerical work, for the first time, computed the fully time-varying flow field for both the fluid inside the impeller passages and that outside. The SM method has now been recognised and used by many researchers to model the complex flows in mixing vessels with internals (Lee *et al.* (1996), Bakker *et al.* (2000)).

7.4.5 Solution Controls

As a result of using the segregated solver, the pressure equation was discretized with the help of the PRESTO scheme (see section 3.3), which is well suited to highly swirling flows. The other discretization schemes employed were the SIMPLEC and the second-order upwind scheme. The SIMPLEC (see section 3.3) was chosen for the pressure-velocity coupling because of its ability to allow faster convergence. The second-order upwind scheme was used for the momentum, turbulence kinetic energy and dissipation rate considering its high accuracy level, despite the fact that it is prone to slow convergence. The under-relaxation factors were generally kept at their default values and were adjusted only when it was necessary to stabilise the solution by controlling convergence.

The solution strategy for the plain disk was identical to that employed for the vortex breakdown simulations (see section 3.3.5).

7.4.6 Convergence Monitoring

Convergence was monitored by checking the information from computed residuals of all variables and also by keeping track of surface monitors. Scaled residuals were primarily used. Computations continued until the values of residuals were progressively reduced by typically five or six orders of magnitude, although in a few cases this could not be achieved. For the bladed impeller, the main convergence monitoring tools employed were surface monitors. Three surface monitors were used, one for the mass flow rate through a circumferential curved surface at the impeller blade tip radius and

two for the integral of static pressure on the leading and trailing sides of the impeller blade. For the plain disk the mass flow rate through a line (in 2D), about 5% away from the disk tip, spaning the disk thickness was evaluated and monitored as the solution progressed. Convergence was considered to have been achieved when values of the monitors were constant to within ± 0.01% over 500 iterations. Such convergence criteria are very stringent and likely to ensure that the results were fully converged.

7.4.7 Turbulence Modelling

Characterisation of flow regimes was done based on the Reynolds number, defined by Equation 7.1. This is the ratio of inertia forces, or forces that give rise to the fluid motion, to frictional forces, or those that cause the fluid to slow down. Therefore, the state of fully turbulent flow was considered to be reached when the inertia forces were significantly higher than viscous forces whereby $Re \geq 10^4$.

Turbulent flow is characterised by fluctuations in the mean velocity and other variables. It is therefore necessary to incorporate the effect of these fluctuations into the CFD model to ensure that simulated results are meaningful. This is achieved by using turbulence models, which are included in the Navier-stokes equations. The most widely used turbulence models for calculating industrial flows are based on the Reynolds-Averaged Navier-Stokes (RANS) models, where time-averaging of the conservation equations is employed. This way, the velocity is represented as the sum of two components, one being steady and the other fluctuating as shown in Equation 7.14

$$U = U_i + u_i' \ . \tag{7.14}$$

By time-averaging over so many cycles, the fluctuating components disappear except for the term representing the product of two fluctuating velocity components. The general form of the Reynolds Averaged Navier-Stokes equation for momentum is defined as

$$\frac{\partial(\rho U_i)}{\partial t} + \frac{\partial}{\partial x_j}(\rho U_i U_j) = \frac{\partial P}{\partial t} + \frac{\partial}{\partial x_i}\left(\mu\left(\frac{\partial U_i}{\partial x_j} + \frac{\partial Uj}{\partial x_i} - \frac{2}{3}\frac{\partial U_k}{\partial x_k}\delta_{ij}\right)\right) \quad (7.15)$$

$$+ \frac{\partial}{\partial x_{ji}}\left(-\rho\overline{u_i' u_j'}\right) + \rho g_i + F_i ,$$

where ρg_i is the gravitational force, F_i is a generalised force term, δ_{ij} is the Kronecker delta which serves to make the formula applicable to the normal Reynolds stresses for which $i = j$. The new terms involving $\overline{u_i' u_j'}$ are part of the Reynolds stresses which constitute new unknowns. To evaluate these new unknowns, relationships with other known variables have to be established. This task is accomplished by a variety of turbulence models of which the main ones are:

- The RANS-based two-equation models: Standard k-ε, RNG k-ε, Realizable k-ε, Standard k-ω and the shear stress transport k-ω.
- The Reynolds Stress Model (RSM).
- The Large-Eddy Simulation (LES) model.

(i) The Boussinesq Hypothesis

The Boussinesq hypothesis assumes that Reynolds stresses can be represented using the gradients of the mean velocity:

$$\rho\overline{u_i' u_j'} = \frac{2}{3}\rho k\delta_{ij} + \left(\mu_t\left(\frac{\partial U_i}{\partial x_j} + \frac{\partial U_j}{\partial x_i}\right)\right), \quad (7.16)$$

where the constant μ_t represents the eddy or turbulent viscosity. By substituting Equation 7.16 into Equation 7.15 a new term μ_{eff} known as the effective viscosity is introduced:

$$\mu_{eff} = \mu + \mu_t .$$

(7.17)

It therefore follows that the kinetic energy of turbulence is introduced to relate the three fluctuating components of velocity as follows:

$$k = \frac{1}{2}\left(\overline{u'^2} + \overline{v'^2} + \overline{w'^2}\right).$$

(7.18)

Turbulence models are then used to calculate the Reynolds stresses to be substituted in Equation 7.15. To do this, the turbulence models use some approximations depending on the flow physics of a specific problem.

(ii) Turbulence Models

Brief descriptions of the models used in the present study are presented in the following sections.

(a) The Standard *k-ε* Model

The standard *k-ε* model (Launder and Spalding (1974)) is a semi-empirical model that uses empirical constants to solve two transport equations. These are for the kinetic energy of turbulence *k* and the rate of dissipation of turbulence *ε*. From the solution of *k* and *ε* the turbulent viscosity is computed by

$$\mu_t = \rho C_\mu \frac{k^2}{\varepsilon},$$

(7.19)

where C_μ is a constant which has a value of 0.09 obtained from experimental data.

Having computed the turbulent viscosity μ_t and the turbulent kinetic energy *k,* the Reynolds stresses can be computed from the momentum equations. Furthermore, the

new velocity components obtained from the momentum equations are used to compute the turbulence generation term and the calculations proceed iteratively until a converged solution is reached.

The standard k-ε model has been used in a variety of engineering applications for many years now, especially those associated with very high Reynolds numbers. It is credited for being very computationally economical and robust. However, this turbulence model is not very accurate especially when applied to flows with high strains.

(b) The RNG k-ε Model

The Renormalization Group or RNG k-ε model (Yakhot and Orszag (1986)) is another of the two-equation RANS models which was developed to address some of the weaknesses exhibited by the standard k-ε model. In this model the constants in the k-ε equations are derived using the renormalization group (RNG) theory. This model has been known to perform better than the standard k-ε model when used in applications involving more complex shear flows and flows with high strain rates, swirl and separation. After solving the differential equation for turbulent viscosity, the coefficient C_μ is found to assume the value of 0.0845. This is about 7% less compared with the empirical value above (Equation 7.19). This is achieved partly by solving a differential equation to obtain the turbulent viscosity and also by modifying the dissipation equation to better represent complex flows.

(c) The Shear Stress Transport (SST) k-ω Model

The flows in the transitional region were modeled using the two-equation k-ω turbulence model. This model has two options, the standard k-ω (Wilcox (1993)) and the SST k-ω model of Menter (1994). In this work only this newly incorporated shear stress transport (SST) k-ω model was used because of its applicability to transitional flows. One advantage of this model is that, unlike other RANS-based models, it can be integrated to the wall without using any damping functions.

(d) The Reynolds Stress Model (RSM)

In this model, the Boussinesq hypothesis is not valid so the stresses $\overline{u_i' u_j'}$ are computed individually. As a result, for 2D models like the plain disk, four transport equations are added. In contrast, for 3D models like the bladed impeller, six additional transport equations are required. The invalidity of isotropic turbulent viscosity is relevant for flows with high swirl and rapid changes in the strain rate which are well treated by this model. Compared to the other RANS-based models, the RSM model provides good predictions for most types of flows. The main disadvantage is that it takes longer to directly solve all the transport equations for the Reynolds stresses compared with the time it takes to compute the two-equation models. In view of the relatively good accuracy that the RSM method provides and the fact that the large eddy simulation model (LES) requires considerably more computational resources, this method has become the preferred option in applications such as mixing in stirred vessels.

(iii) Near Wall Grid Refinement

The grids shown in Table 7.1 were sufficiently dense for laminar flow conditions. However, grid refinements were required for turbulent flow conditions. To better resolve the flow in the near wall regions, especially the rotating walls of the impeller blades, solution adaptive refinements were applied. By adapting the mesh this way cells were added where they were required without affecting the other regions of the flow domain, therefore keeping the grid size to an optimum level. Moreover, it is always very difficult to correctly predict the required resolution of the mesh near walls while generating the grid. Hence, the automatic y^+ adaption is generally the best way to refine the mesh during the solution process. Great care was taken to ensure that the centroid of the first cell near the wall was such that $y^+ \approx 1$, which is the optimum value when using the enhanced wall treatment.

On the whole, the journey towards improving CFD techniques, especially turbulence modeling, has not always yielded encouraging results. Many researchers have continually reported substantial under-predictions of turbulence levels compared to experimental data (Ranade and Joshi (1990b); Tabor *et al.* (1996); Daskopoulos and

Harris (1996); Ng *et al.* (1998)). So far, for good prediction the best CFD turbulence modeling method is the Large Eddy Simulation also known as the "LES" (Eggels (1996); Revstedt *et al.* (1998); Derksen (2001)). However, this approach is computationally very intensive.

7.5 Results and Discussion

In this section, numerical results of mixing in a stirred vessel are presented. The results are grouped into two, depending on the type of agitator used to stir the fluid. The first part deals with predictions from simulations using a plain disk as agitator and the second part is concerned with results from simulations where a bladed (paddle) impeller is the agitator.

7.5.1 Plain Disk

The plain disk results presented here consist of flow visualization using streamlines, locus of the centre of recirculation, and the dependence of global mixing quantities on Reynolds number. These global quantities are the circulation flow rate (Q_c) and circulation flow number (N_{qc}), the pumping flow rate (Q_p) and the pumping flow number (N_{qp}). All simulations involving the plain disk were performed with the assumption that the flow was laminar. This assumption is justified based on the evidence from vortex breakdown studies (Lopez (1990); Bhattacharyya and Pal (1998)), where the flows can be considered as similar to the present situation. The experimental results by Nagata *et al.* (1958) are the closest data involving a plain disk agitator that this author found in the open literature. Hence, Nagata's system specifications were duplicated numerically and the predicted results (pumping flow number N_{qp}) compared with their data for validation purposes.

(i) Flow Visualization

Two plain disk sizes were used for the flow visualization results described in this section. These are, a smaller disk with a diameter $d = 0.325D$ and a larger disk with $d = 0.50D$. The larger disk was located at an off-bottom clearance $C = 0.50D$, whereas the smaller disk was placed at four different axial locations namely, $C = 0.50D$, $C = 0.35D$,

$C = 0.25D$ and $C = 0.15D$. In this thesis the two disks are sometimes referred to as d_0325 and *d_050* while the four axial positions as *C*_0.50, *C*_0.35, *C*_0.25 and *C*_0.15.

The flow patterns generated by a centrally located disk (Figures 7.8(a-c)) are symmetrical with respect to the disk horizontal mid-plane. This is due to the geometrical symmetry of the system. In Figure 7.8(a), a double circulation loop is clearly visible, i.e. two recirculation zones, above and below the impeller. Also, two recirculation centres are shown symmetrically located on either side of the impeller. As the Reynolds number increases the flow topology changes accordingly. The radial flow emanating from the disk becomes stronger hence altering the shape of the two recirculation regions resulting in the movement of the recirculation centre away from the disk. It was observed, as can be seen in Figures 7.8(a-c), that despite increasing the Reynolds number from $Re = 20$ to 1000 the flow remained symmetric about the impeller. It is important to note that with a smaller size agitator dead regions appear in the corners. The level of fluid motion in the proximity of these corners is dependent on the Reynolds number. After the agitator was moved below the mid-horizontal plane (i.e. $C < 0.50D$) the flow topology changed. Figures 7.8(d-f) show flow visualization for the case where $C = 0.35D$ still exhibiting two recirculation regions but this time the flow is not symmetric about the impeller. The recirculation region above the impeller grew in size while the bottom region became smaller but with faster moving fluid. The pumping jet remained horizontal, impinging on the vertical cylindrical wall at right angles. For this reason, the plain disk can be regarded as a quasi-radial flow impeller. With a high Reynolds number, small recirculation regions appeared in the top and bottom right corners. The formation of these second recirculation regions can be attributed to the fact that for low Reynolds numbers the radial jet emanating from the agitator tends to be diverted upwards and downwards parallel to the vertical wall (Figures 7.8(a) & (d)) but when the Reynolds number is relatively higher it tends to deflect at an angle away from the vertical wall, while still moving upwards and downwards as illustrated in Figures 7.8(f) and 7.9(c).

Figures 7.9(d-f) depict the flow with the impeller axially located much closer to the vessel bottom with an off-bottom clearance $C = 0.15D$. In this case the flow is very

asymmetrical, and for the first time the pumping jet emanating from the disk is similar to the jet from an axial flow impeller. In other words, the pumping jet is no longer purely radial but is inclined at an angle of approximately 45° for Re = 20 and about 80° for Re = 1000 with respect to the horizontal plane cutting through the middle of the disk. Figures 7.9(d-f) shows the upper recirculation region extending beyond the disk to occupy a significant portion of the bottom region as the Reynolds number increases. This behaviour has been reported by other researchers in the case of baffled vessels agitated by radial flow impellers (Komori and Murakami (1988); Montante *et al.* (1999)). Using a radial flow impeller, Montante *et al.* (1999) found that at an impeller clearance C = 0.20D the characteristic double-loop flow pattern undergoes a transition to a single-loop pattern with the impeller stream direction becoming partly axial and inclined at around 25° to 30° to the horizontal. One advantage of this flow transition, from double loop to single loop is that it causes a sharp fall in power number (N_p) (Sicardi *et al.* (1979); Conti *et al.* (1981). This is a very attractive situation for process industry for instance. Conti *et al.* also observed that this flow transition due to the reduction of off-bottom clearance ($C/D \approx 0.22$ in their case) also resulted in a reduction of the "just suspended speed" (this is the minimum impeller speed to cause suspension of particles off the bottom of a mixing vessel). Clearly, knowledge of this transitional off-bottom disk clearance is vitally important in solid suspension applications. It is therefore encouraging to know that a plain disk can also trigger a flow transition from a double-loop to a single-loop.

In Figure 7.10(a), the larger disk ($d = 0.50D$) is shown centrally located at an axial location corresponding to $C = 0.50D$. As in the previous case where the smaller disk was centrally located (Figures 7.8(a-c)), the flow topology exhibits a high degree of symmetricity about the horizontal mid-plane through the disk. Again, when the Reynolds number is low (Re = 20) the radial jet is diverted parallel to the vertical cylindrical wall (Figure 7.10(a)). However, it is deflected away from the wall when the Reynolds number increases (Figures 7.10(b) & (c)). The most striking observation is the undulation of streamlines next to the surface of the shaft observed particularly at Re = 1000. The waviness distortion of streamlines is akin to vortex breakdown formation along the axis of a swirling flow (vortex breakdown was the subject of the preceding chapters). These wavy streamlines near the shaft surface are thought to be the early

indication of flow recirculation. This tendency was not observed when a small disk was employed (Figure 7.8(c)) although the Reynolds number was the same as in Figure 7.10(c). It can be deduced that this phenomenon is dependent on the size of the disk, and of course the Reynolds number and gap between the impeller and the endwall. This gap is similar to the aspect ratio in the case of confined swirling flow with rotating endwall. The vortex breakdown set up is essentially an extension or special case of the current mixing configuration when the plain disk assumes the size of the inner cylinder diameter and is located at the top end to replace the top lid (i.e. $C = D$). It is this striking similarity between the two systems that explains the presence of the two studies in this thesis.

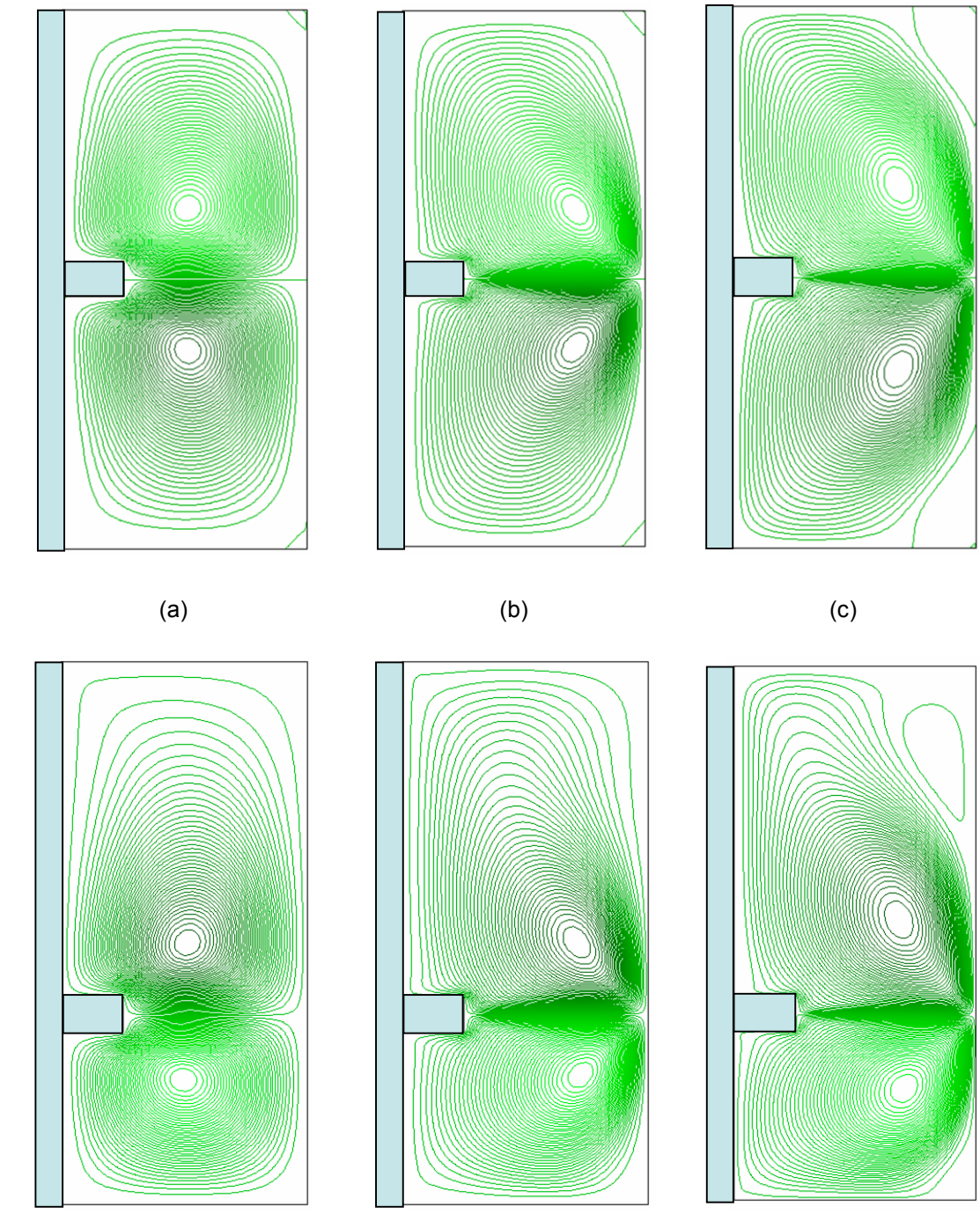

Figure 7.8 Flow visualization showing stream lines in a mixing tank agitated by a plain disk d = 0.325D: C = 0.50D: (a) Re = 20; (b) Re = 300; (c) Re = 1000; and C = 0.35D: (d) Re = 20; (e) Re = 300; (f) Re = 1000.

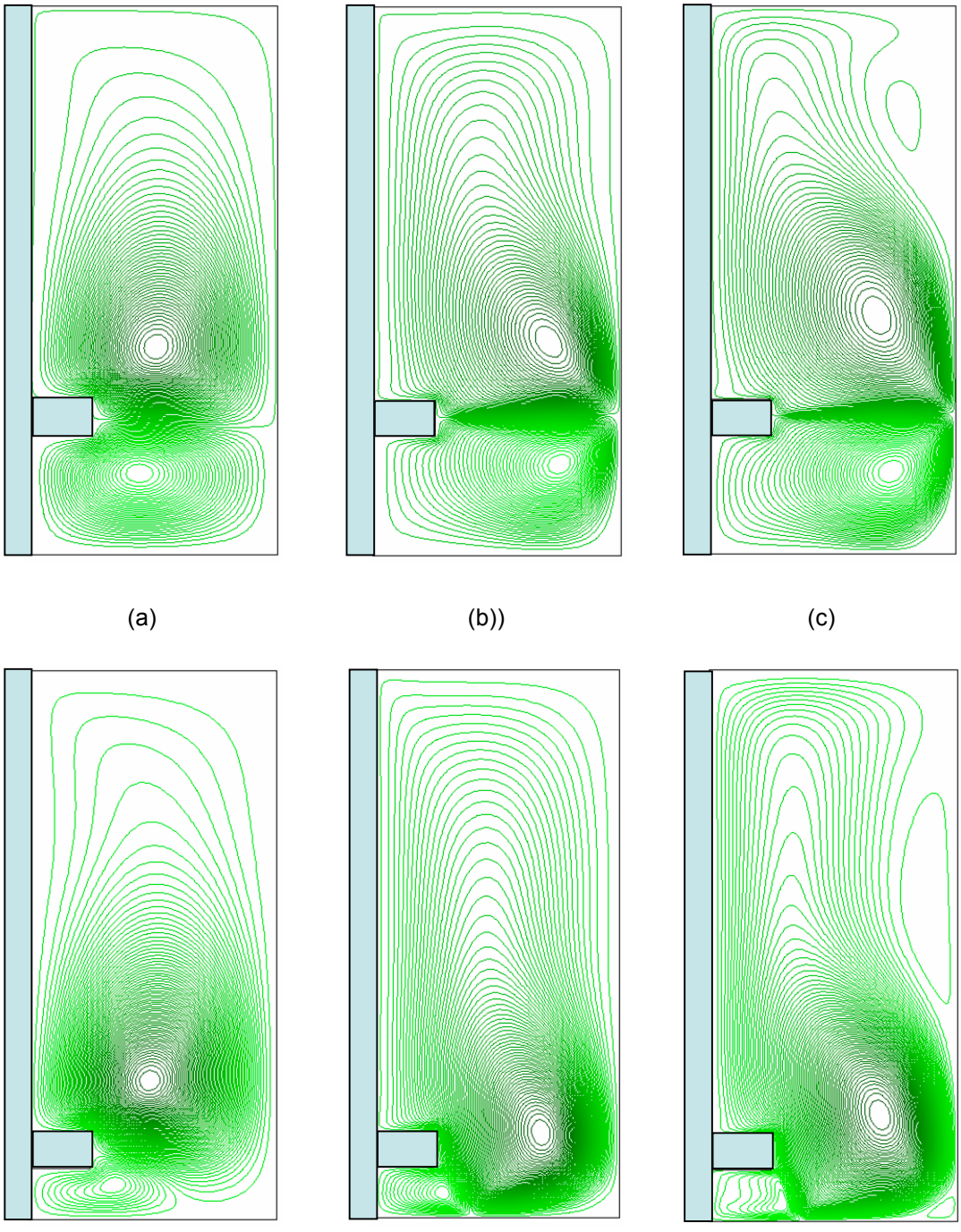

Figure 7.9 Flow visualization showing stream lines in a mixing tank agitated by a plain disk d = 0.325D: C = 0.25D: (a) Re = 20; (b) Re = 300; (c) Re = 1000; and C = 0.15D: (d) Re = 20; (e) Re = 300; (f) Re = 1000.

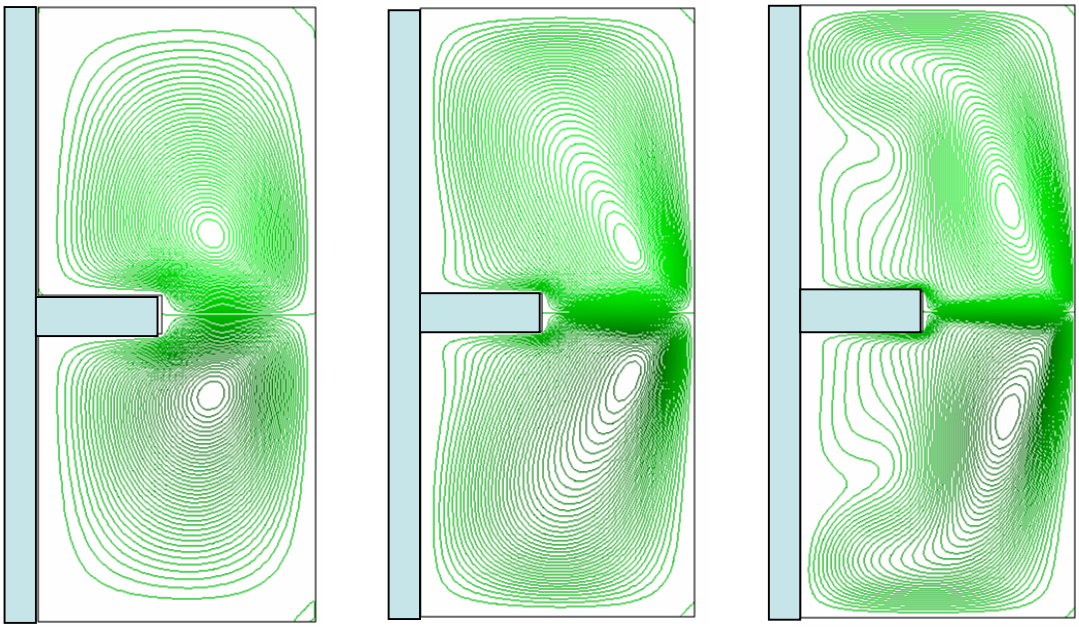

(a)) (b) (c)

Figure 7.10 Flow visualization showing stream lines in a mixing tank agitated by a plain disk: d = 0.513D, C = 0.50D and (a) Re = 20; (b) Re = 300; (c) Re = 1000.

(ii) Locus of the Recirculation Centre

An important step in understanding the behaviour of the Isolated Mixing Regions or *IMRs*, usually present in laminar mixing, is to be able to predict their movement under different mixing conditions. These regions form around the centres of recirculation and do not actively interact with the rest of the flow in the mixing vessel. In fact, Makino *et al.* (2001) showed that the centres of these *IMRs*, correspond to the centre of the recirculation regions (described in the next section). They examined the movement of the centres of the *IMRs* and found that it was shifting outwards, away from the impeller tip towards the vessel cylindrical wall. The same tendency was observed by Lamberto *et al.* (1999). The work presented here extends the above mentioned studies and those of Mununga *et al.* (2001) by covering a wide range of *Re* using different configurations as described later in this section (see also Mununga *et al.* (2003)).

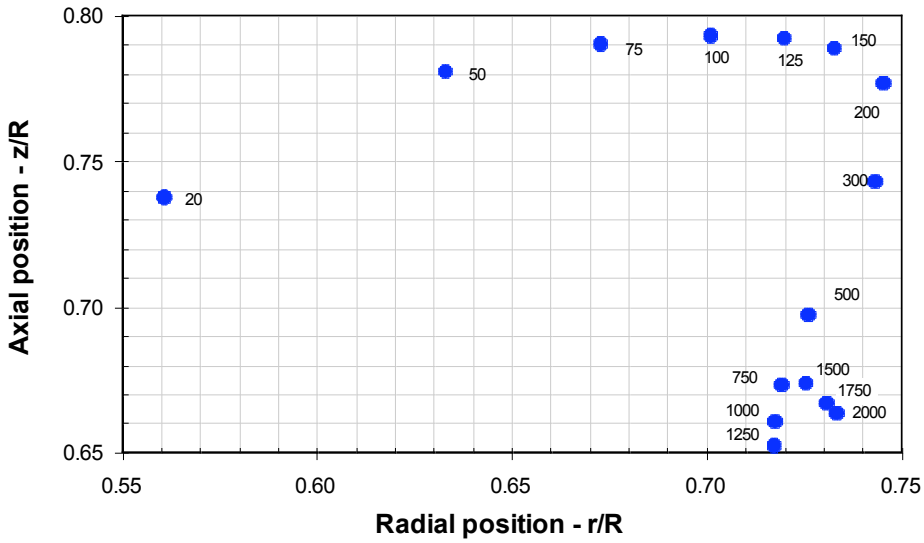

(a)

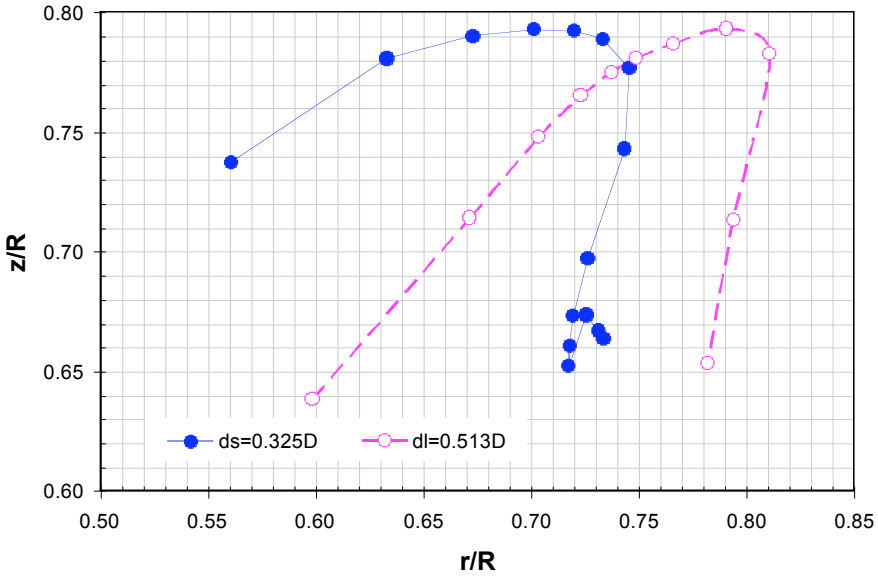

(b)

Figure 7.11 The locus of the centre of the lower recirculation region: (a) small disk (d0325) with C = 0.25D; (b) open symbols are for the smaller disk (d_0325) and filled symbols for the larger disk (d_0513) with both located at C = 0.50D.

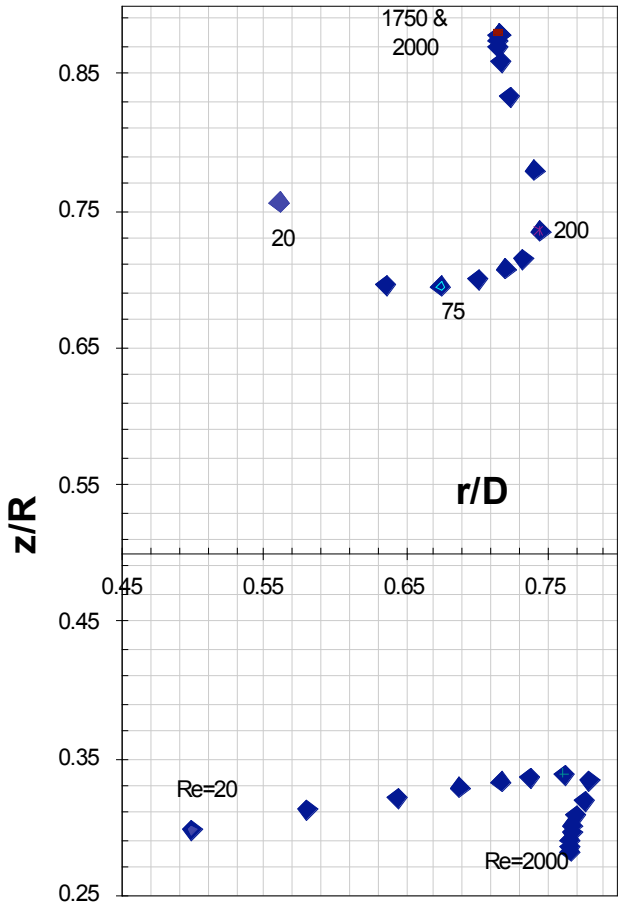

Figure 7.12 The loci of the centres of the lower and upper recirculation regions for the smaller disk (d0325) located at C = 0.25D.

Figures 7.11 (a) and (b) describe the loci of the centre of recirculation region (or centre of an *IMR*), in the lower left half of the cylinder, for different *Re*. The axial (z) and radial (r) positions are normalised with respect to the vessel radius (R). Each point in these figures corresponds to a specific Reynolds number as follows: *Re* = 20, 50, 75, 100, 125, 200, 300, 500, 750, 1000, 1250, 1500, 1750 and 2000.

Figure 7.11(a) shows the locus of the small disk (d_0325) at a clearance of $C = 0.25D$ while Figure 7.11(b) illustrates the loci of both the small disk and the larger disk (d_0513) which is identical to the one used by Nagata *et al.* (1958). Because of symmetry, it was found that the centres of the two recirculation regions (lower and

upper) followed identical loci; hence only one of them is shown here. In Figure 7.11(a) the centre of the *IMRs* was seen to initially move radially away from the disk or axis of rotation, as described by previous researchers Lamberto *et al.* (1999). What other researchers did not observe was that the centre tends to move closer to impeller in the axial direction. The two motions continue until a transition point is reached, when the motion of the centre reverses in both directions, moving radially towards the axis of rotation and axially, at a much faster rate, away from impeller. The turning point for this particular case was observed to be $Re \approx 150$.

In Figure 7.11(b), the loci of the centres of the lower recirculation region generated by the smaller (*d*_0325) and larger (*d*_0513) disks operating at an axial off-bottom clearance $C = 0.50D$ are presented. It can be seen that the general motion of the centres is as explained above (Figure 7.11(a)). Once again, the two loci, for the lower and upper centres were found to be identical, which validates the assumption that up to a $Re = 2000$ the flow can be treated as symmetrical and stable. This observation is in agreement with the findings of Gelfgat *et al.* (1996) and Hourigan *et al.* (1995). The locus of the centre of the larger disk appears shifted, mainly in the radial direction compared to that for the smaller disk. The differences in the axial locations may be attributed partly to the fact that the larger disk was relatively wider than the smaller disk. Another difference between the two loci is that the turning point for the larger disk was $Re \approx 500$ as opposed to $Re \approx 150$ for the smaller disk. It follows, therefore, that the positions of the *IMRs* depend on the radial size as well as the width of the disk (which would correspond to the impeller blade tip location for the bladed impeller case).

When the rotating disk is axially located in a position other than the horizontal mid-plane, it is evident that the loci of the lower and upper recirculation centres will have different shapes. Figure 7.12 illustrates this point by depicting the loci of the two recirculation centres for the same range of Reynolds numbers as above. The smaller disk was used and its axial location was $C = 0.25D$. The obvious differences between the two loci are evidence of the flow asymmetry, as expected, given that the disk is axially off-centred. The overall trend of the motion of the two recirculation centres is as explained above except that in the smaller region (lower) the initial radial shift away from the impeller is much faster than the initial axial shift. The turning point for the

lower centre is at $Re \approx 300$ whereas that for the upper centre is $Re \approx 200$. For both the lower and upper regions, it was found that beyond the turning point the axial shift became more pronounced than the radial shift.

From the above results, it can be said that the movement of the recirculation centres, and by implication the position of the *IMRs,* strongly depends not only on the Reynolds number but also on the radial and axial size of the disk and its axial location along the swirl axis.

In the next two sections the results that are presented correspond to the case where agitation is achieved by rotating the small disk *d_0325* located at four different axial locations $C = 0.50D$, $C = 0.35D$, $C = 0.25D$ and $C = 0.15D$.

(iii) Circulation Flow Number

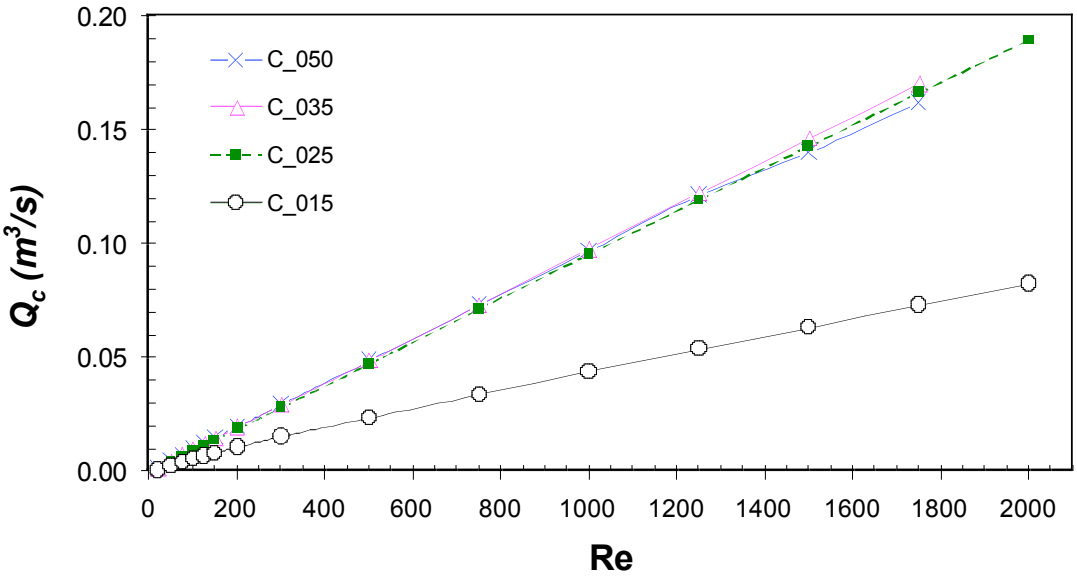

Figure 7.13 Variation of circulation flow rate with Reynolds number. The small disk is tested at four axial locations (C = 0.50D, C = 0.35D, C = 0.25D & C = 0.15D).

The location of the centre of recirculation is of critical importance in computing the values of circulation flow rate (Equations 7.6 & 7.7). Figure 7.13 shows the effect of *Re* on the circulation flow rate (Q_c) for different configurations. There appears to be a

linear relationship between the circulation flow rate, Q_c, and Re. Of particular importance is the fact that the circulation flow rate curves for C_050, 035 and 025 almost merge into a single line and lie above the one corresponding to C_015. From the above results it appears that circulation flow rate is not sensitive to the change of off-bottom clearance at least within the tested range $0.25D < C < 0.50D$. However, circulation flow rate is significantly decreased when the clearance is further reduced ($C = 0.15D$). This means that smaller impeller clearances, although useful for transitional flow from double loop to single loop, as shown in Figure 7.9(f) and also reported by Conti *et al.* (1981) and Yianneskis *et al.* (1987), are damaging to the net circulation flow rate.

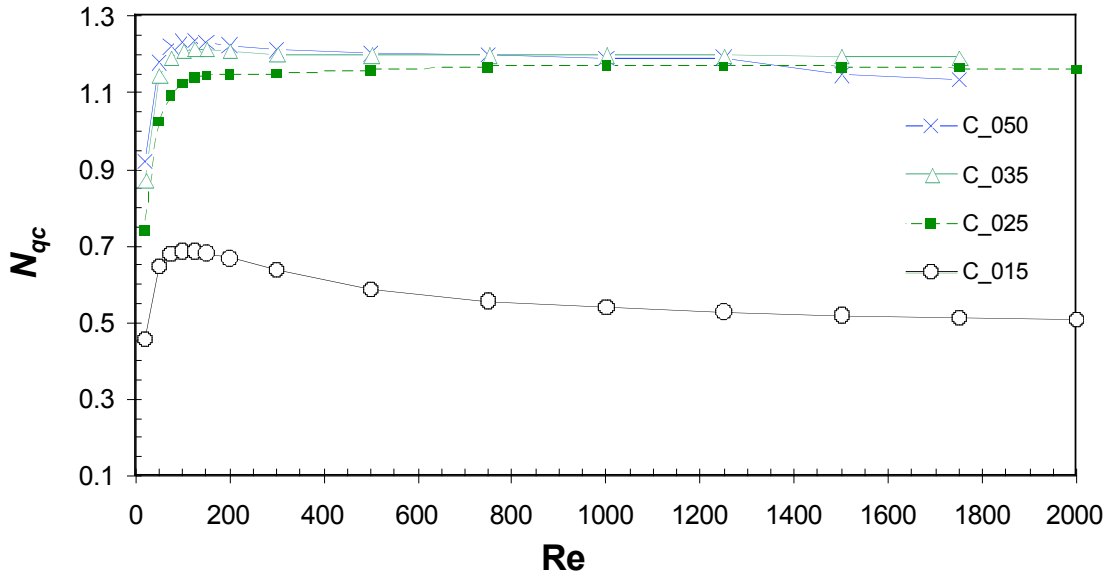

Figure 7.14 Variation of circulation flow number with Reynolds number. The small disk is tested at four axial locations (C = 0.50D, C = 0.35D, C = 0.25D & C = 0.15D).

The variation of the circulation flow number, N_{qc}, with Re is shown in Figure 7.14, which is a direct product from Figure 7.13, and as such it is not surprising that similar trends are observed. The important feature to note here is that for flow condition with $Re < \approx 300$ N_{qc} is not constant. At low Reynolds numbers the value of N_{qc} experienced a rapid rise before it attained a constant value of $N_{qc} = 1.2 \pm 0.05$ at $Re \approx 300$ for the three upper axial positions and $N_{qc} \approx 0.55$ at $Re \approx 1000$ for the lowest axial position (C_015)

of the disk. The values of N_{qc} found here are about three times smaller than the ones for radial flow impellers. This is as expected because a radial flow impeller has much greater capacity to circulate flow compared with a plain disk, which largely depends on the Ekman layer pumping effect.

(iv) Pumping Flow Number

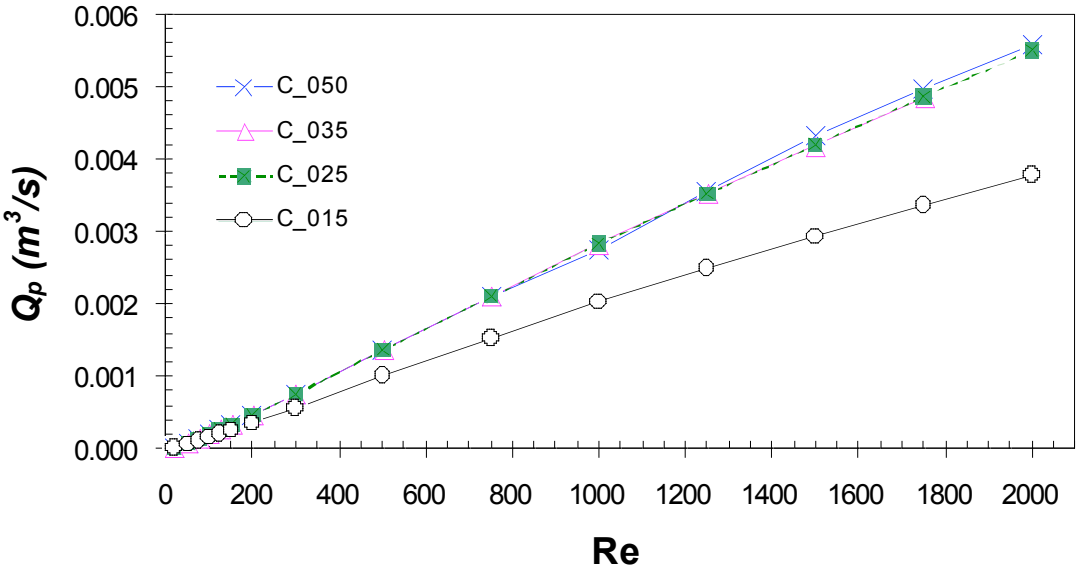

Figure 7.15 Variation of the discharge flow rate with Reynolds number. The small disk is tested at four axial locations (C = 0.50D, C = 0.35D, C = 0.25D & C = 0.15D).

The discharge flow rate (Q_p) was observed to be varying depending on the radial position at which it was computed from. Revill (1982) observed that over the years researchers have used different ways to define the pumping flow rate (Equation 7.3 & Figure 7.5). Because of the lack of a commonly acceptable definition, published values of Q_p an N_{qp} are often different. The experimental results of Nagata *et al.* (1958) for a plain disk, similar to the large disk used here (*d*_0513), were used to validate the current numerical results. From Nagata's results it was established that Q_p was computed from a radial location 3% of the vessel radius *(R)* away from the disk periphery. This was mainly to avoid excessive amount of induced flow from the lower and upper recirculation regions.

In Figure 7.15 a comparison of the discharge flow rates for the four configurations at various Reynolds numbers is presented. In all the configurations the discharge flow rate is seen to increase almost linearly with corresponding increases in Reynolds number. It is interesting to note that discharge flow rates for the disk at $C = 0.50D$, $0.35D$ and $0.25D$ are almost identical as they appear to merge. However, the discharge flow rate registers a substantial drop when the disk is operating at its lowest position (*C_015*).

This behaviour is similar to what was observed in the case of circulation flow rate. This seems to suggest that the above three clearance values are equally effective with respect to pumping flow and circulation flow (as shown earlier). It means that smaller clearances ($C \leq 0.15D$) tend to reduce the amount of discharge and circulation for all Reynolds numbers tested. The results imply that except for the case where the off-bottom clearance is very small (*C*_015) the pumping flow rate and circulation flow rate are not affected by the axial location of the disk. Incidentally, the same conclusion can be drawn for the maximum flow rate; as can be seen in Figure 7.16 the curves for the three higher clearances seem to merge. Again, the smallest off-bottom clearance registered a significantly low maximum discharge flow rate.

It was found that the radial location corresponding to the maximum pumping flow rate was observed to vary with the Reynolds number, between the tip of the disk and the vessel wall, Figure 7.17 presents the radial position at which the maximum flow rate occurs as the Reynolds number changes. The radial position was normalised by the vessel radius R. The results show that in general the radial location at which the maximum flow rate occurs remains fairly constant as the Reynolds number increases, except at the lower end of Reynolds numbers ($Re < 600$). For the three higher locations of the disk, it was found that $(r/R)_{Qp\_max} \approx 0.80$. Undoubtedly, the maximum flow rate computed at such a distant radial location would have a relatively significant contribution from induced flow. When the disk was located in the lowest position the maximum flow rate was observed to occur at about $0.4R$ for $Re < 500$. However, a

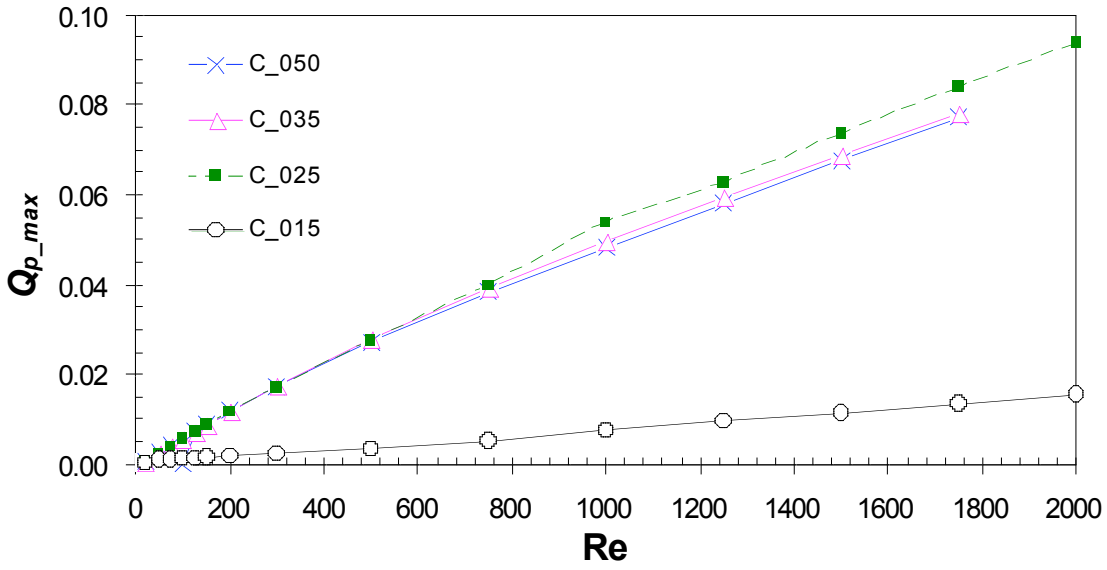

Figure 7.16 Dependence of the maximum pumping flow rate on Reynolds number.

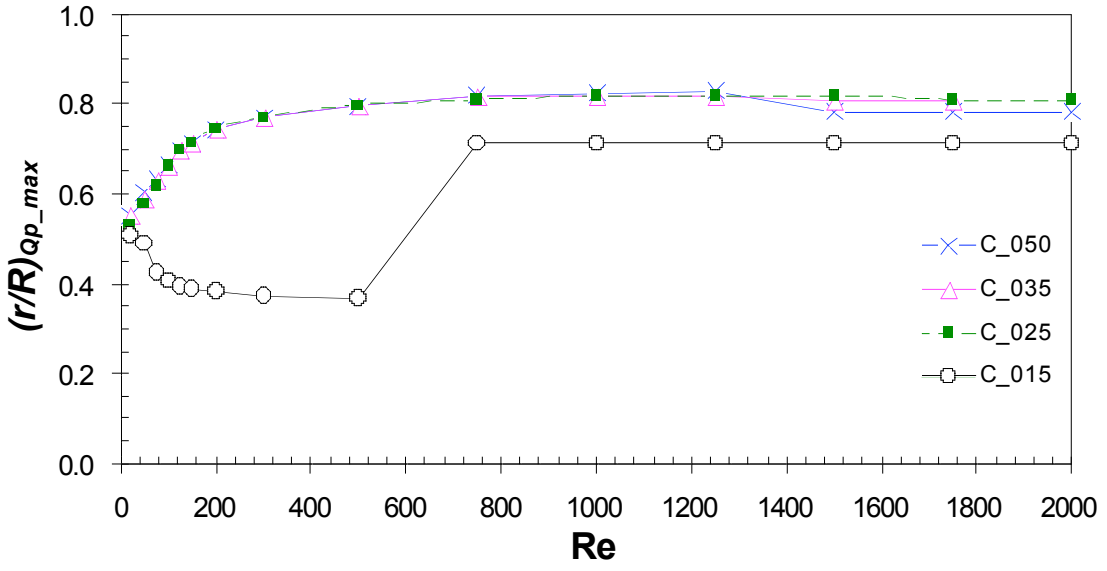

Figure 7.17 Variation of the radial location of the maximum pumping flow rate with Reynolds number.

sudden jump was noted at $Re \approx 700$ with the radial location assumed the value of approximately $0.70R$. This jump further highlights the criticality of smaller clearances as already mentioned above.

The variation of the non-dimensional discharge flow number (N_{qp}) with Re is shown in Figure 7.18 for all the four configurations. The results exhibit a general trend that is in agreement with the results of Nagata (1975) for unbaffled vessels agitated by an 8-blade paddle. Figure 7.18 shows very low values of N_{qp} for lower Reynolds numbers and rapidly increasing as the Re is augmented until it reaches what appears to be a maximum in the range $500 < Re < 700$. Beyond this transition stage with the smaller disk located tat C_050, C_035 and C_025 the N_{qp} is fairly constant with a value of about 0.034. However, a lower value of $N_{qp} \approx 0.024$ is shown to correspond to the lowest axial location of the disk (C_015). Nagata (1975) reported the value $N_{qp} = 0.031$ from his experimental work for a turbulent flow case involving a plain disk with dimensions identical to d_0513. He also reported a theoretical value of $N_{qp} = 0.027$ for the same disk. The numerically computed value of the pumping flow number in the fully turbulent flow regime ($Re = 5\text{x}10^4$) using the disk d_0513 was found to be $N_{qp} = 0.026$, which was very close to the above theoretical value but relatively less than Nagata's experimental value. This comparison was used to validate the numerical procedures employed in this study and the result is very satisfactory. The predicted value for the small disk in the fully turbulent flow regime was found to be $N_{qp} = 0.016$ which is less than the one found in the laminar flow regime above. It is the view of this author that the plain disk is relevant when used as an agitator in the laminar flow regime applications. These applications include those where the products being mixed are shear sensitive such as in cell or tissue growth research in bioreactors.

The dependence of N_{qp} on Re and C has been a subject of controversy; what the research presented here has shown is that N_{qp} is not constant over the entire range of Re, although it seems constant in the laminar region, about 0.034 (for d_0325), and slightly dropping in value within the turbulent region to about 0.026 (not shown in Figure 7.18). Once again the smaller clearance configuration exhibited the lowest values of N_{qp} in the laminar flow regime. This seems to suggest that excessive reduction of impeller clearance has an adverse effect on the discharge flow characteristics. This trend

confirms the findings of Nagata (1975). It is also worth noting that the reduction of C to values less than $0.15D$ causes a significant reduction in power consumption, as reported by Conti *et al.* (1981).

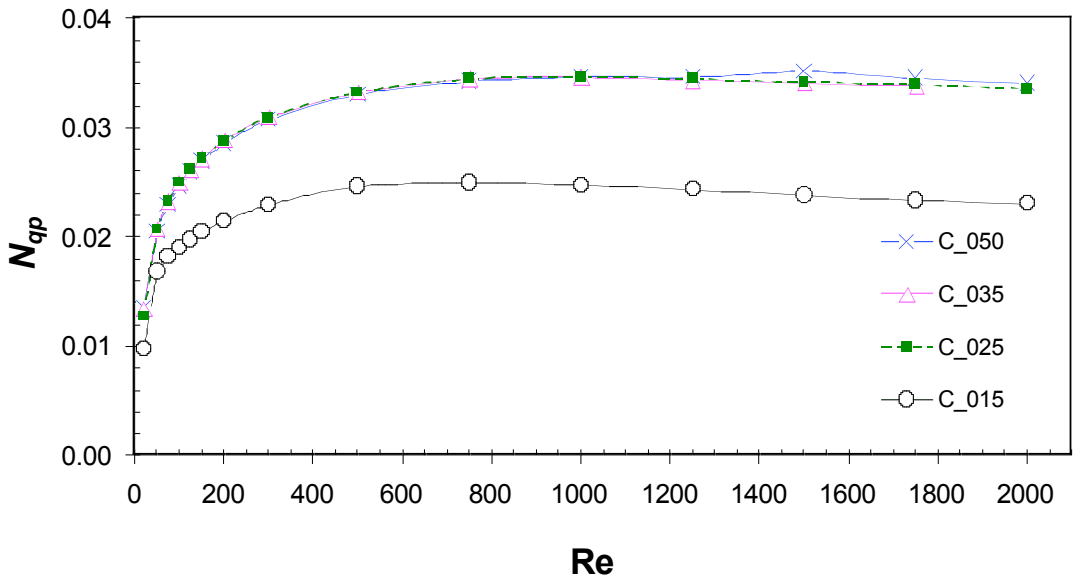

Figure 7.18 Variation of the discharge flow number with Reynolds number. The small disk is tested at four axial locations (C = 0.50D, C = 0.35D, C = 0.25D & C = 0.15D).

The values of discharge flow number are of an order of magnitude smaller than the ones for radial flow impellers. On the other hand, the circulation flow number for the plain disk is only about half that for the radial flow impeller. While for instance Dong *et al.* (1994a) reported that the ratio $N_{qc} / N_{qp} \approx 3.2$ for a paddle impeller and other researchers found it to be about 4.0. This research has found that $N_{qc} / N_{qp} \approx 35.0$ for a plain disk, which is an order of magnitude higher. These findings indicate that the plain disk has a relatively poor pumping capacity, but it has a very good circulation capacity which is a good characteristic for mixing.

7.5.2 Bladed Impeller

The numerical predictions presented here are based on flow generated in the mixing vessel (Figure 7.1) with a six-bladed paddle impeller. The vessel diameter d = *D*/3, and axially located at an off-bottom clearance C = *D*/3. Simulations covered a wide range of Reynolds numbers corresponding to laminar, transitional and turbulent flow regimes. The results are presented as flow visualization and also in graphical format. The mixing global parameters investigated included the pumping flow rate and number, power number, pumping effectiveness and efficiency.

(i) Validation of Results

Table 7.3 Validation of numerical results. The last column shows the different studies the results of which are used for comparison with this study's predictions: A is Nagata (1975); B is Hiraoka et al. (2003); C is Ciofalo et al. (1996).

Re	Impeller details				Predicted results				Known results				
	b/D	d/D	C/D	n	Nq	Np	Nq/Np	NpxRe	Nq	Np	Nq/Np	NpxRe	
2	0.103	0.514	0.50	6	0.032	15.78	-	31.6	-	17.97	--	35.95	A
5	0.103	0.514	0.50	6	0.084	6.60	-	33.02	-	7.91	-	39.54	A
10^4	0.103	0.514	0.50	6	0.37	1.09	0.339	-	0.308	0.97	0.318	-	B
$5x10^4$	0.103	0.513	0.50	8	0.36	0.95	0.379	-	0.3	1.00	0.37	-	C
10^5	0.103	0.513	0.50	8	0.36	0.95	0.379	-	0.34	0.95	0.358	-	A

Numerical simulations performed in this study were validated by quantitatively comparing the predictions with some of the experimental data in the literature as shown

in Table 7.3. Correlations by Nagata (1975) and Hiraoka *et al.* (2003) between N_q, N_p and system geometrical dimensions were also employed to verify the accuracy of the predicted results. The results in Table 7.3 show that in the laminar flow regime the numerical predictions were at worst 15% lower than the experimental and correlation results (for N_pxRe). In the turbulent flow regime the predicted results compared very well with experimental and correlation results to within 6 %. For strongly swirling flow with complex flow dynamics such as was the case here, the above level of accuracy is very satisfactory. For transitional flow regime, no data was readily available for problems similar to this study, which explains why there is no such validation in Table 7.3. It is however felt that since three turbulent flow predictions have been satisfactorily validated the transitional flow predictions can be viewed with the same confidence as the turbulent ones, because the solution process is by and large similar.

(ii) Effect of Turbulence Model

Table 7.4 Comparison of predicted results when using different turbulence models. These results are for the impeller P2 at Re = 10000.

Turbulence model	N_q	N_p	η_e	λ_p
Std. k-ε	0.56	2.41	0.23	0.42
RNG k-ε	0.49	1.94	0.25	0.39
RSM	0.46	1.89	0.24	0.37

Predicted results for N_q, N_p, η_e and λ_p obtained using the standard k-ε, RNG k-ε and RSM turbulence models are shown in Table 7.4. All the results are for a mixing model, fitted with the impeller P2 and operated at $Re = 10^4$. Considering the values predicted by the RSM turbulence model as reference, given that it is supposed to be the most accurate of the three, it was found that both the standard and the RNG k- models tended to over predict. However, the disparity between the predictions is about 20% and 6% for the worst case scenario standard and RNG k-ε models respectively. On average, the

predictions were within 10% and 5% of the RSM predicted values.

(iii) Flow Visualization

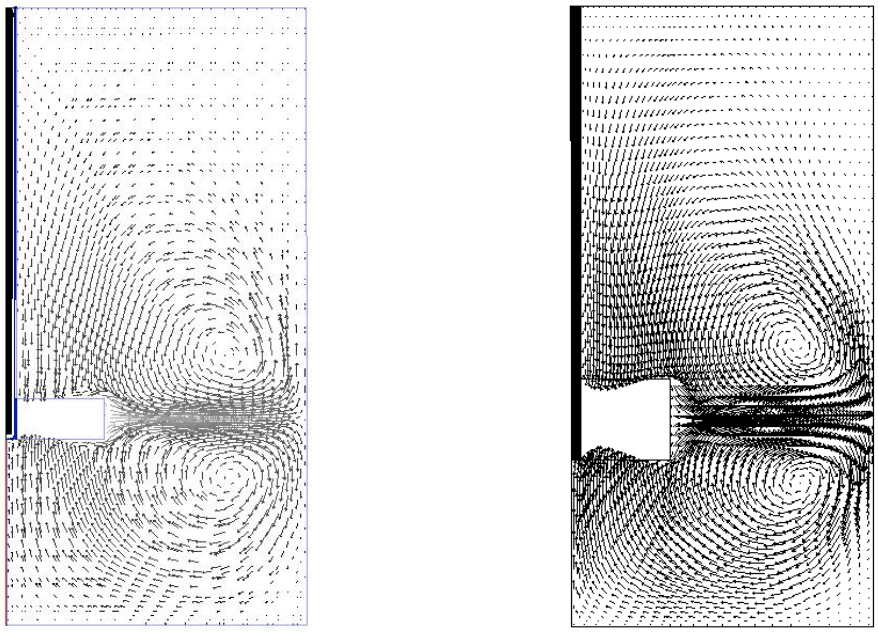

(a) (b)

Figure 7.19 Radial and axial velocity vector plots of the predicted flow fields: (a) for impeller P1 at Re = 10; (b) for impeller P4 at Re = 100.

Figure 7.19 shows flow visualization in the meridional plane of the mixing vessel model agitated by paddle (radial) impellers ((a) impeller P1 at *Re* = 10 and (b) impeller P4 at *Re* = 100. The flow field, in both cases, is characterized by two recirculation regions generated as a result of a purely radial jet emanating from the impeller. It can be seen from the two velocity fields (Figure 7.19) that for laminar flow a small and weak recirculation loop is formed with nearly dead regions away from the impeller. As the impeller speed increases, the transitional flow pattern shows an increase in strength and size of the recirculation loop, hence a reduction in the dead zone area. For much higher Reynolds numbers, the flow patterns revealed strong recirculation covering the entire vessel region. The above differences in flow patterns support findings by other workers (Nagata (1975); Stein (1992)) that the product of the mixing time and the impeller

rotational speed is higher for laminar flow than for turbulent flow.

(iv) Pumping Flow Number

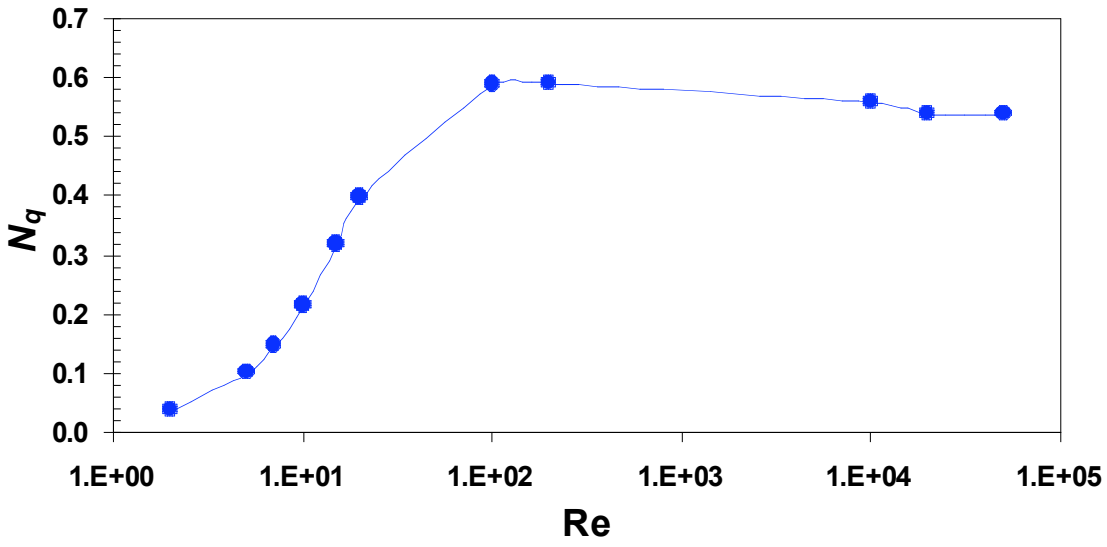

Figure 7.20 Variation of the flow number with Reynolds number for impeller P2.

Figure 7.20 shows the characteristic flow curve for the impeller P2. It is clear that the flow number (N_q) is very low for laminar flow and increases with increasing Re. A salient feature in this graph is that the N_q reaches a maximum value in the transition region, specifically at $Re \approx 200$. In the turbulent flow regime N_q appears to be constant at 0.55. This trend is in agreement with the characteristic flow curve published by Nagata (1975) for an 8 bladed paddle impeller.

Figure 7.21 shows the effect of varying the normalized blade width on N_q considering a representative Reynolds number for each flow regime: $Re = 5$ for laminar; $Re = 100$ for transitional and $Re = 10^4$ for turbulent flow regimes. It is obvious that for all blade widths considered, in the laminar flow regime the N_q values were much lower compared with corresponding values in either the transitional or the turbulent flow regime. Figure 7.21 also reveals that the N_q is highest in the transitional flow regime as was also observed in Figure 7.20. The results described in Figure 7.21 show that the pumping flow number is constant in the turbulent flow regime for normalised blade widths in the

range $0.13H \leq b^* \leq 0.40H$. This result implies that there is an optimum blade width beyond which the pumping flow number does not increase. For the cases investigated in this study that optimum value was found to be $b^* = 0.13H$.

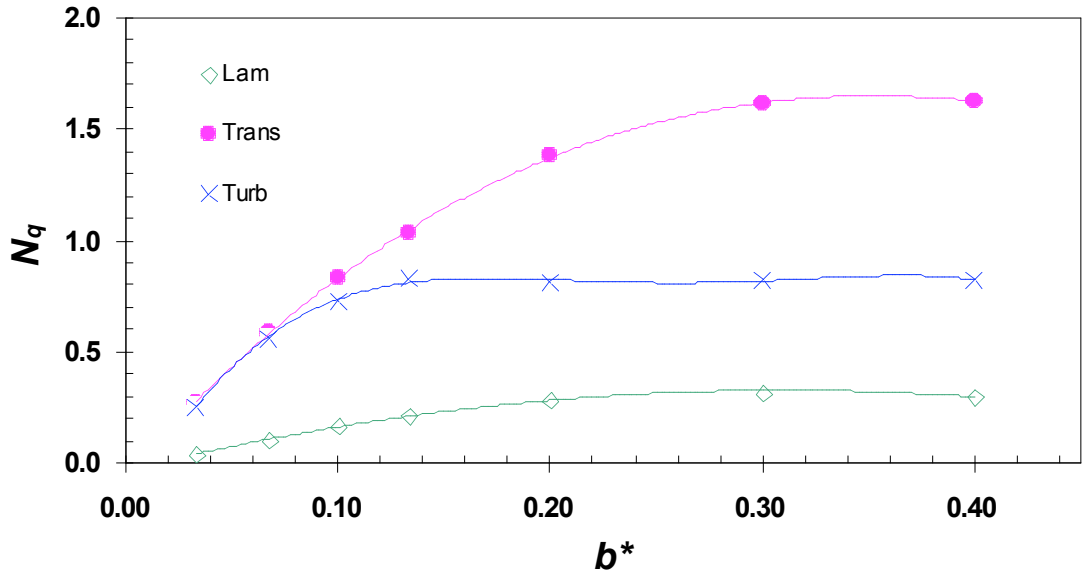

Figure 7.21 Flow number as a function of impeller blade width for: laminar (Re = 5); transitional (Re = 100) and turbulent (Re = 104) flow regimes.

(v) Power Number

The predicted results of the power number N_p against Re for the impeller P2 ($b^* = 0.067$) are shown in Figure 7.22. In the laminar region, the N_p rapidly decreases as the Re increases, almost linearly especially for $Re \leq 7$, in accordance with what most researchers have reported in the past (Nagata (1975); Kuncewicz (1992)). The N_p keeps decreasing in the transition region until it reaches a constant value of about 2.3 in the turbulent flow region ($Re \geq 10^4$). The value of N_p for the impeller P3 was predicted to be approximately 3.04 (Figure 7.23), which is in close agreement with the value of 3.4 computed by Jayanti and Murthy (2002) using Nagata's correlation for a similar impeller.

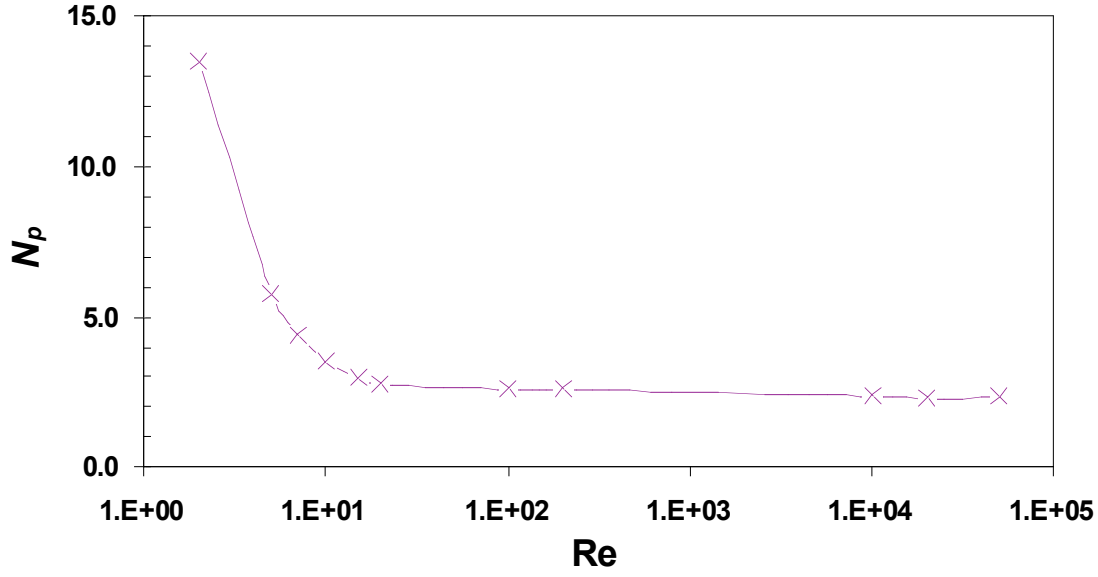

Figure 7.22 Variation of power number with Reynolds number for impeller P2.

In Figure 7.23, the variation of the power number N_p with the normalized blade width (b^*) is reported for laminar, transitional and turbulent flow regimes. It is evident that for both the laminar and transitional flow regimes an increase in impeller blade width results in an increase in N_p. However, in the turbulent region this effect is less significant when using blade widths $b^* < 0.13$ (for P4). Considering all the blade widths used in this investigation, N_p is highest in the laminar region and the lowest in the turbulent regime, which agrees with the results in Figure 7.22. These results suggest that the power number is essentially constant in the turbulent flow regime even though the blade width is increased from $b^* = 0.20H$ (for P5) to $b^* = 0.40H$ (for P7).

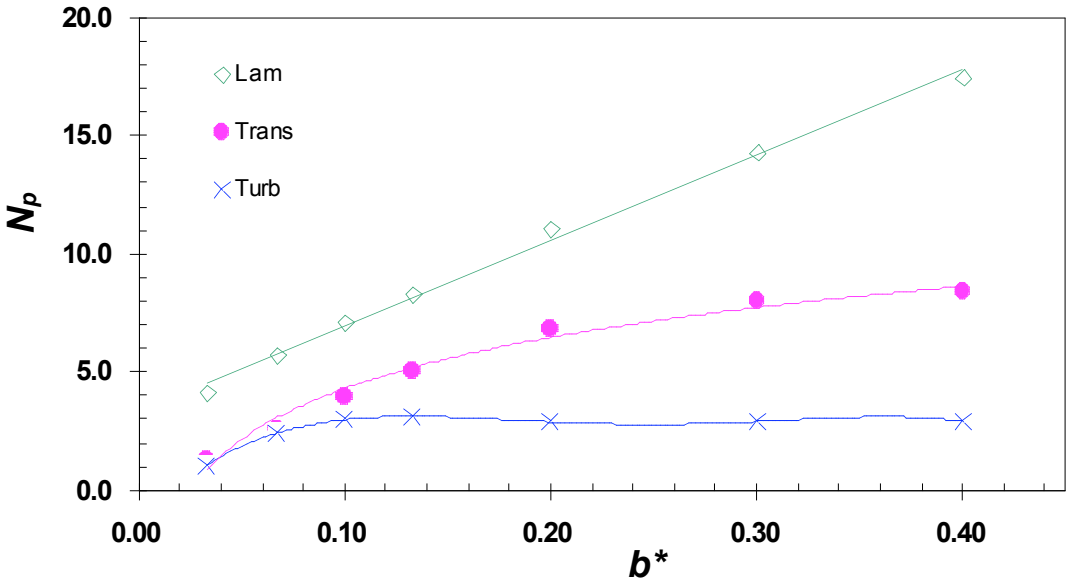

Figure 7.23 Power number as a function of impeller blade width for: laminar (Re = 5); transitional (Re = 100) and turbulent (Re = 104) flow regimes.

(vi) Pumping Effectiveness

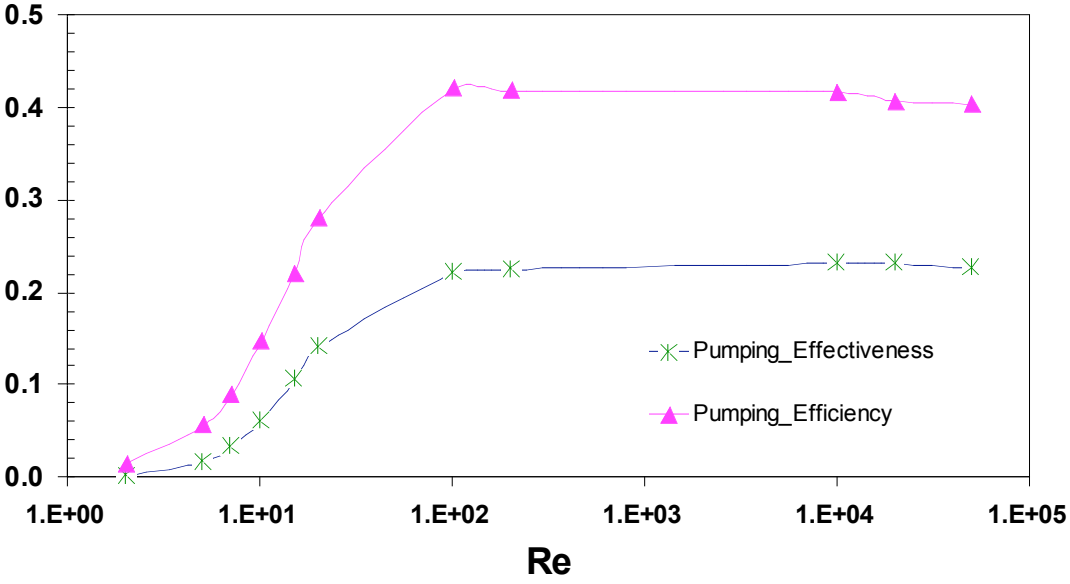

Figure 7.24 Comparison between pumping effectiveness and pumping efficiency at different flow regimes (impeller P2).

A useful index often used to characterize the effectiveness of an agitator in a mixing process is the pumping effectiveness, η_e (Equation 7.12). Another useful correlation is the circulation or pumping efficiency, λ_p, (Equation 7.13), previously used by Wu *et al.* (2001b) for disc turbines.

Figure 7.24 shows the variation of both the pumping effectiveness and pumping efficiency with respect to *Re* for the impeller P2. Both parameters tend to vary in a similar way. They start from low values in the laminar region and increase until they reach maximum values ($\eta_e = 0.23$ & $\lambda_p = 0.41$) in the transitional region. In the turbulent region the two parameters maintain almost their maximum values. The value of $\lambda_p = 0.41$ found here compares very favourably with the finding of Wu *et al.* (2001a) that $\lambda_p = 0.42$ for radial disc turbines, which are essentially similar to the paddle impeller used here, except their blades are attached to a disk (Figure 7.2a).

Figure 7.25 shows the pumping effectiveness as a function of the impeller blade width. The salient feature of Figure 7.25 is that the pumping effectiveness experiences a transition after the blade width is increased beyond that of P3 (i.e. $b^* = 0.10$) with its value changing from $\eta_e = 0.24$ to about 0.27. It means that very small blade widths ($b^* < 0.13$) are not effective in pumping flow. For the transitional flow cases, η_e is almost constant at approximately 0.215 across the whole width range tested in this study. In the laminar regime, increases in blade width were seen to generate corresponding increases in η_e with the largest increase observed from impeller P1 to P2 where η_e was almost doubled; the maximum value being noted for impeller P4. Thereafter, the regression ratio for the other impellers was observed to be about 1.1. The above results have demonstrated that the radial flow impellers employed here are most effective when used in the turbulent flow regime and least effective when used in the laminar flow regime.

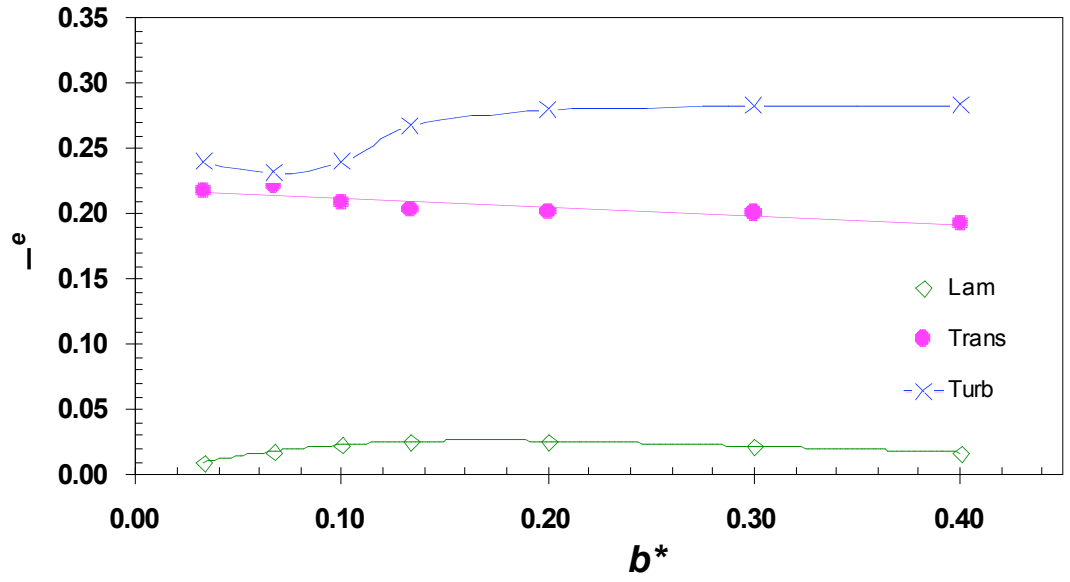

Figure 7.25 Predicted effect of impeller blade width on the pumping effectiveness for: laminar (Re = 5); transitional (Re = 100) and turbulent (Re = 104) flow regimes.

(vii) Pumping Efficiency

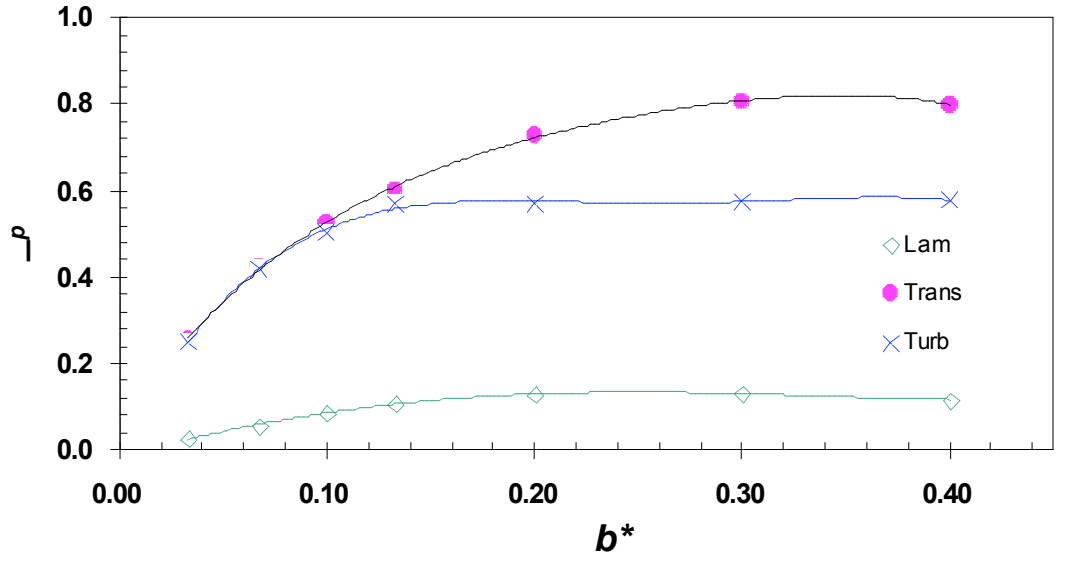

Figure 7.26 Predicted effect of impeller blade width on the pumping efficiency for: laminar (Re = 5); transitional (Re = 100) and turbulent (Re = 104) flow regimes.

Figure 7.26 shows that the pumping efficiency λ_p tends to increase with initial increases in blade width for all flow regimes and then assumes a nearly constant value, which is for laminar flow $\lambda_p \approx 0.12$ and for turbulent flow $\lambda_p \approx 0.56$. The ratio between successive pumping efficiencies decreases for smaller impeller blade widths, as the blade width increases. In the transitional flow regime there appeared to be no plateau in the value of λ_p despite increasing the blade width. Since this impeller is well suited to turbulent flow applications it is important to note that impeller P4 ($b^* = 0.13$) had the optimum blade width size from the pumping efficiency stand point.

7.6 Conclusions and Recommendations

The study of mixing in a closed cylinder has been investigated and presented. Agitation for mixing was achieved by using a plain disk and then a bladed paddle impeller. In the first part of the study, the motion of the centre of recirculation, the circulation and discharge flow rates and their respective non-dimensional numbers were investigated for a mixing vessel agitated by a plain disk. All these aspects of mixing using a plain disk have been investigated and presented in detail for the first time. In the second part of the study, involving a bladed impeller, the effect of the off-bottom axial location on global mixing parameters was investigated. These global parameters are pumping flow rate and pumping number, power number, pumping effectiveness, and pumping efficiency.

Investigations developed and presented in this thesis have been performed in a unique way that has led to new insights. These are outlined as conclusions in the following sections.

7.6.1 Plain Disk

The locus of the recirculation centre has been found to follow a general trend, initially moving radially away from the axis of rotation, but axially closer to the impeller. After going through a turning point the centre of recirculation moves in the reverse direction. Results have shown that the loci of the recirculation centres are largely influenced by not only the Reynolds number but also the radial and axial size of the disk and its axial

location along the swirl axis. This is also true about the position of the Isolated Mixing Regions (*IMRs)*. Knowledge of this motion will help researchers understand the motion of the *IMRs* commonly present in laminar mixing and improve the design of mixing vessels.

Flow visualization results have revealed that the plain disk operating with a very small off-bottom clearance, such as $C = 0.15D$, can trigger flow transition from a double-loop to a single-loop. This transition is useful in many applications, such as those concerned with solids suspension, given that it leads to a substantial reduction in the power number.

The circulation flow rate Q_c was observed to be linearly dependent on the Reynolds numbers. However, both Q_c and N_{qc} were observed not to depend on the off-bottom disk clearance within the range $0.25D \leq C \leq 0.50D$. When the disk was placed at an off-bottom clearance $C = 0.15D$, simulated results revealed a significant reduction in both Q_c and N_{qc}.

The discharge flow rate Q_p was also shown to be dependent on the Reynolds number. However, both Q_p and the discharge flow number N_{qp} appeared not to be influenced by the axial location C of the disk except when $C \leq 0.15D$. The behaviour of Q_p and N_{qp} with respect to C was similar to that of Q_c and N_{qc}.

For the plain disks studied the ratio *Nqc*/*Nq* was found to about 35. This is an order of magnitude higher than the value for an equivalent radial flow impeller. Such a high ratio indicates that the plain disk has a relatively poor pumping capacity, but a very good circulation capacity which is a good characteristic for mixing. For this reason, the plain disk can be effectively used for laminar flow mixing.

Both the circulation (*Nqc*) and discharge (*Nq*) flow numbers appear to assume constant values for $Re > 700$, but for lower Reynolds numbers they tend to increase with corresponding increases in *Re*.

Beyond $Re \approx 700$ it was found that the radial location $(r/R)_{Qp\_max}$ at which the pumping flow rate was maximum was almost constant at approximately $0.8R$ and $0.7R$ (for $C =$ 015*D*). At this critical off-bottom clearance (*C*_015) and $Re \approx 700$ a jump in the value

of $(r/R)_{Qp\_max}$) from about 0.4R to approximately 0.7R was observed. This shift underlines the criticality of this small off bottom clearance.

On the whole, the study has clearly shown that a small off-bottom disk clearance can lead to a significant reduction in circulation and pumping flow rates as well as their corresponding non-dimensional numbers. However, these reductions are compensated by a attractive reduction in power input as shown by previous researchers using different agitators.

7.6.2 Bladed Impeller

Numerical modeling of flow in an unbaffled vessel agitated by a 6 bladed paddle impeller has been presented. The rotating reference frame method was employed in the solution process. Numerical predictions of the variation of N_q, N_p, η_e and λ_p with Re and the normalised blade width (b*) have been presented. Some results have been compared with the classical data of Nagata (1975) and other researchers' findings and overall good agreement has been observed. Conclusions drawn from the results are presented next.

The predicted characteristic curves for *Nq* and *Np* have shown similar trends to previous results. The *Nq* increases steadily in the laminar region until it reaches its maximum value in the transition region and maintains a constant value in the turbulent region. The *Np,* on the other hand, decreases linearly at a fast rate in the laminar region through to the transition region. It tends to assume a stable value in the turbulent regime.

In general, for smaller blade widths ($b^* < 0.13$), increases in blade width generate corresponding increases in N_q,, N_p, λ_p and η_e and at least for the range of blade widths covered here.

The pumping flow number was constant in the turbulent flow regime for $0.13H \leq b^* \leq 0.40H$. This result implies that $b^* = 0.13H$ is the optimum blade width beyond which the pumping flow number remains constant. Similar results were observed in the case of N_p but the optimum blade width was found to be 0.2H.

For all widths considered here N_p was highest in the laminar region and lowest in the

turbulent region, whereas N_q was highest in the transitional region but experienced a slight reduction in the turbulent region.

Impellers with smaller blade widths ($b^* < 0.13$) were less effective in pumping flow within the mixing vessel. A rise in the pumping effectiveness was seen to be due to the increase in the blade width ($b^* > 0.13$) for impellers operating in the turbulent flow regime.

The results have demonstrated that the radial flow impellers used here are most effective when used in the turbulent flow regime and least effective when used in the laminar flow regime.

Both the pumping effectiveness and the pumping efficiency are constant in the turbulent regions for impellers with $0.13 < b^* < 0.40$.

7.6.3 Suggestions for Future Research

While this work has shed some light of a number on a number of issues relevant to mixing in a vessel agitated by a plain disk and a radial flow impeller, a number of questions have also been raised which require further investigations. These are listed below:

(i) Plain Disk

- Knowledge of the transitional off-bottom disk clearance is vitally important in applications such as solids suspension. While the present research has shown that a plain disk has the capability of triggering this flow transition (from double-loop to single-loop) between $0.15D < C < 0.25D$, it is essential to accurately establish the value of this transitional off-bottom clearance.

- Investigate whether this transitional clearance depends on the relative size of the disk (i.e. diameter) with respect to the vessel diameter.

- Once the above issues have been resolved, it is crucial to study the effect of this transition on the power input to the plain disk.

- Examine the loci of the centres of the recirculation regions for different disk sizes and at varying axial locations. This study should extend the range of Reynolds numbers to include turbulent flow regime.

(ii) Bladed Impeller

- Examine the sudden rise observed in pumping effectiveness when $b^* > 0.13$ to establish whether this change is abrupt or progressive.
- Investigate the effects of impeller size and off-bottom clearance on the pumping effectiveness and efficiency, and on the ration.
- Investigate the effect of the axial location of the impeller on the ratio Nqc / Nqp for unbaffled mixing vessels operating under turbulent conditions and also.
- Examine the effect of impeller diameter on the pumping effectiveness and the flow structure such as the transition from double-loop to single-loop.

References

Abid, M., Xuereb, C. & Bertrand, J. (1994), Modeling of the 3d Hydrodynamics of 2-Blade Impellers in Stirred Tanks Filled with a Highly Viscous Fluid. *Canadian Journal of Chemical Engineering* **72**, (2), 184-193.

Akili, H. & Sahin, B. (2003), Control of vortex breakdown by a coaxial wire. *Phys Fluids* **15**, (1), 123-133.

Althaus, W., Brucker, C. & Weimer, M. (1995), Breakdown od slender vortices. In Fluid vortices - Fluid Mechanics and its applications, vol. 30, Dordrecht: Kluwer Academic, 373-426.

Anderson, J. D. (1995), Computational Fluid Dynamics, The Basics with Applications, McGraw-Hill, Inc., 547.

Armenante, P. M. & Chou, C.-C. (1994), Experimental LDV measurement and numerical CFD determination of the fluid velocity distribution in an unbaffled mixing vessel. *American Institute of Chemical Engineers Symposium Series* **90**, (299), 33-40.

Armenante, P. M. & Chou, C.-C. (1996), Velocity profiles in a baffled vessel with single or double pitched-blade turbines. *AICHE Journal* **42**, (1), 42-54.

Armenante, P. M., Chou, C. C. & Hemrajani, R. R. (1994), Comparison of experimental and numerical fluid velocity distribution profiles in an unbaffled mixing vessel provided with a pitched-blade turbine. *Proceedings of the 8th European Conference on Mixing*, Institution of Chemical Engineers, Rugby, U.K., Cambridge,

U.K., 1994, September 21-23, 349-356.

Armenante, P. M., Luo, C. G., Chou, C. C., Fort, I. & Medek, J. (1997), Velocity Profiles in a Closed, Unbaffled Vessel - Comparison between Experimental Ldv Data and Numerical Cfd Predictions. *Chemical Engineering Science* **52**, (20), 3483-3492.

Armenante, P. M., Nagamine, E. U. & Susanto, J. (1998), Determination of Correlations to Predict the Minimum Agitation Speed for Complete Solid Suspension in Agitated Vessels. *Canadian Journal of Chemical Engineering* **76**, (3), 413-419.

Aubin, J., Mavros, P., Fletcher, D. F., Bertrand, J. & Xuereb, C. (2001), Effect of axial agitator configuration (up-pumping, down-pumping, reverse rotation) on flow patterns generated in stirred vessels. *Chemical Engineering Research & Design* **79**, (A8), 845-856.

Bakker, A. & Fasano, J. B. (1994), Effects of flow pattern on solids distribution in a stirred tank. *Proceedings of the 8th European Conference on Mixing*, Institution of Chemical Engineers, Rugby, U.K., Cambridge, U.K., 1994, September 21-23, 1-8.

Bakker, A., Laroche, R. D., Wang, M. H. & Calabrese, R. V. (1997), Sliding mesh simulation of laminar flow in stirred reactors. *Chemical Engineering Research & Design* **75**, (A1), 42-44.

Bakker, A., Myers, K. J., Ward, R. W. & Lee, C. K. (1996), The Laminar and Turbulent Flow Pattern of a Pitched Blade Turbine. *Chemical Engineering Research & Design* **74**, (A4), 485-491.

Bakker, A., Oshinowo, L. M. & Marshall, E. M. (2000), The use of Large Eddy Simulation to study vessel hydrodynamics. *Proceedings of the 10th European Conference on Mixing*, Elsevier Science B.V., Delft, Netherlands, 2000, July, 2-5, 247-254.

Bakker, A. & Van den Akker, H. E. A. (1994), Single-phase flow in stirred reactors. *Chemical Engineering Research & Design* **72**, (A4), 583-593.

Basu, A. J. & Khalili, A. (1996), Numerical study of axisymmetric vortex breakdown.

Journal of the Indian Institute of Science **76**, (4), 477-486.

Benay, R. (1984), Numerical Modeling of a Vortex Breakdown in a Laminar-Flow of Revolution. *Recherche Aerospatiale*, (4), 251-263.

Benjamin, T. B. (1962), Theory of vortex breakdown phenomenon. *J. Fluid Mech.* **14**, (Part 4), 593-629.

Benjamin, T. B. (1965), Significance of vortex breakdown phenomenon. *American Society of Mechanical Engineers -- Transactions -- Journal of Basic Engineering* **87**, (2), 518-524.

Benjamin, T. B. (1967), Some developments in theory of vortex breakdown. *J. Fluid Mech.* **28**, (Part 1), 65-84.

Berger, S. A. & Erlebacher, G. (1995), Vortex breakdown incipience. Theoretical considerations. *Phys. Fluids* **7**, (5), 972.

Bertela, M. (1979), Effect of the chamber depth on the steady and unsteady flow of a rotating fluid in a finite cylindrical container- I. *Computers & Fluids* **7**, (4), 231-246.

Bertela, M. & Gori, F. (1982), Laminar flow in a cylindrical container with a rotating cover. *J. Fluids Eng. Trans. ASME* **104**, 31-39.

Bhattacharyya, S. & Pal, A. (1998), Axisymmetric Vortex Breakdown in a Filled Cylinder. *Int. J. Eng. Sci.* **36**, (5-6), 555-563.

Bhattacharyya, S. & Pal, A. (1999), Generation (or degeneration) of a separation bubble in a liquid-filled cylinder through spin-up (or spin-down) process. *Journal of Applied Mechanics, Transactions ASME* **66**, (4), 1023-1026.

Bouyer, D., Line, A. & Do-Quang, Z. (2004), Experimental analysis of floc size distribution under different hydrodynamics in a mixing tank. *AIChE Journal* **50**, (9), 2064-2081.

Brons, M., Voigt, L. K. & Sorensen, J. N. (1999), Streamline topology of steady axisymmetric vortex breakdown in a cylinder with co- and counter-rotating end-covers.

J. Fluid Mech. **401**, 275-292.

Brown, G. L. & Lopez, J. M. (1990), Axisymmetric vortex breakdown. 2. Physical mechanisms. *J. Fluid Mech.* **221**, 553-576.

Brucato, A., Ciafalo, M., Grisafi, F. & Rizzuti, L. (1990), Computer simulation of turbulent flow in baffled and unbaffled tanks stirred by radial impellers. In "Computer Applications to Batch Processes", Cengio, Italy, 28-30 March, 90.

Calabrese, R. V. & Stoots, C. M. (1989), Flow in the impeller region of a stirred tank. *Chemical Engineering Progress* **85**, (5), 43-50.

Cassidy, J. J. & Falvey, H. T. (1970), Observations of unsteady flow arising after vortex breakdown. **41**, (pt 4), 727-736.

Chandrasekhar, S. (1961), Hydrodynamic and hydromagnetic stability, Oxford: Clarendon Press.

Chao, Y. C., Leu, J. H., Hung, Y. F. & Lin, C. K. (1991), Downstream boundary effects on the spectral characteristics of a swirling flowfield. *Exp. Fluids* **10**, (6), 341-348.

Cheng, C. Y., Atkinson, J. F. & Bursik, M. I. (1997), Direct Measurement of Turbulence Structures in Mixing Jar Using Piv. *Journal of Environmental Engineering* **123**, (2), 115-125.

Cheng-Hsiung, K. & Ni-Yu, L. (1995), Vortex characteristics over delta wing subject to transient along-core blowing. *AIAA J.* **33**, (12), 2418-2420.

Ciofalo, M., Brucato, A., Grisafi, F. & Torraca, N. (1996), Turbulent Flow in Closed and Free-Surface Unbaffled Tanks Stirred by Radial Impellers. *Chemical Engineering Science* **51**, (14), 3557-3573.

Conti, R., Sicardi, S. & Apecchia, V. (1981), Effect of stirrer clearance on particle suspension in agitated vessels. *Chem Eng Commun* **22**, 247-249.

Costes, J. & Couderc, J. P. (1988), Study by Laser Doppler Anemometry of the

turbulent flow induced by a Rushton turbine in a stirred tank:. *Chemical Engineerng Science* **43**, (10), 2751-2764.

Daskopoulos, P. & Harris, C. K. (1996), Three-dimensional CFD simulations of turbulent flow in baffled stirred tanks: an assessment of the current position. *Proceedings of the 1996 Fluid Mixing 5 Conference*, Institution of Chemical Engineers Symposium Series. n 140 1996. Inst of Chemical Engineers, Rugby, Engl., Bradford, UK, 1-8.

Davis, J. T. & Rideal, E. K. (1963), Interfacial phenomenon, (2nd ed.), Academic Press, London.

Delery, J. M. (1994), Aspects of vortex breakdown. *Progress in Aerospace Sciences* **30**, (1), 1-59.

Derksen, J. (2001), Assessment of large eddy simulations for agitated flows. *Chemical Engineering Research & Design* **79**, (A8), 824-830.

Desouza, A. & Pike, R. W. (1972), Fluid dynamics and flow patterns in stirred tanks with a turbine impeller. *The Canadian Journal of Chemical Engineering* **50**, 15-23.

Dong, L., Johansen, S. T. & Engh, T. A. (1994a), Flow induced by an impeller in an unbaffled tank - I. Experimental. *Chemical Engineering Science* **49**, (4), 549-560.

Dong, L., Johansen, S. T. & Engh, T. A. (1994b), Flow induced by an impeller in an unbaffled tank - II. Numerical modelling. *Chemical Engineering Science* **49**, (20), 3511-3518.

Earnshaw, P. B. (1964), Measurements of vortex-breakdown position at low speed on a series of sharp-edged symmetrical models. RAE Technical Report No. 64047.

Earnshaw, P. B. & Lawford, J. A. (1964), Low-speed wind-tunnel experiments on a series of sharp-edged delta wings., ARC R & M No. 3424.

Eggels, J. G. M. (1996), Direct and Large-Eddy Simulation of Turbulent Fluid Flow Using the Lattice-Boltzmann Scheme. *Int. J. Heat Fluid Fl.* **17**, (3), 307-323.

Elle, B. J. (1958), An investigation at low speed of the flow near the apex of thin delta wings with sharp leading edges. Ministry of Aviation, ARC Tech. Rep. R. & M. No. 3176,, 1-19.

Elle, B. J. (1960), On the breakdown at high incidences of the leading edge vortices on delta wings. *J. R. Aero. Soc.* **64**, (546), 491-493.

Escudier, M. (1988), Vortex breakdown: Observations and explanations. *Progress in Aerospace Sciences* **25**, (2), 189-229.

Escudier, M. P. & Keller, J. J. (1983), Vortex breakdown: A two-stage transition. AGARD CP-342.

Escudier, M. P. & Keller, J. J. (1985), Recirculation in swirling flow: a manifestation of vortex breakdown. *AIAA J.* **23**, (1), 111-116.

Escudier, M. P. & Zehnder, N. (1982), Vortex-flow regimes. **115**, 105-121.

Escudier, R. (1984), Observations of the flow produced in a cylindrical container by a rotating endwall. *Exp. Fluids* **2**, 189-196.

Faler, J. H. (1976), Some experiments in swirling flows: detailed velocity measurements of a vortex breakdown using a laser Doppler anemometer. *Ph. D. dissertation (Available as N.A.S.A. Contractor Rep. no. 135115.)*, Cornell University and N.A.S.A. Contractor Rep. no. 135115.

Faler, J. H. & Leibovich, S. (1977), Disrupted States of Vortex Flow and Vortex Breakdown. *Phys. Fluids* **20**, (9), 1385-1400.

Faler, J. H. & Leibovich, S. (1978), An experimental map of the internal structure of a vortex breakdown. *J. Fluid Mech.* **86**, (part2), 313-335.

Fujimura, K. & Koyama, H. (2002), Experimental study of vortex breakdown in a cylindrical container. *Nippon Kikai Gakkai Ronbunshu, B Hen/Transactions of the Japan Society of Mechanical Engineers, Part B* **68**, (666), 417-423.

Fujimura, K., Koyama, H. S. & Hyun, J. M. (1997), Time-dependent vortex

breakdown in a cylinder with a rotating lid. *J. Fluids Eng. Trans. ASME* **119**, (2 Jun), 450-453.

Fujimura, K., Koyama, H. S. & Hyun, J. M. (2004), An experimental study on vortex breakdown in a differentially-rotating cylindrical container. *Exp. Fluids* **36**, (3), 399-407.

Galletti, C., Brunazzi, E., Yianneskis, M. & Paglianti, A. (2003), Spectral and wavelet analysis of the flow pattern transition with impeller clearance variations in a stirred vessel. *Chemical Engineering Science* **58**, (17), 3859-3875.

Gangulee, D. & Ng, T. T. (1995), Vortex control over sharp-edged slender bodies. *Journal of Aircraft* **32**, (4), 739-745.

Gartshore, I. S. (1962), Recent work in swirling incompressible flow. *NRC Can. Aero Rep.*, LR-343.

Gartshore, I. S. (1963), Some numerical solutions for the viscous core of an irrotational vortex. *NRC Can. Aero Rep.*, LR-378.

Gelfgat, A. Y., Baryoseph, P. Z. & Solan, A. (1996), Stability of Confined Swirling Flow with and without Vortex Breakdown. *J. Fluid Mech.* **311**, 1-36.

Gordnier, R. E. & Visbal, M. R. (2004), Computation of the aeroelastic response of a flexible delta wing at high angles of attack. *Journal of Fluids and Structures* **19**, (6), 785-800.

Grabowski, W. J. & Berger, S. A. (1976), Solutions of the Navier-Stokes equations for vortex breakdown. **75**, (pt 3), 525-544.

Grant, I. (1997), Particle Image Velocimetry - A review. *Proceedings of the Institution of Mechanical Engineers Part C-Journal of Mechanical Engineering Science* **211**, (1), 55-76.

Gu, W., Robinson, O. & Rockwell, D. (1993), Control of vortices on a delta wing by leading-edge injection. *AIAA J.* **31**, (7), 1177-1186.

Gursul, I., Srinivas, S. & Batta, G. (1995), Active control of vortex breakdown over a delta wing. *AIAA J.* **33**, (9), 1743-1745.

Hall, M. G. (1972), Vortex Breakdown. *Ann. Rev. Fluid Mech.* **4**, 195-218.

Harris, C. K., Roekaerts, D., Rosendal, F. J. J., Buitendijk, F. G. J., Daskopoulos, P., Vreenegoor, A. J. N. & Wang, H. (1996), Computational Fluid Dynamics for Chemical Reactor Engineering. *Chemical Engineering Science* **51**, (10), 1569 ff.

Harvey, J. K. (1962), Some observations of vortex breakdown phenomenon. *J. Fluid Mech.* **14**, (Part 4), 585-592.

Harvey, P. S. & Greaves, M. (1982), Turbulent flow in an agitated vessel Part II: Numerical solution and model predictions. *Trans IChemE* **60**, 201-210.

Herrada, M. A. & Shtern, V. (2003a), Control of vortex breakdown by temperature gradients. *Phys. Fluids* **15**, (11), 3468-3477.

Herrada, M. A. & Shtern, V. (2003b), Vortex breakdown control by adding near-axis swirl and temperature gradients. *Physical Review E* **68**, (4 1), 412021-412028.

Hiraoka, S., Tada, Y., Kato, Y., Murakami, Y., Sato, Y., Matsuura, A. & Yamaguchi, T. (2003), Correlation of discharge flow rate in a vessel with pitched blade paddle impeller. *Journal of Chemical Engineering of Japan* **36**, (2), 187-197.

Hockey, R. M. & Nouri, J. M. (1996), Turbulent flow in a baffled vessel stirred by a 60[deg] pitched blade impeller. *Chemical Engineering Science* **51**, (19), 4405-4421.

Hoffler, K. D. & Dhanvada, M. R. (1985), Investigation of the tabbed vortex flap. *Journal of Aircraft* **22**, (6), 490-497.

Houcine, I., Marcant, B., Vivier, H., Plasari, E., David, R. & Villermaux, J. (1994), Comparison of mixing action of several stirrers by laser sheet visualization and image processing. *Proceedings of the 8th European Conference on Mixing*, Institution of Chemical Engineers, Rugby, U.K., Cambridge, U.K., 1994, September 21-23, 97-104.

Hourigan, K., Graham, L. J. W. & Thompson, M. (1995), Spiral strikes in pre-vortex

breakdown regions of axisymmetric swirling flows. *Phys Fluids* **7**, (12), 3126-3128.

Howard, L. N. & Gupta, A. S. (1962), On hydrodynamic and hydromagnetic stability of swirling flows. *J. Fluid Mech.* **14**, (Part 3), 463-476.

Hummel, D. (1967), Zur Umstroemung scharfkantiger schlanker Deltfluegel bei grossen Anstellwinkeln. *Zeitschrift fuer Flugwissenschaften* **15**, (10), 376-385.

Hummel, D. & Srinivasan, P. S. (1966), Vortex breakdown effects on the low-speed aerodynamic characteristics of slender delta wings in a symmetrical flow. *J. R. Aero. Soc.* **71**, 319-322.

Husain, H. S., Shtern, V. & Hussain, F. (2003), Control of vortex breakdown by addition of near-axis swirl. *Phys. Fluids* **15**, (2), 271-279.

Hyun, J. M. (1985a), Flow in an open tank with a free surface driven by the spinning bottom. *J. Fluids Eng. Trans. ASME* **107**, (4), 495-499.

Hyun, J. M. (1985b), Transient starting flow in a cylinder with counter-rotating endwall disks. *J. Fluids Eng. Trans. ASME* **107**, (1), 92-96.

Jaworski, Z., Dyster, K. N. & Nienow, A. W. (2001), The effect of size, location and pumping direction of pitched blade turbine impellers on flow patterns: LDA measurements and CFD predictions. *Chemical Engineering Research & Design* **79**, (A8), 887-894.

Jaworski, Z., Nienow, A. W., Koutsakos, E., Dyster, K. & Bujalski, W. (1991), LDA study of turbulent flow in a baffled vessel agitated by a pitched blade turbine. *Chemical Engineering Research & Design* **69**, (4), 313-320.

Jayanti, S. & Murthy, S. (2002), CFD study of power and mixing time for paddle mixing in unbaffled vessels. *Chemical Engineering Research and Design* **80**, 482-498.

Johari, H. & Moreira, J. (1996), Delta wing vortex manipulation using pulsed and steady blowing during ramp-pitching. *Journal of Aircraft* **33**, (2), 304-310.

Jones, J. P. (1960), The breakdown of vortices in separated flow. *U.S.A.A.*, Uni.

Southampton, Report No. 140.

Jones, J. P. (1964), On the explanation of vortex breakdown. *Proc. IUTAM Symp. on vortex breakdown*, Ann Arbor, Michigan.

Jones, M. (2002), A study of the mechanism for vortex breakdown and some measures for its control. *PhD*, Department of Mechanical Engineering, Monash University, Melbourne, 203.

Ju, W., Huang, X., Wang, Y., Shi, L. & Zhang, B. (2000), Investigation of the flow field of viscoelastic fluid in a stirred vessel. *Proceedings of the 10th European Conference on Mixing*, Elsevier Science B.V., Delft, Netherlands, 2000, July 2-5, 313-320.

Kegelman, J. T. & Roos, F. W. (1989), Effecys of leading edge shape and vortex burst on the flowfield of a 70-degree-sweep delta wing. *AIAA Paper No. 89-86*.

Khang, S. J. & Levenspiel, O. (1976), New scale-up and design method for stirrer-agitated batch mixing vessels. *Chem Eng Sci* **31**, 569-577.

Klute, S. M., Rediniotis, O. K. & Telionis, D. P. (1996), Flow control over a maneuvering delta wing at high angles of attack. *AIAA J.* **34**, (4), 662-668.

Komori, S. & Murakami, Y. (1988), Turbulent Mixing in Baffled Stirred Tanks with Vertical-Blade Impellers. *AICHE Journal* **34**, (6), 932-937.

Kresta, S. M. & Wood, P. E. (1991), Prediction of the three-dimensional turbulent flow in stirred tanks. *AICHE Journal* **37**, (3), 448-460.

Kresta, S. M. & Wood, P. E. (1993), Mean flow field produced by a 45 degree pitched blade turbine: changes in the circulation pattern due to off bottom clearance. *Canadian Journal of Chemical Engineering* **71**, (1), 42-53.

Kuncewicz, C. (1992), Three-dimensional model of laminar liquid flow for paddle impellers and flat-blade turbines. *Chemical Engineering Science* **47**, (15-16), 3959-3967.

Lambert, C. & Gursul, I. (2004), Characteristics of fin buffeting over delta wings. *Journal of Fluids and Structures* **18**, (SUPPL), 307-319.

Lamberto, D. J., Alvarez, M. M. & Muzzio, F. J. (1999), Experimental and computational investigation of the laminar flow structure in a stirred tank. *Chemical Engineering Science* **54**, (7), 919-942.

Lamberto, D. J., Muzzio, F. J., Swanson, P. D. & Tonkovich, A. L. (1996), Using time-dependent RPM to enhance mixing in stirred vessels. *Chemical Engineering Science* **51**, (5), 733-741.

Lambourne, N. C. & Bryer, D. W. (1961), The bursting of leading edge vortices - some observations and discussionof the phenomenon., Aeronautical Research Council,, Reports & Memoranda R. & M. No. 3282, 1-36.

Launder, B. E. & Spalding, D. B. (1974), The numerical computation of turbulent flows. *Computer Methods in Applied Mechanics and Engineering* **3**, (2), 269-289.

Lee, K. C., Ng, K. & Yianneskis, M. (1996), Sliding mesh predictions of the flows around Rushton impellers. *Fluid Mixing V. I.Chem.E. Symposium Series*, No. 140,, 47-58.

Leibovich, S. (1978), The structure of vortex breakdown. *Ann. Rev. Fluid Mech.* **10**, 221-246.

Leibovich, S. (1984), Vortex stability and breakdown: Survey and Extension. *AIAA J.* **22**, (9), 1193-1206.

Leibovich, S. & Stewartson, K. (1983), Sufficient Condition for the Instability of columnar vortices. *J. Fluid Mech.* **126**, 335-356.

Li, M., White, G., Wilkinson, D. & Roberts, K. J. (2004), LDA measurements and CFD modeling of a stirred vessel with a retreat curve impeller. *Industrial and Engineering Chemistry Research* **43**, (20), 6534-6547.

Liu, Y. Z., Chen, H. P. & Koyama, H. S. (2001), 3-D measurement of vortex

breakdown in closed cylindrical container via LDV. *Journal of Hydrodynamics* **13**, (2), 24-28.

Liu, Y.-Z., Chen, H.-P. & Koyama, H. S. (2003a), 3D flow inside bubble-type vortex breakdown: An experimental investigation via LDV. *Journal of Hydrodynamics* **15**, (3), 44-48.

Liu, Y.-Z., Koyama, H. S. & Chen, H.-P. (2003b), Experimental investigation of vortex breakdown in spin-up and spin-down processes via PIV. *Journal of Hydrodynamics* **15**, (2), 58-63.

Lopez, J. M. (1990), Axisymmetric vortex breakdown. 1. Confined swirling flow. *J. Fluid Mech.* **221**, 533-552.

Lowson, M. V. (1991), Visualization Measurements of Vortex Flows. *Journal of Aircraft* **28**, (5), 320-327.

Lowson, M. V. & Riley, A. J. (1995), Vortex breakdown control by delta wing geometry. *Journal of Aircraft* **32**, (4), 832-838.

Lucca-Negro, O. & O'Doherty, T. (2001), Vortex breakdown: a review. *Progress in Energy and Combustion Science* **27**, (4), 431-481.

Ludwieg, H. (1962), Zur erklarung derinstabilitat der uberangestellten Deltaflugelm auftretenden freien wirbekeme. *A Fluidgwiss* **10**, (6), 242-249.

Ludwieg, H. (1970), Vortex breakdown. *Deutsche Luft- und Raumfahrt*, Forschungsbereicht DLR FB, 40-70.

Lugt, H. J. & Haussling, H. J. (1973), Development of flow circulation in a rotating tank. *Acta Mechanica* **18**, 255-272.

Lugt, H. J. & Haussling, H. J. (1982), Axisymmetric vortex breakdown in rotating fluid within a container. *Journal of Applied Mechanics, Transactions of the ASME* **49**, 921-923.

Luo, J. Y., Gosman, A. D., Issa, R. I., Middleton, J. C. & Fitzgerald, M. K. (1993),

Full flow field computation of mixing in baffled stirred vessels. *Chemical Engineering Research & Design* **71**, (A3), 342-344.

Luo, J. Y., Issa, R. I. & Gosman, A. D. (1994), Prediction of impeller induced flows in mixing vessels using Multiple Frames of Reference. *Proceedings of the 8th European Conference on Mixing*, Institution of Chemical Engineers, Rugby, U.K., Cambridge, U.K., 1994, September 21-23, 549-556.

Mager, A. (1972), Dissipation and Breakdown of a Wing-Tip Vortex. *J. Fluid Mech.* **55**, (OCT24), 609-628.

Maines, B. H., Moeller, B. & Rediniotis, O. K. (1999), The effects of leading edge suction on delta wing vortex breakdown. *37th AIAA Aerospace Sciences Meeting and Exhibit.*, AIAA-99-0128.

Makino, T., Ohmura, N. & Kataoka, K. (2001), Observation of isolated mixing regions in a stirred vessel. *Journal of Chemical Engineering of Japan* **34**, (5), 574-578.

Mao, D. M., Feng, L. F., Wang, K. & Li, Y. L. (1997), The Mean Flow Field Generated by a Pitched Blade Turbine - Changes in the Circulation Pattern Due to Impeller Geometry E120. *Canadian Journal of Chemical Engineering* **75**, (2), 307-316.

Markopoulos, J. & Kontogeorgaki, E. (1995), Vortex depth in unbaffled single and multiple impeller agitated vessels. *Chemical Engineering & Technology* **18**, (1), 68-74.

Mavros, P., Mann, R., Vlaev, S. D. & Bertrand, J. (2001), Experimental visualization and CFD simulation of flow patterns induced by a novel energy-saving dual-configuration impeller in stirred vessels. *Chemical Engineering Research & Design* **79**, (A8), 857-866.

Maxworthy, T. (1982), Laboratory modelling fo atmospheric vortices: Acritical review. *In Topics in Atmoshepheric and Oceanographic Science: Intense Atmospheric Vortices*, Springer Verlag, Berlin.

Mazzarotta, B. (1993), Communition phenomena in stirred sugar suspensions. *AICHE Journal Symp. Ser. 89*, (293), 112-117.

Medek, J. & Fort, I. (1994), Liquid circulation in mechanically agitated closed vessel. *Proceedings of the 8th European Conference on Mixing*, Institution of Chemical Engineers, Rugby, U.K., Cambridge, U.K., 1994, September 21-23, 473-480.

Menter, F. R. (1994), Two-equation eddy-viscosity turbulence models for engineering applications. *AIAA J.* **32**, (8), 1598-1605.

Metzner, A. B. & Taylor, J. S. (1960), Flow patterns in agitated vessels. *American Institute of Chemical Engineers Journal* **6**, (1), 109-114.

Middleton, J. C., Pierce, F. & Lynch, P. M. (1986), Computations of flow fields and complex reaction yield in turbulent stirred reactors, and comparison with experimental data. *Chem. Eng. Res. & Des.* **64**, 18-22.

Mishra, V. P. & Joshi, J. B. (1993), Flow generated by a disc turbine: part III. Effect of impeller diameter, impeller location and comparison with other radial flow turbines. *Chemical Engineering Research & Design* **71**, (A5), 563-573.

Mitchell, A. M. & Delery, J. (2001), Research into vortex breakdown control. *Progress in Aerospace Sciences* **37**, (4 May), 385-418.

Montante, G., Lee, K. C., Brucato, A. & Yianneskis, M. (1999), An experimental study of double-to-single-loop transition in stirred vessels. *Canadian Journal of Chemical Engineering* **77**, (4), 649-659.

Montante, G., Lee, K. C., Brucato, A. & Yianneskis, M. (2001a), Numerical simulations of the dependency of flow pattern on impeller clearance in stirred vessels. *Chemical Engineering Science* **56**, (12), 3751-3770.

Montante, G., Micale, G., Magelli, F. & Brucato, A. (2001b), Experiments and CFD predictions of solid particle distribution in a vessel agitated with four pitched blade turbines. *Chemical Engineering Research & Design* **79**, (A8), 1005-1010.

Mullin, T., Kobine, J. J., Tavener, S. J. & Cliffe, K. A. (2000), On the creation of stagnation points near straight and sloped walls. *Phys. Fluids* **12**, (2), 425-431.

Mullin, T., Tavener, S. J. & Cliffe, K. A. (1998), On the Creation of Stagnation Points in a Rotating Flow. *J. Fluids Eng. Trans. ASME* **120**, (4), 685-689.

Mununga, L., Hourigan, K. & Thompson, M. (2001), Comparative study of flow in a mixing vessel stirred by a solid disk and a four bladed impeller. *14th Australasian Fluid Mechanics Conference*, Adelaide University, Australia, 10-14 December 2001, 661-664.

Mununga, L., Hourigan, K., Thompson, M. C. & Johnson, S. (2003), Numerical investigations of discharge flow and circulation flow in an unbaffled mixing vessel agitated by a plain disk. *2nd Iternational Conference on Heat Transfer, Fluid Mechanics and Thermodynamics.*, HEFAT, Victoria Falls, Zambia, 23-26 June, Paper No. ML1.

Mununga, L., Hourigan, K., Thompson, M. C. & Leweke, T. (2004a), Confined flow vortex breakdown control using a small rotating disk. *Phys. Fluids* **16**, (12), 4750-4753.

Mununga, L., Hourigan, K., Thompson, M. C. & Leweke, T. (2004b), Control of vortex breakdown in a torsionally driven closed cylinder by addition of swirl using a small disk. *2004 ASME Heat Transfer/Fluids Engineering Summer Conference*, ASME, Charlotte, North Carolina, July 11-15.

Myers, K. J. & Bakker, A. (1998), Solids Suspension with up-Pumping Pitched-Blade and High-Efficiency Impellers. *Canadian Journal of Chemical Engineering* **76**, (3), 433-440.

Myers, K. J., Bakker, A. & Corpstein, R. R. (1996), Effect of flow reversal on solids suspension in agitated vessels. *Canadian Journal of Chemical Engineering* **74**, (6), 1028-1033.

Nagata, S. (1975), Mixing Principles and Applications, John Wiley & Sons, New York, 458p.

Nagata, S. K., Yamamoto, K. & Naruse, Y. (1960), Flow patterns of liquid in a cylindrical mixing vessel with baffles. *Memoirs of the Faculty of Engineering, Kyoto University* **21**, 260-274.

Nagata, S. K., Yamamoto, K. & Ujihara, M. (1958), Flow patterns of liquid in a cylindrical mixing vessel without baffles. *Memoirs of the Faculty of Engineering, Kyoto University* **20**, 336-349.

Nakamura, Y., Leonard, A. & Spalart, P. R. (1986), Internal structure of a vortex breakdown. *AIAA/ASME 4th Fluid Mechanics, Plasma Dynamics and Lasers Conference.*, AIAA, New York, NY, USA, Atlanta, GA, USA, 13.

Nakamura, Y. & Uchida, S. (1980), Contribution to the occurence of axisymmetric type of vortex breakdown. **23**, (60), 79-90.

Ng, K., Fentiman, N. J., Lee, K. C. & Yianneskis, M. (1998), Assessment of Sliding Mesh CFD Predictions and LDA Measurements of the Flow in a Tank Stirred by a Rushton Impeller. *Chemical Engineering Research & Design* **76**, (A6), 737-747.

Nienow, A. W. (1968), Suspension of solid particles in turbine agitated baffled vessels. *Chemical Engineering Science* **23**, (12), 1453-1459.

Nienow, A. W. (1998), Hydrodynamics of stirred reactors. *Applied mechanics reviews* **51**, (1), 3-32.

Nouri, J. M. & Whitelaw, J. H. (1990), Flow characteristics of stirred reactors with Newtonian and non-Newtonian fluids. *AICHE Journal* **36**, (4), 627-629.

Ogawa, Y. & Iwatsu, R. (2002), Numerical study of axisymmetric vortex breakdown flows in an open cylindrical container with rotating bottom wall. *Nippon Kikai Gakkai Ronbunshu, B Hen/Transactions of the Japan Society of Mechanical Engineers, Part B* **68**, (667), 740-747.

Okulov, V. L., Sorensen, J. N. & Voigt, L. K. (2004), Vortex scenario and bubble generation in a cylinder cavity with rotating top and bottom. *European Journal of Mechanics B/Fluids*.

Owens, D. B. & Perkins, J. (1995), Vortex suppression on highly-swept wings by suction boundary layer control. *33rd AIAA Aerospace Sciences Meeting and Exhibit.*, AIAA-95-0683.

Panton, R. L. (1990), Effects of a contoured apex on vortex breakdown. *Journal of Aircraft* **27**, (3), 285-288.

Pao, H. P. (1970), A Numerical Computation of a Confined Rotating Flow. *Journal of Applied Mechanics* **37**, (2), 480-487.

Pao, H. P. (1972), Numerical Solution of Navier-Stokes Equations for Flows in Disk-Cylinder System. *Phys. Fluids* **15**, (1), 10-&.

Patanka, S. V. (1980), Numerical Heat Transfer and Fluid Flow, Hemisphere, Washington, D.C.

Paul, E. L., Atemo-Obeng, V. A. & Kresta, S. M. (2004), Handbook of Industrial Mixing, A. John Wile & Sons, Inc., New Jersey, xxxiii.

Payne, F. M., Ng, T. T., Nelson, R. C. & Schiff, L. B. (1988), Visualization and wake surveys of vortical flow over a delta wing. *AIAA J.* **26**, (2), 137-143.

Peckham, D. H. & Atkinson, S. A. (1957), Preliminary results of low speed wind tunnel tests on a gothic wing of aspect ratio, 1.0. *Aeronautical Research Council Technical Report*, TN No. Aero. 2504, C. P. No. 508.

Pereira, J. C. F. & Sousa, J. M. M. (1999a), Confined vortex breakdown generated by a rotating cone. *Journal of Fluid Mechanics* **385**, (Apr), 287-323.

Pereira, J. C. F. & Sousa, J. M. M. (1999b), Confined vortex breakdown generated by a rotating cone. *J. Fluid Mech.* **385**, 287-323.

Prasad, A. K. & Adrian, R. J. (1993), Stereoscopic Particle Image Velocimetry Applied to Liquid Flows. *Exp. Fluids* **15**, (1), 49-60.

Ranade, V. V. & Joshi, J. B. (1990a), Flow generated by a disc turbine. Part I experimental. *Chemical Engineering Research & Design* **68**, (1), 19-33.

Ranade, V. V. & Joshi, J. B. (1990b), Flow generated by a disc turbine. Part II. Mathematical modelling and comparison with experimental data. *Chemical Engineering Research & Design* **68**, (1), 34-50.

Ranade, V. V., Joshi, J. B. & Marante, A. G. (1989), Flow generated by pitched blade turbines II: Simulation using k-epsilon model. *Chem Eng Commun* **81**, 225-248.

Rao, D. M. & Johnson, T. D. J. (1981), Investigation of delta wing leading-edge devices. **18**, (3), 161-167.

Rayleigh, L. (1916). *Proc. R Soc. Lond. Ser. A*, 93, 148-154.

Revill, B. K. (1982), Pumping capacity of disc turbine agitators - A literature review. *Proceedings of the Fourth European Conference on Mixing*, Noordwijkerhout, Netherlands, 27-29 April, 1982, 11-24.

Revstedt, J., Fuchs, L. & Tragardh, C. (1998), Large eddy simulations of the turbulent flow in a stirred reactor. *Chemical Engineering Science* **53**, (24), 4041-4053.

Rieger, F., Ditl, P. & Novak, V. (1979), Vortex depth in mixed unbaffled vessels. *Chemical Engineering Science* **34**, (3), 397-403.

Roesner, K. G. (1990), Recirculating zones in a cylinder with rotating lid. *in: A. Tsinober, H.K. Moffat (Eds), Proceedings of the IUTAM Symposium on Topological Fluid Mechanics*, University of Cambridge Press, Cambridge, 1989.

Ronnenberg, B. (1977), Ein selbstjustierendes 3-Komponenten-Laserdoppleranemometer nach dem Vergleichsverfahren, angewandt auf Untersuchungen in einer stationaren zylinder- symmetrischen Drestromung mit einem Ruckstromgebeit. *Max-Planck-Inst. für Strömungsforschung, Bericht 20*.

Rushton, J. H., Mack, D. E. & Everett, H. J. (1946), Displacement capacities of mixing impellers. *Trans Am. Inst. Chem. Engrs.* **42**, 441-454.

Ruszkowski, S. W. & Muskett, M. J. (1985), Comparative mixing times for stirred tank reactors. *5th European Conference on Mixing*, Wurzburg, Germany, June 85, Paper 11.

Rutherford, K., Lee, K. C., Mahmoudi, S. M. S. & Yianneskis, M. (1996a), Hydrodynamic Characteristics of Dual Rushton Impeller Stirred Vessels. *AICHE*

Journal **42**, (2), 332-346.

Rutherford, K., Mahmoudi, S. M. S., Lee, K. C. & Yianneskis, M. (1996b), The Influence of Rushton Impeller Blade and Disk Thickness on the Mixing Characteristics of Stirred Vessels. *Chemical Engineering Research & Design* **74**, (A3), 369-378.

Sachs, J. J. & Rushton, J. H. (1954), Discharge flow from turbine-type mixing impellers. *Chemical Engineering Progress* **50**, (12), 597-603.

Sarpkaya, T. (1966), Forced and periodic vortex breakdown. *ASME Winter Annual Meeting WA/FE-7, Nov 27-Dec 1 1966*, American Society of Mechanical Engineers (ASME), New York, NY, United States, 7.

Sarpkaya, T. (1971), On stationary and travelling vortex breakdowns. *J. Fluid Mech.* **45**, (part 3), 545-559.

Sarpkaya, T. (1974), Effect of the adverse pressure gradient on vortex breakdown. **12**, (5), 602-607.

Schaeffler, N. W., Hoang, N. T. & Telionis, D. P. (1993), Controlling of delta wing vortices with vortex cavity flaps. *Proceedings of the ASME Winter Conference, Nov 28-Dec 3 1993*, Publ by ASME, New York, NY, USA, New Orleans, LA, USA, 1-8.

Schmucker, A. & Gersten, K. (1988), Vortex breakdown and its control on delta wings. *Fluid Dynamics Research* **3**, (1-4), 268-272.

Sharp, K. V. & Adrian, R. J. (2001), PIV study of small-scale flow structure around a Rushton turbine. *AICHE Journal* **47**, (4), 766-778.

Sheng, J., Meng, H. & Fox, R. O. (1998), Validation of Cfd Simulations of a Stirred Tank Using Particle Image Velocimetry Data. *Canadian Journal of Chemical Engineering* **76**, (3), 611-625.

Shi, X. & Shan, X. (1987), Relation between the quasi-cylindrical approximation and the critical theory for swirling flow. *Second International Colloquium on Vortical Flows, BBC*, 72-82.

Shih, C. & Ding, Z. (1996), Trailing-edge jet control of leading-edge vortices of a delta wing. *AIAA J.* **34**, (7), 1447-1457.

Shtern, V. & Hussain, F. (1996), Hysteresis in swirling jets. *J. Fluid Mech.* **309**, 1-44.

Sicardi, S., Conti, R., Baldi, G. & Cresta, R. (1979). *Proceedings of the 3rd European Conference on Mixing*, BHRA Fluid engineering, Cranfield, England.

Sorensen, J. N. & Christensen, E. A. (1995), Direct numerical simulation of rotating fluid flow in a closed cylinder. *Phys. Fluids* **7**, (4), 764.

Sorensen, J. N. & Daube, O. (1989), Direct simulation of flow structures initiated by a rotating cover in a cylindrical vessel. *Advances in turbulence 2: proceedings of the Second European Turbulence Conference*, Springer Verlag, Berlin, 383-390.

Sotiropoulos, F. & Ventikos, Y. (1998), Transition from Bubble-Type Vortex Breakdown to Columnar Vortex in a Confined Swirling Flow. *Int. J. Heat Fluid Fl.* **19**, (5), 446-458.

Sotiropoulos, F. & Ventikos, Y. (2001), The three-dimensional structure of confined swirling flows with vortex breakdown. *J. Fluid Mech.*, (426), 155-175.

Spohn, A. & Hopfinger, E. J. (1993), Observations of vortex breakdown in an open cylindrical container with a rotating bottom. *Exp. Fluids* **14**, 70-77.

Spohn, A., Mory, M. & Hopfinger, E. J. (1998), Experiments on Vortex Breakdown in a Confined Flow Generated by a Rotating Disc. *Journal of Fluid Mechanics* **370**, 73-99.

Squire, H. B. (1962), Analysis of the vortex breakdown phenomenon. Part I,. *Miszellanen der angewandten Mechanik*, Akadmie Berlin, 306-312.

Squire, S. B. (1960), Analysis of the "vortex breakdown" phenomenon, PartI. Imperial College of Science and Technology, Aeraunotics Department, Report No. 102.

Stein, W. A. (1992), Mixing times in bubble columns and agitated vessels. *International Chemical Engineering* **32**, 449-474.

Swithenbank, J. & Chigier, N. A. (1968), Vortex mixing for supersonic combustion. *12th International Symposium Combustion*, The Combustion Institute, 1153-1162.

Syred, N. & Beer, J. M. (1973a), Vortex Breakdown and flow stabilization in swirl combustors. *Combust Inst Eur Symp*, 542-547.

Syred, N. & Beer, J. M. (1973b), Vortex breakdown and flow stabilization in swirl combustors. *Combust Inst Eur Symp, Pap, Engl, Sep 16-21 1973, Sep 16-21 1973*, 542-547.

Syrjanen, J. K. & Maninnen, M. T. (2000), Detailed CFD prediction of flow around a 45 degree pitched blade turbine. *Proceedings of the 10th European Conference on Mixing*, Elsevier Science B.V., Delft, Netherlands, 2000, July, 2-5, 265-272.

Tabor, G., Gosman, A. D. & Issa, R. I. (1996), Numerical simulation of the flow in a mixing vessel stirred by a Rushton turbine. *Proceedings of the 1996 Fluid Mixing 5 Conference*, Institution of Chemical Engineers Symposium Series. n 140 1996. Inst of Chemical Engineers, Rugby, Engl., Bradford, UK, 25-34.

Tatterson, G. B. (1994), Scale up and design of industrial mixing processes, McGraw-Hill Inc., New York.

Thompson, M. C. & Hourigan, K. (2003), The sensitivity of steady vortex breakdown bubbles in confined cylinder flows to rotating lid misalignment. *Journal of Fluid Mechanics*, (496), 129-138.

Tiljander, P. & Theliander, H. (1993), Power Consumption and Solid Suspension in Completely Filled Vessels. *Chemical Engineering Communications* **124**, 1-14.

Tomlan, P. F. & Hudson, J. L. (1971), Flow near an enclosed rotating disk: Analisis. *Chemical Engineering Science* **26**, 1591-1600.

Truneva, E. A. (1976), On the mechanism of vortex breakdown point stabilization for low subsonic flow around a delta wing. **19**, (2), 87-90.

Tsitverblit, N. (1993), Vortex breakdown in a cylindrical container in the light of

continuation of a steady solution. *Fluid Dynamics Research* **11**, (1-2), 19-35.

Uhl, V. W. & Gray, J. B. (1966), Mixing: Theory and practice, Academic Press, 340.

Valentine, D. T. & Jahnke, C. C. (1994), Flows induced in a cylinder with both end walls rotating. *Phys. Fluids* **6**, (8 Aug), 2702.

Ventikos, Y. (2002), The effect of imperfections on the emergence of three-dimensionality in stationary vortex breakdown bubbles. *Phys. Fluids* **14**, (3), 13-912.

Versteeg, H. K. & Malalasekera, W. (1995), An Introduction to Computational Fluid Dynamics, The Finite Volume Method, Longman Scientific and Technical, 257.

Visbal, M. R. (1994), Onset of vortex breakdown above a pitching delta wing. *AIAA J.* **32**, (8), 1568-1575.

Vogel, H. U. (1968), Experimentelle Ergebnisse über die laminare Strömung in einen zylindrischen Gehäuse mit darin rotierender Scheibe. *Max-Planck-Inst., Bericht 6*.

Vorobieff, P. V. & Rockwell, D. O. (1998), Vortex breakdown on pitching delta wing: Control by intermittent trailing-edge blowing. *AIAA J.* **36**, (4), 585-589.

Wahls, R. A., Vess, R. J. & Moskovitz, C. A. (1986), Experimental Investigation of Apex Fence Flaps on Delta Wings. *Journal of Aircraft* **23**, (10), 789-797.

Watson, J. P. & Neitzel, G. P. (1996), Numerical evaluation of a vortex-breakdown criterion. *Phys. Fluids* **8**, (11

Nov), 3063.

Wentz, W. H. & Kohlman, D. L. (1969), Vortex breakdown on slender sharp-edged wings. AIAA Aircraft Design & Operations Meeting, AIAA Paper No. 69-778.

Werle, H. (1960), Sur l'ecoulement des tourbillons d'apres d'une aile delta aux faibles vitesses. *La Reserche Aeronautique* **74**, 23-30.

Wilcox, D. C. (1993), Turbulence modeling for CFD, La Canada, CA: DCW Industries, Inc., 460.

Wolf, D. & Manning, F. S. (1966), Impact tube measurement of flow patterns, velocity profiles and pumping capacities in mixing vessels. *Canadian Journal of Chemical Engineering* **44**, 137-142.

Wong, C. W. & Huang, C. T. (1988), Flow characteristics and mechanical efficiency in baffled stirred tanks with turbine impellers. *Proceedings of the 6th European Conference on Mixing*, Associazione Italiana di Ingegneria Chimica (AIDIC), Pavia, Italy., 1988, May 24-26, 29-34.

Wu, J., Zhu, Y. & Pullum, L. (2001a), The effect of impeller pumping and fluid rheology on solids suspension in a stirred vessel. *Canadian Journal of Chemical Engineering* **79**, (2), 177-186.

Wu, J., Zhu, Y. & Pullum, L. (2001b), Impeller geometry effect on velocity and solids suspension. *Chemical Engineering Research & Design* **79**, (A8), 989-997.

Yakhot, V. & Orszag, S. A. (1986), Renormalization-Group Analysis of Turbulence. *Physical Review Letters* **57**, (14), 1722-1724.

Yianneskis, M. (1991), The effect of flow rateand tracer injection time on mixing times in jet-agitated vessels. *Proceedings 7th European Conference on Mixing*, I, Brugge.

Yianneskis, M., Popiolek, Z. & Whitelaw, J. H. (1987), Experimental Study of the Steady and Unsteady Flow Characteristics of Stirred Reactors. *J. Fluid Mech.* **175**, 537-555.

Zhang, J., Tao, B. & Katz, J. (1997), Turbulent flow measurement in a square duct with hybrid holographic PIV. *Exp. Fluids* **23**, 373-381.

Zhang, W., Luo, S. & Zhu, P. (1991), Numerical simulation of vortex breakdown onset. *Int. J. Eng. Sci.* **29**, (2), 237-242.